Powered motion for molecular robotic devices via chemical and photochemical reactions

Rafael Carrascosa Marzo

Wolfson College

University of Oxford



Thesis submitted in partial fulfilment of the requirements for the degree of

Doctor of Philosophy at the University of Oxford

Hilary Term, 2022

Abstract

Industrial production necessitates ever smaller parts requiring new, more precise manufacturing techniques. Multiple approaches are being researched and tested to reach the goal of Atomically Precise Manufacturing (APM), including Molecular Additive Manufacturing (MAM). The core concept of MAM relies on the build-up, atom by atom, molecule by molecule, of a material or component. The framework necessary for the controlled positioning of these elements needs to have great precision and may be as complex to develop as the product itself.

The robustness and ease of use provided by the DNA origami self-assembly technique can be used as a means for the design and production of these smart material synthesizers. As I will explore in this thesis, the development of such synthesizer requires exploration of different methods of actuation. I will present the development of a device based on a 2D printer capable of traversing a flat substrate on request via the introduction of commands.

Initially I work to develop a dynamic, 3D, DNA origami system capable of linear actuation, that is, 1-dimensional movement. I base its architecture on the rotaxane given its structural particularities, mechanically locked but freely diffusing components. I improve the production of this system through different iterations, originally based on existing examples in the literature before moving onto more original designs that suit better the intended scope of the project. Throughout, protocols of synthesis were tested and improved upon to reduce the amount of time necessary for the assembly of the whole system. I also explore in these initial steps the method of actuating the movement of the slider along the rail, particularly the presence of overhang sequences that interact with the sequences in the slider oligonucleotides. This depends mostly on a “chemical” actuation dependent on the introduction of specific staples that force the detachment / attachment cycle of the slider necessary to produce diffusive motion between two points in the rail via strand displacement reactions (SDRs). The structures and their effective actuation are characterized via agarose gels, TEM, and DNA-PAINT.

As the work progresses, the following step is to obtain motion in 2 dimensions so that a surface area can be covered. To achieve this I developed a polar positioning device reminiscent of a circle quadrant, with a radial arm able to move along the arc while pivoting from the centre of the circle. This arm, like that of an analogue clock, is in turn a rotaxane, with a slider moving up and down its length. That way I obtain a polar system of 2-dimensional motion that covers the area encompassed by one quarter of the circle.

Later in the thesis I explore an alternative method for driving motion of a DNA device by using a photochrome, azobenzene, to induce double-stranded DNA (dsDNA) to dissociate into individual strands by shining UV light onto the modified complexes. The actual versatility and feasibility of the photoactuation is tested in two different prototype systems, a tweezer, and an array of dsDNAs.

Para Armonía, Tere, Pepe y Rafa

Acknowledgements

I would like to give my thanks to my supervisor, Prof Andrew Turberfield, for the opportunity offered to start this DPhil project in his group, and for his guidance and advice throughout it. Although I was given great latitude to work on my own terms, Andrew has always been available to offer help when needed. In the same line I would like to thank Dr Jon Bath for all his sagely advice and help, consistent all along this journey, within and without the lab; a spring of resourceful and practical advice, his patience and kindness have been a boon without a doubt. A true compañero, dale un beso a Claudia de mi parte.

I would also like to thank Dr Erik Benson, having him on this project and as a friend has made all the difference in the world. I couldn't imagine working with someone with a drier humour than him, and I mean this as the highest compliment I could give. I would also want to thank Dr Seham Helmi, her boundless wit, generosity, and warmth when most needed remain unmatched, although she should cool it with the true-crime media consumption (send my love to Francesco from me).

To them I would also like to add my thanks to all members of the Turberfield group that I had the luck of coinciding with in time and space: Alma Chapet--Batlle (thanks for the proofreading annoying Frenchwoman), Antonio Garcia Guerra (it is good that you switched to decaf), Catherine Fan (local fat cat and plushie hoarder), Joel Spratt (keep running, wherever you are now), Joakim Bohlin (bitter companion of ITN and boy-band member), Juan Jin (those masks came in clutch during the pandemic), Qian Zhang (uncle remembers you fondly my niece), Rana Abdul Razzak (Ranita for friends), Robbie Oppenheimer (hands down the best surname), Sam Tusk (tusks not included), and Sing Ming Chan (Monster Hunter machine). Special mention to Sanna Piippo-Henderson and Alan Francis, without their work this would have all fallen apart by now.

Having needed to use the TEM on a regular basis, I shouldn't get away without thanking Dr Errin Johnson and Dr Raman Dhaliwal for their support and mastery of the facilities, I pity those who break the vacuum.

To finish, thank you to my parents for their enduring support, love, and advice; to my grandparents all of them whom I miss dearly every day; and to my friends, away, close (Luisa, you weaboo, I have to name-drop you to reciprocate), and betwixt.

Contents

Chapter 1 1
Introduction 1
1.1 Atomically Precise Manufacturing 1
1.2 DNA nanotechnology 16
1.3 Molecular motors 22
1.4 Summary and Thesis structure 34
Chapter 2 37
DNA Origami Rotaxane for 1-dimensional motion 37
2.1 Aim 37
2.2 Rotaxane precedents 38
2.3 Initial linear structures 40
2.4 1st Iteration of the 1D system 44
2.5 2nd Iteration of the 1D system 62
2.6 Summary 75
Chapter 3 78
DNA Origami Structure for 2-dimensional motion 78
3.1 Aim 78
3.2 DNA origami design of the Bow-and-Arrow (BA) 79
3.3 1st Iteration of the 2D system 86
3.4 2nd Iteration of the 2D system 90
3.5 3rd Iteration of the 2D system 102
3.6 Summary 126
Chapter 4 128
Azobenzene Actuation 128
4.1 Aim 128
4.2 Azobenzene, a photoswitchable chemical in the DNA context 129
4.3 Azobenzene initial actuation system 134
4.4 Conclusion and future perspectives for the design 153
Chapter 5 156
Conclusion 156
Bibliography 160

Glossary

A Adenine.

ACSM Atomic and close-to-atomic scale manufacturing

AFM Atomic force microscopy.

AGE Agarose gel electrophoresis.

Alexa Fluorophore family by Molecular Probes Inc.

APM Atomically precise manufacturing

BsaBI Restriction enzyme

Biotin Vitamin which binds to streptavidin.

bp Base pair.

C Cytosine.

CaDNAno Computer aided DNA origami design software.

Cando DNA origami structure prediction software.

Cy Cyanine flurophore.

DNA Deoxyribonucleic acid.

DNA-PAINT DNA points accumulation for imaging in nanoscale topography

dsDNA Double stranded DNA.

EDTA Ethylenediaminetetraacetic acid: Hexadentate ligand able to chelate metal ions such as magnesium.

FAM Carboxyfluorescein fluorophore.

FRET Förster resonance energy transfer.

G Guanine.

M13 Bacteriophage with single stranded DNA genome.

MAM Molecular Additive Manufacturing

Mismatch Any base pair other than A-T or C-G.

nt Nucleotide.

NUPACK Nucleic acid package: DNA thermodynamics software.

oxDNA Coarse grained model of DNA.

PAGE Polyacrylamide gel electrophoresis.

PAINT Points acquisition for imaging nanoscale topography: Super-resolution localisation technique.

PCR Polymerase chain reaction

PEG Polyethylene glycol

poly-T Polymer of thymine nucleotides

RMSF Root-mean-square fluctuation

RNA Ribonucleic acid

RTPCR Real-time polymerase chain reaction

SDR Strand displacement reaction

SE Standard Error of the mean

SEM Scanning electron microscopy

ssDNA Single stranded DNA

STEM Scanning transmission electron microscopy

STM Scanning tunnelling microscopy

Streptavidin Tetrameric protein with a high affinity for biotin

SYBR™ Gold Nucleic acid stain

SYBR™ Green II Nucleic acid stain with higher relative affintity for ssDNA and RNA than Sybr Gold

T Thymine

TAE Tris acetate EDTA buffer

TE Tris EDTA buffer

TEM Transmission electron microscopy

TMSD Toehold-mediated strand-displacement

U Units (measure of enzyme activity)

U Uracil

UA Uranyl acetate

UV Ultraviolet, electromagnetic radiation with wavelength of 10–400 nm

XmnI Restriction enzyme

Chapter 1

Introduction

In this chapter I will describe the motivation and rationale behind the specifics of the experimental project by explaining the core concepts of this work. Firstly, I will explain the practical motivator of the project, the attempt to provide an alternative means of improving current industrial standards of manufacture by expanding the existing tools within Atomically Precise Manufacturing (APM) and more specifically in Molecular Additive Manufacturing (MAM). Following that I will briefly expound on DNA nanotechnology and, more specifically, DNA origami as both a material and technique of choice to produce the synthesizer or printing device. I will then delve deeper in the current state of the art regarding molecular motors and their actuation mechanisms before moving into the characteristics of a prospective printing method.

1.1 Atomically Precise Manufacturing

There is an increasing need to produce ever smaller and more compact components and to create smart materials with very precise specifications. I will review first the current techniques being used or researched in the field before moving onto the concept behind the approach undertaken in this thesis.

1.1.1 Established approaches

From the host of techniques currently used in manufacture at the micro and nanoscale, modern lithography, a group of techniques that etch away (subtractive) or directly "write" (additive) on a material to produce patterns and structures, is the go-to methodology for manufacturing electronic integrated circuits and other devices. Despite being able to reach sub-nanometre accuracy (1), the materials available to be worked on by these techniques are limited due to the harsh reaction conditions; the scale of production is

limited as well by diffraction limits and quantum tunnelling effects amplified at the defects in the materials. A way of overcoming these physical limitations is to directly manipulate the atoms of the material, via removal, addition, or transformation, when manufacturing goods at the macro, micro, and nanoscale. These techniques can be grouped under the tag of APM or of atomic and close-to-atomic scale manufacturing (ACSM). Below, I discuss the different approaches currently applied to ACSM.

1.1.1.1 Subtractive manufacturing

Removal of atoms from a solid block of material to create 3 dimensional structures falls in the ACSM category of subtractive or destructive techniques. These include, but are not limited to, ultraprecision machining, high energy beam machining, atomic layer etching, and atomic force microscope nanomachining. The inner workings of these techniques are beyond the scope of this thesis, but it is interesting to note that the atomic force microscopy (AFM) nanomachining consists in applying a shearing force in combination with a "mechanochemical" reaction under specific material conditions in silica wafers (2). It is noteworthy that none of these techniques can achieve single-atomic layer or single-atom removal in a consistent fashion, without inflicting mechanical or thermal deformations on the base material, or on a scale that fits the requirements of industry (1).

1.1.1.2 Additive manufacturing

Another strategy is the addition of the atoms or molecules on a surface, be it by chemical reactions, atomic layer deposition, or by means of self-assembling components arranging themselves into the structures of interest without external manipulation.

The self-assembling materials frequently studied are DNA molecules, peptides, proteins, and other biopolymers. They act as atomically precise building blocks. Both protein and peptides have seen interesting developments in this field (3,4), particularly peptides (5,6), but their application to create synthetic structures is still at an early stage

of development. The production of these precisely ordered assemblies, of these biomolecules, that posses advanced functions is yet to be controlled and consistent. DNA is a particularly versatile molecule for this purpose due to its physical characteristics, allowing for the self-assembly of structures with very precise nanoscale features (7,8).

A common thread in studies of these types of substrate for additive, atomically precise manufacturing is that they can present high error rates (9) and some problems in the scale-up. Application of these molecules in MAM requires robust parallel systems capable of both transporting the self-assembling molecules and allowing for their specific mechanical interactions that lead to the self-assembly (1).

Some viable techniques for position-directed assembly have been advanced, such as scanning probe nanofabrication technologies, in the shape of dip-pen nanolithography (DPN). Still, the issue of scalability and production speed remains.

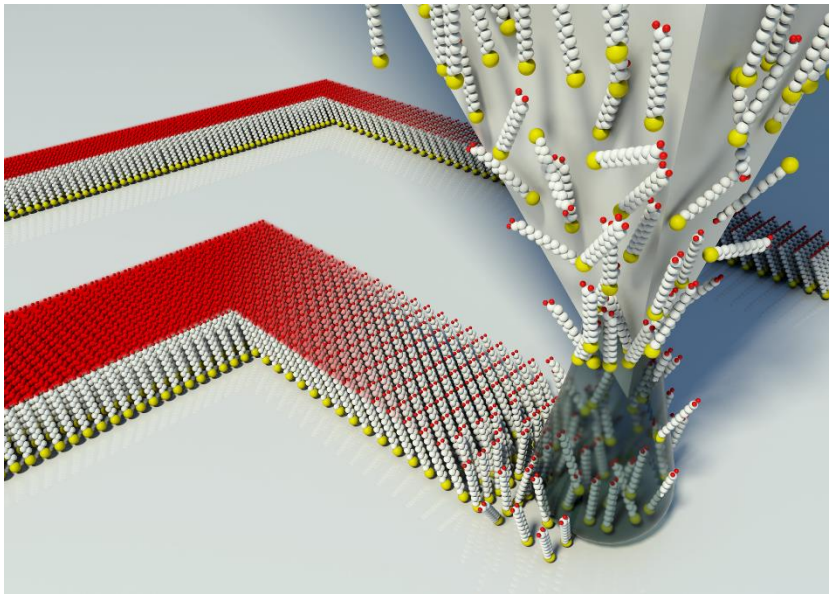

Figure 1.1. Graphic representation of a DPN mechanism, molecules are distributed from a tip onto a surface using a water meniscus. Taken from NanoInk Inc. (Illinois, USA)

It will be clear that these are among the main drawbacks of using scanning probes in ACSM as I will explore in the next section regarding transformative manufacturing techniques.

The scope of this thesis is to ultimately provide such a transport/localising system for molecular building blocks. The system would not be limited to biomolecules as substrates, but it would be made out of self-assembled DNA. This system is not without its weaknesses, as I will explain below, but it could be understood as a starting point for the introduction of other materials better suited for the task of MAM.

1.1.1.3 Transformative manufacturing

A third category of ACSM techniques, transformative manufacturing consists of the displacement of single atoms from one location to another on the target material, mostly through scanning tunnelling microscopy (STM), scanning transmission electron microscopy (STEM) or AFM.

The STM setup consists of a thin needle point, of atomic sharpness, that conducts current, that is brought to proximity, "a few atomic diameters" to a substrate. Scanning does not require physical contact between tip and substrate as the voltage applied to the tip allows for electrons to tunnel in the vacuum gap. Due to the sensitivity to distance of this tunnelling, changes of the needle position with a subatomic level of precision can be easily achieved by measuring the variation of tunnelling current and using it to control the gap length. It is used as an imaging technique since, either by maintaining the height or the current of the voltage of the tip, a clear profile of a surface can be made out with the tunnelling current or height variation as a feedback signal (10).

This technique allows for different ways in which the needle tip can interact with single atoms on the substrate and displace them (11), either laterally (lateral manipulation or LM) or vertically (vertical manipulation, VM). In the former case, the tip approaches an atom adsorbed in a surface until the force between tip and atom has reached a sufficient value that, by maintaining the current of tunnelling constant, when moving the needle across the surface the atom follows suit. Once the desired location is reached the tip-atom

distance is increased until the force weakens, and the atom remains in its new location. In the VM the tip gets close enough to the atom so that there is a physical contact, and it is adsorbed to it due to the greater strength in the tip-atom binding than with the surface. When retracting the tip, the atom is then taken with it. The needle then is placed to the new location and is lowered again, at this point applying tunnelling current or mechanical motion allows the atom to be deposited on the surface in this secondary location (12). Given these characteristics, STM is currently being used for producing atomic scale structures in research (13) and in APM manufacture of single-atom transistors (14), among other products (15,16).

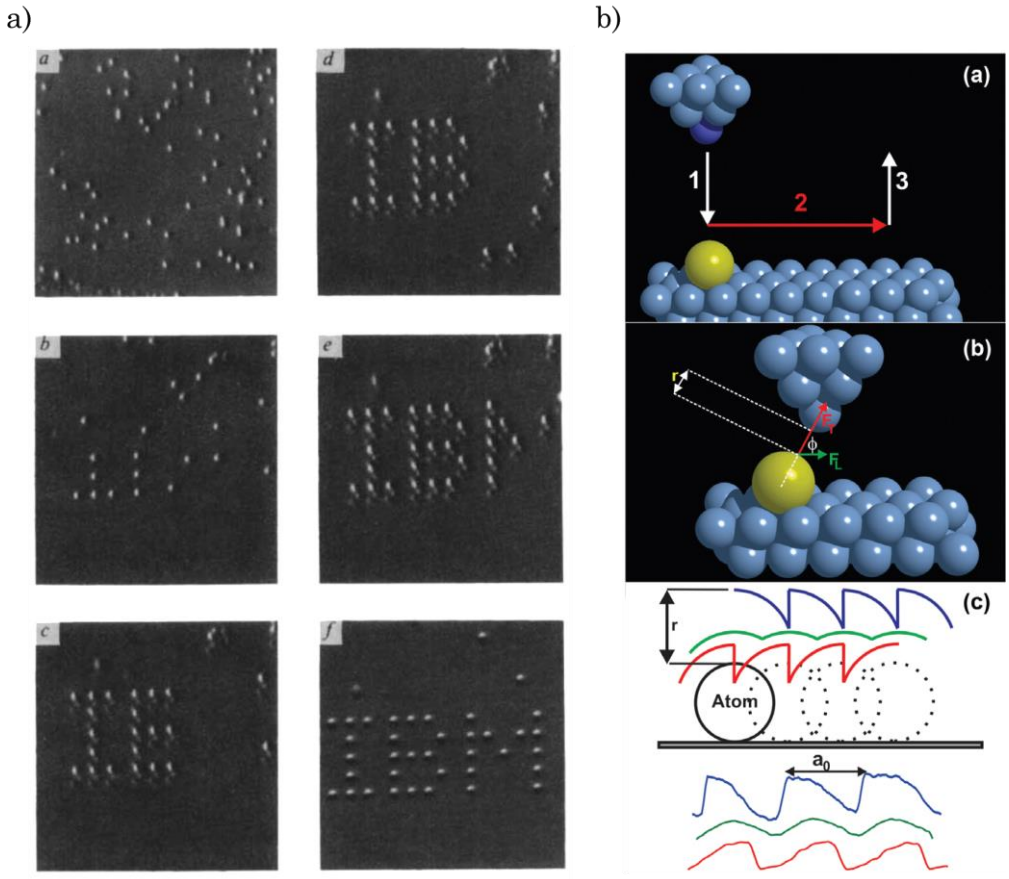

Figure 1.2. STM used in transformative manufacturing. a) Xenon atoms arranged in a nickel (110) surface. Taken from (11). *b) Schematic representation of LM, the geometry of the system, and the different types of interactions the tip can have on the adsorbed atom (pulling (blue), pushing (green), and sliding (red), included a drawing of the manipulation signals). Taken from* (12).

This technique is not without its drawbacks. It requires sophisticated instruments and electronics, great operational expertise, and extremely well-controlled environments. Throughput is extremely low, making it a technique inadequate for the scaling up necessary for industrial-level manufacture. The range of materials that can be modified with this technique is also limited since they have to be electrically conductive and able to withstand the ultrahigh vacuum and cryogenic temperatures needed for the operation of the technique (17).

Another transformative ACSM technique is AFM, which also relies on a sharp needle or tip interacting with a substrate. In this case, and unlike the STM, the tip is on a flexible cantilever and the physical principle of interaction with the atoms in the surface is not that of quantum tunnelling but that of atomic forces of attraction and repulsion. These interactions affect the cantilever by displacing it, these changes are registered by a laser that is trained on it and whose reflection, and its change, is registered by a photosensitive detector (18–20). There are different modes in which an AFM can operate when imaging a surface, contact, noncontact, and tapping mode.

Contact mode has the tip come into direct contact with the surface and, while maintaining the interaction force, the displacement of the tip of the cantilever by the repulsive forces is measured. Noncontact mode has the cantilever oscillating at a specific frequency while lowering it towards the surface; when within the van der Waals force range (30-150 Å) this vibration frequency is disrupted. In response to this the system corrects the height of the tip so that the frequency is maintained constant. The feedback signal allows for a reconstruction of the surface's contour. In the tapping mode, the tip, oscillating near or at its resonance frequency, coming into contact with the sample surface only intermittently, which causes a change in the amplitude of the oscillation. The laser reflection system relays these changes which provides a force-distance curve characterizing that spot in the surface.

Much like STM, the AFM can move atoms laterally or vertically but in this case the forces at play are van der Waals, electrostatic, and magnetic dipole interactions, mostly done in tapping mode (17). In the case of vertical manipulation of atoms, AFM presents some benefits over STM. In AFM there is the possibility of a thermally activated exchange of the atoms between tip and surface at room temperature, given reduced thresholds of interaction of energy barriers upon the gradual lowering of the tip (21). This reduces the time to produce atomic patterns, which, along with the ability of manipulating non-conductive materials, could make the AFM an improvement over the STM, although its implementation is still under development (1).

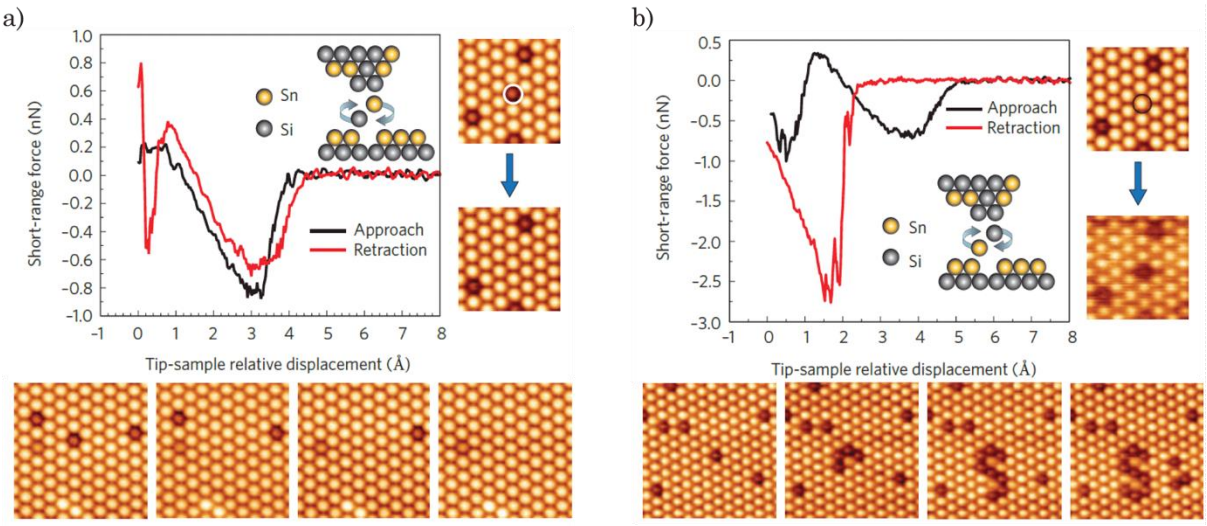

Figure 1.3. AFM used in transformative manufacturing. Vertical-interchange atomic manipulation allows the a) addition or b) removal of atoms from a surface. Taken from (17).

Lastly, STEM has also been explored as a transformative technique. In the case of TEM, a sample can be analysed with a beam of electrons that, being irradiated over the whole field of view, goes through the substrate and is scattered. This scattering is used as the basis for the imaging of the sample. In STEM the electron beam is focused into a much smaller beam by using condenser lenses. The smaller beam sweeps over the sample and its scattering is used to synthesize the image. Unlike SEM, STEM has an atomic level scale of resolution when used for imaging (22), although it has also been used in single-

atom manipulation (23,24). In this context, the movement of atoms is achieved by using the focused electron beam to irradiate an atom of the layer, on occasions causing the exchange in position between the irradiated atom and the neighbouring atom that was the objective of the transposition. A continuation of this procedure can induce the displacement of a specific atom across a sample surface, although it does not reach the precision level of STM due to the possibility of the irradiated atoms to be knocked off or the target atoms to move to unexpected/uncontrolled positions in the lattice. STEM as an atom-manipulating technique is, therefore, still in its very early stages.

1.1.2 Molecular Additive Manufacturing

Outside of these approaches to the current technological challenge of APM, molecular additive manufacturing (MAM) presents an interesting, alternative outlook towards true, fully customisable, bottom-up synthesis of materials and parts by direct single-atom/molecule manipulation. The principles applied in this type of manufacturing follow those of nanotechnology or "molecular technology".

The concept of molecular technology to describe the production of elements of interest at the atomic scale was explored in Erik Drexler's landmark work "*Engines of Creation*". It described the possibilities that nanotechnology presented when being directed to generate materials by handling individual atoms and molecules in a bottom-up approach, in clear break from the traditional top-down techniques we still use, labelled in contraposition as "bulk technology". Drawing inspiration from the molecular machines found in nature, proteins, and enzymes more specifically, and the use that we make of them in the biochemical sciences, Drexler envisioned a host of man-made nanomachines with characteristics more suitable for industrial manufacture. See below Figure 1.4 for some examples.

a)

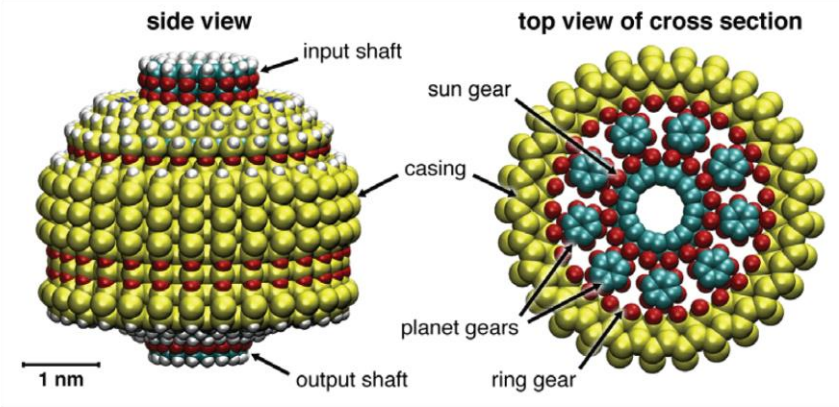

b)

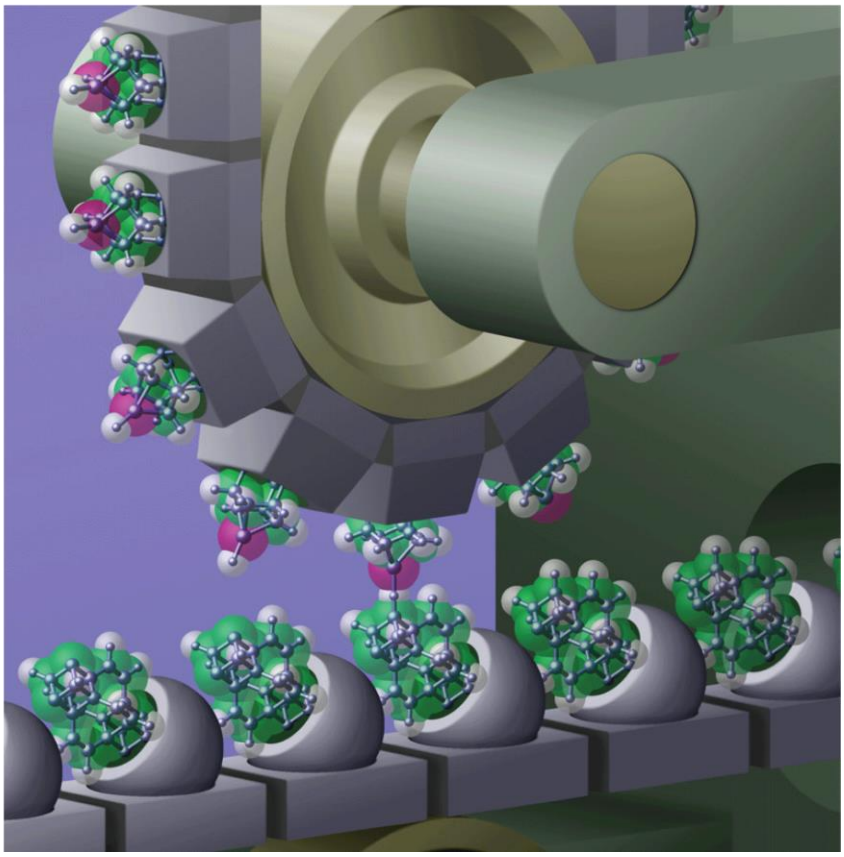

Figure 1.4. Hypothetical nanoscale systems. a) A molecular planetary gear based off macromolecular examples of this mechanism capable converting high speed/low torque rotations of a shaft into low speed/high torque ones. b) A schematic illustration of a molecular mill depositing single hydrogen atoms on a nanoscale parts on a moving belt. Taken from (25).

Natural nanomachines handle molecules and atoms directly, "grabbing" them from the environment, bringing them together in specific orientations and binding them so by catalysing chemical reactions; their hypothetical artificial counterparts would perform in

the same way but with greater flexibility (26). They would be able to perform what Drexler termed as “mechanosynthesis”, which is the guidance, through mechanical means, of chemical synthesis. This mechanical positioning is atomically precise and it is not constrained by the steric or electronic properties of the reacting elements, quality that differentiates it from enzymatic and currently developed synthetic processes (27).

Drexler’s proposition was to approach biochemistry from an engineering outlook, trying to take the elements that nature uses when designing functional proteins and making designs of our own. The key idea would be to design proteins that would fold predictably so that *de novo* proteins could be develop to perform tasks of interest, effectively increasing the toolbox of molecular engineering. A thorough understanding of the principles determining protein structure and folding has allowed for the design of *de novo* proteins with atomic accuracy (28,29). The introduction of new functions on these newly designed proteins is an ongoing effort, given the complexities of introducing active sites into idealized *de novo* protein designs; some functionalities that have been achieved are designs of axle-rotor systems (30), and protein pH switches (31).

Since proteins are not without drawbacks in the industrial context, he advocated for using naturally occurring nanomachines, these proteins, to synthesize the first generation of the artificial nanomachines. The building blocks of these second generation machines would be better suited for its human-devised applications. Sequences of iteration would follow and finally move this manufacturing devices to the realm of engineering. The newly developed synthesizers, called “assemblers” would be able to work with programmable precision in harsh environments and allow for the study of materials and products that can be designed in theory but do not exist in the natural world (26). In the context of this prospective APM technique, one of the main issues with the previously mentioned techniques is eliminated; MAM can be parallelized by having many of the assembler devices working in solution or on the same substrate simultaneously since, as with other

self-assembly methods, there is no need for a microscopic probe to direct the atomic alterations.

Although Drexler addresses certain caveats to this hypothetical direction that nanotechnology could take, physical and biological points of constriction, the proposition drew some critiques as to the actual feasibility of this technology, given the non-trivial constraints that the chemical processes and their controlled execution present. Nobel prize winner prof. Richard Smalley dismissed the idea of these assemblers due to the nature of chemical reactions and bond formation since these reactions come about from the concerted interaction, in the right environment, of 5-15 atoms. A prospective assembler, as described by Drexler, would require as many operator arms as atoms involved in the reaction, which would become very cumbersome. There is only a very limited space in which these atomic interactions occur, nanometre per side; it would be unfeasible to have a multitude of, even if atomic-sized, arms interacting in that same space. Another physical impossibility raised was the fact that this arms, when picking up atoms of the materials or of chemical reagents, would have no way of dropping them in the precise location as they would remain stuck to the arms. These critiques were coined as fat and sticky fingers respectively (32).

In a response from the Institute for Molecular Manufacturing, Drexler addressed these issues. Regarding the "fat fingers", it was pointed that there are many examples of chemical reactions involving only two reactants. An example of this is the STM version of transformative APM that could "push" an atom towards another fixed atom on a substrate and make them react (33). When having steric constraints on the arm of the operator, to produce bulk nanoparts that have sizes between 10-100 atoms, solution or gas phase chemistry can be relied upon. These nanoparts can then be directed via intermediate devices into specific positions in a manufacturing process, much like the mechanism of the ribosome. Despite not having an atomically precise control of the protein structure,

the ribosome can, by programmed concatenation of amino acids, achieve molecular control of the peptide synthesis that yields an atomically precise product. Regarding the "sticky fingers", the problem, although existing in some reactions, is not a constant of chemistry. Back again in the STM-aided manufacture, VM shows that an atom can be removed from the tip of the tool by charging the tip voltage (33). Other scanning probe microscopy techniques have shown the ability to drive a chemical reaction in a specific location of a molecular substrate by means of a functionalized probe (34,35). Ultimately, Drexler called for the need of further research in the area to prove or disprove the validity of the proposed system of MAM (36).

Further discussion between the two figures (37) did not lead to a decisive resolution (38).

1.1.3 Applications of APM

Whatever the route to atomically precise manufactured products, what might be the key applications of a technology to manufacture "single-atom-devices or complex nanosystems with atomic-level precision"? (1). To assemble with atomic-level precision implies the introduction of new functionalities into these nanosystems along with key improvements in their industrial production such as, low-variability among the units produced, ultra-high performance of the process, and reduced costs of production (energy and materials).

It is essential for the continued improvement of current electronics, particularly in following Moore's Law, to break through the current fabrication limitations and going down to the ultimate, perceived limit of structural control at the atomic level. In doing so: the spatial resolution of current microfabrication techniques, e.g., nanolithography, referred to earlier in the chapter, could be further improved; defects in production, and their great effect on device functionalities, could be minimized. Sustainability of

manufacture, would be substantially improved as the energy cost and material wastage would be reduced (39). By eliminating the need for refined starting materials, casting processes, or machining/destructive processes that require a great input of energy. Due to the scale of the process the starting materials could be introduced in liquid format, so that no physical modification of solids, and subsequent waste of material, takes place. Another intrinsic benefit to APM is the improvement of the devices produced over the ones produced using conventional manufacturing techniques, since a greater degree of optimization at the material level could be achieved. Material properties would be considered as a part of the design of the devices themselves.

The main industries that currently benefit from APM to some extent are those that are making use of atomic-layer deposition in photovoltaics, and other fuel cells (40), and in the semiconductor industry (41). Aside from this, these manufacturing techniques have the possibility of improving many other fields, materials, life sciences, agriculture, and information technology (42). Potential applications include "thermoelectrics and anisotropic heat spreaders, solid-state lighting, molecular electronic and plasmonic circuits, selectively permeable membranes, and self-repairing materials with high strength-to-weight and fracture resistance" (43).

In the area of nanoelectronics, examples of applications include quantum computers. Earlier concepts of quantum devices base them on arrays of atoms in a surface that embody qubits as nuclear spin states have been produced with a combination of STM and lithography (44).

In life sciences, improved understanding of self-assembling biomolecules (DNA, peptides, proteins), would advance the development of molecular/cellular biophysics and industrial applications including biomimetic systems and improved diagnostics and therapeutics for human health (9).

Some examples of "bio-inspired design features" are superhydrophobic surfaces that imitate the lotus leaf surface and other architectures by producing structures and patterns at the nanoscale (45); superadhesive materials that use nanopillar patterns such as those found in gecko toes (46); or optical elements such as cameras (photodiodes and microlenses) that imitate compound eyes from insects to achieve superior field of view (47).

An important contribution in both the biotechnological and medical field brought about by APM will be the further development of lab-on-a-chip devices (LOC) that integrate a complete laboratory workflow on a compact chip, incorporating nanoscale structures, channels and patterns (48).

1.1.4 Regarding the proposed system

Having presented the state of the art and outlooks in the field of APM, and having also discussed interesting approaches that one could take when tackling the inherent problems of these manufacturing techniques via MAM, I will proceed now to give a schematic explanation of our proposed system and the short-medium-long term perspectives we have on it.

Our system will act as a transport/localising apparatus for self-assembling molecules in APM. Its functionality is that of a 2D printer working at the molecular scale. It is based on a framework constructed with DNA, via DNA origami techniques, providing sub-nanometre precision in its assembly. These structures will be dynamic in nature, to enable 2D motion of the printer, and will be actuated by the introduction of instruction sequences in the shape of DNA strands that will induce strand displacement reactions (SDRs), achieving positioning with nanometre precision.

These DNA printers are intended to be initial prototypes in the development of MAM, a schematic of which can be seen in Figure 1.5. They will be slow and error-prone. They

will also be limited to aqueous solutions with no harsh chemistries, due to the nature of the material of the system and its actuation mechanisms. Regardless of these limitations, the system lends itself to great levels of parallel production, as we can have many molecular devices in simultaneous operation. In the medium term this system will allow for an initial, imperfect foray into APM and could be used as a first step in an iterative production cycle of improvement. Imperfect printers producing less flawed printers, out of materials that do not suffer from the intrinsic functional and structural limitations of DNA (highly stable (crosslinked), multi-nanometer-scale building blocks synthesized by bulk chemistry, e.g. spiroligomers (49)) and that allow for harsher manufacture conditions, with greater rigidity, therefore producing more precise and adaptable printers. This will also lead to an improvement in the molecular additive process itself, the local control of chemical reactions. We envision that in the long term this iterative cycle will produce devices apt for transferring MAM into industrial manufacture levels.

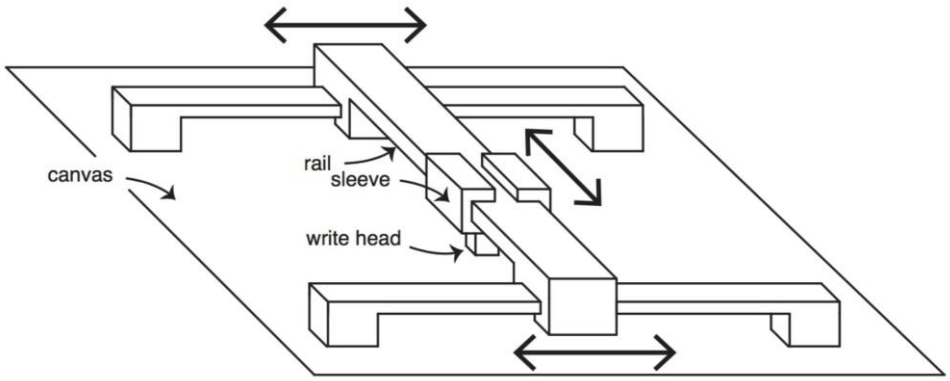

Figure 1.5. Schematic illustration of the proposed system. Taken from "DNA Strand Displacement driven Molecular Additive Manufacturing (DSD-MAM), Contract Number: EE0008310, Dana-Farber Cancer Institute/University of Oxford".

1.2 DNA nanotechnology

1.2.1 Molecular and structural properties of DNA

The main role played by DNA in the biological setting is the storage and replication of the genetic information. This subsection will focus on the chemical and physical characteristics of the molecule that are relevant to the development of DNA nanotechnology and DNA origami in particular.

A DNA molecule is composed of a sequence of nucleotides, the monomers of this biopolymer, that consist of a pentameric sugar (deoxyribose) linked to a phosphate group at the 5' carbon and to a nucleobase at the 1' carbon. When these monomers polymerize, they do so by linking the phosphate group of one monomer to the 3' hydroxyl of another to form a phosphodiester bond. The alternation between the pentoses and the phosphate groups constitute the backbone of the DNA polymer.

Within the structure of the nucleotide, the nucleobase, also referred to as nitrogenous base or base, can be one out of four: adenine (A), cytosine (C), guanine (G) and thymine (T). A and G are fused rings (hexagon bound to a pentagon) that are derived from the purine structure, hence their shared category name of purine bases. T and C are single rings (hexagon) derived from the pyrimidine structure, pyrimidine bases. These bases interact with one another, normally, in defined pairs, A-T and G-C, via hydrogen bonds, 2 and 3 respectively, between amine and carbonyl groups. This, along with hydrophobic forces (stacking interactions) of the aromatic rings in consecutive monomers, gives great structural stability to the interaction of two strands of DNA (50).

It is as double-stranded polymers that DNA is usually found in nature, only separating partially into individual strands during the events of replication and transcription of genetic information. Double stranded DNA (dsDNA) is an antiparallel duplex. The configuration of DNA in nature, most commonly the B-form helix, was discovered in 1953

by Franklin, Watson, and Crick (51–53). The helix has a 2 nm diameter, each turn is ~10.5 base pairs long, it winds in a right-handed manner with the base pairs in an inclined plane, the bases are not positioned at the same level as their counterparts. This leads to the appearance of two types of indentations or grooves between strands, along the helix, the major and minor grooves.

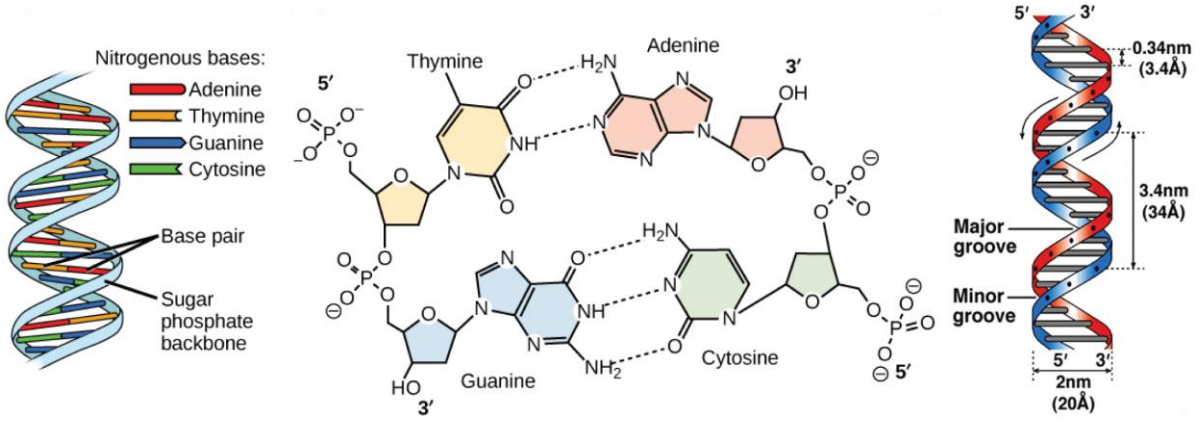

Figure 1.6. Structure of DNA: Schematic representation of a DNA B-helix, chemical structure of a DNA base pair, physical measurements of the DNA B-helix. Taken from Introduction to Biology (Openstax).

By exploiting the Watson-Crick base pairing rules, it is possible to use DNA as a building block for an accurate and programmable construction using component strands whose sequences precisely determine the design of structures at the nanoscale. Some of the early examples of using DNA sequence specificity for producing non-natural structures dates to Seeman's nucleic acid junctions (54). DNA also presents propitious physical characteristics for use as a building block; dsDNA has a persistence length of ~50 nm (55) whereas ssDNA has one of ~0.75 nm (56), this gives DNA the possibility of both being a stiff polymer, that aids with motif positioning at the nanometre scale, and a more flexible element that gives customizable freedom of movement to interconnected parts in the structure.

To these favourable characteristics, is added the fact that there is an abundance of techniques for its handling and manipulation. Being a component in biological systems,

there is a wide variety of enzymes and molecules that can act upon it, modifying its length or chemical modifications (i.e., restriction enzymes, ligation enzymes, kinases, phosphatases, etc.). Additionally, the development of solid support synthesis techniques, such as the phosphoramidite method (57), has made the production of custom designed oligonucleotides an efficient process, producing longer and more complex sequences with a decreasing cost over the years (58,59).

Due to this, DNA nanotechnology has evolved in a relative short period, from the original designs to examples of growing complexity such as 2D crystals (60), nanotubes (61), arrays (62), and 3D structures (63,64).

1.2.2 DNA origami

Some of the original DNA nanostructure designs depended on a precise stoichiometric balance of all strands involved in the nanostructure for the end product to be assembled. Due to the inherent difficulty of achieving this requirement, their self-assembly lead to low yields of the target structure and many unwanted by-products that would require several steps of purification. An improvement in design for self-assembly is the introduction of an order in the steps, having sub-sections of the structure forming first through deliberately strong interactions, followed up by later weaker ones that join these pre-formed sub-units (60,62,65–67).

Another approach to solve the complex stoichiometric issue of DNA structures' self-assembly was the use of a long "scaffold" strand to which the rest of the strands or "staples", much shorter oligonucleotides, would bind to create the desired shapes. Along with the improved yields, this strategy also simplifies purification, the staples can be added in excess and then be easily removed from the solution since their molecular weight is much less than that of the structures produced.

A landmark study within the field, produced by Rothemund (68), gave way to a new building technique, using this scaffold strategy, called DNA origami. In DNA origami, it is possible to produce complex architectures in a one-pot assembly reaction by having hundreds of staples bind by base complementarity to two or more distinct sections of the scaffold, forcing bends and shapes to form (Figure 1.7). This scaffold is often circular and usually extracted from biological sources, the sequence usually being irrelevant to the design. In origami structures, all base-pair interactions occur between the staples and the scaffold, meaning that different set of staples will produce different structures even when using the same scaffold sequence. This ease of use paired with the ease of purification and high yield made DNA Origami a key technique in DNA nanotechnology.

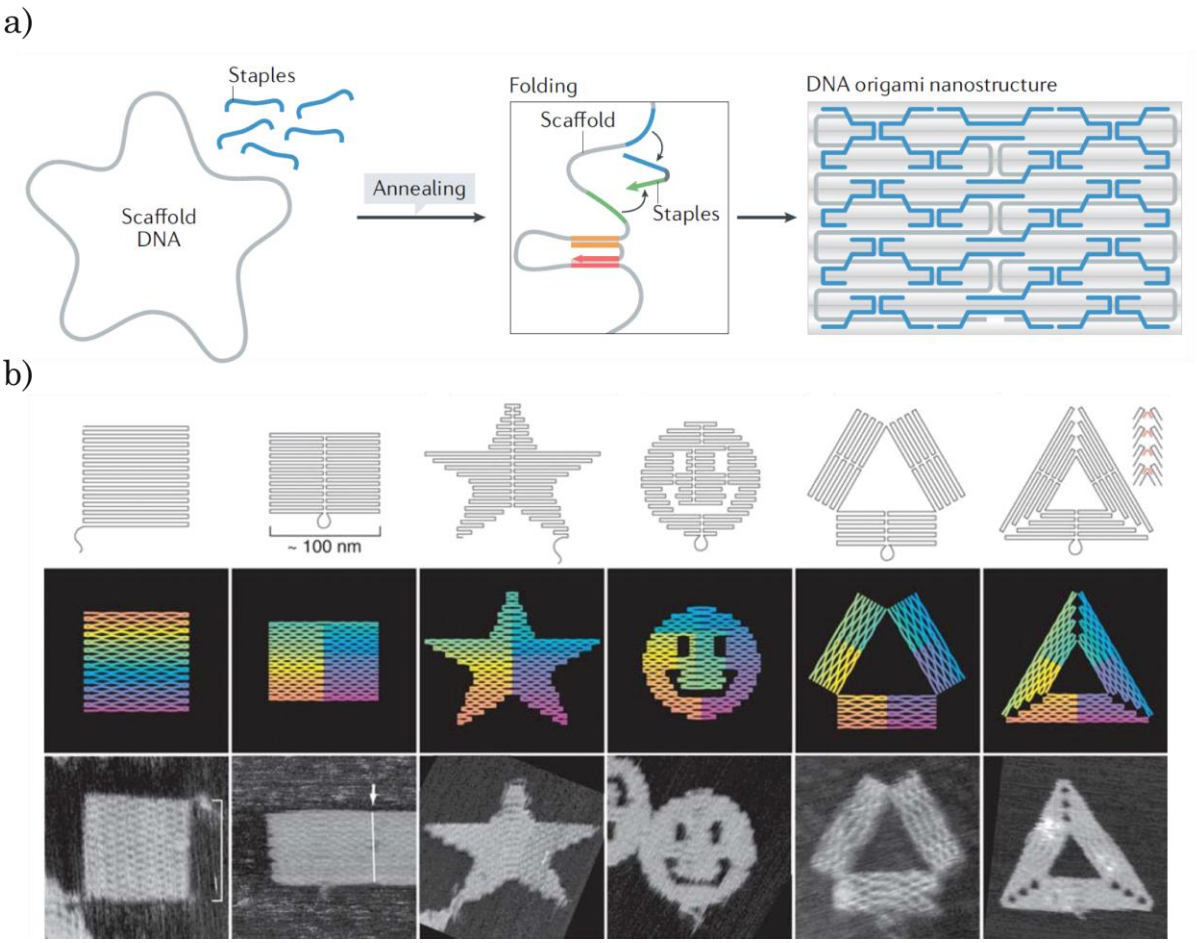

Figure 1.7. DNA origami method. a) Schematic representation of the DNA origami folding, the long, circular strand in grey (scaffold) is bound to shorter strands (blue) after an annealing process, inducing bends and shaping into pre-defined forms. Taken from (69). *b) Dangling curves and loops represent unfolded sequence. Second row from top, diagrams*

showing the bend of helices at crossovers (where helices touch) and away from crossovers (where helices bend apart). Colour indicates the base-pair index along the folding path; red is the 1st base, purple the 7000th. Bottom row, AFM images. All images and panels are 165 nm × 165 nm. Figure and caption taken from (68).

Initially, its application was restricted to sheets formed from single layer of parallel helices to fill in the target shape. These helices are composed of the scaffold and the staples and are interconnected by both types of strands "crossing over" between neighbouring strands in locations permitted by the DNA helical structure. These crossovers are placed in the locations of closest proximity to the continuous helix, meaning that there should be an even number of half turns (~10.5 bps) between crossovers to the same helix, but an odd number of half turns between crossovers to the two different neighbouring helices (in a single layer architecture). Scaffold crossovers to neighbouring helices are placed where necessary for the contour of the shape, and staple crossovers where they can produce and stabilize the bends needed in the scaffold strand to produce the target shape. By introducing extra nucleotides, or removing them, from these arrangements one can induce twists and curvatures in these single layers (70). By having sections of the scaffold unpaired, flexible single-stranded regions can act as hinges in between stiffer regions, providing additional dimensions of complexity and dynamism to designs (71).

As the technique was developed, the complexity of the nanostructures also escalated, to include multiple-layer 3D structures. The distribution of the helices can be that of a honeycomb (71,72) or square (73). Given the increasing size and complexity of the nanostructures, planning of their design was greatly simplified by the development of the open-source software CaDNAno (72). Although its interface and some of its functionalities have evolved over subsequent editions of the program, the core has remained the same; with CaDNAno one can produce a cross section of the helix distribution in the prospective structure, following it up with a design of the scaffold routing and crossover distributions of these helices. After having the scaffold in place, the structure is populated with the

staple sequences, placing them in the necessary spots to ensure the cohesion and stability of the structure. Ultimately, after adding all extra features that the user may want in their design, the sequence of the scaffold is introduced and the set of sequences for the staples are generated. The designed architectures can then be studied, in their 3D appearance, in a variety of programs such as CanDo (74), OxView (75), or OxDNA (76); the later providing coarse-grained simulations of the DNA nanostructures.

DNA origami has been used to produce many 3D structures (See Figure 1.8), one of the strategies being the superimposition of the simpler 2D single-layers, with some omitted sections of the helices in the central areas to create hollowed-out structures (70,77,78). Origami structures have been used to realize biophysical studies (68,79–81), and initial designs for therapeutics (82–84), manufacture (85–87), and plasmonics and electronics (88,89). DNA origami has also been used in the production of dynamic structures such as opening receptacles (77,90–93), rotor arms (94–99), and sliders (86,87,99–101).

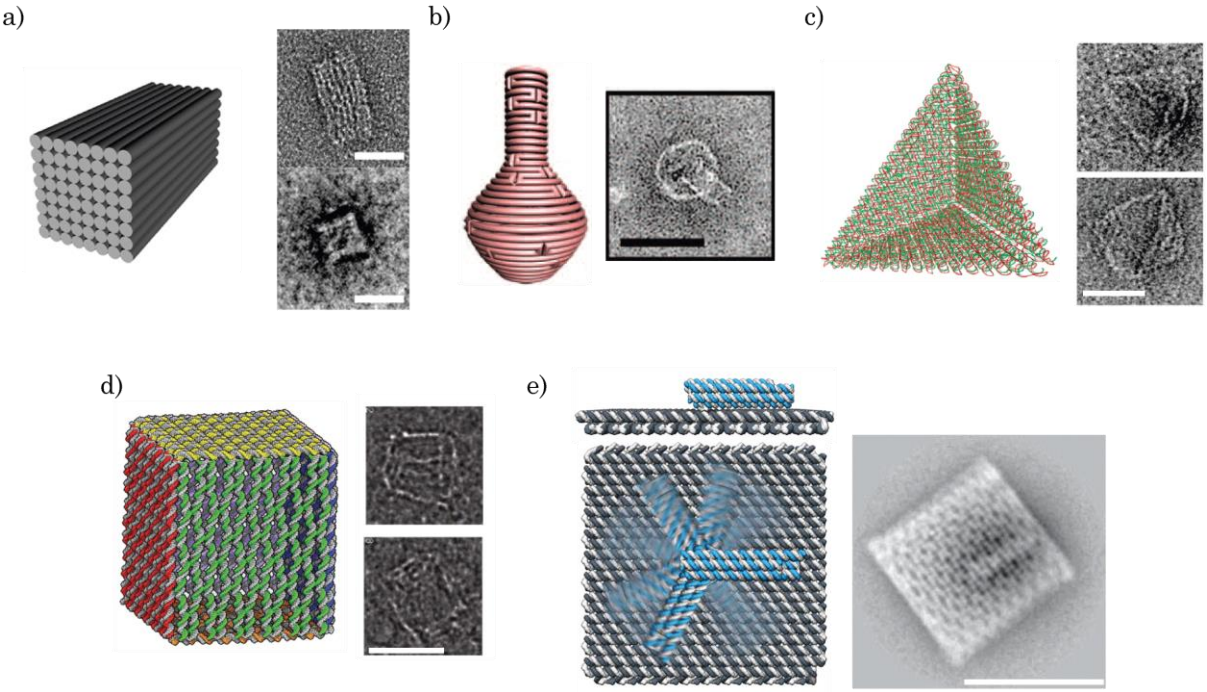

Figure 1.8. 3D DNA origami structures. a) 8-layer solid block of DNA origami. Scale bars are 20 nm. Taken from (73). *b) Nanoflask, complex 3D structure with curved surfaces. Scale bar is 50 nm. Taken from* (70). *c) 3D DNA origami tetrahedron. Scale bar is 50 nm.*

Taken from (77). *d) Hollow box. Scale bar is 50 nm. Taken from* (90). *e) Platform with integrated rotating arm. Scale bar is 50 nm. Taken from* (98).

1.3 Molecular motors

Capable of precise actuation, at high speeds, and with great reliability in the completion of their task, molecular motors manage to perform the variety of actions they undertake in the cell despite the crowded environment. There are many examples of these molecular motors and their actions: myosin in muscle contraction; dynein and kinesin in transport of cargo along microtubules; the complexes of proteins involved in flagellar motion and ATP synthesis.

Due to the diminutive size and energy expenditure of motors, such as kinesin, it has been argued that they behave as the Brownian machines theorised by Feynman (102). Given that thermal noise is ever-present, an interesting approach is to try to make use of it. However, extracting work from a motor that feeds exclusively on random, thermal noise, would be in violation of the 2nd Law of Thermodynamics. There is only so much work that can be produced from a heat exchange process; in a system of two bodies at the same temperature no work at all can be produced from thermal fluctuations alone.

Astumian discussed different types of systems that could try to take advantage of the Brownian motion by introducing external energy sources, while keeping the system isothermal. He discussed how chemical energy could be applied in fluctuation-based motion to achieve directional transport of elements in the micro- and macroscale. These systems would not need macroscopic forces or gradients, just the thermal noise causing Brownian motion, anisotropy in the structure of the system, and a source of energy caused by either changes in the constraints of the system, or a chemical reaction far from equilibrium. These Brownian machines need to possess the characteristics that molecular motors have, complex interactions between motor and track, regulated coupling of the chemical and mechanical parts, and structural flexibility (103).

When attempting to exploit or reproduce in an artificial device capable natural machines such as myosin and kinesin, initial attempts have produced disappointing results. Original devices produced had reduced yields, very short lifetimes, elevated sensitivity to the environment, and they were actuated via inefficient controls (104). To be able to use molecular motors in manufactured devices these issues need to be resolved.

The production at the nanoscale of hybrid systems, that make use of parts or complexes of naturally occurring molecular motors, have mostly done so by using linear motors from the families of myosins, kinesins and dyneins (105). This work builds on extensive research previously done on these structures due to their relevance in the biological and medical fields: understanding their structures and different conformational states comes through X-ray crystallography (106,107), and their biological roles via biochemical and biophysical assays (108). These hybrid systems include actuators (109,110), sensors (111,112), biocomputers (113).

Much work has been done by synthetic chemists on the development of fully artificial molecular motors. The innate architectures of this prospective molecular machines can have two different inspirations, a technomimetic one or a biomimetic one. The former is based on the usage of elements and structures found in classical, macroscopic mechanisms due to the complete understanding we have of their working principles; it is in following of the precepts and theorisations of the work done by Drexler (27). Examples of these are nanocars (114,115), and molecular pistons (116) among others. The drawbacks are that macroscopic mechanical principles do not transfer to the molecular landscape, inertial forces have no relevance in these small scales, viscosity becomes a dominating parameter that causes momentum to be irrelevant. Motion is determined only by which forces are applied on that specific moment with Brownian motion having palpable effects due to the scale. Unexpected issues may come from drawing too close of a parallel between macroscopic machines and molecular ones.

Biomimetic motors are based on the usage of established knowledge of biological machines to inspire the design of synthetic motors. The existence of natural molecular motors provides proof of the feasibility of molecular machines being able to perform efficiently. The elements that should be included in a synthetic design to behave as its biological counterpart are most importantly, among others: the ability to operate at ambient or near-ambient temperatures; usage of chemical energy as fuel, breaking/forming covalent bonds; capability of working in viscous media; utilisation of Brownian motion for the initiation of movement and the diffusion of fuel and other components; presence of structures that limit the degrees of freedom of the motion of the moving parts of the machine, so that the system's parts are associated throughout their operation; exploitation of non-covalent bonds in both operation and constitution of the machine; and the synthesis of the machines come from parallel processes and self-assembly, using simple building blocks. It should also be noted that when producing these machines artificially there is a greater range of options in the "materials" to be used than those found in nature (117).

Examples of biomimetic machines include switches with the structure of catenanes and rotaxanes (118–122). The catenane structure consists of two interlocked rings, the rotaxane structure of a ring threaded on a bar that presents stoppers at each extreme, topologically locking the ring in place (See Figure 1.9). More on the latter structure will be explained on the molecular motors chapter and in the appropriate experimental chapter.

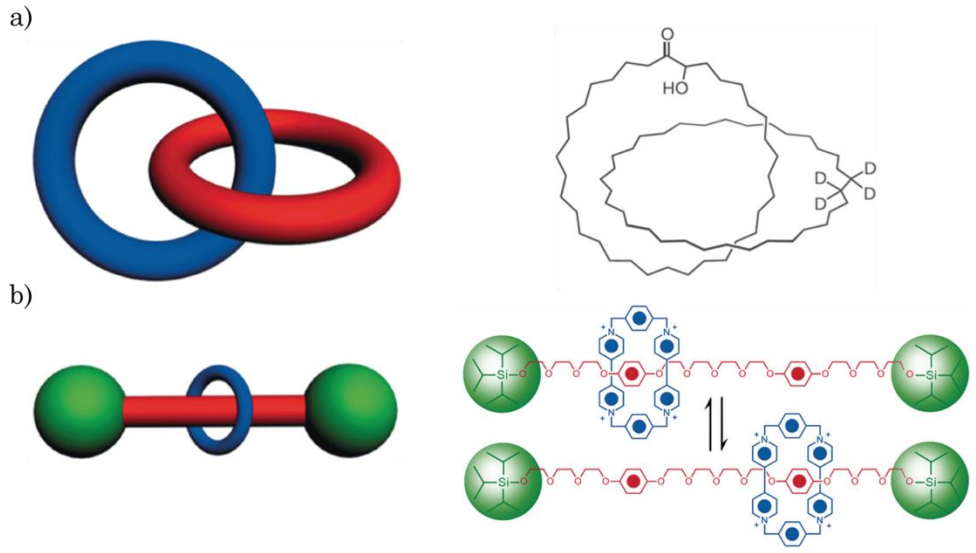

Figure 1.9. Biomimetic switches. A) Catenanes, two chemical rings interlocked. Taken from (123) *and* (124). *B) Rotaxanes, a dumbbell structure with a ring threaded through the bar. Taken from* (125).

The limitation of these machines is that they can only perform simple tasks and need to be used in conjunction with other elements to produce a complex motion that is greater than which could be achieved with each element on its own, in simultaneous but independent action (126). Working along this line, the combination of different elements with rotaxane and catenane architectures can introduce complexity to the system; this enables progression from a simple on/off switch, in which work is undone in every cycle of actuation, to motors that produce linear or rotational motion by the concerted interplay of affinities and blockers. Rotational motion in a unique (127), or interchangeable (128), direction has been demonstrated by modification of affinities to docking sites between rings, and the removal or addition of elements that constrain the diffusive motion of the rings. The same was done with rotaxanes (129), with the possibilities of developing different types of machines, such as a molecular pump of sorts, by introducing some structural changes but with essentially the same principle of motion (130,131). Expanding on molecular motors' architectures, the concept of walkers, more closely resembling the biological motors such as myosin and kinesin, is also imitated by synthetic chemists

(132,133). This concept, however, was first developed in systems using DNA, instead of a varied gamut of other synthetic molecules, as building block.

The use of DNA, a ubiquitous molecule in nature, for designing and building molecular machines is in line with the biomimetic approach to synthetic machine production; its qualities and our understanding of them, previously expounded on, make for a good substrate to work with when developing the dynamic structures needed to produce complex motion.

1.3.1 Dynamic DNA nanotechnology

Unlike their static counterparts discussed earlier, structures classified under dynamic DNA nanotechnology have out-of-equilibrium dynamics and are capable of performing motion or work, effectively machines made out of DNA. There is a wealth of early examples, particularly switches and tweezers (134–138), but there are also other structures such as gears (139) or springs (140), as can be seen in Figure 1.10.

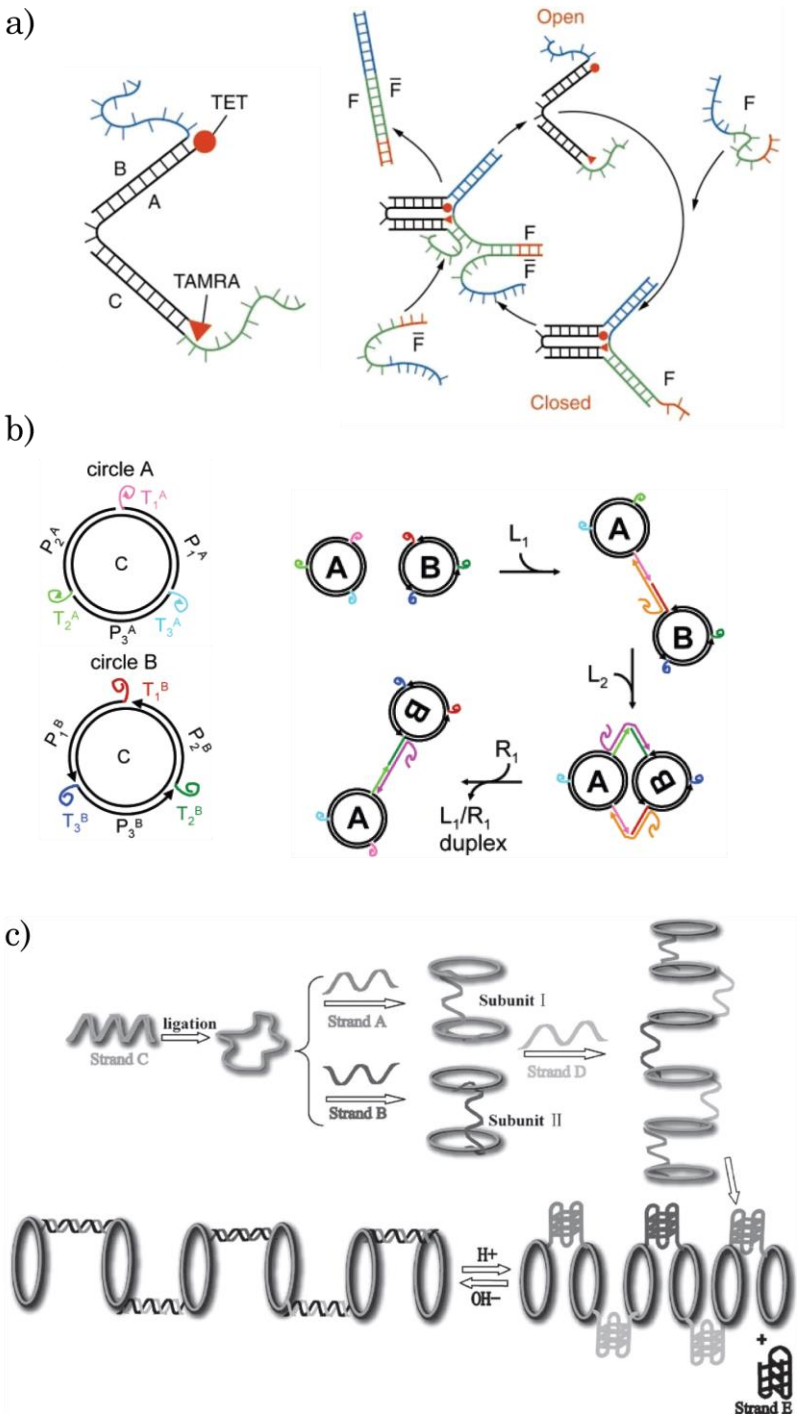

Figure 1.10. Examples of dynamic DNA nanotechnology. a) Molecular tweezers actuated by SDR. Taken from (138). *b) DNA gears capable of performing rolling processes. Taken from*(139). *c) DNA nano-spring actuated by pH changes. Taken from* (140).

Looking into the type of DNA machines that draw inspiration from naturally occurring molecular motors, linear motors such as the DNA walker have been greatly explored.

The working mechanism of some of these structures, a very relevant mechanism for the actuation of the architectures developed in this thesis, is based on DNA hybridisation kinetics and the interplay between diverse strands. The thermodynamics of this process has been extensively studied and allows for accurate prediction and design of these systems. Mechanisms rely on strand displacement reactions (SDRs) based on hybridisation of two strands which complement each other totally, or at least partially, while removing a previously bound strand (for a schematic see Figure 1.11). The process is initiated by a single-strand domain that is complementary to the incoming strand; the sections are called toeholds and act as the necessary first step for the displacement. Following this initial hybridisation there is a branch migration process; a series of reversible binding and unbinding events between identical domains concluding in the displacement of the strand initially bound to the duplex. The kinetic characteristics of this process are dependent on the length and sequence of the toehold, the rate of the reaction varying between 1 and 6 x 10^6 M^{-1} s^{-1} (141,142).

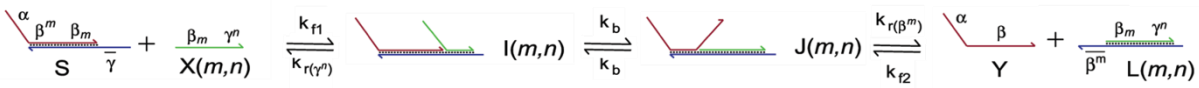

Figure 1.11. Toehold strand displacement schematic diagram including intermediate states. Taken from (142).

This process was first used in a tweezer structure capable of cycling between an open and a closed conformation via SDRs (138), seen in Figure 1.10.This showed that global conformational changes in DNA constructs could be undertaken in a sequence-specific manner, unlike other strategies previously explored that used environmental cues such as pH (143), salt concentrations (144), or temperature (145).

The implementation of SDRs for the linear motion of DNA machines such as the DNA walker was first done by Seeman (146) and by Pierce (147). In their designs, the non-autonomous walker imitated biological processive motors such as kinesin by being

composed of two "feet" that are bound to a track and can be displaced by a process of iterated, individual detachment and subsequent reattachment at a different, consecutive location. At all times a "foot" is attached to the track, preventing the walker structure from diffusing away from its fixed position; the tracks present overhanging, single-stranded sequences that act as attaching points or stators for the walker. These earlier walkers depended on the addition of sequences that act as bridges between the walker's "feet" and the attaching positions in the track. Once bound into position by each "foot", in order to actuate the machine, the addition of an invading input sequence removes one of the bridge sequences by SDRs (the bridge strands have suitable toeholds for the invading sequences); one of the "feet" is released from its current attachment point and it can diffuse freely again. The addition of the bridge sequence to the next attaching point in the track eventually binds the free "foot" to the next "foot-hold" in the track, effectively stepping forward. The process yields waste output complexes and has to be repeated with a different set of invading and bridge sequences to induce the step of the other "foot". Other later examples of these type of walkers used different architectures, more than two "feet" (148), or containing substructures that affect functionality that are in turn affected by environmental factors such as pH (149).

These walkers are considered non-autonomous since they require the addition of the sets of sequences, or fuel strands, for the actuation of each step; it would be functionally interesting to produce a DNA walker capable of continuous actuation in the presence of fuel. With that aim in mind, a new strategy for inducing stepping in DNA walkers was developed shortly after the aforementioned early walkers were published. In this new model of actuation, the driving motor for the displacement the "feet" of the walker was the use of enzymes, be it using multiple enzymes (ligases, restriction enzymes) and ATP hydrolysis as an energy source (150) or just a single restriction enzyme (151). Still acting as autonomous DNA walkers, enzyme-free systems were also developed (152–155) by

tuning the structural characteristics of the system, affinities and overlaps between hybridising sequences, although with varying degrees of success and complexity.

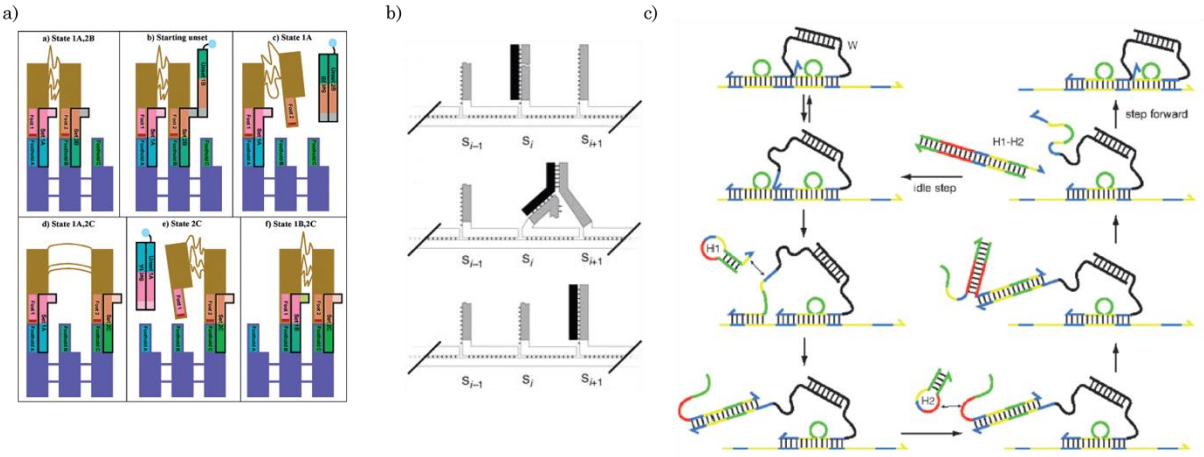

Figure 1.12. DNA walkers. a) One of the first DNA walkers, actuates its stepping by TMSD. Taken from (146). *b) DNA walker actuated by the activity of a nicking enzyme. Taken from* (151). *c) An enzyme-free autonomous walker. Taken from* (153).

The motion of the DNA walker in the examples above has been strictly limited to a single track, but research has also been done in the development of multitrack systems in which the DNA walker can discriminate between paths through a combination of fuel strands that interact with the specific spots in the track and the walker itself, and additional elements such as enzymes or small molecules such as adenosine (156–158).

1.3.1.1 Dynamic DNA origami

Dynamic DNA origami structures can also be actuated using a variety of elements. To use SDRs to change the conformation of DNA origami structures, key staples, in specific regions of the structure that are undergoing the conformational change, have to present toeholds so that they will be successfully removed by the addition of fuel strands. A new set of staples needs then to be added so that they can bind to the aforementioned regions and effect the conformational change. Examples of this process can be found in a Möbius strip (159), in DNA origami frames (160), and in a DNA brick assembly (161). The use of SDRs can be used reversibly to alter structures and functionalities in origami structures, be it in a switch system or in other machines like motors.

Conformational changes in the origami structure can also be induced via ionic strength or temperature gradients, by making use of structural motifs such as stacking interactions that arise from the shape-complementary sections of the origami which are weak enough to be reversible and therefore easily influenced by changes in salt concentrations or in temperature (162). At higher concentrations of salts, such as magnesium, the charges in the structures are shielded enough to allow for assembly, at low enough temperatures the thermal fluctuations are reduced and the structure also remains with the features stacked; various structures capable of conformational changes under these environmental changes have been studied (162,163).

Other types of conformation-changing stimuli that have been explored are the uses of electric and magnetic fields (96,164), and of photochromes that undergo conformational changes when illuminated with specific wavelengths (165,166), see Figure 1.13.

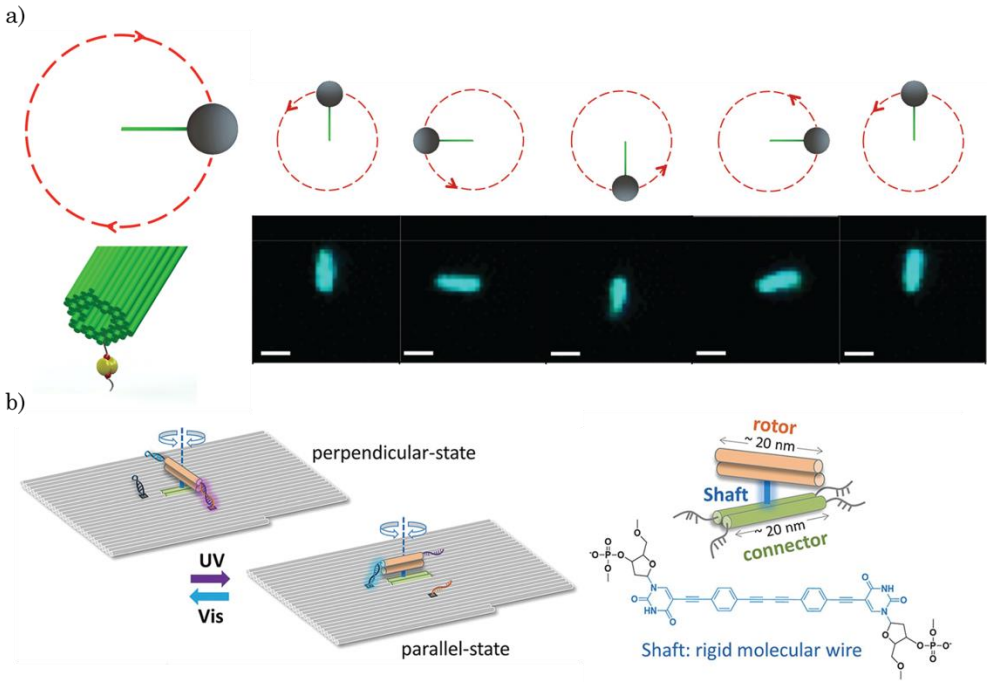

Figure 1.13. Dynamic DNA origami alternative actuation. a) Movement of a rotor arm actuated by means of magnetic fields, micro magnetic bead attached to the extreme of the rotating structure. Scale bar is 1 μm. Taken from (96). *b) Photoactuation of the orientation of a rotor with respect to a canvas. Taken from* (166).

A recurring structure with interesting applications such as the delivery of therapeutic elements is that of a container or box (91) which could be used to encapsulate materials of interest. A DNA origami box capable of opening and closing one of its faces, acting then as a lid, has been developed. The mechanism of opening and closing the lid depends in the use of SDRs on two overhanging strands that are the only elements attaching the lid; introducing invading strands that bind to the toeholds present on one of the strands in each locking site causes the lid to open (90). Additional levels of complexity can be added to the workings of the box, by adding specific locking sequences that only function with specific molecules or nucleotide sequences of biological interest (microRNAs) (92,93); or by making each lock different from the other and introducing Boolean logic gates to the opening (93).

Rotor arms are well-suited structures to be reproduced in DNA (99). Initial examples lacked control over their rotation, random rotation being generated once the structure was assembled (163), but many types of actuation and control of rotation have been implemented since. Some rotors have been controlled by means of hybridisation of overhanging strands between the rotor arm and as origami base plate below allowing the rotor to be placed in specific positions in the circumference of movement (95). Electrical fields have been applied to rotors to control their rotation and positioning. Further control was achieved by the introduction of docking sites in the surface (164). Similar results were obtained by using magnetic fields in combination with magnetic beads attached to rotor tips, but positional control was less precise and required strong fields to overcome Brownian fluctuations (96). Proteins that interact with DNA, such as helicases, have been used in connection to an origami 4-armed rotor to actuate rotational motion. The motion can be somewhat modulated by the concentration of the ATP fuel but no discrete control of the arms of the rotor was achieved (94).

1.3.2 Interlocked architectures

Another type of architecture used in the construction of molecular machines is that of interlocked structures, such as ring threaded on a bar or rail, rotaxanes and semi-rotaxanes; or two interlocked, catenanes. These mechanically bonded designs have been explored to a great degree in the supramolecular chemistry examples (118–122), but also in the DNA nanotechnology field. The rotaxane, first developed with a variety of organic molecules (167), was later produced with individual DNA helices by Famulok (168).

Marras *et al* (86) produced a collection of structures with limited dimensionality in their motion, that through different types of joints, working in concert, could produce complex 2D/3D motion. Structures include a crank-slider mechanism. Although strictly speaking not a rotaxane, due to the lack of a stopper in one of the extremes of the rail, this design shows the feasibility of a threaded ring and its thermal diffusion along an axis in a DNA origami nanostructure. The assembly of this "pseudo rotaxane" required a directed folding pathway that would sequentially preform sections of the final structure (100). This was achieved by customising the melting temperatures of sets of strands, so that in the temperature ramp selected sections assemble first into the correct intermediate structures, a technique adapted from Dunn *et al* (169).

List *et al* (87) developed actual rotaxanes with DNA origami, circumventing the complexities of hierarchical folding by separating the components' assembly and generating the final rotaxane architecture by a posteriori interaction of an open, flexible ring and the fully formed dumbbell. Different lengths of rotaxanes, and pseudo rotaxanes were successfully achieved; the ring in the rotaxane was capable of switching between two positions, a process actuated by the introduction of specific sets of strands. The extended rotaxane showed longer linear motion while being assisted by an AFM tip pushing the ring along the rail. Loading of the ring with different sizes of gold nanoparticles was also done to demonstrate the cargo-carrying capabilities of the system.

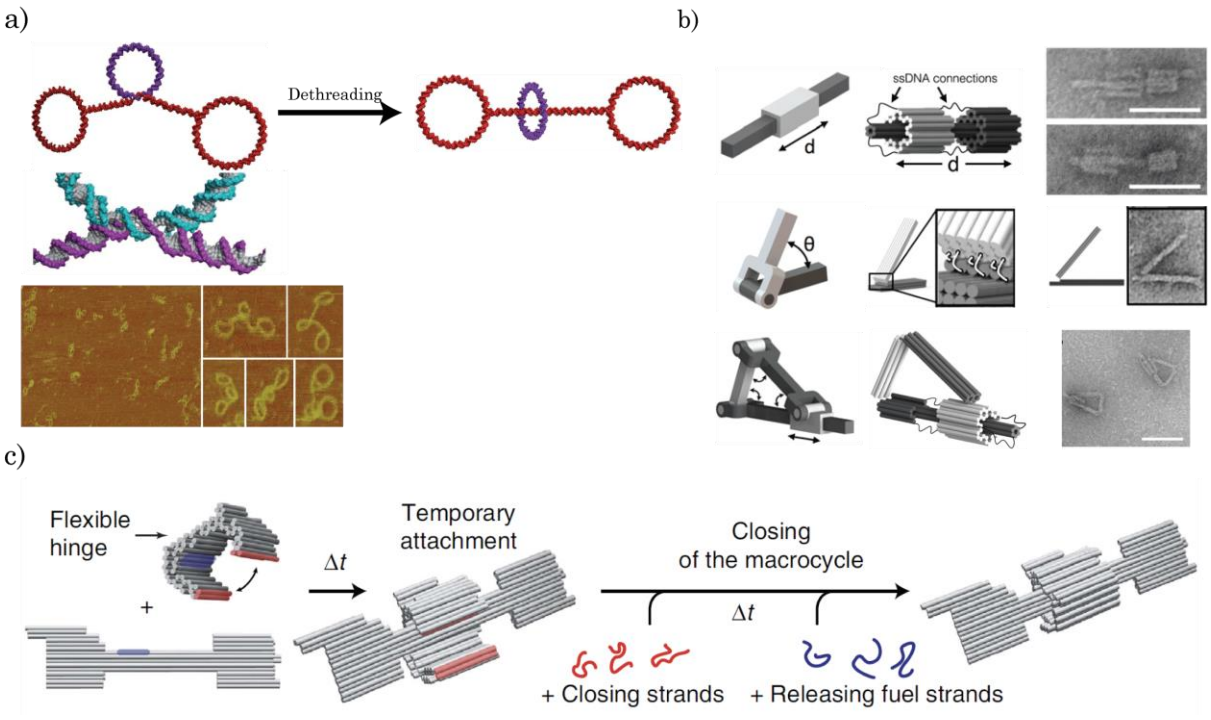

Figure 1.14. DNA rotaxanes and other DNA origami mechanisms. a) First example of a rotaxane built out of DNA. Taken from (168). *b) Collection of DNA origami mechanisms, the first one being a pseudo-rotaxane (due to the lack of a dumbbell. Taken from* (86). *c) DNA origami rotaxane produced from the interaction of two separate assemblies. Taken from* (87).

The relative ease of design and manufacture of interlocked origami structures makes rotaxanes very interesting candidates as components of a molecular machine capable of precise, prospectively multidimensional, positioning of a probe or "manufacturing" element on a surface, and therefore, MAM.

1.4 Summary and Thesis structure

In this chapter the field of atomically precise manufacturing (APM), its characteristics and current techniques, was explored. The sub-molecular additive manufacturing was described in more detail since, despite remaining a complex and controversial approach to APM, it is the motivation for the structures herein designed and produced.

DNA is the material of choice for the creation of molecular machinery for nanofabrication. A brief review of its most notable physical characteristics, that lend the molecule as an interesting and versatile building block, was presented. This was followed

by a short description of the assembly technique used all throughout the thesis, DNA origami, a technique that greatly simplifies the creation of complex, self-assembling architectures out of DNA.

Finally, the essential topic of synthetic molecular motors was addressed. If these DNA constructs are to aid in the development of MAM systems, their motion has to be designed and controlled. Exploring the literature, it has been shown that there are many examples of mechanisms made out of DNA, including switches and rudimentary motors that imitate natural molecular motors or create novel mechanisms of displacement, some of them based on mechanical structures found in the macroscale. Some of these have been produced via DNA origami and have taken the shape of the topologically interesting rotaxane structure.

In chapter 2 I will relate initial steps towards the development of a 1-dimensional motion system, based on a rotaxane structure. There will be several redesigns on the system for the sake of optimisation of the structure with the goal of characterising the controlled positioning of a ring/slider element along a 1D path/rail. The 2nd iteration of the design will produce a structure capable of cycling the slider into 3 different positions along the rail.

In chapter 3 I will apply the know-how obtained in the first half of the project into the development of a more complex system capable of 2-dimensional motion. The chosen structure is reminiscent of a quarter of a circle, named Bow-and-Arrow (BA). One axis of motion will be a rotaxane, the slider being threaded through a rail that can, in turn, pivot on one end and move along the arc of the quarter of a circle with the opposite end, this motion constituting the second axis. The design will pose more complications than the one of the 1D system, given the necessity to bend some sections and shape a relatively complex

structure. The 3rd iteration of the BA, along with a newly designed slider, will achieve 2D motion.

To conclude the experimental section, in chapter 4 I will discuss a parallel project that was related to the actuation of the designed structures. In an attempt to delve deeper into the different actuation systems, I will study the photoactuation of strand-displacement as an alternative to the usual TMSD reactions that are not without drawbacks. Two preliminary systems and different measuring set-ups will be developed to try and gauge the feasibility of introducing photoactuation into systems such as the ones developed in the thesis.

In chapter 5, a summary of the totality of the thesis is presented.

Chapter 2

DNA Origami Rotaxane for 1-dimensional motion

In this chapter, I will describe the design and production of a DNA origami linear actuator structure capable of one-dimensional motion. First I will discuss briefly the architecture of choice for this linear motion, then describe the development of the design of the origami rail. Taking into account considerations that stemmed from the first design, I made an improved version of the 1-D actuator that would allow for better study of the dynamics of the slider when threaded on the rail. I will conclude the chapter with a demonstration of the controlled attachment of the slider on the rail and its potential to perform a diffusive "stepping" motion along the rail.

2.1 Aim

The production of a system with the ability to precisely position a write-head or similar structure in a 2-dimensional, or even 3-dimensional, space is a necessary preliminary step in the development of a device capable of MAM.

To produce and study the characteristics of a structure capable of achieving motion in two dimensions, a robust, simplified, system needs to be developed first that is capable of achieving one-dimensional motion. Linear actuators are commonplace constructs in engineering. DNA origami allows for very precise and straightforward assemblies of complex nanostructures with great uniformity and versatility. The characteristic distribution of parallel DNA helices in the origami technique provides the necessary robustness and rigidity that our system must have in order to achieve the desired precise positioning capability.

The structure chosen for the linear actuator is the rotaxane. The rotaxane is a device consisting of a rod or rail, with stoppers at both ends, and a ring or slider threaded on it. The stoppers in the rail prevent the threaded slider from falling off, effectively locking it in place but still allowing for its free diffusion along the length of the rail. The disposition of the rotaxane makes it mechanically interesting as the slider is topologically locked in a position that still allows it to diffuse linearly.

2.2 Rotaxane precedents

There are many examples of rotaxanes and other similar structures in the literature mostly in the field of supramolecular chemistry (167,170–174). The first rotaxane using DNA as a building block did so by constructing the different parts with a single helix of double stranded DNA (168). In this example, and in later versions of the rotaxane and similar structures (87,175–178), the position of the threaded slider has been controlled with SDRs (168), pH (179), and light (180). It has also been actuated by a catalytic event (181) or by the activity of an enzyme (182).

The first origami mechanism with similar characteristics that achieved free linear diffusive motion, despite not being a rotaxane strictly speaking, was created by Marras *et al* (86) (Figure 2.1a). In this case both the rail and the slider come from the same origami scaffold; the regions dedicated to each substructure were connected with sections that were left unpaired and therefore more flexible. After this "one-pot" assembly, where the whole dynamic structure is produced from a single scaffold, "two-pot" assembly, where the different parts of the rotaxane are assembled separately using two different scaffolds, was demonstrated. One strategy was to have the slider close around the rail after attaching it in place and before releasing it (87) (Figure 2.1c); the other was to thread a slider through a half of the rail and anchoring it in place to the stopper before attaching the missing second half of the rail and releasing the slider (178) (Figure 2.1b).

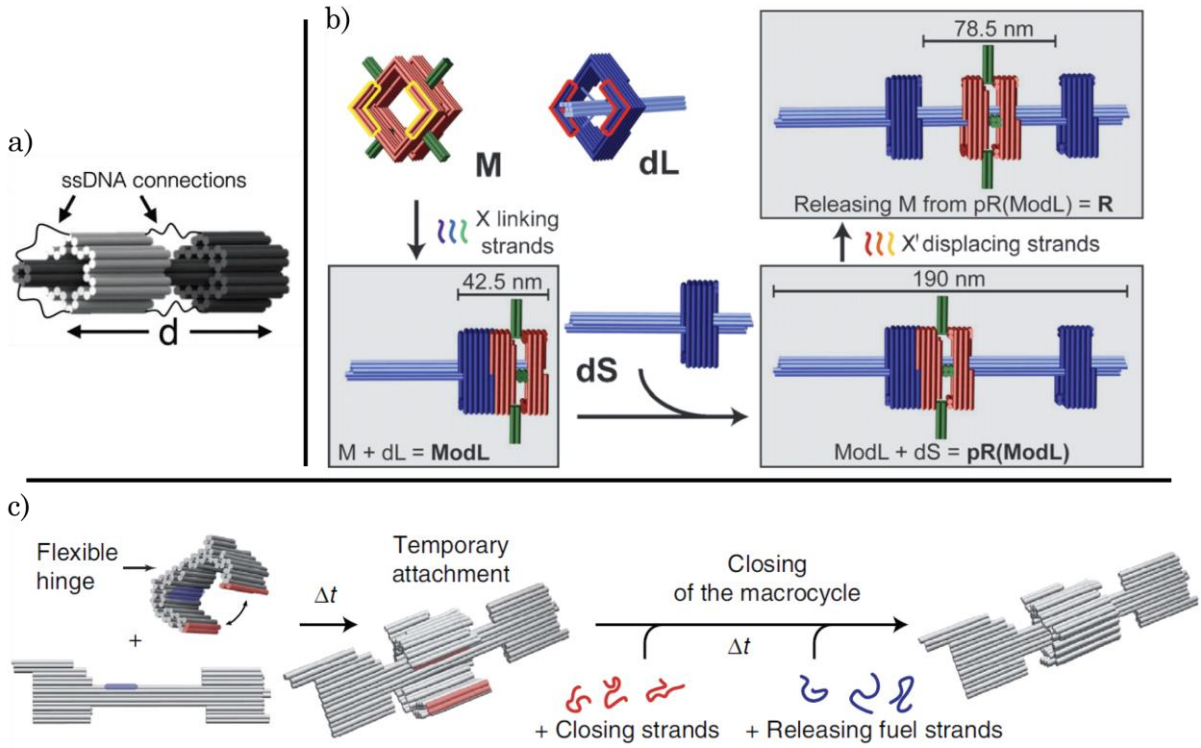

Figure 2.1. Schematic representations of different pseudo-rotaxane/rotaxane DNA origami structures. a) Pseudo-rotaxane example of "one pot" assembly. Taken from (82). b) Rotaxane produced by threading the slider through the rail before adding the second half of the rail, "two pot" assembly. Taken from (178). *c) Rotaxane produced by the slider wrapping up around the rail, "two pot" assembly. Taken from (83).*

The two strategies for producing the rotaxanes have their advantages and drawbacks. When using the "one-pot" strategy one has a limitation of size based on the finite length of the scaffold that has to yield both components of the rotaxane. The design of the overall structure becomes more complex in "one-pot" approaches as onehas to take into account the possible unintended misfolds that can come from the assembly process. It is challenging to create two different components that should interact in one specific way, the threading of the slider on the rail, but that also have the capacity of interacting in many unexpected ways. The solution may involve a sequential staple addition or a careful planning on where the different regions of the sequence of the scaffold will be situated. The "two-pot" strategy, by virtue of having two separate scaffolds and folding processes, presents none of these design and structural issues.

Design aspects aside, another important facet of the comparison between strategies is the loading of the slider on the rail necessary to obtain the rotaxane architecture. In the "one-pot" system, the connection between parts, via unhybridized 'linear' sections of scaffold (labelled as ssDNA connections in Figure 2.1a), ensures the slider and rail to be at a high effective local concentration regardless of the actual overall concentration of the sample and guarantees correct stoichiometry. In the case of the "two-pot" system, the rate of loading is slower as it is dependent on the concentrations of the different, interacting parts and it may be necessary, to achieve a good yield of loading, that one of the parts should be added in excess. Consequentially, following steps of purification to obtain a loaded sample in apposite yield for further tests are needed.

I will base the first iterations of my own linear actuator on the "two-pot" strategy, that can be seen in Figure 2.1c, due to the ease of design and the reduced constraint in terms of size of the components.

The system of actuation of the rotaxane will be dependent on SDRs. A distinct set of overhanging sequences per position, found in both rail and slider, will be complementary and allow the slider to attach to different locations along the rail. Initially closely resembling the system explored in (87), see Figure 2.1c, the initial part of the "stepping" motion of the slider will rely on diffusion along the rail and hybridisation to an available set of sequences. To attach the slider to a specific point in the rail, the specific set of sequences in that position will have to be free. By means of strand displacement of these attachments, with a set of invading oligos, the slider is removed from one location back into free diffusion, closing then the stepping cycle.

2.3 Initial linear structures

Before moving onto the initial architecture for one-dimensional motion, I did some preliminary studies on the necessary considerations for the actuation mechanism. The

actuation of the slider along the rail is dependent on the presence of protruding ssDNA sections that are used as attachment sites for complementary, protruding sequences on the slider to bind to. The design of these sequences will be explored in-depth in the next subsection; the focus in these first steps was to design staples that would present protruding attaching sites with a uniform distribution along the rail. To allow for these protrusions to be in the external face of the rail, nicks have to be introduced in the staples' sequences in the right place on the CaDNAno design, so that, on that end of the staple, the protruding sequence can be added during the synthesis phase.

Therefore, preceding the first iteration of the 1-D system, I did a short, preliminary design study on a 6-helix bundle structure to see how many nicks, and with which periodicity, could be introduced in the staples, in an architecture reminiscent of the rail in the rotaxane. Bundles with a staggered, mid-seam layout of the scaffold and with frequent, sequential nicks in the staples could be successfully assembled, as per AGE and TEM characterisation as shown in Figure 2.2.

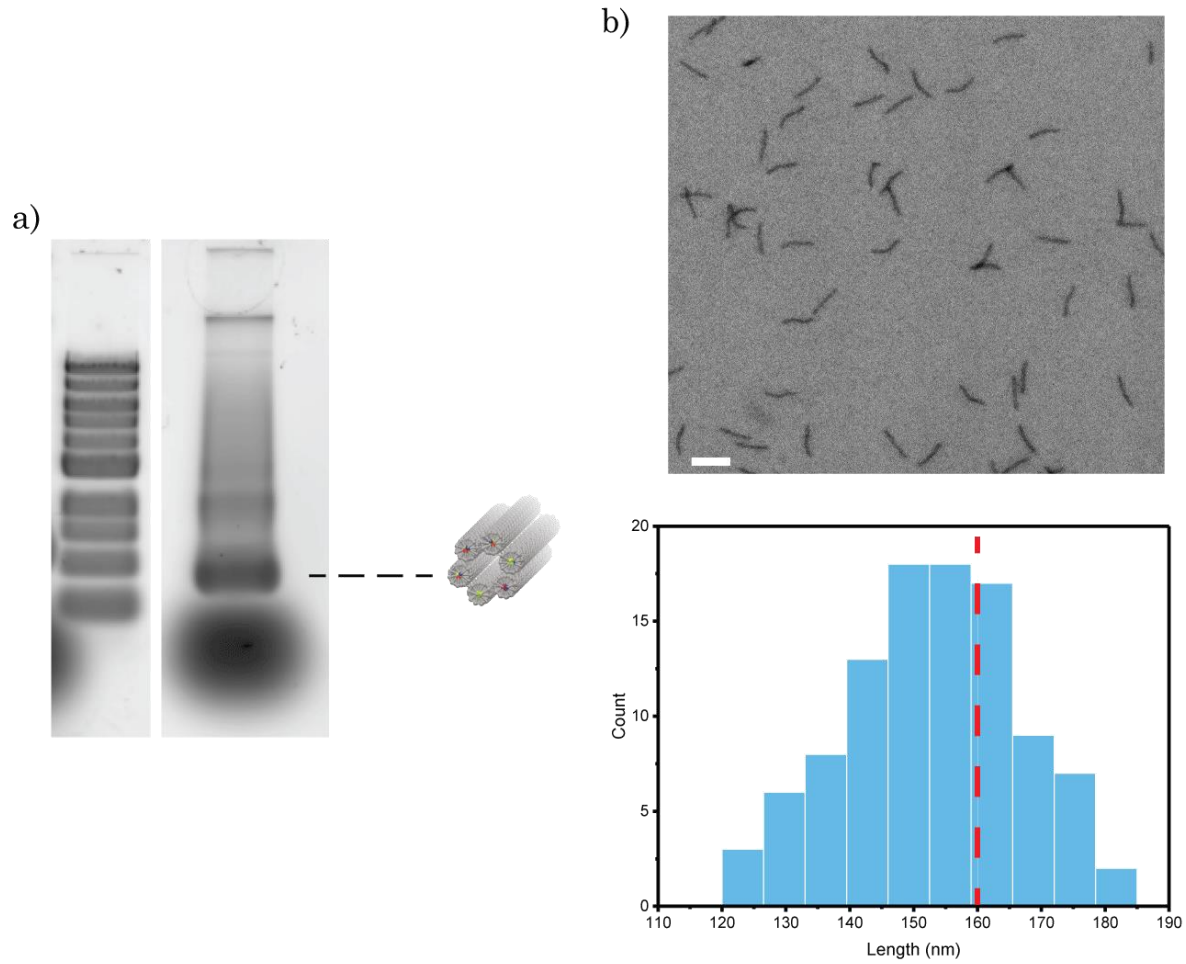

Figure 2.2. 6-helix rail a) AGE, Lanes 1 & 2 are, 1 kb Ladder (NEB), and assembled 6-helix rail, respectively. b) TEM of the 6-helix rail and histogram of the rail size distribution, expected length of the rail marked by a dashed red line (160 nm). The scale bar is 200 nm.

The resulting rails assemble with an efficiency of 68% as measured from the AGE band intensity. The expected length of the rails was of 160 nm, the observed average length from the TEM data was 153 nm ± 13 (SD, n = 102)

The objective was to see how often these nicks could be placed all along the length of the rail given the constraints that they would be outward facing and in locations that wouldn't affect negatively the structural integrity of the rail. A high density of nicks in the structure would allow for smaller step sizes in the one-dimensional motion, increasing the resolution of the write-head. In the model, useful nicks could be placed around once every 32 nt within a helix. In principle, when considering all 6 helices in the bundle, nicks could be placed on the outside of the rail 2-3 nt apart, going around the whole structure.

In practice, placing nicks close to scaffold crossovers would compromise the stability of the structure so nicks must be placed in the available regions in-between the scaffold crossovers. With the initial scaffold routing, consisting of a repeated mid-seam motif of 32 nt in length, this distribution leads to nicks positioned according to the schematic in Figure 2.3.

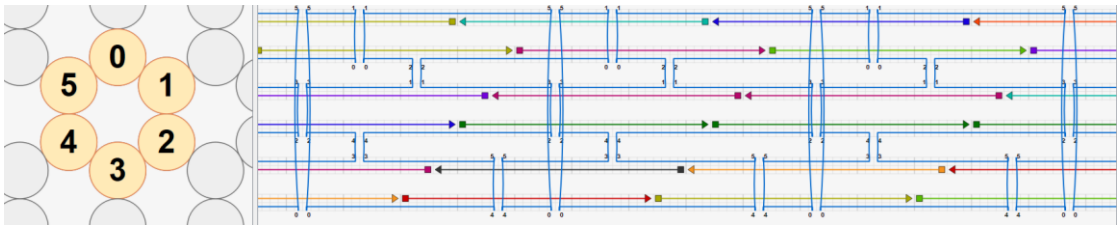

Figure 2.3. CaDNAno schematic of 6-helix rail (32 nt). The scaffold (blue) runs in a repeated mid-seam motif, with some sections presenting high density of scaffold crossovers, delineated by a dashed-line box. The staples (different colours) present breaks or nicks, where useful, to achieve a distribution as close to continuous as possible.

The issue with this distribution was the presence of areas on the rail lacking the necessary nicks for actuation, due to the presence of scaffold crossovers (area enclosed by a dashed-line box in Figure 2.3). This would increase the step size, which would in turn reduce the possible resolution of the prospective printer, the number of different positions in a determined distance being diminished. This issue can be resolved by re-routing the scaffold. An alternative distribution of nicks on a simplified, mid-seam scaffold routing was tested (See Figure 2.4), so that their placing was unencumbered by scaffold crossovers. In this alternative distribution, canonical (allowed by the CaDNAno software) nicks could be placed every 7 nt all around the helices of the bundle; the new distribution compromised the integrity of the structure due to the sparseness of the stabilizing crossovers, both scaffold and staple ones. The bundle must therefore be reinforced with

the addition of extra staple crossovers if structural stability is to be maintained.

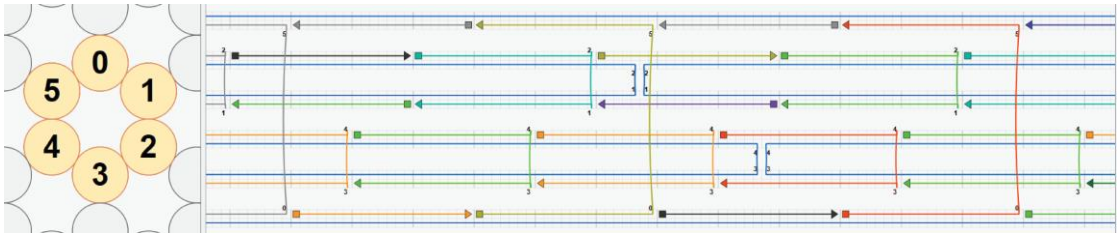

Figure 2.4. CaDNAno schematic of 6-helix rail with mid-seam scaffold routing. The scaffold (blue) runs in a single mid-seam motif. The staples (different colours) present breaks or nicks, where useful, to achieve a seamless distribution of protrusion sites every 7 nt. The homogenous, spiral distribution of nicks across the helix is delineated by a dashed-line box.

Note that the distribution of nicks on both Figures 2.3 & 2.4 would not be on a straight line along a helix but rather arranged in a spiral all around the bundle. This would lead to a translational and rotational motion if used. Although interesting in its own right, the nature of the mechanism that I intend to actuate does not benefit from such rotational behaviour.

In order to decorate a 6-helix bundle surface with nicks, a balancing act needs to take place between the frequency of said breaks in the staples and the structural integrity of the bundle. Excessive numbers of nicks will interfere and weaken staple crossovers, key elements in keeping the helices together. Additionally, the choice of scaffold routing will also impact greatly the availability of sites for nicks to be present; a complex routing, while potentially increasing the helix bundle cohesion, can reduce greatly the periodicity of the nicks.

2.4 1st Iteration of the 1D system

The initial structure that I worked on was a version of List *et al* (87) published structures, specifically the rotaxane assembled from its open ring (R1) and its dumbbell (D1) (see Figure 2.5).

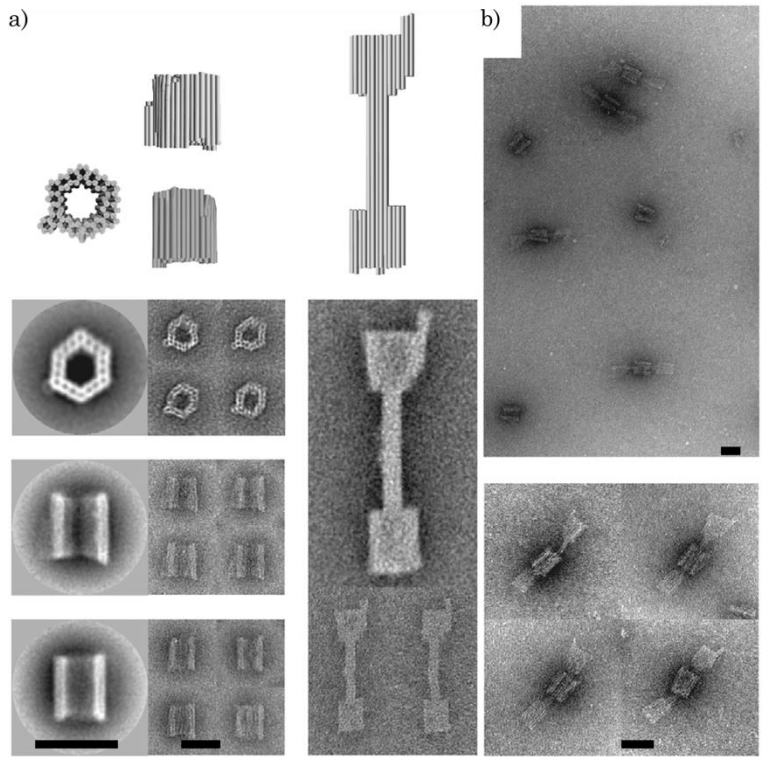

Figure 2.5. a) 3D models and averaged TEM images of the List's et al open ring (R1) and dumbbell (D1) structure. Also shown are exemplary single-particle images. b) TEM images of the completely assembled rotaxanes (R1D1). All scale bars are 50 nm. Taken from (87).

For the first iteration of the 1D system, R1 remained unchanged (referred to as slider from now on), with 35 nm length, 31 nm total width, and 15 nm of inner cavity width. It is composed of two rigid halves, made of two layers of helices, that on one extreme present a single-stranded, flexible section that acts as a hinge. On the other extreme, the staples crossing over between the two halves are not included in the initial staple mix for the assembly of the origami. This is done to prevent the slider from being locked in a closed state which would be unable to wrap around the rail; the "closing" strands are added after both origamis have been incubated together, in order to lock the slider around the rail and produce the desired rotaxane architecture.

The rail section of the dumbbell, D1, was modified by changing it from a 10-helix bundle to a 6-helix bundle. The thinner rail allows for a longer rail with more room between the rail and the walls of the slider. This should allow the slider to diffuse along the rail more

readily but it might also reduce the precision of the positioning of the slider on the rail because there would be more room for fluctuation when attached to the rail.

The initial rail staple distribution design had a set of numerous equidistant nicks similar to those presented in Section 2.3, but this density of nicks is expected to compromise the rail integrity, as seen in simulation on CanDo on Figure 2.6a. For the sake of stability, a more rigid version of the rail was designed (Figure 2.6b) with nicks every 21 nt in the top helices. Of these, two sets of 4 in two different helices and positions on the rail (at both extremes, by the stoppers) were used as the overhang locations for the two attaching locations that the slider had in this design.

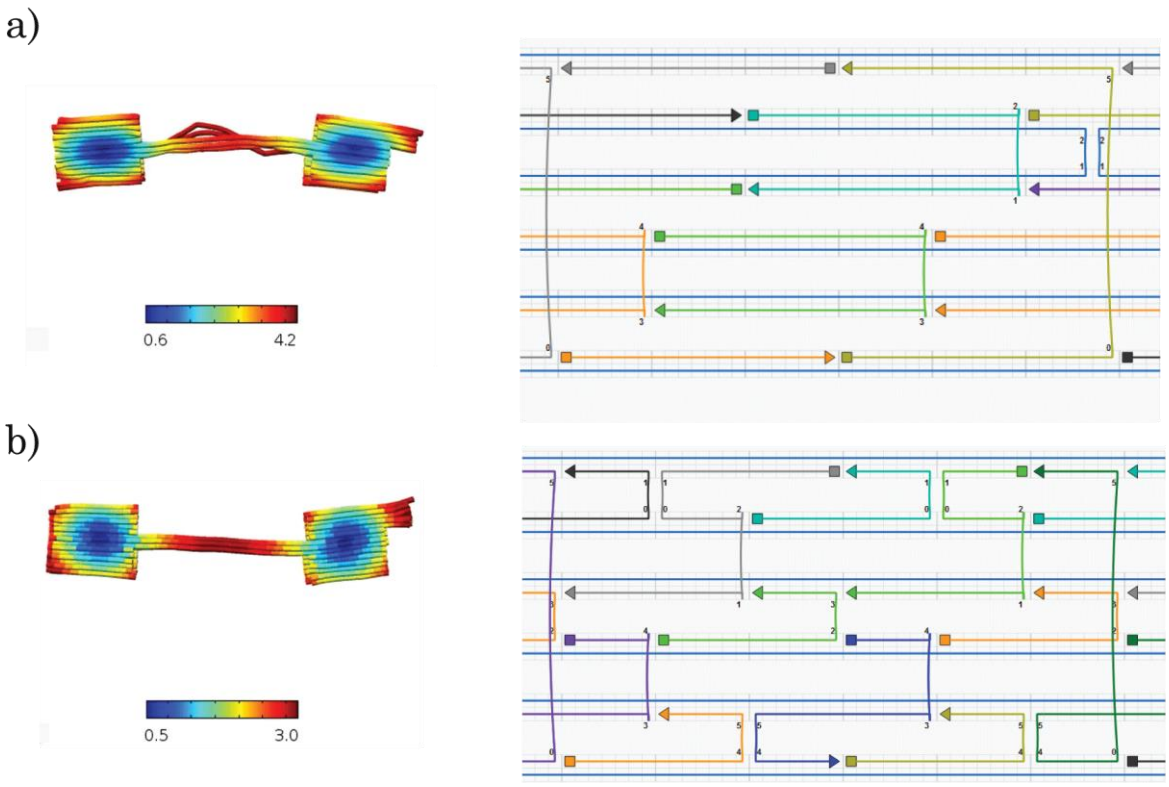

Figure 2.6. Stability study of the 1st iteration of the rail. CanDo simulation (presenting RMSF values distribution) of the rail design with the useful nicks present a) around the structure every 7 nt and b) only in the top helices of the structure every 21 nt. CaDNAno schematic of said designs on the right.

Despite CanDo simulations producing an oversimplified structure, basic assessments of the cohesiveness of the rail can be extracted, particularly when the stability problem may stem off the crossovers in-between the helices. The root-mean-square fluctuation

(RMSF) metric on the simulations in Figure 2.6a & b show the fluctuation of a specific particle over time with respect to determined position, in this case the expected position in the design. Higher values (warmer colours) imply higher instability, this instability being higher in the Figure 2.6a design version due to the lower number of staple crossovers.

The way that both the slider and the rail attach is through two sets of 18 nt, complementary overhangs; stepping from one position to another is facilitated by a cycle of detachment, diffusion and attachment. This chemical actuation is shown in Figure 2.7.

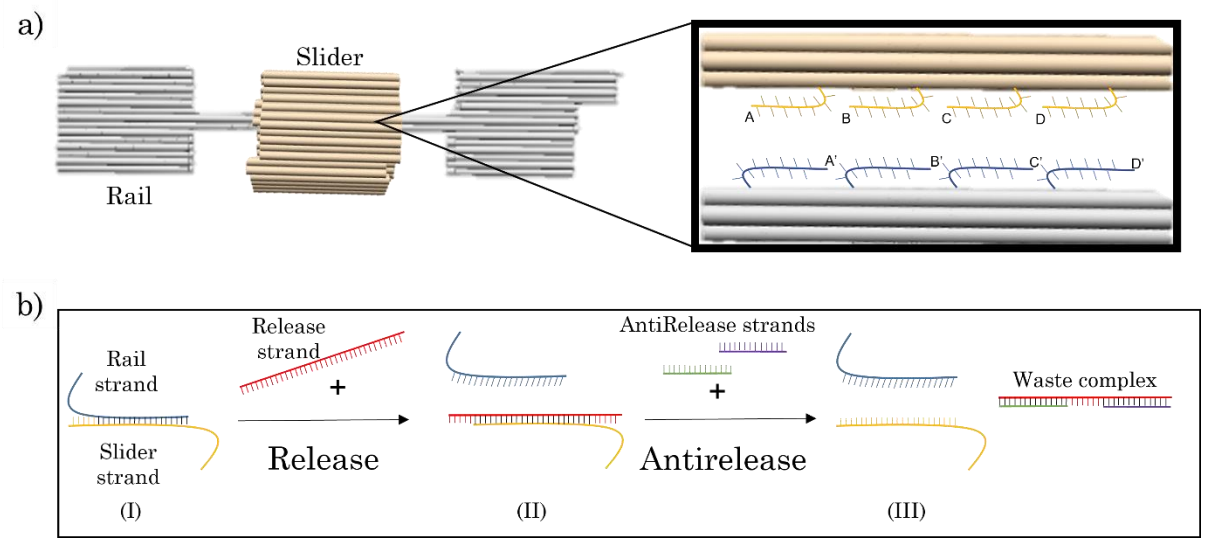

Figure 2.7. Chemical actuation system. a) Assembled rotaxane and distribution of the attaching point; b) Toehold-mediated release and antirelease mechanism. Initial position of slider attached to the rail (I), dettachment process yielding a blocked position and a free moving rotaxane (II), unblocking of the position, allowing for the reattachment of the slider and rail as in the initial position (III).

At each of the two attachment points on the rail there are 4 overhangs each with a unique sequence. They hybridize to specific overhanging sequences that are found in an equal distribution decorating the inner face of the slider (See Figure 2.7b (I)). The sequences on the slider present an 8 nt toehold that is accessed by the release strand, which detaches the slider from the rail via toehold-mediated strand-displacement (TMSD) (See Figure 2.7b (II). The release strands, aside from the 18 + 8 nt sequence that hybridizes to the slider overhangs, present an 8 nt toehold at each end. These toeholds

are used to reverse the blocking of the slider overhangs and allow them to be free to hybridize again. A combination of two strands of different length (15 nt & 23 nt), named antirelease strands, is added, hybridizing to the release strand from both ends, displacing it by TMSD from the slider, and generating a waste complex of release-antirelease strands (See Figure 2.7b (III). Since all the sequences are unique and the attachment points are comprised of 4 different overhangs, 4 release strands and 4 pairs of antirelease strands are added to complete a cycle.

For the attachment of the slider on the rail, D1 and R1 are incubated in a 1:1 proportion at 30℃ for 7 days. Once attached the slider is closed, around the rail by addition of the closing staples and incubation at 35℃ for >3 hours.

2.4.1 Initial screening of conditions and characterization of the structures

In List *et al* structures (87), the thermal ramps used for annealing are 4h long over a range of 4℃, 58-55℃ for D1 and 56-53℃ for R1 at 20mM $MgCl_2$ and in 1x TAE buffer (40 mM Tris, 20 mM acetic acid, 1 mM EDTA). Since some structural modifications were introduced in the designs, a study of the thermal ramp and a change of the assembly buffer was conducted.

For the design of the of the thermal ramp of the rail and slider structures an annealing experiment using an rt-PCR machine to follow fraction of base pairs formed as a function of temperature (see Appendix A.1.2 for the methodology) was conducted on both structures using the origami assembly buffer at a 10 mM $MgCl_2$ concentration (See Figure 2.8).

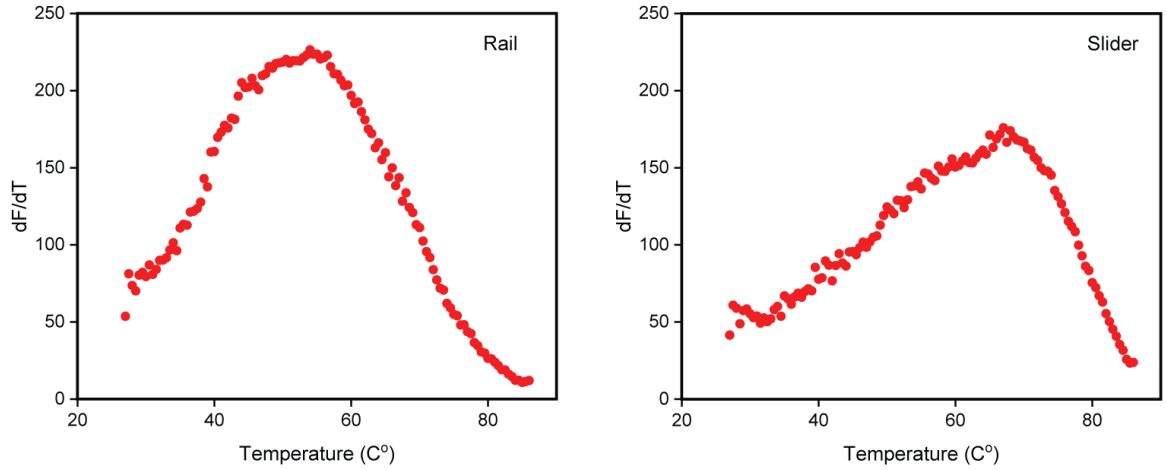

Temperature at half maximum 1	Temperature at half maximum 2
69.5 °C	34 °C

Temperature at half maximum 1	Temperature at half maximum 2
78.5 °C	43 °C

Figure 2.8. Annealing experiment of the rail and slider structures with both half maximum temperatures of each peak.

The peak in the graph represents the temperature at which the fastest increase in the fluorescence occurs, which correlates directly to the temperature at which the structures are half-assembled. By calculating the temperatures at full width half maximum of the peak, I can obtain the range of melting temperatures (Tm) of the staples, the temperatures at which half of them are hybridized and half are free in solution. For both rail and slider, this range is quite wide so the thermal ramp used from now on is a 14h long assembly ramp that can be used for both structures while comfortably covering at an appropriate rate parts of both Tm ranges.

The $MgCl_2$ concentration was screened using AGE (see Appendix B for the methodology), testing the structure with a range of concentrations from 0 to 18 mM $MgCl_2$. A well-folded origami is expected to form a sharp band and to be relatively free of aggregated material in the wells. Based on these criteria, I picked the concentration of 12 mM $MgCl_2$ for the assembly buffers of both structures.

Figure 2.9 shows the AGE & TEM characterisation of both the rail and the slider. Post assembly the rail and slider structures were PEG purified (Appendix A.2.1.) then characterised by TEM (negative staining with 2% uranyl acetate, see Appendix C.1.).

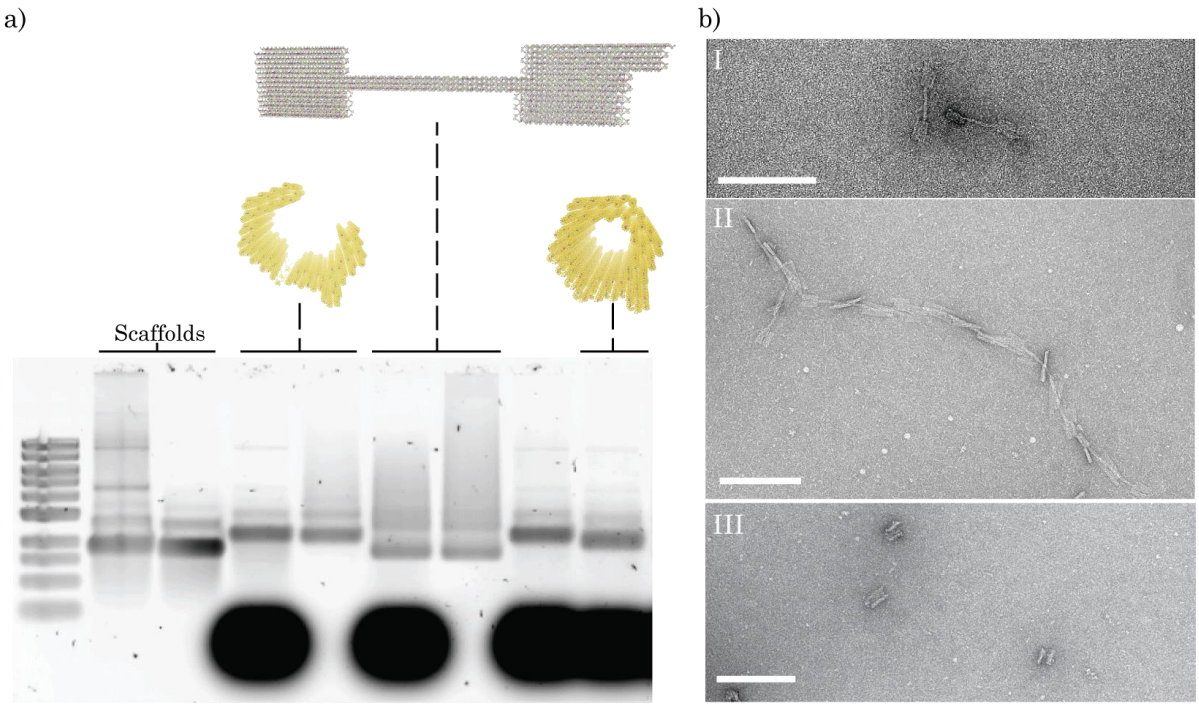

Figure 2.9. Characterization of 1st iteration individual slider and rail. a) AGE of both structures. Lanes 1 & 2 are scaffolds of both slider and rail (p8064 & p7560); Lanes 3 & 4 are open slider before and after PEG purification; Lanes 5 & 6 are rail before and after PEG purification; Lane 7 is as lane 3; Lane 8 is closed slider before PEG purification. b) TEM images of rail (I), rail aggregation (II), and open slider (III). All scale bars are 200 nm.

The slider yield was 70% as per the intensity of the AGE band, and 74% as per the TEM imaging (n= 68); the rail yield was 60% as per the intensity of the AGE band, and 92% as per the TEM imaging (n= 134). There was aggregation in the rail, observed in above in 2.9b III, that was addressed later down the line.

2.4.2 Assembly into rotaxane and design improvements

Purified rail and slider were then used to assemble rotaxanes. Initial attempts, following the published protocol of 30°C incubation for 1 week (87) were unsuccessful, as no rotaxane structures could be identified in TEM (See Appendix G.2.1). Due to this issue, I explored other conditions for improving the rotaxane assembly, among them using crowding agents.

Crowding agents are cosolutes in a mix of biomolecules that, through exclusion of volume, among other factors, drive up their effective concentrations. The change of the kinetics of the origami structures could also be due to other factors such as ionic interactions, dielectric constants and preferential interactions between biomolecules and the crowders (183). This concept has been applied to induce DNA hybridizations with the use of PEG and NaCl (instead of $MgCl_2$ to prevent aggregation due to high local concentrations) (184,185). Other condensing agents have also been studied (186). Trying to apply this concept, I screened PEG-containing buffers with different concentrations of salts ($MgCl_2$ & NaCl) and different time points (3- & 7-day incubations at 37°C). The experiments were not successful as the crowding agents caused aggregation in most conditions (BuffersV1, V2, and V3, see Appendix E.5) and time frames tested (3 & 7 day-long incubations). With exception of buffer V1 (25% of product in well after 3 day-long incubation), V2 & V3 buffers had high levels of aggregation in well (~40-70% of product in well after 3 & 7 day-long incubations)(See Appendix G.1.1). Additionally, no example of a properly formed rotaxane was found in TEM either in the less aggregated samples (V1 & V3 buffers after 3 day-long incubation)(See Appendix G.2.2).

The origami design was reviewed and some minor changes were introduced to try to solve the aggregation issue of the rail and to facilitate the interaction between attaching overhangs. A common source of aggregation in DNA origami structures is by stacking the ends of helices; this type of aggregation can be mitigated by the addition of short ssDNA sequences protruding from these ends, acting as an steric impediment (See Figure 2.10). These type of sequences are known as passivating sequences. Passivating overhangs were added in some of the stoppers edges that did not have them from the beginning.

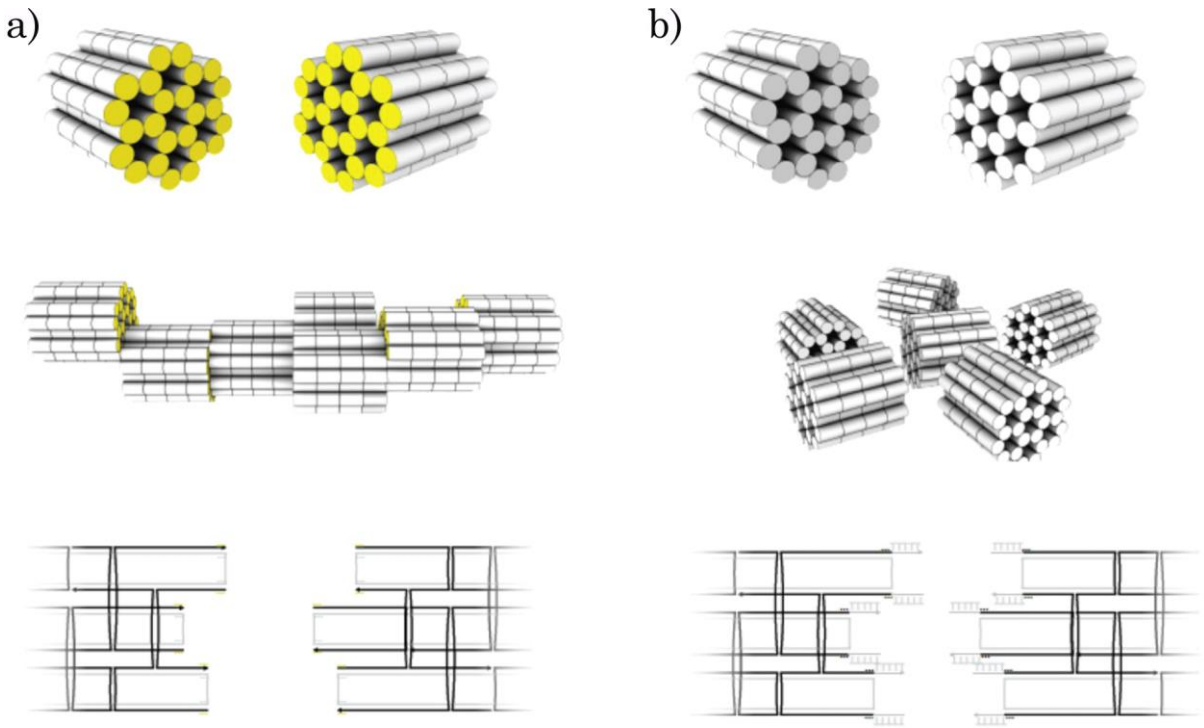

Figure 2.10. Schematic of the action of passivating overhangs. a) DNA origami units without passivating overhangs at the ends of their constituting helices. This design allows them to interact inespecifically from the ends, the hydrophobic interior of the helices promotes the stacking of the helices' ends. b) The addition of short overhangs protruding out if the helices ends sterically impede this stacking, allowing for the individual units to remain monomeric. Taken from (187)

The orientation of the interacting overhangs was changed so that the "tip" of the overhangs, the furthest bases from the origami, interacted together. Prior to this change the sequences interacted starting from the "bottom" of the overhangs and the origami structures had to be closer still to be able to attach. See Figure 2.11 for a schematic representation of this change in sequence orientation.

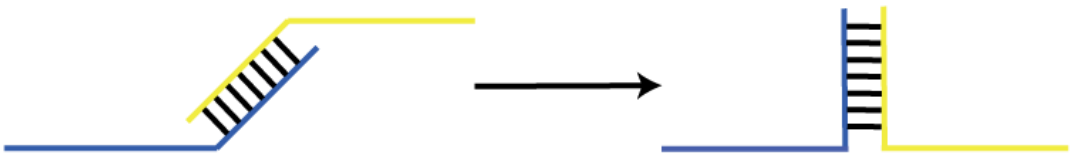

Figure 2.11. Sequence orientation change in rail (blue) to improve the ease of interaction with the slider (yellow).

With the newly redesigned rail I did another set of experiments screening for different times of incubation (1-, 3- & 7-day incubations, still at 37°C) in AGE and following up with TEM. The results can be seen in Figure 2.12:

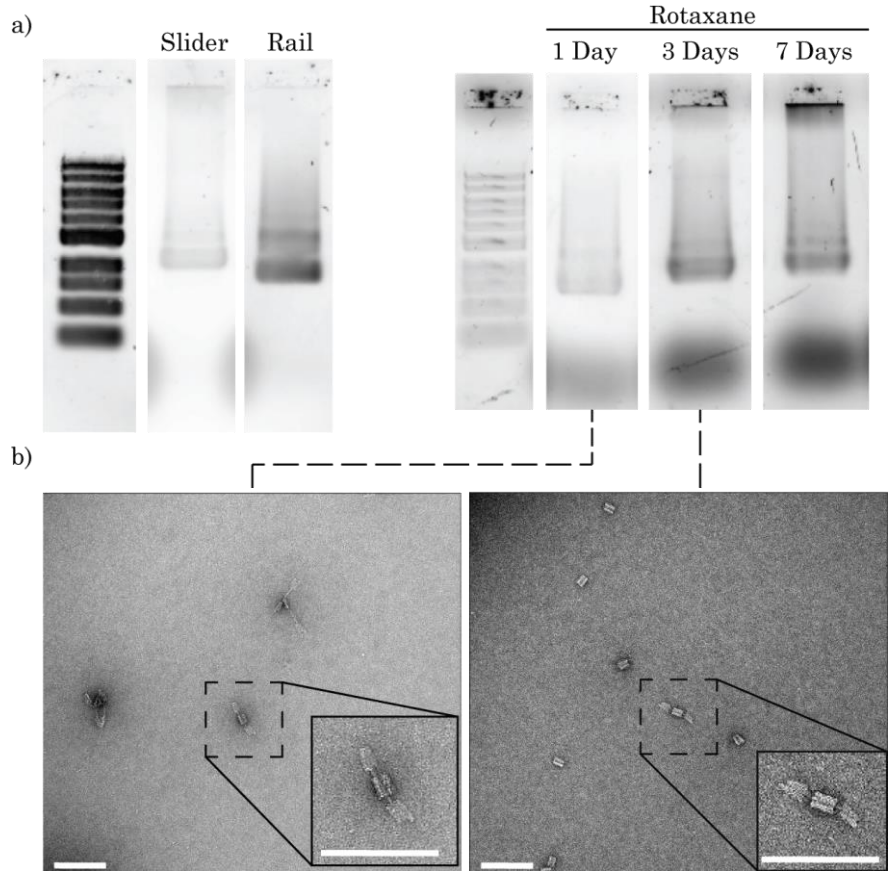

Figure 2.12. Assembled rotaxanes. a) AGE of individual components, slider and rail (lanes 1 & 2) / AGE of assembled rotaxanes after 1-day incubation, 3-day incubation, 7-day incubation (lanes 1, 2 & 3). b) TEM of rotaxane after 1-day incubation and 3-day incubation with a zoom-in of the assembled rotaxane. All scale bars are 200 nm.

The individual components were also run in AGE this time and in every iteration of the subsequent experiments done, 14 separate occasions, which demonstrates the reprodubicibility of the assembly of the origami designs (yield of 68% and 66% of slider and rail respectively).

In the gel the lanes present a single band that migrates at the same speed as the rail (yield of 50%, 55%, and 34% of the 1-day, 3-day, and 7-day incubations as seen in the fast migrating band), but no discernible band at the level of the slider. In the TEM images all time points show successfully assembled rotaxanes but the yield of the reaction could be

improved (18% and 25% for 1-day and 3-day incubations respectively). A change in the conditions of the assembly was introduced.

So far the proportions used have been 1:1 for rail and slider interactions, with the aim of trying to solve the low yield issue, and given that in the TEM images there were many examples of vacant rails, different increments of slider excess were added to the incubation process. Concomitantly, the rail and the slider were labelled, with Cy3 & Cy5 fluorophores respectively, in order to have a clearer idea of their distribution once mixed together and incubated at different time lengths and at different proportions. The details of these tests can be found in Figure 2.13.

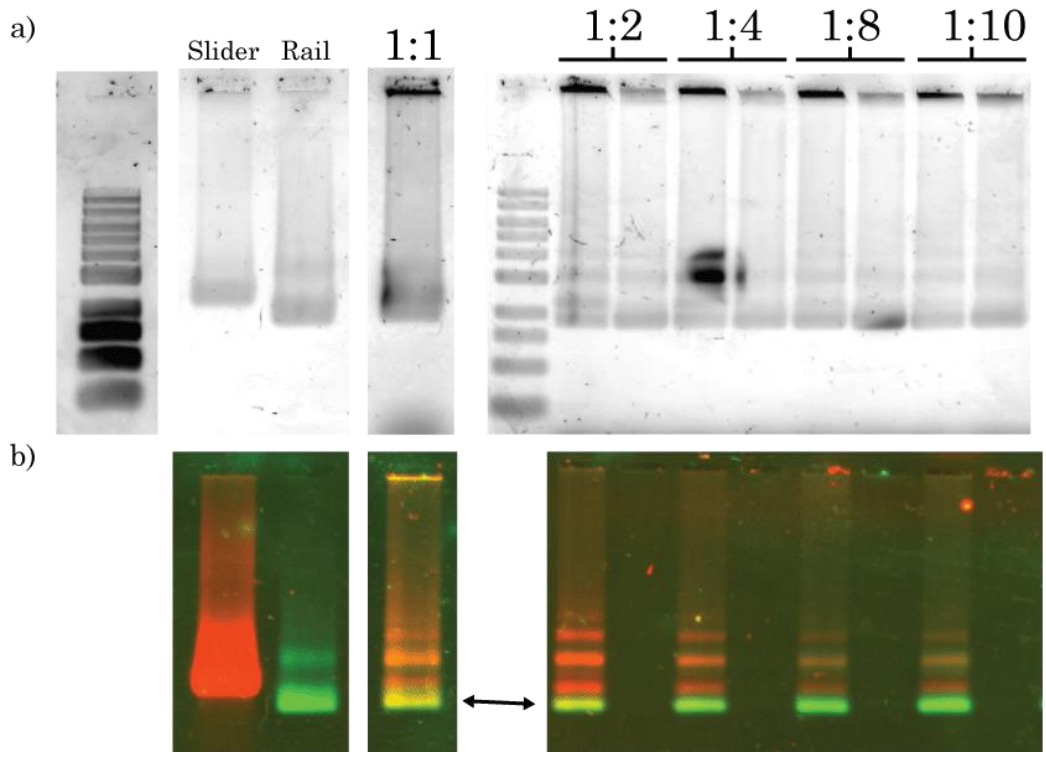

Figure 2.13. Screening proportions of assembly, all assemblies done in 1-day incubations. a) AGE of individual components, slider and rail (lanes 1 & 2), and the assembled rotaxane in a 1:1 proportion / AGE of assembled rotaxanes in 1:2, 1:4, 1:8, 1:10 proportions (lanes 1, 3, 5 & 7 with the fluorescent labelling, lanes 2, 4, 6, 8 without the fluorescent labelling). b) A superposition of the gel in a) scanned for Cy3 (green), rail, and Cy5 (red), slider. Double-headed black arrow pointing to the rotaxane containing band.

As can be seen in the gel, particularly in the superimposed version of the Cy3 & Cy5 scan, 1:1 and 1:2 proportions of rail:slider show the best overlap of bands (yields of 57%

and 53% respectively), confirming as well the observation made in Figure 2.12 about the band distribution. What I presume to be the band of the rotaxane migrates faster than the open slider and around the same level as the rail. Incubations at 3 days and 7 days in Figure 2.12 show some smearing, coming mostly from the rail sample; from this point forward the incubations will be done at double excess of slider (1:2) for 1 day. Some parallel tests were done about which type of gel suited best my characterization needs, either TAE or TBE, ultimately deciding on TBE since I found the sharpness of the scanning to be increased.

2.4.3 Closing and releasing of the slider

The rotaxanes could be distinguished for the conditions chosen (incubation at excess of slider (1:2) for 1 day) in the gel and in the TEM (See Appendix G.2.3). The next steps in the assembly and functionalization of the structure were the closing of the slider around the rail and its release from the rail attachment sites. Using AGE and scanning using the fluorophore filters, the effect of the closing and releasing set of strands can be distinguished in Figure 2.14.

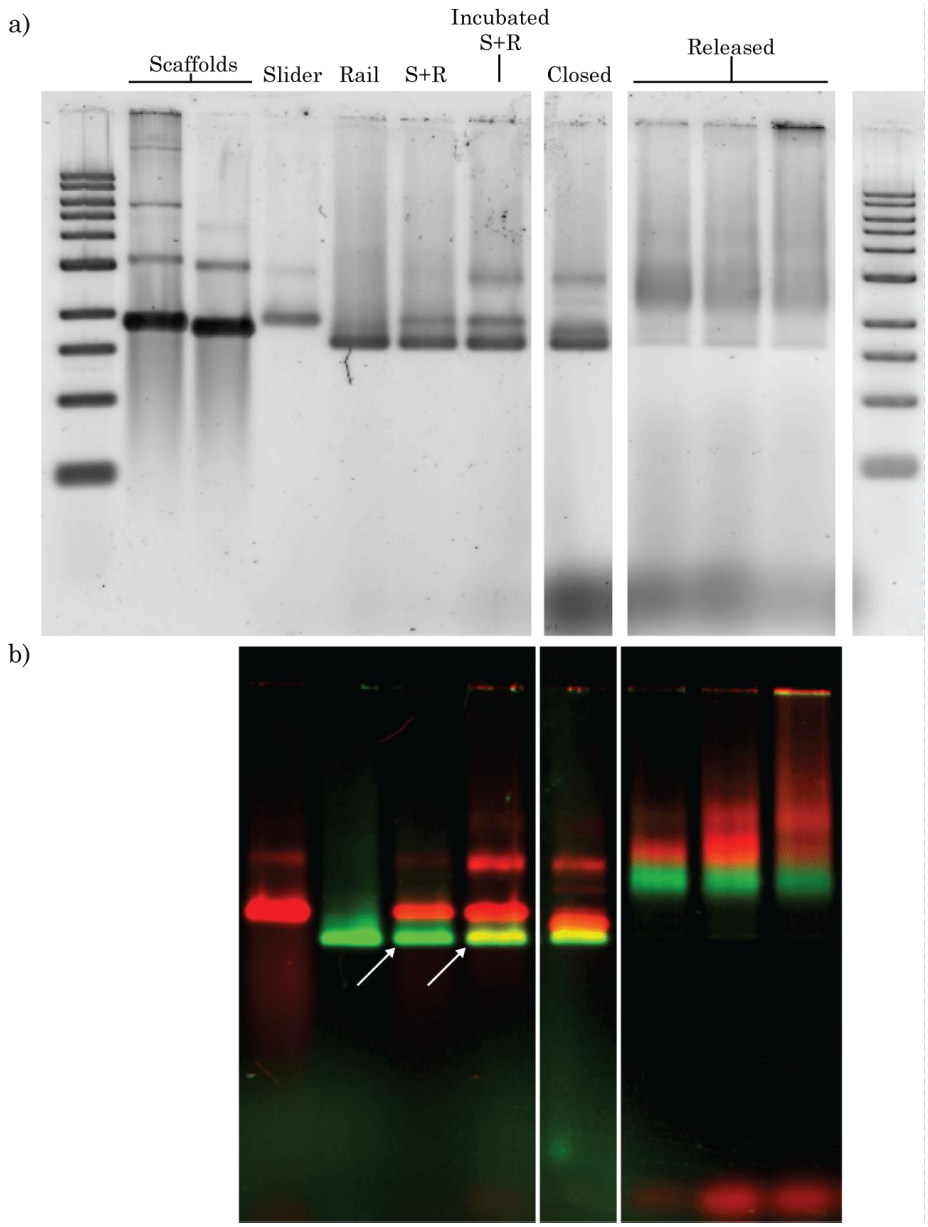

Figure 2.14. AGE study of the release strands. a) SYBR Gold scan, lanes 1 & 2 are scaffolds of both slider and rail (p8064 & p7560); lanes 3 & 4 are open slider and the rail; lane 5 is a 1:2 mixture of rail and slider with no incubation time; lanes 6 & 7 contain rotaxanes with an open and closed slider, respectively; lanes 8, 9 & 10 content are as in 5, 6 & 7, plus the addition of the release strands. b) A superposition of the gel in a) scanned for Cy3 (green), rail, and Cy5 (red), slider. White arrows pointing to the change in fluorescence due to rotaxane formation after incubation.

As can be seen in the gel from the fluorescent signal, in lane 5, incubation is a necessary step for the slider and rail to interact, as can be seen by the change in the fluorescence signal in the bands between lanes 5 and 6 in 2.14b (no rotaxanes in lane 5 vs rotaxane yield of 42% in lane 6). The addition of closing strands (at a concentration of 100 nM, incubating at RT for 2h) causes the faster migration in the left-over slider band, as seen

in Figure 2.9; no noticeable change can be directly seen in the rotaxane band. The moment the release strands are added (at an excess of 1 mM at RT for 40 minutes) the bands become smeared and migrate much slower, with no distinction in effect between a mixture of unassembled components (lane 8), rotaxanes with an still open slider (lane 9), or with a closed one (lane 10).

Given the drastic change in the appearance in the gel, I did a screening of the effect of the different inputs (incubation, adding closing strands, adding releasing strands) in each structure individually. This was done to try to see if any of these strands, or their combination, affected in an unexpected way the structures, the results can be seen in Figure 2.15.

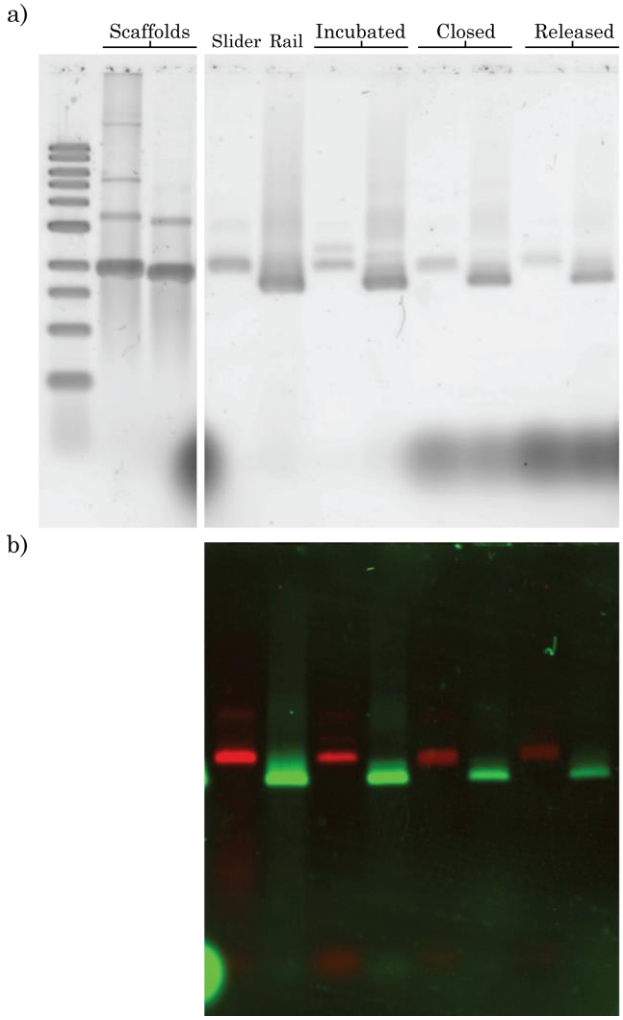

Figure 2.15. AGE study of the release strands. A) SYBR Gold scan, lanes 1 & 2 are scaffolds of both slider and rail (p8064 & p7560); lanes 3 & 4 are open slider and the rail; lanes 5 & 6 are slider and rail, respectively, incubated for 24h; lanes 7 & 8 are slider and rail, respectively, incubated for 24h and closed; lanes 9 & 10 are slider and rail, respectively, incubated for 24h, closed, and released. B) A superposition of the gel in a) scanned for Cy3 (green), rail, and Cy5 (red), slider.

The individual bands of both rail and slider remain unchanged after the sequential steps needed for the production of the rotaxane, aside from the subsequent dilution of the sample due to the addition of the different strands. The anomalous migration comes then, from the presence of both structures in solution, the unexpected interaction between rail, slider, and release strands.

Given the difficulty of characterising structures with either AGE or TEM, a superresolution microscopy technique was used, DNA-PAINT.

DNA-PAINT depends on transient colocalizations of the imager strands on the docking sequences that decorate the surface of the structure. Because of the weakness of their hybridization, they attach and detach fairly often. When free in solution, the imager strands diffuse over multiple pixels, during a single frame, causing them to remain undetected by the camera. The signal of the fluorophore is only detected then when it is bound to the docking sequences and remains in a fixed position long enough for photons to accumulate. The blinking caused by this transient attachment allows for the individual signal coordinates' to be registered with subdiffraction precision.

The microscope used is the Nanoimager (See Appendix C2), in which the excitation laser used (532 nm-laser) was in objective-based Total Internal Reflection Fluorescence (TIRF) mode, meaning that it hit the glass surface at an incident angle of ~54° (true illumination angle of ~61°). In TIRF, when operating the laser with a high angle of incidence, known as the critical angle, a portion of the inciding laser is not reflected off the surface of the sample and penetrates it in the form of an electromagnetic field parallel to it. This area is called evanescent field, it has the same frequency as the inciding laser and it excites fluorophores (imager strands) located a within a maximum distance from the surface. This is caused by the exponential decay of the intensity with distance from the refracting surface. The depth of this field ranges between 250 nm to 60 nm, and is dependent on the wavelength of excitation; the incident angle; the type of TIRF, in this case objective-based; and the refractive indexes (immersion oil, glass surface, sample media) (188). The latter is in turn affected by temperature, which was monitored inside the microscope's stage area at around 31°C by the software and different temperature gauges (although none were placed in the sample/objective area, the registered temperature is an average of 12 different gauges). In the working conditions and parameters of these experiments, the depth of the field was ~200 nm.

The strands transiently bound to the structure will detach in a small window of time; the imager strands bound inspecifically to the surface will bleach if bound for too long, their signal then being weaker noise found on the background of the images obtained. In order to discourage this behaviour, the buffers used contained a detergent (Tween-20), see Appendix E.

The images of the transient colocalizations are collected by the Nanoimager and treated with a Python image-processing pipeline; the threshold that determines if a colocalization (fluorophore emission detected) is represented as a pixel in the final image depends on the number of times that said colocalization occurs in a specific spot. By lowering the threshold more noise appears in the image but less static elements become detectable, in the shape of a weaker fluorophore signal that covers the locations where it has been. The epithet of exchange denotes that the DNA-PAINT was done using two different imager probes (sequence-wise, but with the same fluorophore in our case) in succession. One type for the stoppers and the other for the slider, using different colours for the colocalizations to be able to differentiate the signals when the images are superimposed (189,190).

Some design modifications were introduced in the rail and the slider to be able to characterise them with DNA-PAINT. The two main changes required were the introduction of 4 modified staples in the bottom helices, in both stoppers, that presented a biotin group each in their 5' end; and a number of 3' overhangs distributed in both the slider (8 overhangs in each end of the slider) and the rail (asymmetric distribution in the stoppers, 16 overhangs in one and 8 in the other) that present the docking strand for short, fluorescently-labelled probes (imager strands) used in the technique. Once the structures were designed and characterised with AGE, finding them in agreement with the previous characterizations, I performed a DNA-PAINT analysis of them. The modified rotaxane

was fixed on a glass surface and prepared as specified in the methodology (Appendix C.2). The results can be seen in Figure 2.16.

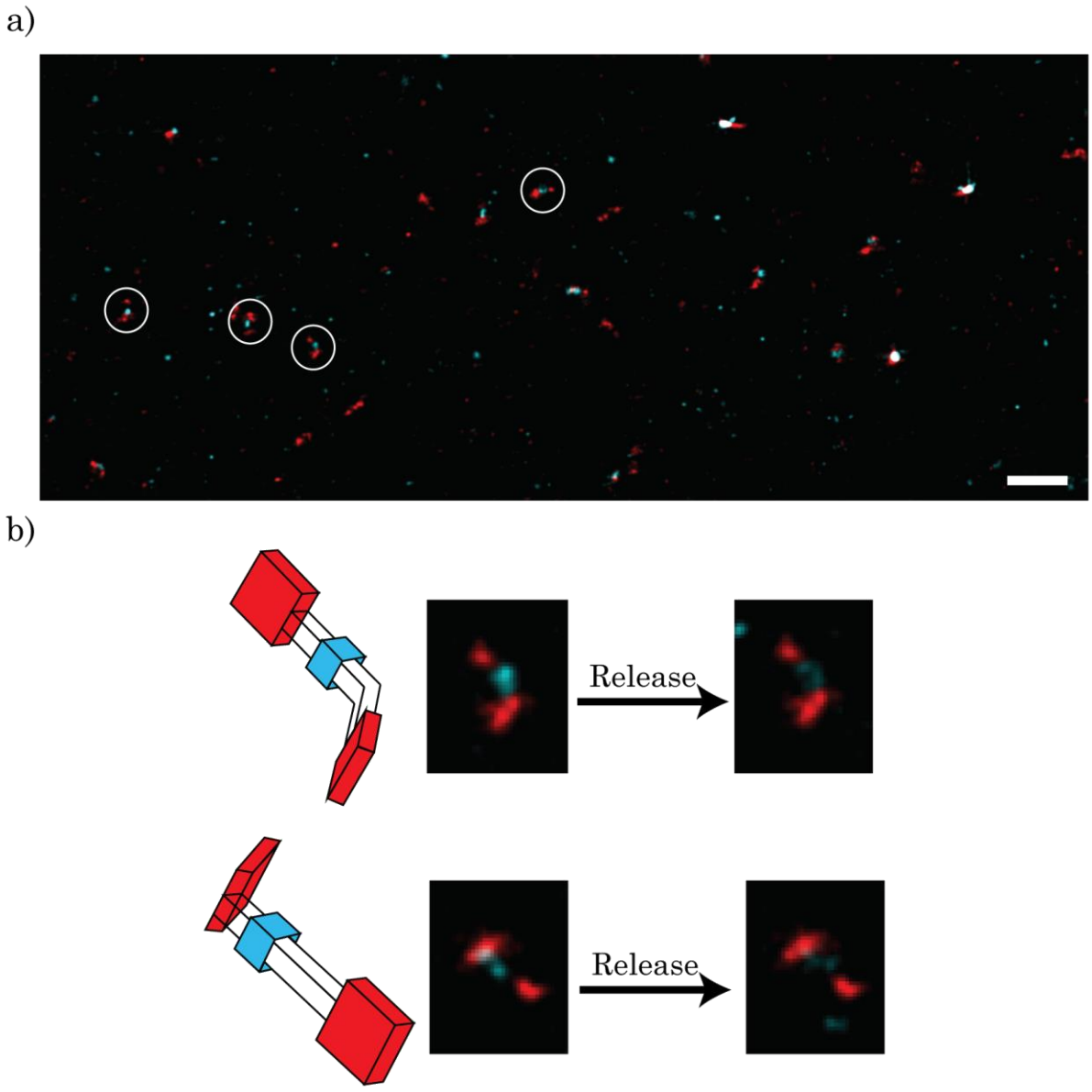

Figure 2.16. (Exchange) DNA-PAINT characterisation and study of the rotaxane. a) Wide field of view of rotaxanes (with attached slider) through DNA-PAINT super resolution microscopy technique, in red the position of the stoppers, in blue the position of the sliders. Scale bar is 500 nm. b) Individual examples of rotaxanes before and after being flushed with the release strands.

In the imaged, functionalized glass surface, many examples of properly folded, non-aggregated rotaxanes can be seen, in contrast with their relative low yield as seen in TEM. By imaging first the rotaxane structures with the slider attached and closed in position, I could assess the effectiveness of the assembly process (55% yield of rotaxanes); to see if

the release strands are capable of detaching the slider from its position from the rail, an incubation with the release strands was done in between measurements. The addition of the release strands weakened the signal in the subsequent imaging of the slider, meaning that the slider had successfully detached from position and was either free roaming along the rail (if closed correctly) or floating in solution. In both cases, its sudden capability to diffuse causes the imaging technique not to detect it unless the threshold of detection of colocalizations is low enough. The yield of the release of the slider was 41% from the correctly assembled rotaxanes.

Before delving deeper in this set of experiments and fine-tunning the conditions to properly check the effectiveness of both closing and release strands, plus later attachments to the secondary position, I decided to re-evaluate the design to better fit it to the future experiments and prospective applications.

2.5 2nd Iteration of the 1D system

In the process of working with the design of the rotaxane inspired by List *et al* (87), I came to the realization that, if I wanted to be able to easily see the effect of actuation of movement by the position of the slider on the rail, I had to introduce drastic changes in the design of both structures.

Firstly, two main changes have to be introduced in the design of the dumbbell structure. The first change deals with the length of the rail around which the slider wraps and diffuses; a greater distance needs to be covered in order to simplify characterising the different positions that the slider can occupy. The current rail length is barely longer than the length of the current slider, causing difficulty in distinguishing between the two different positions that it could occupy. The change introduced in the design increases the rail length from 199 nt (67.66 nm) to 654 nt (222.36 nm).

This change allows me to test how well the system works when covering larger scales; although it is true that the main aspect that a molecular-additive printer should have is the resolution it can achieve, that is, the smallest interval that it can cover in a stepping event.

The second necessary change is in the stoppers. In order to facilitate the diffusion of the slider when threaded through the rail, particularly when the rotaxane is attached to a surface, such as in DNA-PAINT or prospective printing environments, enough bottom clearance is required. Since the main role of the stoppers thus far has been that of end blockers to prevent the slider from falling off the rail, a complete overhaul of the design is required. In these second-generation stoppers, the bulk structure is found protruding from the surface-facing side of the rail, shaped as an equilateral triangle with the rail bundle in the vertex at the top. This way, enough clearance is obtained between the rail and the surface and the slider is still locked in place, despite lacking obstacles on the top side. The redesign of the stoppers shorten them from the current 107 nt (36.38 nm) to 69 nt (23.46 nm).

Regarding the slider, the main issue of the current one is its great size. While robustness is a positive aspect of its design, being too voluminous could impede the free diffusion along the rail given the aforementioned circumstances (when attached to a surface). By modifying the structure from a double-layer of helices to a single one, the resulting thin slider should have no issues when diffusing between attaching points. The length of the slider remains virtually unchanged from ~100 nt (34 nm). Another modification is the removal of the toe-hold parts of the overhangs in the slider, relocating them to the overhangs in the rail; the only actual change this causes is that the release strands will bind to the rail attaching positions, not the slider ones.

As follows from important structural changes, the scaffolds used in the structures also changes. For the long rail, the scaffold used was the standard p8064, for the thin slider a shorter, phagemid-based scaffold of 2880 nt that was previously used in initial linear structures. The attachment overhangs were still located in each extreme of the traversable rail; biotin-containing strands were still placed in the bottom of the stoppers; and the DNA-PAINT docking strands remained as well. The distribution of the later in the slider were as before, 8 docking strands in each end of the slider, but in the rail, although still asymmetrically distributed, the docking sites are placed along the rail, 16 in one end and 8 in the other. See below a schematic of the new designs in Figure 2.17.

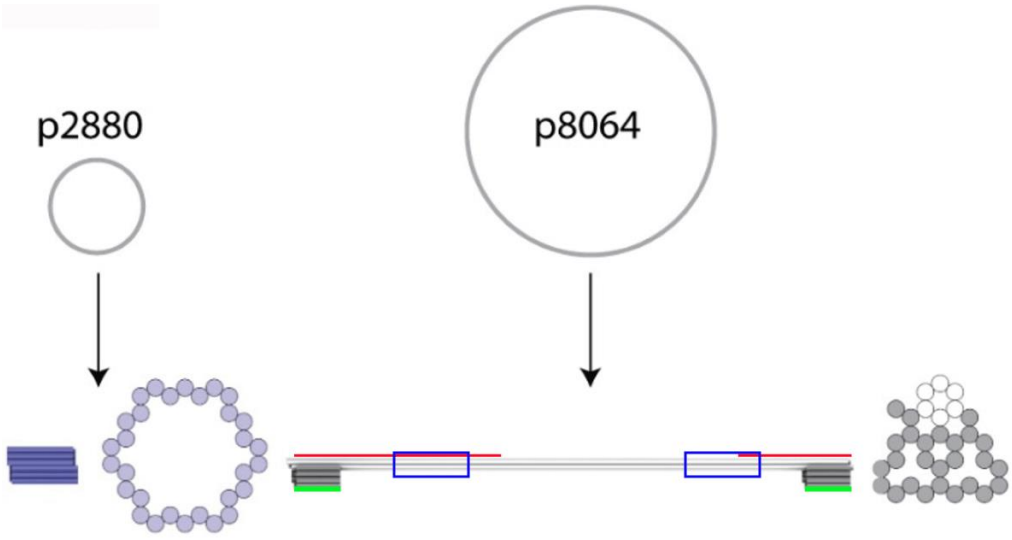

Figure 2.17. Schematic representation of the components of the 2nd iteration 1D rotaxane. The thinner slider on the left, constituting scaffold of p2880; the longer rail in the right, constituting scaffold of p8064, highlighted the areas with biotins (green), DNA-PAINT docking overhangs (red), and attachment locations for the slider (blue squares).

2.5.1 Initial screening of conditions and characterization of the structures and the rotaxane

As with the first iteration, once the design is completed and the staples have been ordered and received, the first step is to do a $MgCl_2$ test to identify the best concentration to use in the assembly of both structures (See Appendix G1.2). The gradient of concentrations used spanned from 0 to 22 mM $MgCl_2$. Based on the appearance of bands and presence of aggregation in the wells of the gels, I picked the concentration of 10 mM

$MgCl_2$ for the assembly buffer of the thin slider, and 14 mM $MgCl_2$ for the buffer of the long rail.

The structures, and the screening of some conditions for their assembly into rotaxanes can be seen in Figure 2.18:

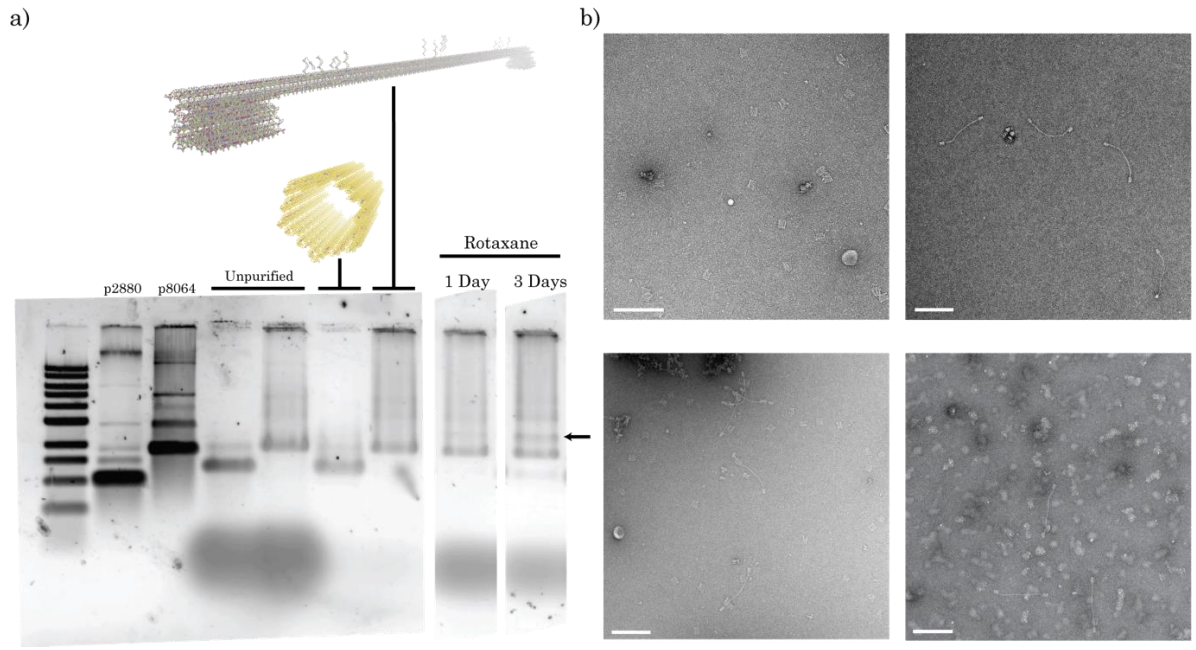

Figure 2.18. Characterization of 2nd iteration of individual slider and rail. a) AGE of both structures. Lanes 1 & 2 are scaffolds of both slider and rail (p2880 & p8064); Lanes 3 & 4 are slider and rail before PEG purification; Lanes 5 & 6 are rail after PEG purification; Lane 7 is the assembled rotaxane (with a closed slider) at a proportion of 2:1 rail:slider after a 1-day incubation; Lane 8 is the assembled rotaxane (with a closed slider) at a proportion of 2:1 rail:slider after a 3-day incubation. b) From top to bottom, left to right, TEM images of slider, rail, rotaxane after 1-day incubation, band gel-extracted from the rotaxane after 3-day incubation (marked with black arrow in a). Scale bars are 200 nm.

Both the thin slider and long rail assemble at 72% and 55% yields respectively, and can be purified via PEG without issues. As with the first iteration, despite it not being easy to tell from the AGE, the structures assemble into rotaxanes within the 1-day mark of incubation; the proportion used in this case is a 2-fold excess of rails over sliders. The appearance of the marked band in the 1-day and 3-day incubation lanes (yields of 17% and 19% respectively) prompted me to try and see if I could correlate it with the rotaxane band. A TEM characterization of the gel extracted band showed some examples of both rotaxanes and vacant rails, at the same proportion as the "whole-lane" TEM sample (20%

yield of successfully assembled rotaxanes),so there were not strong hints that this band would be the rotaxane one.

2.5.2 Free rotaxane synthesis

After characterising the structures and the rotaxanes, the next step consists in releasing the slider in order to see if it is capable of freely diffusing along the rail. This step also helps in checking the success of the closing step, which was already performed in the gel rotaxane lanes at the usual concentration of 100 nM of closing strands. For the release, the releasing strands were added at a concentration of 1 mM, and the resulting structures imaged in DNA-PAINT.

The experiments were done with either the release strand set for one position or for both positions, but nothing could be distinguished clearly in the gel once the release strands were added. In order to characterize the release process, TEM grids were prepared from these samples, along with a third option in which one of the possible attaching points was blocked by the *a priori* addition of the release strands to the rail. Given the characteristics of the attaching system, when mixing the sliders with the rails there is the possibility of having a rail occupied by two sliders concomitantly (Figure 2.19a); the attaching points are readily available for attachment by default. If the release strands are added beforehand the sites they bind to can be effectively blocked to the slider, due to the greater complementarity of the release strands for the attachment overhangs in the rail. The TEM imaging of these tests can be seen in Figure 2.19:

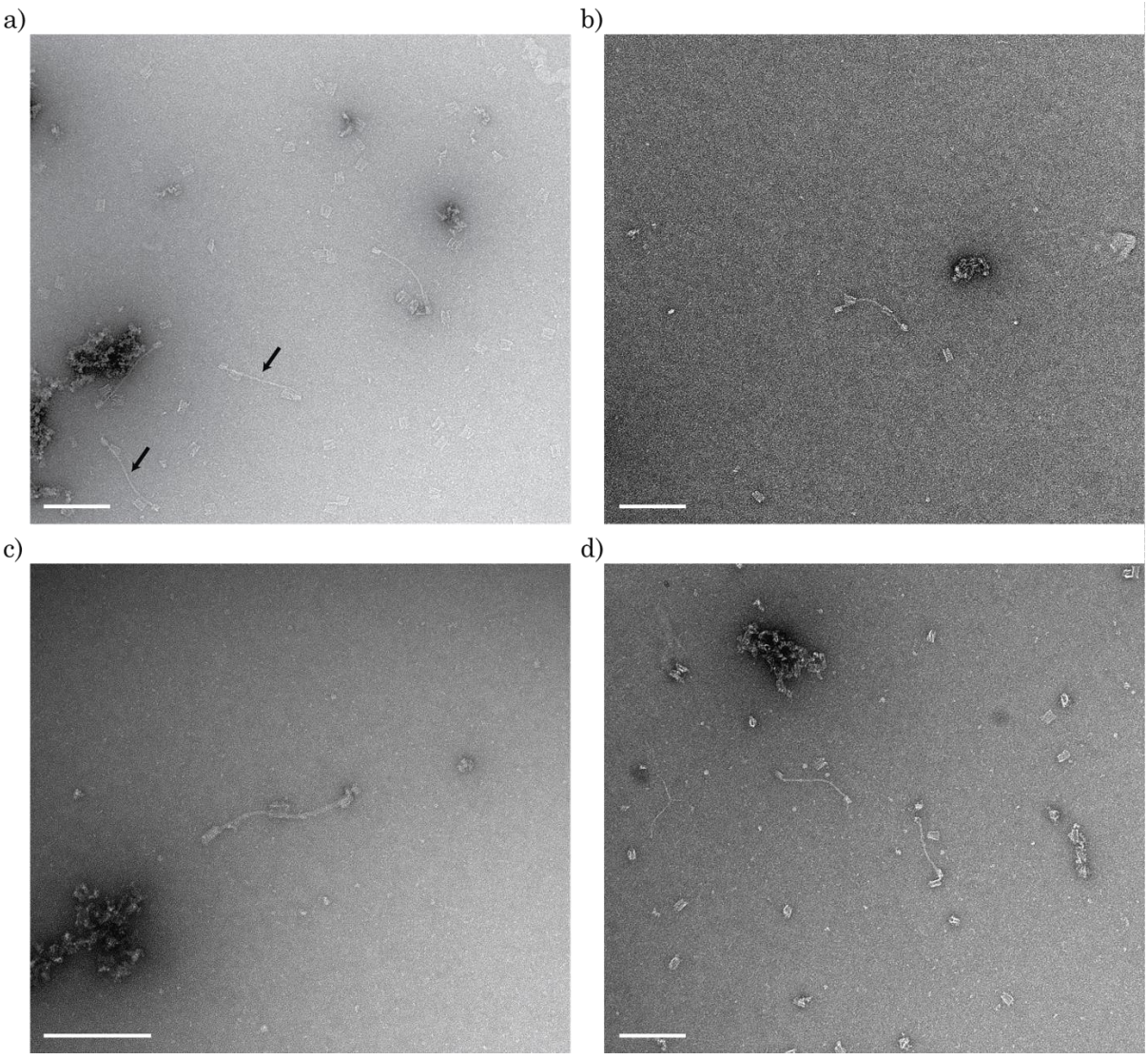

Figure 2.9. TEM characterization of the release of the slider in the rotaxane (all examples are assembled, closed the slider at a proportion of 1:2 rail:slider after a 1-day incubation). a) Rotaxanes presenting both attaching points occupied by sliders (marked with black arrows). b) Rotaxane released with one set of releasing strands. c) Rotaxane released with two sets of releasing strands. d) Attempt at assembly of slider + "pre-blocked" rail with a set of releasing strands. Scale bars are 200 nm.

The effectiveness of the release strands is not easy to gauge in this structure and in TEM for a series of reasons. This structure is symmetrical, if I use a single set of release strands it is not possible to differentiate between a successful event of release and attachment to the other attaching site and an unsuccessful event of release. The only way of distinguishing a successful release event in that case is the presence of sliders in areas other than any of the attaching points or the example that can be seen in Figure 2.19b. In this TEM image the rail presents two sliders, one bound to position and a second one

roaming freely; the implication is then that one of them was successfully released by the set of strands whereas the other remains attached to the rail. It can also be confirmed the successful effect of both sets of release strands in the case of 2.19c, which presents a slider freely roaming along the rail, unable to bind to either spot. It could be argued though, that the slider is only unable to bind to one of the attaching points and that by chance, or lack of time, it has not diffused enough to bind to the other, available, attaching point. There is no way of discerning this finer point with the low populations of successful structures and in TEM (22% yield of successful rotaxanes overall but very low sample sizes of released working rotaxanes, n= 20), but later developments in the study of the rotaxane dynamics showed that both set of release strands worked as expected when detaching a slider from a spot and preventing it from attaching in there in the first place. The alternative approach of limiting the attaching point in advance can be seen in Figure 2.19d, which shows the failed assembly of rotaxanes that used a "pre-blocked" rail (in one position only). Despite the set of release strands added only affecting one of the attaching points, no examples of successfully assembled rotaxanes could be seen in all of the TEM grid. As a follow up to contrast this observation, a DNA-PAINT experiment was done with the same set-up and conditions as in Figure 2.16. In this case the distribution of fluorophores is as stated above, 8 overhangs in each end of the slider, asymmetrical distribution in the rail with 16 overhangs in one end and 8 in the other (See Appendix G.3.1).

Through the DNA-PAINT experiment, the complete lack of successfully assembled structures when "pre-blocking" the rail becomes further confirmed. The presence of those strands appears to impede the interaction between the rail and the slider, perhaps because they caused unspecific interactions or overcrowded the reaction environment; the issue was not studied in depth but set the limitation that defined the workflow used from now on to produce rotaxanes in appropriate yields for the following stepping experiments.

To reliably obtain free rotaxanes, individual structures were folded as usual and incubated together for at least 1 day at a 1:1 proportion. After the incubation, all the sets of release strands, except the ones of one specific site, were added at an excess of 1 mM. This will cause all attaching points to be blocked and sliders to be removed, with the exception of one point and any slider bound to it. Following this mass release step, the slider is closed (100 nM of closing strands) and the set of release strands that were not previously added are introduced. The end result will be rotaxanes with a single slider freely diffusing along the rail, the addition of the specific set of antirelease strands will allow the slider to attach to a specific location, thus completing a stepping cycle.

To test this process in a gel to try to identify changes in the band distribution, a set of samples was run in AGE.

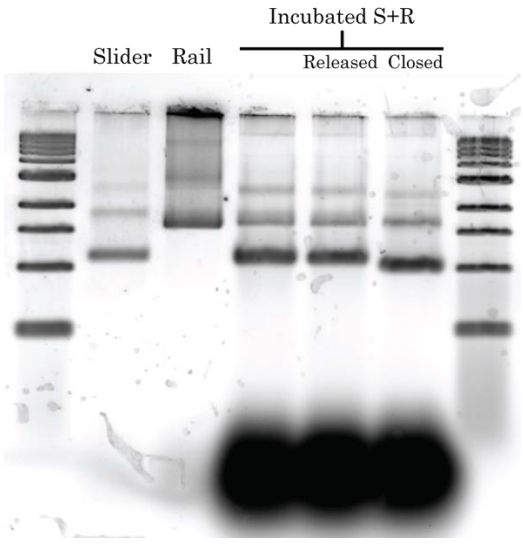

Figure 2.20. AGE characterization of the different steps of the free rotaxane proposed workflow. Lanes 1 & 2 are slider and rail after PEG purification; Lanes 3-5 are the assembled rotaxane (with an open slider) at a proportion of 1:10 rail:slider after a 3-day incubation in different steps of the process, Lane 4 presents the incubated rotaxane after the addition of one set of releasing strands, Lane 5 presents the incubated and released rotaxane after the addition of the closing strands.

Upon mixing and incubation of the thin slider and the long rail, at an excess of sliders to ensure that all rails are populated, a thin band appears above where the monomeric band of the rail is (intensity of the band is 13% in all three incubated rotaxane lanes). In Figure 2.18 I conjectured that this band, which appears more intensely after a 3-day

incubation, is the one of the rotaxane. Its extraction then showed both rotaxane and unpopulated rails on TEM, but the yield was low enough (20% as in the unextracted sample) for me to not be able to conclude strongly about the nature of this band. In this gel, the introduction of one of the sets of releasing strands doesn't visibly affect the overall distribution and intensity of the bands, whereas the closing strands do. The addition of the closing strands causes the monomeric slider band to migrate faster (as seen in the first iteration Figure 2.9); it also seems to have such an effect in the suspected rotaxane band, which could confirm the presence of sliders in this slower band.

2.5.3 Redesign and optimization of the synthesis

Before moving on to the confirmation of the rotaxane band, and the further curation of the production workflow, I decided to introduce some minor structural changes as well as methodological ones. Taking advantage of the extra space available in the rail in this design, I added a third attaching position in the mid-section, equidistant from the stoppers. This position helps break the symmetry of the structures which will be important later on, particularly when checking the stepping capabilities of the system. In its composition, the overhangs follow the same structure and distribution as it has been since the first iteration. Methodology-wise, after the different proportions of rail:slider that I have been testing across the previous experiments, I decided to start using 1:1 proportions as the results did not improve when adding an excess of sliders or rails. Originally, I did the former to prevent rails being left unoccupied after incubations, but the yield of the rotaxanes did not change in a noticeable manner.

With these changes in place, I decided to confirm that the upper band is the rotaxane. In AGE, a large volume of the incubated rotaxane was run with a single-tooth comb in order to increase the amount of the band to be obtained via gel extraction (See Appendix A.2.3). The gel and subsequent TEM imaging can be seen in Figure 2.21.

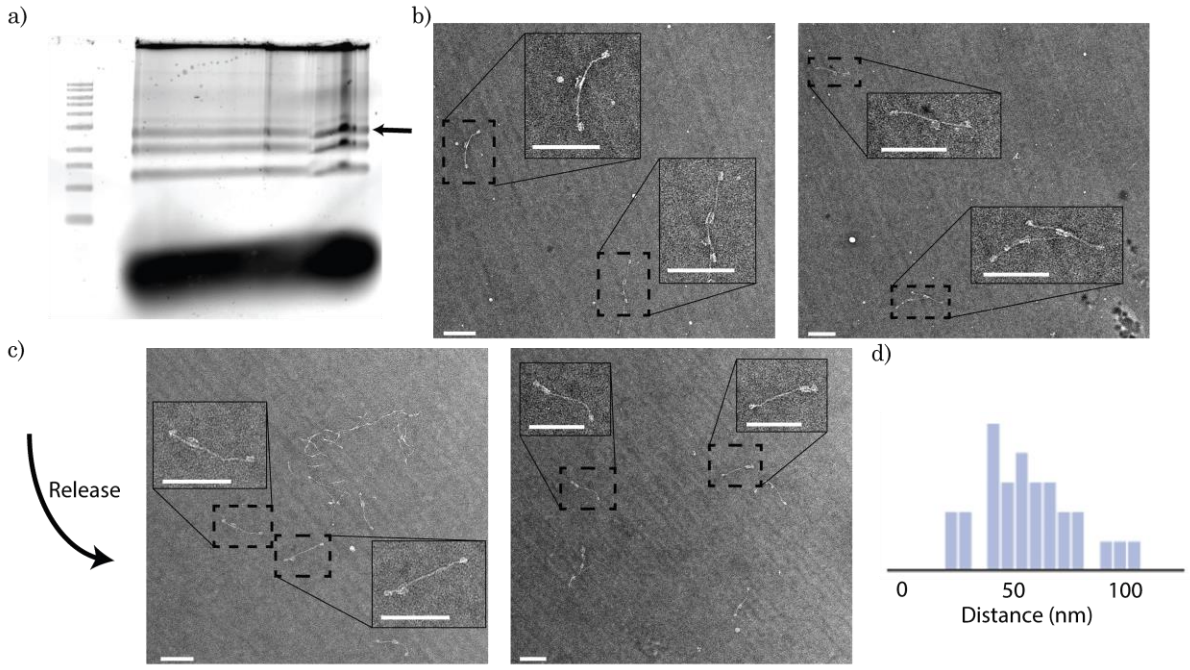

Figure 2.21. Gel extraction of rotaxane band followed by TEM imaging of the structure and the following release step. a) AGE of the assembled rotaxane (1:1 rail:slider) after a 3-day incubation, release of the attaching positions by the stoppers (sliders can only be present in the centre of the rail), and closing of the slider. Black arrow points to the suspected rotaxane band that was extracted. b) TEM imaging of the extracted rotaxane band. c) TEM imaging of the extracted rotaxane band after releasing the slider from the middle position into free diffusion along the rail. d) Histogram of the distribution of locations of the slider along the rail measured by the distance between the slider and its closest stopper. All scale bars are 200 nm.

The extracted band of the AGE had an intensity of 23%, almost doubled in its intensity when compared to the band under the previous incubation conditions in Figure 2.20 . TEM images clearly show the slider in its intended docking position in the middle (with a yield of 80%), and no more than one slider per rail was seen. Upon addition of the specific set of releasing strands for the middle position in the usual excess (1 mM at RT for 40 minutes) to the extracted sample, the majority of the sliders have moved from their locked positions to random positions along the rail in an even way, as seen in Figure 2.21d . This is to be expected of a closed slider around the rail that is suddenly free to diffuse along the length of the rotaxane.

Regarding the process though, placing a great volume in a single, wide lane on a gel is not without its issues and inefficiencies, as can be seen from the irregular migration

profile of the bands and the apparent aggregation in the well. These factors make adequate gel extraction more difficult. In future applications of this purification technique, such as in the following experimental chapter, gel extractions will be performed using the usual 15-teeth combs, all lanes containing the same sample.

Putting aside the technicalities of the AGE, the extracted band showed predominantly rotaxane structures; the yield is fairly low as gel extractions usually recover less than 50% of the initial structures, particularly when taking into account the issues mentioned above.

2.5.4 Actuation of the rotaxanes

The next logical step in the workflow, the addition of the set of "antireleasing" strands to free up a secondary attaching point for the slider to diffuse to (at concentration of 1 mM at RT for 40 minutes), was also performed in this extracted sample. Unlike with the releasing strands, the TEM imaging of this step showed no clear examples of stepping, most structures were englobed in uniform blobs in the grid. My hypothesis is that the blobs come from the aggregation of the excess of staples added, compounded by the fact that at this step the addition had happened for a second time. To corroborate this hypothesis, I run a gel of the samples imaged in Figure 2.21, as well as the failed stepping described above.

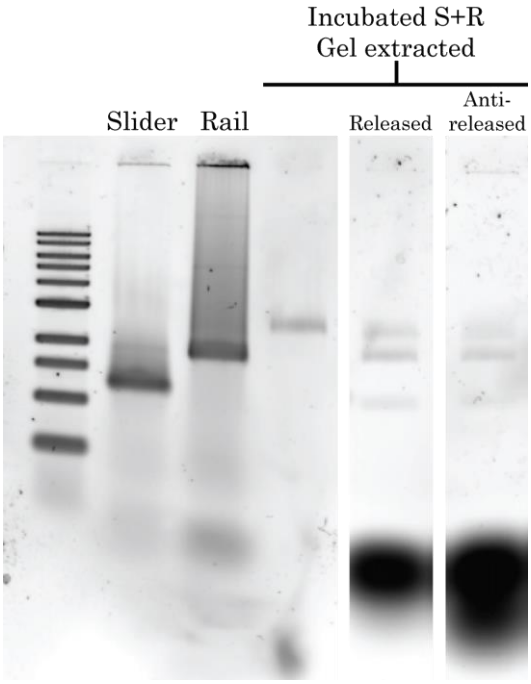

Figure 2.22. AGE of the gel-extracted rotaxane and following steps of actuation. Lanes 1 & 2 are slider and rail after PEG purification; Lane 3 is the assembled rotaxane band extracted from the gel in Figure 2.21; Lane 4 presents the extracted rotaxane after the addition of the set of releasing strands for the middle position; Lane 5 presents the extracted and released rotaxane after the addition of the antirelease strands.

In the gel the successful extraction of the sample is confirmed, along with the effect of the release strands. The latter lane also shows the appearance of monomeric slider and rail bands (intensities of 39% and 21% respectively), which points to a defective or inefficient closing of the slider. Issues with the closing aside, the antirelease lane presents fainter bands, as the structures are diluted further with each step, and a great excess of staples.

To try to improve the final conditions of the rotaxanes in solution two changes were introduced in the process. The first, obvious change is the decrease of the concentration of added release strands, at first from 1 mM to 500 nM. Concomitantly, the temperature was raised from RT to 37°C. The results then, as imaged with TEM, were still clouded with the excess of strands, so the concentration was further dropped to 50 nM. A gallery of the TEM imaging done on these new conditions can be seen in Figure 2.23 and in Appendix G.2.4.

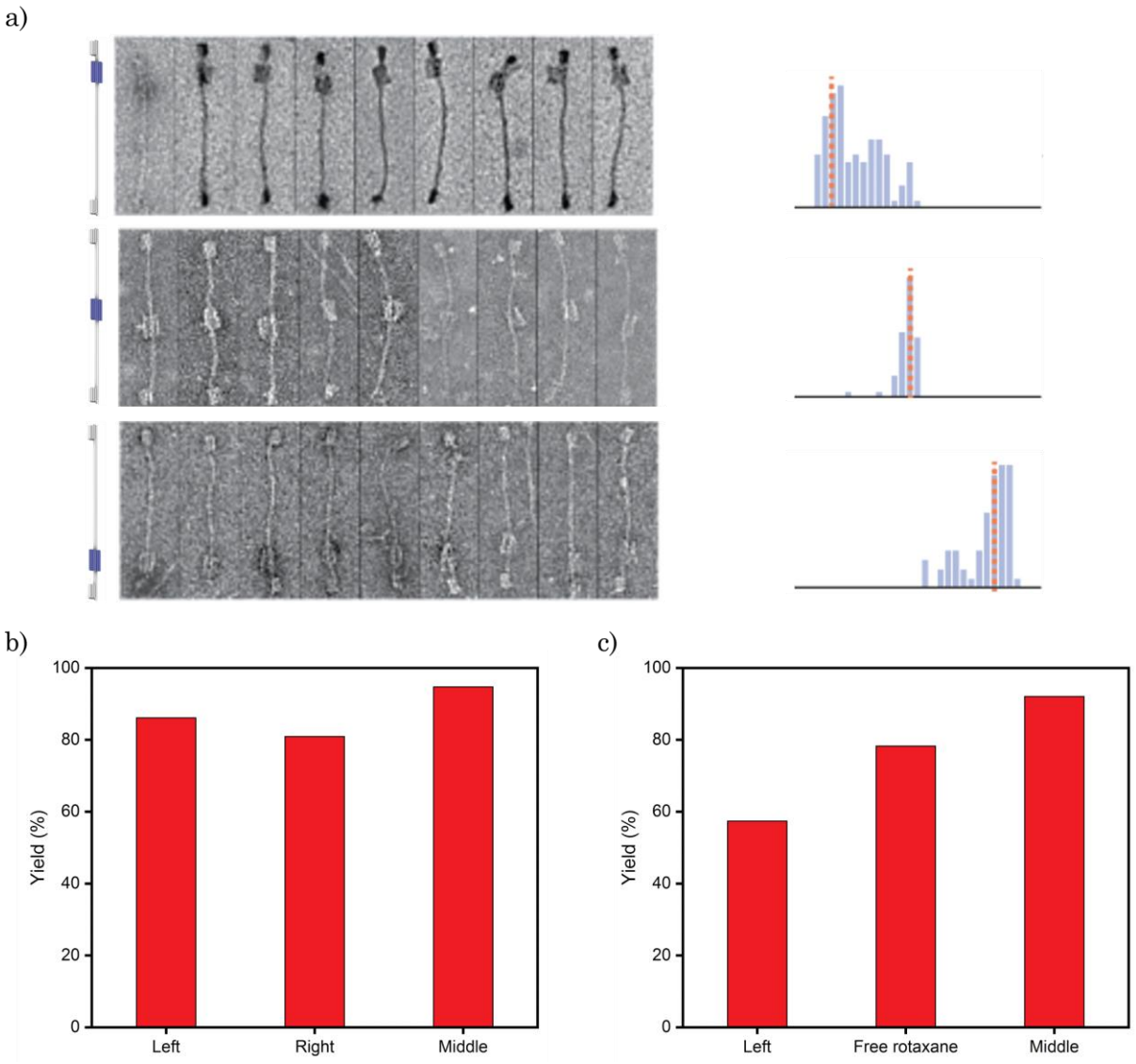

Figure 2.23. TEM and quantification of positioning and stepping with the free rotaxane. a) TEM images of free rotaxanes after addition of left/right/middle sets of antirelease strands, as seen top-to-bottom. On the right of each row, histograms representing the distribution of the positions of the slider on the rail (the red dotted lines represent the expected slider position). b) Histogram containing the yields of successful attachment into specific positions after addition of specific antirelease strand sets; data obtained from TEM images. c) Histogram containing the yields of successful attachments and detachments constituting a stepping cycle within the same sample; data obtained from TEM images..

From the free rotaxane sample that was also imaged, prior to any further addition of strands for stepping, the yield of the production and extraction of free rotaxane was calculated to be 43% ± 6 (SD, n=3). The addition of the specific sets of antireleasing strands, at the reduced concentration, produced the desired attachment of the slider into the specific positions and allowed for a clear TEM grid to image. When producing the percentages of successful attachment, and successful stepping between positions in the

same sample, the average number of structures counted for each position was at least around 200, although they all come from the same experiment (n=1). Overall, the attachment from free rotaxane to a specific position (2.23b) achieved a high yield; the stepping cycle within the same structure had a relatively low yield in the first step, in contrast with the attachment to the secondary position. It is my hypothesis that the attachment in the middle yield is inflated by structures that did not undergo the cycle and were stuck in the middle since the very beginning, given that the middle is the initial attachment point when assembling the rotaxanes in the first place.

2.6 Summary

A one-dimensional actuator was constructed following the rotaxane architecture. The slider threaded through could be reversibly positioned in 3 different positions on the rail upon the introduction of the specific set of instructions (strands). The structure assembly and purification is labour-intensive due to the idiosyncrasies of the rails and the sliders. The points that could see improvement would be around the incubation processes, particularly the mechanisms of attachment between the two structures, perhaps a screening of different sequences and structures in the overhangs could produce a more suitable system. On that line, tests could also be conducted by use of specialized software such as OxDNA (76), that allows to study, in a coarse-grained simulation, the interactions of sequences taking into account the context of the origami structures. The inability to pre-block sites, since it leads to the complete disruption of the slider-rail interaction, is a problem that remains unexplored and its solution could hint towards unexpected interactions of the release strands with the rail, aside from the expected ones in the specific overhang regions. Addressing the first point raised regarding the incubation bottleneck could shed some light in that aspect.

Following this, seen from the results, particularly those in Figure 2.18, the closing process could definitely be improved, since failure to close the slider properly spoils any

successful assembly between the slider and rail. A possibility is that the addition of the closing strands at an excess causes different strands to bind to the opposite ends of the seam in the slider, preventing the slider from being able to close successfully. A screening of different concentrations and times of incubation, perhaps even temperature, of closing on assembled rotaxanes would be necessary to understand the dynamics of closing when the slider is wrapped around the rail.

Another interesting aspect that was left unexplored in the system was the actuation speed. The times used, 3-day incubation, 2h closing, standard 40 minute incubation for each stage in stepping, come from alterations made along the course of the project on the initial time scale developed by List *et al* (87). A possible series of experiments on the Nanoimager, with a labelled slider and flushing in the different structural and actuating set of strands, could provide some insights into this question.

In order to fully solve the symmetry issue that arises when trying to quantify the efficiency of the stepping, in a more definitive way than introducing a middle point of attachment, the attachment of gold beads to one of the stoppers was studied. Although it never came to fruition, staples with overhangs capable of binding to functionalized gold nanoparticles were introduced in the design. By having such nanoparticles attach to a particular side of the rotaxane, differentiation of sides would have been trivialized in TEM.

Despite obtaining good yields in single positioning/steps, the system as it is faces the inability of performing multiple cycles unhindered in solution due to the eventual crowding of waste strand complexes in the environment (each sequential addition of release/antirelease is made in slight excess over the preceding addition to ensure that all sliders are released/attached). A straightforward solution that has been contemplated from the onset of the project is to have the rotaxanes functioning in a flow-chamber. Flushing in the determined set of “orders” at a time, and intercalated by washing cycles,

would solve the issues of declining efficiency overtime; the cap of efficient cycles in that setup would theoretically be non-existent and could have great numbers of rotaxanes working on surfaces/DNA origami canvases in simultaneity.

Many of the issues that remain on this rotaxane model are not without possible solutions and avenues of study, as detailed above, but given the quick pace of the project and adherence to timed project milestones, once actuation in the 1D was observed, the project progressed onto its second stage, the development of a system capable of the same actuation but in 2D. I will explain the efforts made on that direction in the chapter that follows.

Chapter 3

DNA Origami Structure for 2-dimensional motion

As the continuation of the previous chapter, and following the logical progression of developing a molecular printer, the next objective to achieve is the addition of a 2nd axis of movement for the system. A 2-dimensional mechanism is capable of covering a determined area and introduce modifications on it, although this chapter will focus exclusively on the development of this second axis of movement and its actuation, concomitantly with the initial 1-dimensional system. The system of choice has the shape of a quarter of a circle, one axis being the displacement along the arc of this section of circumference, the other being along its radius in a fashion very similar to that of the rotaxane. The process of its design will be an iterative one, as different issues with the different scaffold routings will appear throughout the initial designs. The means of actuation will be modified from the direct attachment explained in the previous chapter to an indirect form of interaction between the moving parts of the system. After successful actuations of the different individual parts, as characterised by AGE and TEM, 2-dimensional motion will be verified with DNA-PAINT.

3.1 Aim

"The production of a system with the ability to precisely position a header or a structure of the like in a 2-dimensional, or even 3-dimensional, space is a necessary preliminary step in the development of a device capable of MAM".

As with the linear actuator, there are many different ways of achieving the desired 2-dimensional motion, but since we are using the structures developed earlier, one of the axis will be a rotaxane. The remaining axis could be another rotaxane perpendicular to

the initial one, so that a square area could be covered and the slider placed following a cartesian coordinate system. The design chosen covers the area of a quarter of a circle and the positioning of the slider follows a polar coordinate system, the actuation dependent now on the introduction of a set of instructions for each axis. Given the similarity of the described 2D system to a bow and arrow, tensed before a shot, the new system will be referred to from now on as a Bow-and-Arrow (BA). This nomenclature does not include the presence of the slider threaded on the rail, or "arrow" under the new naming.

3.2 DNA origami design of the Bow-and-Arrow (BA)

The BA design can be broken down in 4 interacting subunits made of helix bundles, three straight sections and a curved one composed by a continuous scaffold. The three straight sections are, the two "strings" or lines parting from the edges of the circumference arc converging together in the central point of said circumference; and the "arrow" or mobile radius that is loosely connected to the central point and displaces itself over the curved subunit. This curved subunit, or "bow", is the arc section. An early schematic can be seen in Figure 3.1.

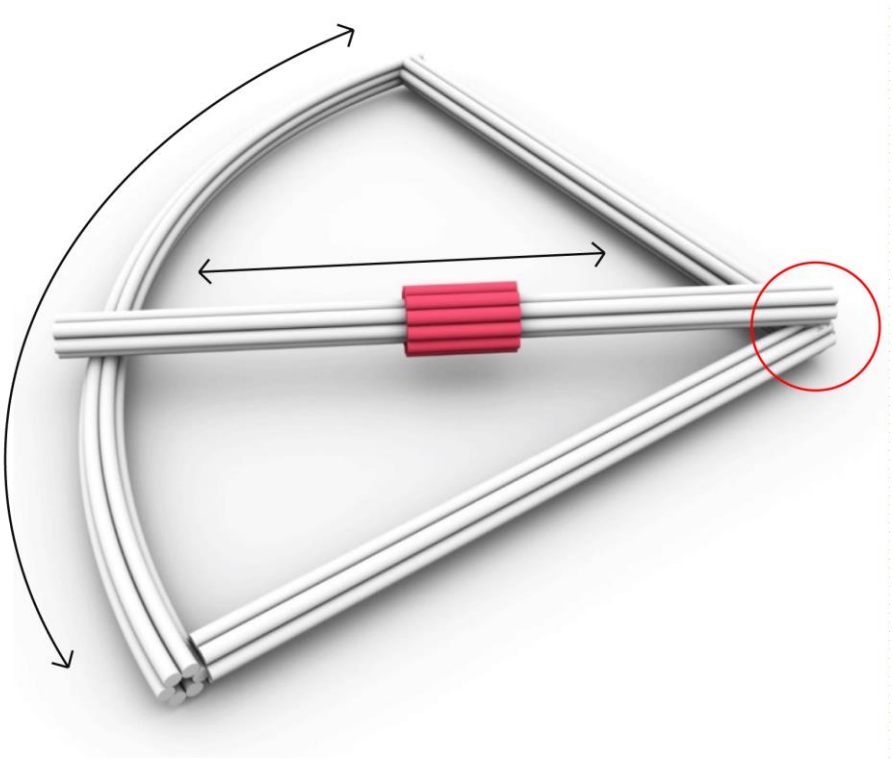

Figure 3.1. Schematic representation of Bow-and-Arrow, with slider in red. Black arrows mark the 2 axis of motion; red circle marks the centre of the circumference were the strings and the arrow connect by two strands of 3 unpaired nucleotides.

Given that all these subunits are connected and that curvature must be induced in the bow, the scaffold routing is not trivial and presents some particularities of DNA origami design not discussed so far.

The BA subunits' conformation was 6-helix bundles or 7-helix bundles (depending on the design iteration). The variation in number affects the scaffold routing but not the overall functionality so for the general explanation of the structure I will not make distinctions. The only bundle that needed specific modifications was the bow, where a curvature through a 90° angle had to be induced. Dietz *et al* (191) discuss how twisted and bent structures can be produced with DNA origami bundles made of tightly cross-linked duplexes by the insertion and/or deletion of base pairs (bps). In a DNA bundle in honey-comb lattice pattern (the one used in all structures used throughout the thesis), and provided there are no scaffold crossovers between neighbouring duplexes, staple crossovers can be distributed as often as every 7 bps. It is commonly assumed that the

nature of the B-form DNA helix is such that in that space of 7 bps the helix turns 240° (191); this is a natural unit from which to build the pattern of crossovers. This 7 bps-sections are constrained by their neighbouring sections, if an base pair is added/deleted it strains the structure causing an underwinding/overwinding of the section, respectively. This in turn causes a push/pull force from the affected section towards its neighbours. To compensate for this, the bundle will globally twist right-/left-handedly and bend towards/away from the modified section.

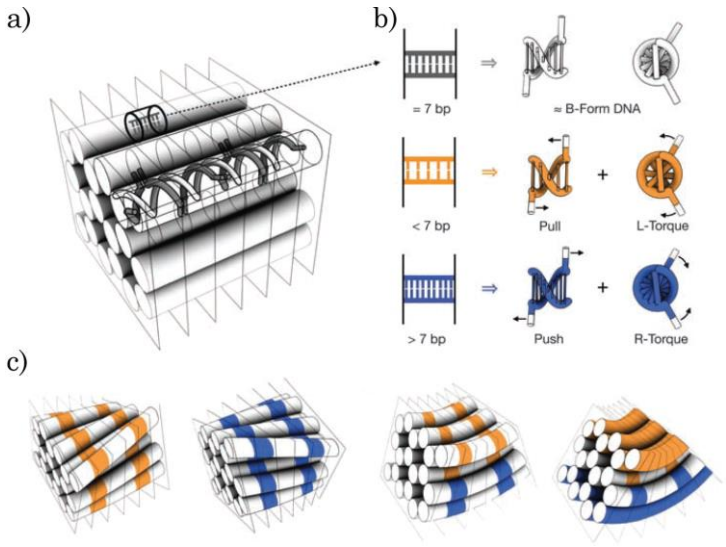

Figure 3.2. Twisting and bending DNA origami bundles. A) schematic representation of the 7 bp-long sections in the helices of a bundle in a honey comb lattice pattern. B) Visual representation of the direction the disruptive forces take when caused by deletions and insertions of base pairs in a section. C) Models of reinforced twisting / bending deformations. Taken from (191).

As can be seen in the models of the bottom row of the Figure 3.2c, if only modifications of the same type are distributed evenly among the helices comprising the bundle, then global bending can be prevented while twisting is induced. Alternatively, if for every insertion there is a deletion at the same level, in a gradient through the cross section of the bundle, the global twisting is eliminated but the bending is maintained. The steepness of the bend can be customized by increasing the number of insertion/deletions.

Before designing the distribution of insertions/deletions in the bow I designed the overall dimensions of the BA. Knowing that the length an arc equals the radius of the

circumference * the angle of the arc in radians, and that the amount of material I could work with was a maximum of 8064 nucleotides (p8064 scaffold), I calculated the longest strings I could make with 6-helix bundles while still having enough material for the rest of the system so that the angle of the arc was 90°. An iterative process yielded that the length of the strings should be around 89 nm, the length of the arc would then be 140 nm; the arrow should be longer than the rails, and account for the extra helices at the tip that act as an stopper for the threaded slider (element not included in schematic 3.1). The arrow was around 97 nm in length for the arrow, the stopper being around 15 nm in length and 14 helices tall. This values of the lengths are derived from the conversion of 1 nucleotide having the length of 3.4 Angstrom or 0.34 nm. Adding up all the lengths of all the helices, all subunits are 6-helix bundles except for the stopper that is composed of 14 helices, yields a total length of 2713 nm (7982 nts used out of 8064 nts). These are rough numbers as not all helices in each subunit could be of the same length, the numbers provided above are the average lengths of all the helices included in each subunit. See Figure 3.8 for a schematic representation of the scaffold routing and the disparity in helices' lengths.

In the aforementioned study of twisted and bent origami structures (191), there were some examples of 90° angle arcs, and the distribution of insertions/deletions was two of each in the cross section, one deletion in each of the two "inner" helices of the bend and one insertion in each of the two "outer" helices (See Figure 3.3 for the schematic representation of this type of distribution). The frequency was every 14 nt, or two sections. The main issue is that I could not make direct comparisons since the structures in which the bending was tested in the literature is different from the 6-helix bundle. Another factor to take into account was the difference in length. To determine the appropriate in/del distribution and periodicity, I made three versions of the bow separated from the rest of the structure to simulate in OxDNA (76), see Figure 3.3.

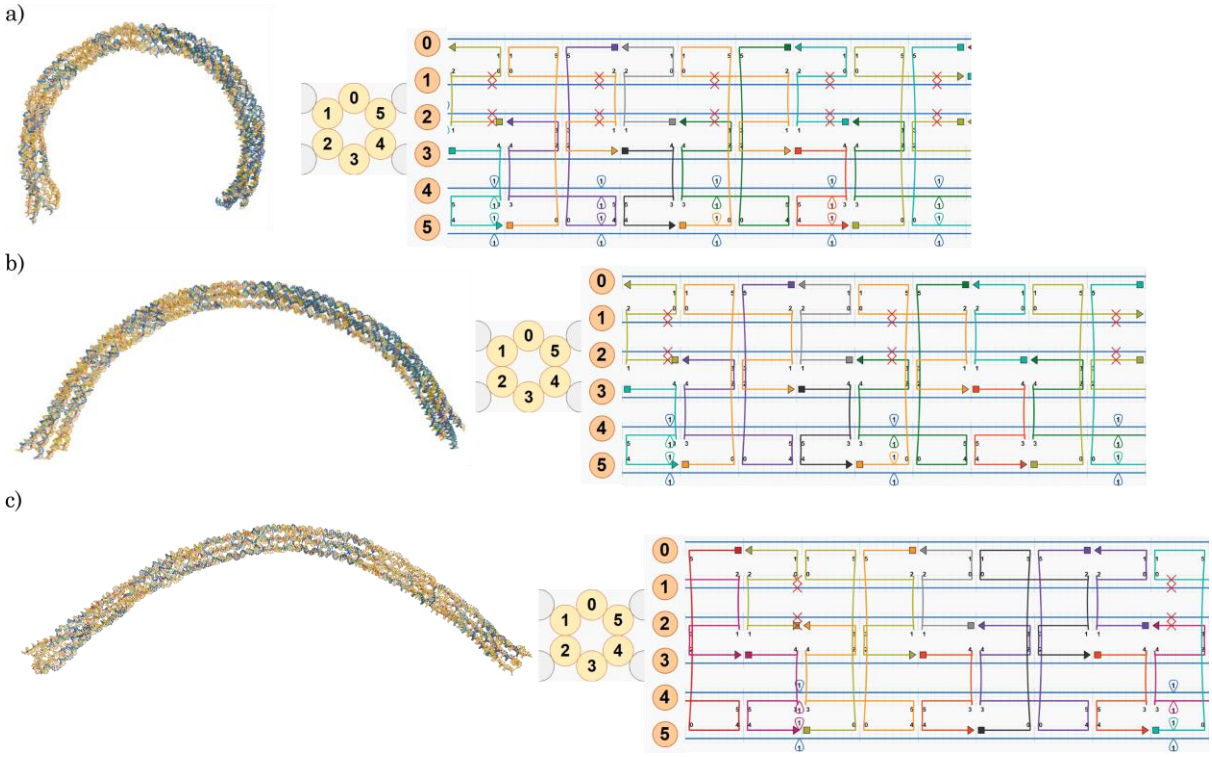

Figure 3.3. OxDNA simulations of the bow structure and a section of the bow as design in CaDNAno, red crosses marking the deletions and the teardrops marking the insertions. Insertions/deletions every a) 14 nt, b) 28 nt, c) 46 nt.

The first bow, following the literature's periodicity, presented an angle that was obtuse (~290°) and therefore incompatible with the BA system , halving this periodicity once (every 28 nts) and twice (every 46 nts) improved the shape by reducing the angle, to ~150° and to ~90° respectively. Ultimately I chose the bow with the insertions/deletions every 46 nts since it was the correct angle to fit in the OxDNA simulations of the whole structure (Figure 3.4).



Figure 3.4. OxDNA simulation of the 1st iteration of the BA.

As it was mentioned in the introduction, OxDNA is one of the tools that can be reliably used in DNA origami design simulation (192). In the design of the BA, this coarse-grained simulation is relied upon, mostly due to the increased complexity of the structure and some of its characteristics, such as the bent section of the bow. The simulations have a wealth of past studies that can be found in the literature, where they have been pitted against empirical studies of the simulated structures, and where they have been validated as a useful tool for guiding design choices (193–195).

These bows and BA simulations belong to the first iteration of the design but the main characteristics of the bending of the bow and sizes of the subunits were left mainly unchanged, I will specify those variations in the appropriate sections of the chapter. I have left out of the explanation the main difference in-between the iterations, the scaffold routing, how the different subunits were attached together. This I will explain in each dedicated section as well.

3.2.1 Modified strands and overhangs in the BA

As with the 1D system, the structure has some modified strands and specific overhangs for its future characterisations and measurements. In order to be able to study the structures with DNA-PAINT, it was necessary to add biotins in the bottom of the BA; 10 strands with a biotin on the 5' end were added to the structure, 3 under each string and 4 under the bow; and to add the docking overhangs to the top of the structure, 12 per string and in the arrow, and 19 in the bow. These numbers would later be reduced since an excess of docking sites can be deleterious to the clarity and quality of the imaging; breaking the symmetry of the system will also be a motivation for the elimination of some of the docking sites.

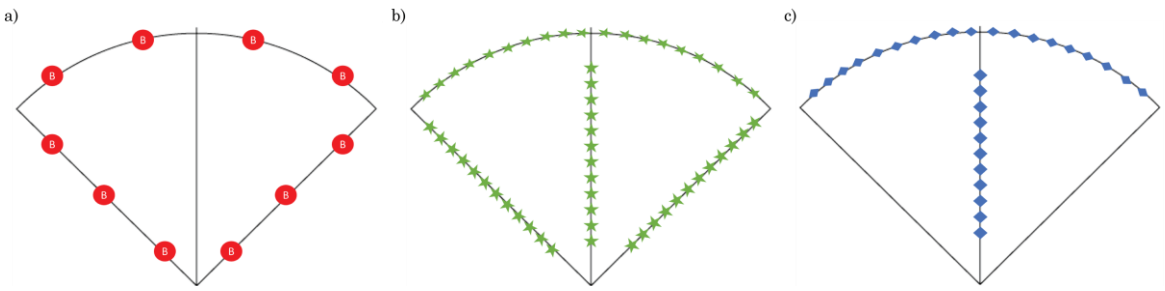

Figure 3.5. Schematic representation of the distribution of modified/overhanging sequences on the 1st iteration of the BA. a) Biotin groups protruding from the bottom helices of bow and strings. b) DNA-PAINT docking sequences protruding from the top helices of bow, strings and arrow. c) Attaching sequences for arrow and slider protruding from the top helices of bow and arrow, respectively.

The remaining overhang strands are related to the attaching systems in place for both the slider and the arrow. The attachment mechanism in place for the 1D system was based on the direct attachment between the overhangs of both the slider and the rail, and, while it produced successful attachments it was not a good fit for the BA. This is mostly due to the fact that it needs 4 specific overhangs for each position, in both moving elements (the arrow and the slider threaded through), which is not space efficient and limits the spots into which the moving parts can attach to. An alternative attachment system, that was demonstrated to work in a rotaxane (196) very similar in structure to that one of the 1D rotaxane, was used instead in the 2D BA to attach the tip of the arrow to the bow and the slider to the arrow shaft.

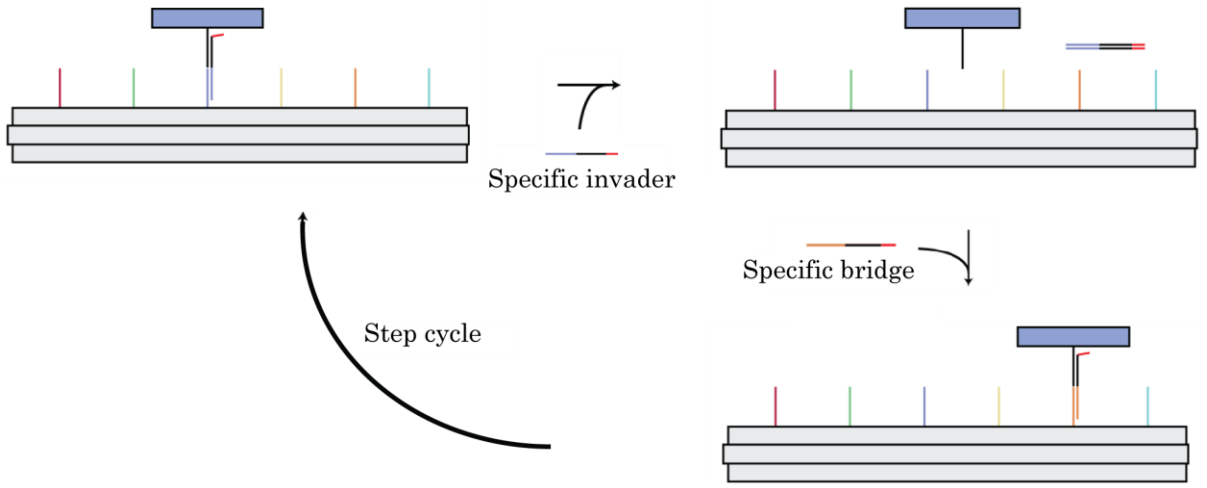

Figure 3.6. Schematic of the indirect attaching system. The overhangs of both moving parts do not interact directly, a bridge strand is complementary to both and attaches the moving structure into place. By addition of a specific invader strand the bridge strand is removed by TMSD, detaching the two parts. By addition of a specific bridge strand the moving structure attaches to another, specific position, completing thus a step cycle.

As seen in Figure 3.6, by making the interaction indirect, there is no need to crowd the tip of the arrow or the slider with as many sets of overhangs as possible positions of attachment; only two overhangs are present then and make the arrow and the slider available for attachment to any two adjacent overhangs in the bow or in the arrow shaft. In the design of these overhang positions along the bow and along the arrow shaft, all of them were placed equidistantly (every 21 nt). Because of this distribution, there are as many positions of attachment as possible that can all be occupied given the appropriate combination of the two bridge strands.

3.3 1st Iteration of the 2D system

After explaining the main, common details of the BA's design, I will proceed to explain its first iteration and the initial experiments. I will leave for the end of this section the particularities of the scaffold routing since they were pivotal in the behaviour of the first version of the BA.

After performing the mixes of the DNA origami structure at the usual proportions (Appendix A.1.3), a $MgCl_2$ test in AGE was performed followed by TEM imaging.

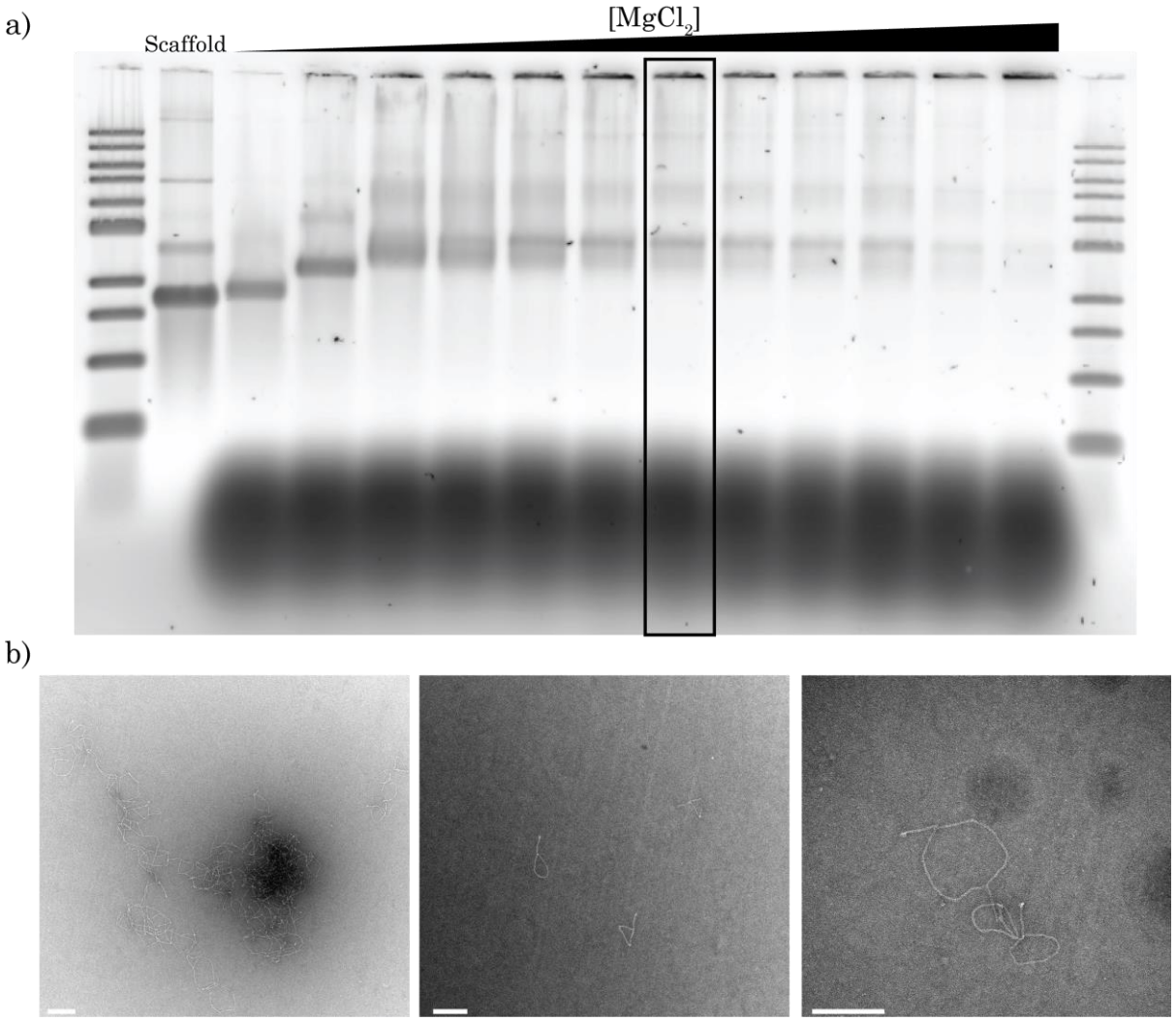

Figure 3.7. Characterization of 1st iteration BA. a) $MgCl_2$ test in AGE, the scaffold used was p8064, the gradient of concentrations go from 0 to 22 mM. In a black rectangle the chosen concentration (12 mM) b) TEM imaging of the 1st iteration BA, from left to right, overview of aggregated structures, monomeric structures, misassembled structures. All scale bars are 200 nm.

The chosen concentration was 12 mM $MgCl_2$ and, although a clearly defined monomeric band could be seen (yield of 41%), there is a strong aggregation in the well (32% of the intensity in the lane). The TEM imaging shed some light on the gel bands: although there is a fair amount of monomeric, well-assembled BAs, there are also great amounts of aggregation and some unexpected misassembled structures. The latter seem to be two different BAs that had their bows broken in half and fused together, but given that I had a certain amount of properly folded structures I decided to attempt locking the arrow into

position (incubation at RT for 40 minutes with a 20x excess of the bridge strands for the middle of the bow) and characterize it via AGE and DNA-PAINT.

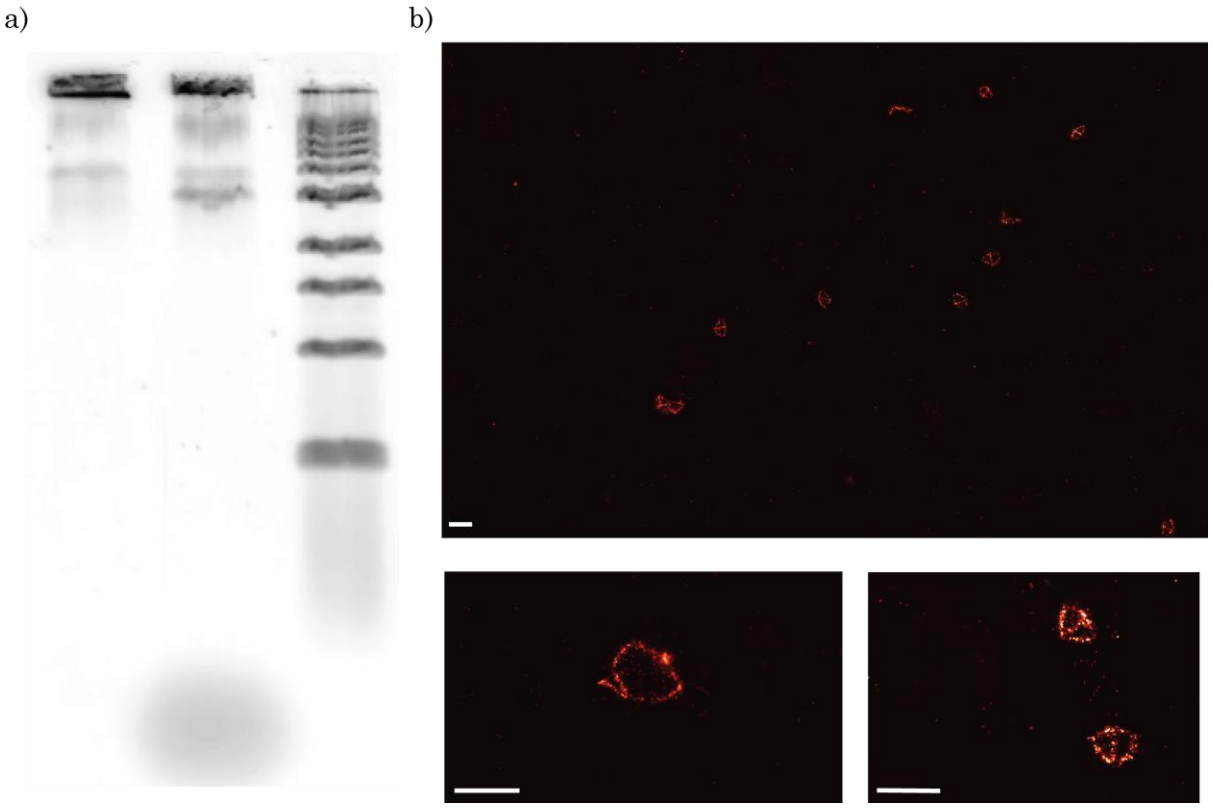

Figure 3.8. Characterization of the 1st iteration BA with arrow locked in the middle of the bow. a) AGE of the BA, lane 1 presents the BA with a free arrow, lane 2 contains the BA with the arrow locked. b) DNA-PAINT imaging of the locked BA, close-ups of the correctly assembled BA with the arrow locked in the middle and of the misassembled structures. All scale bars are 200 nm.

From the AGE, despite the amount of aggregation in the wells (72% of the product is in the well, being reduced to 50% when adding the locking strands), the monomeric, unlocked band shows a yield of the assembly of 20%. The locking of the arrow into the middle position seems to be successful, since a migrating band faster than the monomeric, unlocked one appears with a yield of 19%. As seen in Figure 3.8, from DNA-PAINT, the yield of these correctly folded and locked structures is of 36%, with unlocked structures at 47%, and misassembled ones being 17% of the total BAs.

Upon closer study of the scaffold routing it is clear that there are some mistakes that could be leading to an unravelling of the structure that would cause the aggregation in the well and the appearance of the "fused" bows.

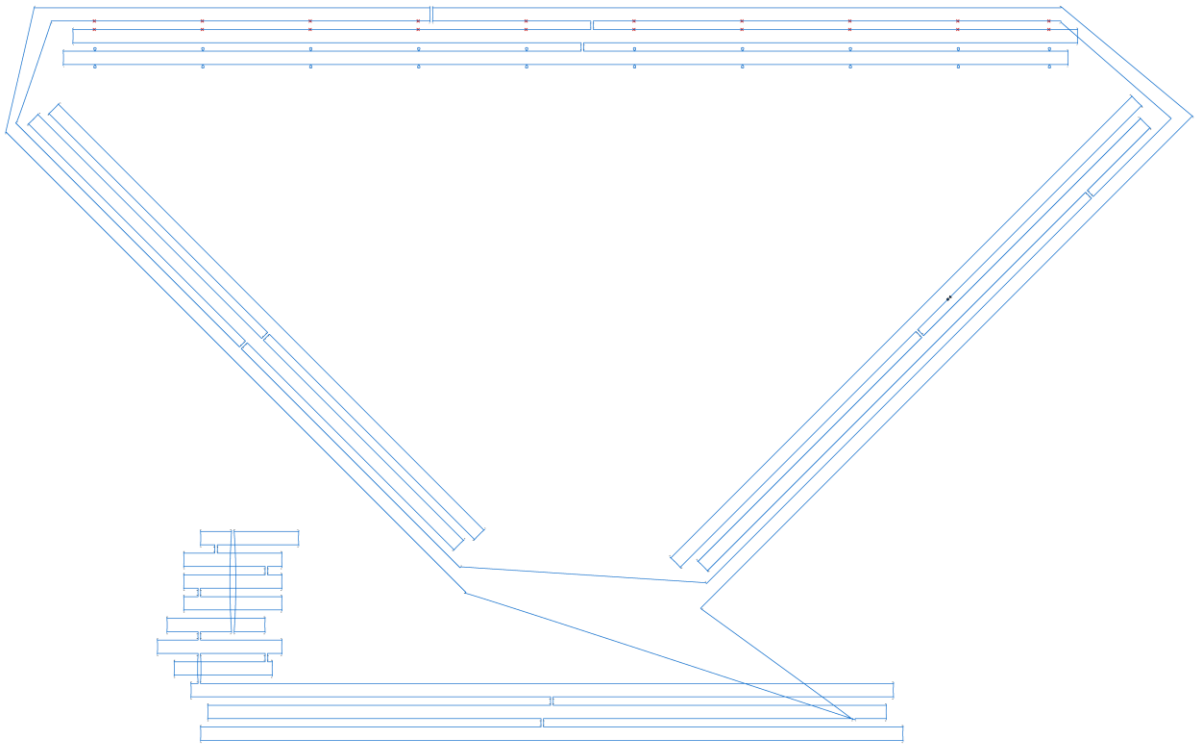

Figure 3.9. Schematic representation of the scaffold routing in the 1st iteration BA. Straight lines connecting subunits do not represent nucleotide strings, they have been elongated for aesthetics and clarity, the scaffold jumps with no single-stranded sections in-between subunits (with the exception of the strings-arrow connection that has 3 nts unpaired). Deletions and insertions in bow represented as red crosses and blue teardrops respectively.

As it can be seen in Figure 3.9, the scaffold has to do two "laps" around the structure, the even number of helices in each subunit prevents the scaffold from simply forming each subunit at a time. The top most helix in each of the strings of the BA is completely disconnected from its neighbouring helices (no scaffold crossovers between them), depending solely on staple crossovers. The staple crossovers are in turn less frequent than in the other helices (at least one every 21 nt) since the attachment overhangs are placed here and the nature of their nicks conditions and restricts the possible placement of the staple crossovers (when taking into account the hybridization stability of said staple, i.e.

not having in close consecution crossovers). This, added to the seam in the bow that shows two completely separate sides, one making up most of the bow and the other one being a small fraction in the top left corner, as seen in Figure 3.9, causes the structure to have a fairly disconnected scaffold routing, which can affect the yield of correctly folded origamis (169). In particular, I hypothesize that the BA unfolds from the bow due to the weakness of the seam and the added tension in that area due to the in/dels that cause the bending; these "broken" BAs find similarly affected structures and complement eachother, joining together into the fused structure from Figure 3.7b (right-most) & 3.8b (bottom left). This could reasonably drive the formation of misassembled structures and aggregation during the thermal ramp and does not have a simple solution, except for a redesigning of the whole BA that would avoid these issues.

3.4 2nd Iteration of the 2D system

To be able to have a routing that runs through the whole of each subunit of the BA in a self-contained manner before moving on to the next one, an odd number of helices in the bundle is required. With this motivation the "heptabundle" version of the BA, 7-helix bundles instead of 6, is designed as follows:

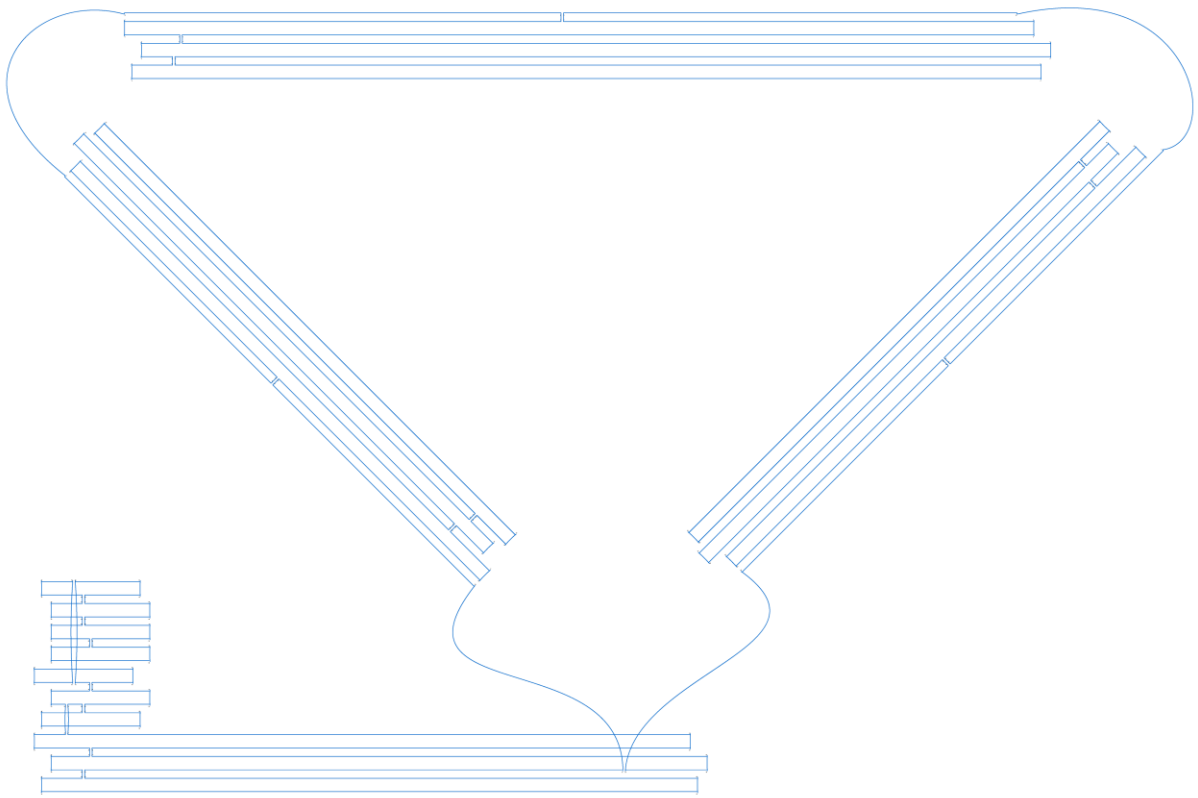

Figure 3.10. Schematic representation of the scaffold routing in the 2nd iteration BA ("heptabundle"). Curved lines connecting subunits do not represent nucleotide strings, they have been elongated for aesthetics and clarity, the scaffold jumps with no single-stranded sections in-between subunits (with the exception of the strings-arrow connection that has 3 nts unpaired). Deletions and insertions in bow are not represented but follow the same distribution as the ones in Figure 3.9.

Following this design should be able to solve the issues that I hypothesize caused the aggregation and the "fused" BAs, but since I am adding three new helices I have to reduce the size of the structure to accommodate for that extra expenditure of the scaffold material. In the new "heptabundle", the length of the strings is reduced to 80 nm (9 nm shorter), the length of the arrow is 92.82 nm (5 nm shorter) with the stopper remaining unchanged, and the bow is now 123 nm (~16 nm shorter). An OxDNA simulation was done on the structure to see if it had the expected shape and stability.



Figure 3.11. OxDNA simulation of the 2nd iteration of the BA ("heptabundle"), side and top view.

There seemed to be a bit of fraying in the corners of the structure, the point of contact between the strings and the bow, but since the simulation provided a stable result I went ahead and started the assembly of the structure. Fraying proved to be the main motivation for the third redesigning of the structure, as it will be discussed by the end of this section.

As follows, a $MgCl_2$ test was done on the structure, followed by a characterization with DNA-PAINT.

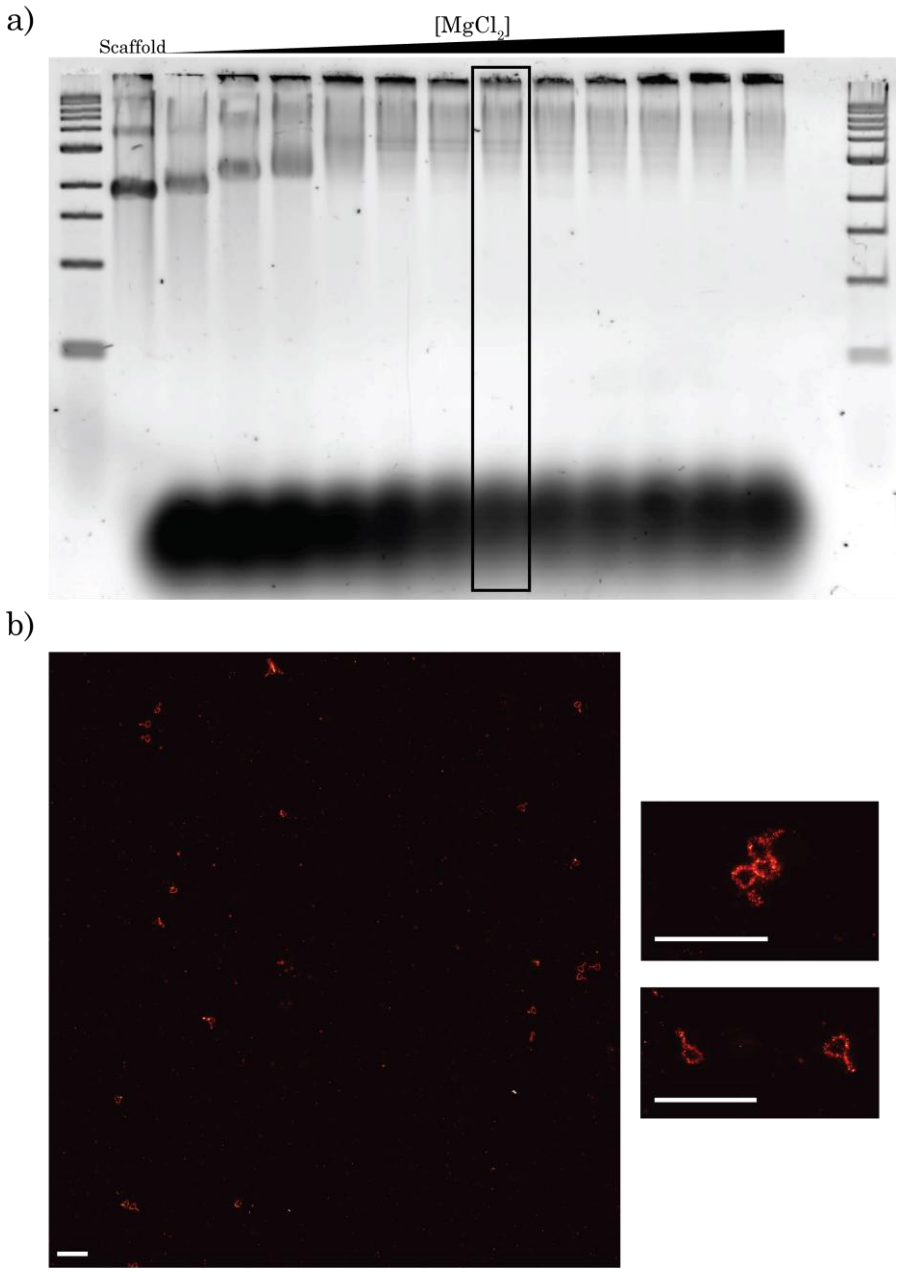

Figure 3.12. Characterization of 2nd iteration BA (Heptabundle). a) $MgCl_2$ test in AGE, the scaffold used was p8064, the gradient of concentrations go from 0 to 22 mM. In a black rectangle the chosen concentration (12 mM) b) DNA-PAINT of the 2nd iteration BA, an overview of the results and two magnifications, one unexpected BAs interactions (top) and another of monomeric BAs (bottom). All scale bars are 500 nm.

The concentration of $MgCl_2$ chosen for the heptabundle was 12 mM, the issue with the aggregation worsened (61% of product in well) and there was an added unexpected development. In the spot of the monomeric structure band there were now two bands in its stead (17% & 10% of products in top and bottom bands respectively), and a slow moving pair of bands had appeared as well, probably a dimer of the 2nd iteration BA (yield of 31%,

including both bands). These two sets of bands had a similar amount of the product formed as per the intensities of the AGE. DNA-PAINT showed a similar result to the one done for the 1st iteration of the BA (82% of monomeric, correctly folded BAs), the main difference being that there were no more "fused" misassemblies, instead there were structures that resembled dimers (18%). In order to better be able to study the result structures another gel was run, the different bands were extracted and imaged with TEM (See Figure 3.13). For the gel extraction procedure the protocol was slightly changed, given the uneven band migration when the teeth of the comb are fused together into one big lane, the 15-teeth comb was left unmodified but the same sample was run in each sample (Appendix A.2.3). This change greatly improved the quality of the extractions and will be used from this point forward.

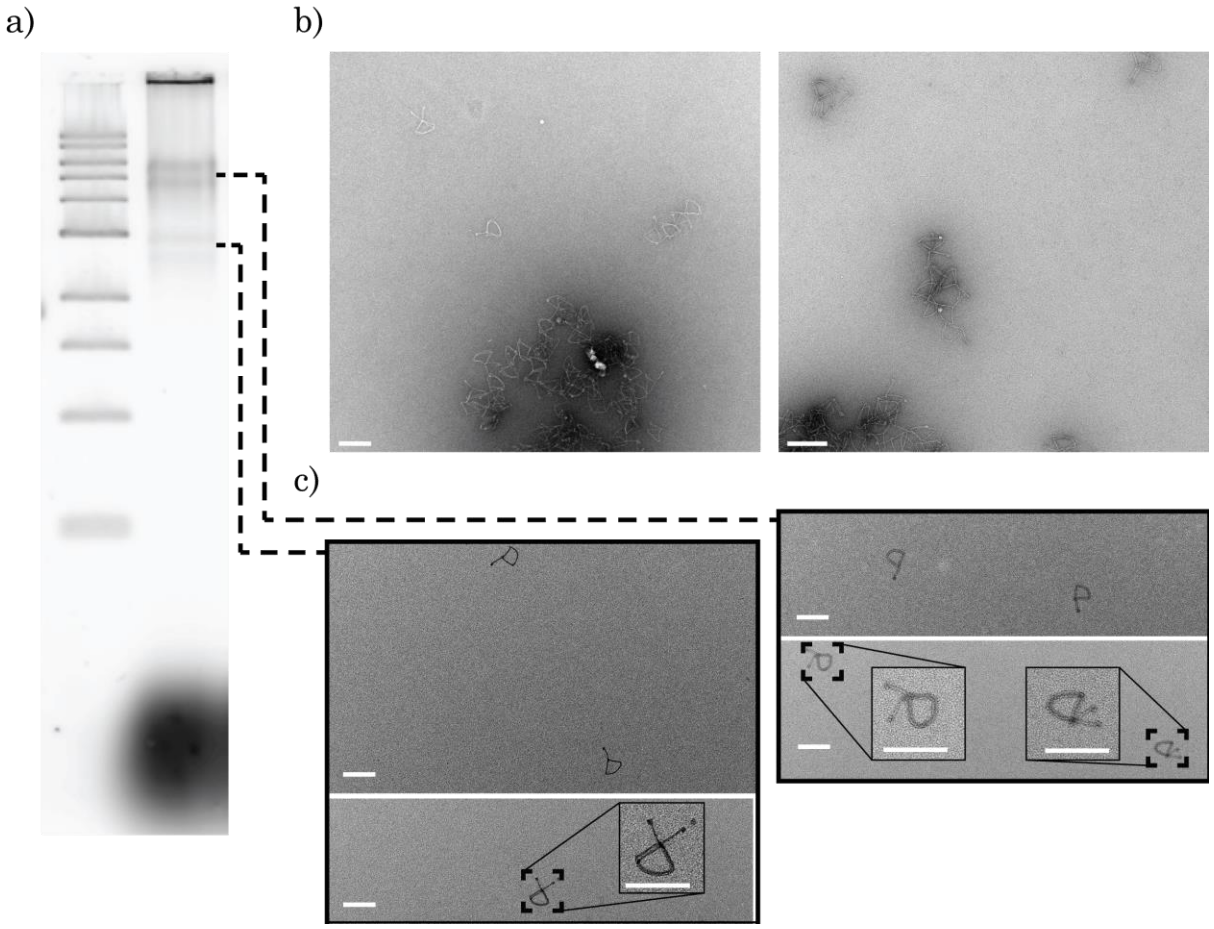

Figure 3.3. 2nd Iteration BA characterization. a) AGE of the 2nd iteration BA. b) TEM imaging of the sample. c) TEM imaging of gel extracted bands presenting monomers and dimers (two BAs overlapping). All scale bars are 200 nm.

In the gel, aside from the aggregation (45% of the product), two pairs of bands can be seen migrating, the faster pair is found around the expected level for the monomeric BA (7% & 5% respectively), the slower pair could present the dimers seen in Figure 3.12 (21% & 22% respectively). In order to study the specific elements of each, they were extracted as specified before and imaged in TEM along with the full sample. The full sample shows mostly aggregated BAs, particularly forming dimers (84% of non-aggregated, distinguishable structures) but, upon imaging of the slower pair of bands (due to the smearing I could not clearly separate them in individual-band extractions), monomers (35%) could be seen along with dimers (65%); the inverse distribution was seen for the slower of the bands in the faster pair (85% of monomers and 15% of dimers). The fastest of the bands only presented monomers but at very low concentration, only 11 structures

could be identified in the grid (See Appendix G.2.5). The widespread distribution of both monomers and dimers among the different bands led me to hypothesize that the dimerization was transient.

Upon closer examination of the dimers (Figure 3.14), most of them happened by the seeming interaction of the bows (29% of the dimers) or the regions of interaction between the bow and the strings, overlapping each other (71% of the dimers).

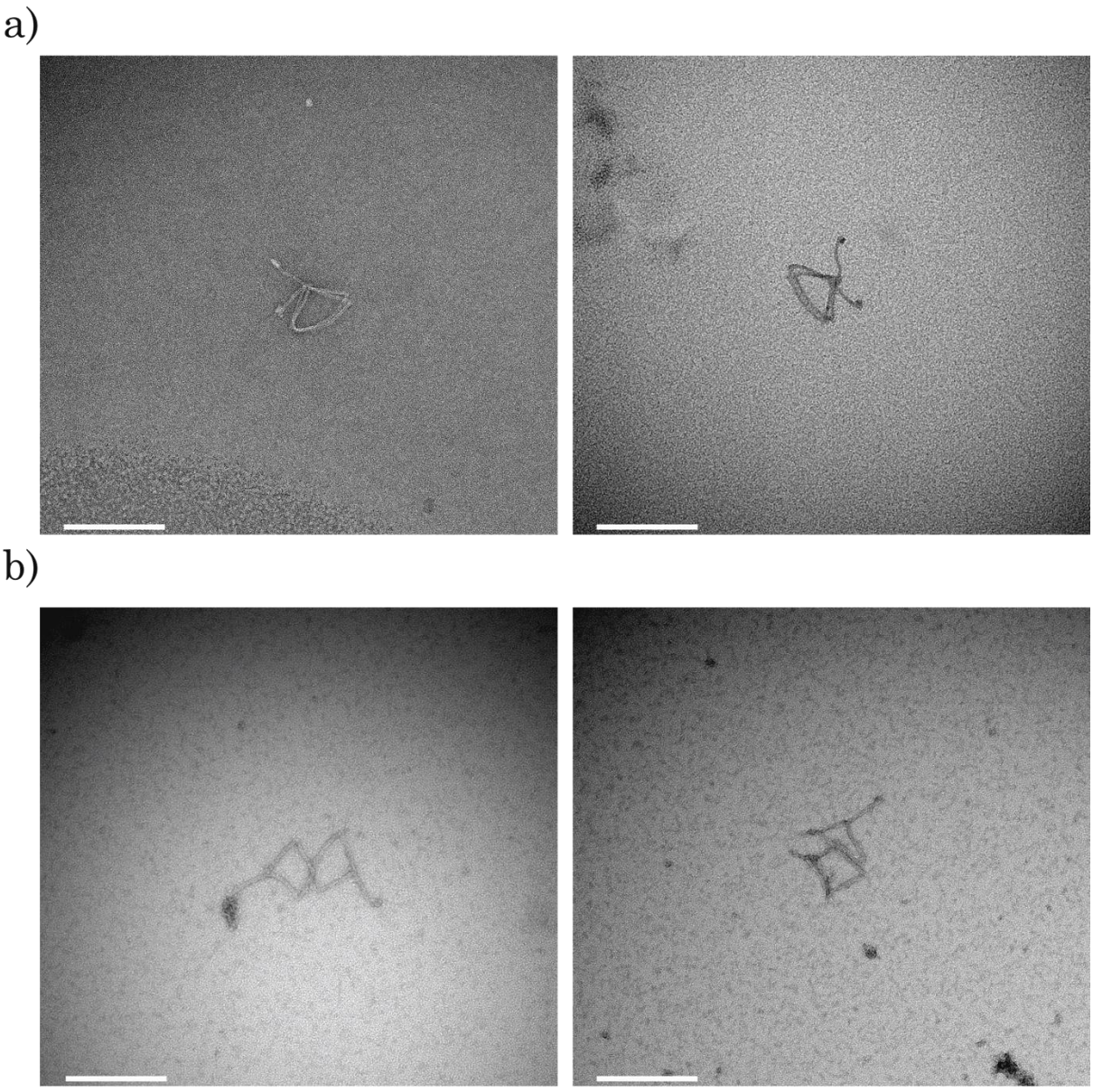

Figure 3.14. 2nd iteration BA dimers. a) TEM imaging of superposed dimers. b) TEM imaging of touching-bows dimers. All scale bars are 200 nm.

This type of interaction was probably fuelled by the frayed constitution of the bow and the string ends, caused in turn by an excess of strain in that region of the structure. This behaviour was noted in passing in Figure 3.11 and could be explained by the persistent mistake I made when designing the structure, not leaving flexible spacers made of single-stranded scaffold in-between the subunits of the BA.

Since the dimers were not permanently reducing the yield of monomeric BAs and the experiments were straightforward to do, I attempted locking the arrow into place (incubation at RT for 40 minutes with a 20x excess of the bridge strands for the middle of the bow, as in the 1st iteration) and loading in the slider (1:1 proportion at 37°C for 3 days, as with the 1D rotaxane).

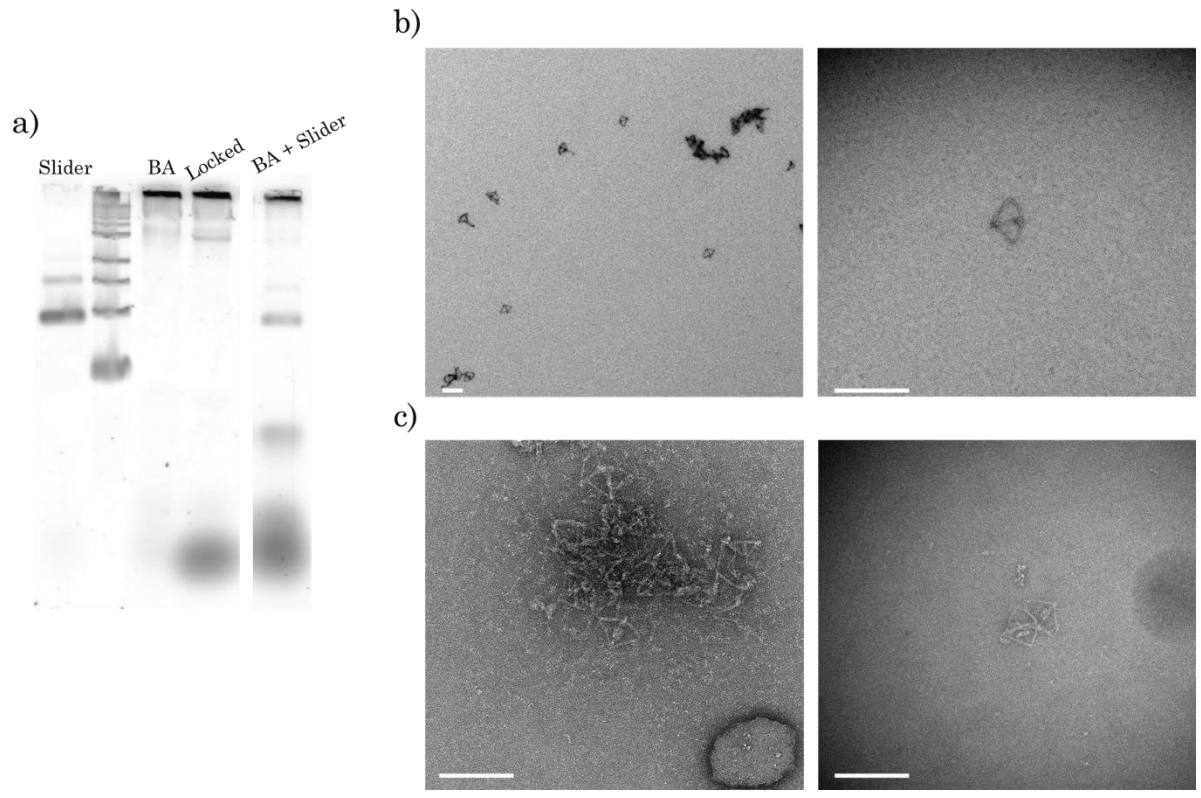

Figure 3.5. 2nd Iteration BA attaching of the arrow and loading of the slider. a) AGE of BA locking and loading with slider; Lane 1 presents the slider (same one from 1D system); Lane 2 presents the 2nd iteration BA; Lane 3 presents BA with the arrow attached in the middle of the bow; Lane 4 presents the product of the incubation of BA and slider. b) TEM imaging of the BA with the arrow attached in the middle. c) TEM imaging of the BA incubated with the slider. All scale bars are 200 nm.

The gels show very high levels of aggregation in the wells (~75% of the total product across the lanes), irrespective of the locking or the loading. Locking the arrow seemed to enrich the monomeric band (16% as opposed to 10% in the unlocked BA), a behaviour shared with the 1st iteration of the BA, but the loading of the slider on the arrow changed the pattern of migrating bands in a way that seemed to make the BAs disappear (6% product in the monomeric band). This disruption caused by the loading will also be present in the later iteration. Only by means of TEM imaging it can be confirmed that the loading was successful, albeit very marginally (13 loaded structures identified on the sample); as expected from the previous experiences and from the gel, locking in the arrow was a successful step with a yield of 50% of all non-aggregated structures.

It is worth noting that, given the shortening of the axis along which the slider diffuses, the thin slider used since the 2nd iteration of the 1D rotaxane is no longer suitable for studying the positioning along the arrow of BA; due to its length it occupies much of the possible run of the rail (the arrow shaft), which makes it inconvenient for moving it along the rail and assessing the success of this actuation via TEM and/or DNA-PAINT. Much like with the original slider, a redesigning was done on the structure, in this case this was done by Dr Erik Benson, producing the MicroSlider. The current slider has 32 helices shaped into a single layer cylinder that has a length of 72 nts, using a 2880 nts-long scaffold. The new slider is composed of 20 helices disposed in a single layer with three sections that have a second layer of 4 helices; it is 44 nts-long and uses a 1418 nts-long scaffold product of the partial digestion of p8064 (Appendix A.3). The MicroSlider is fluorescently labelled with 5 strands containing FAM so that its position could be distinguished from the rest of the bands in AGE, particularly when incubated with the BA. The attaching system was the indirect attaching system, earlier described, from this point onwards, the previous experiment with the thin slider (Figure 3.14) still used the direct attaching system for the loading. The only change made in regards of the attaching

system was the introduction of three overhangs that were exclusively used for the initial docking of the slider on the arrow shaft. The overhangs protrude from three different positions in the inner face of the slider and bind to the rail following the manner shown in Figure 3.15b.

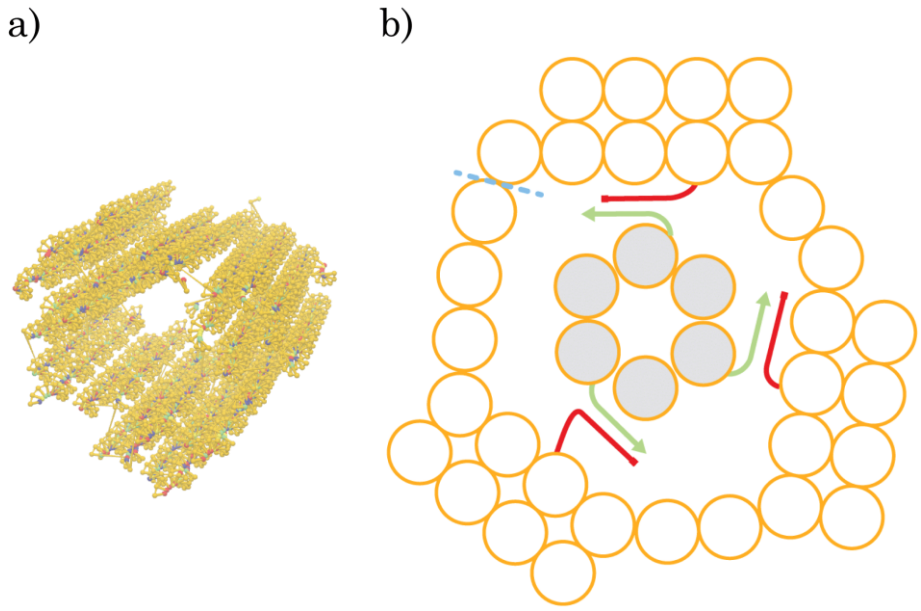

Figure 3.16. Schematic representation of the MicroSlider. a) Oxview model of the MicroSlider. b) Cross-section of the MicroSlider wrapped around the arrow shaft, blue dotted line marks the opening of the slider, strands in red represent the initial attaching overhangs, in green their complementary strands in the arrow shaft.

The MicroSlider was previously tested by Dr Erik Benson, and a $MgCl_2$ test had already been done, the ideal concentration being 10 mM. With this concentration the structure was assembled and run in AGE, followed by its incubation with the BA (still 1:1 at 37°C for 3 days).

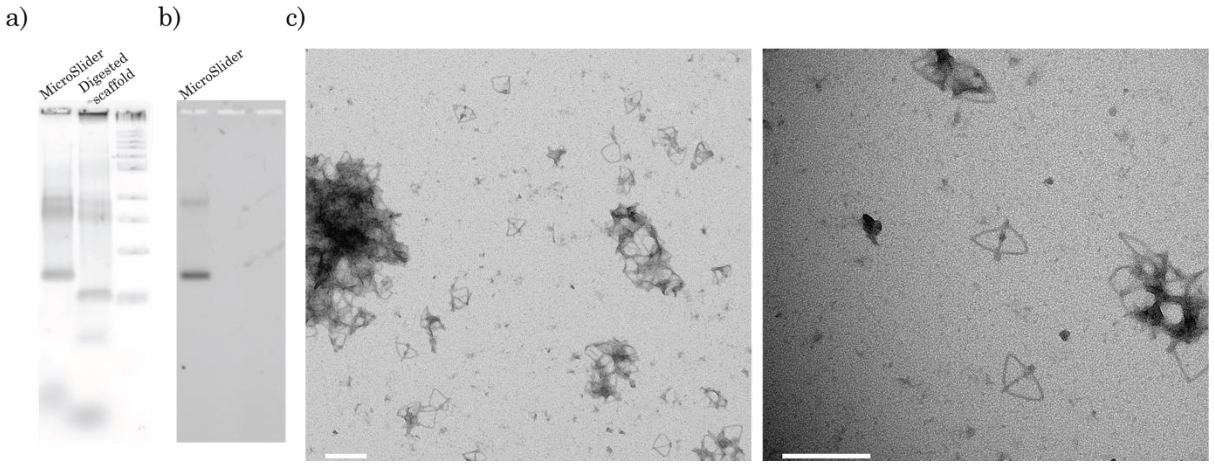

Figure 3.17. MicroSlider characterization and loading onto 2nd Iteration BA. a) AGE of MicroSlider, MicroSlider in Lane 1; Digested scaffold p8064 in Lane 2. b) Same gel as in 3.16a but under FAM scan (Appendix B.3). c) TEM imaging of the BA incubated with the MicroSlider. All scale bars are 200 nm.

The assembly of the MicroSlider was as expected, a very fast migrating band containing the slider (27% of the total product) and a slower one containing the remaining fragments of the digestion of the scaffold (54% of the material in the lane). The incubation with the BA produced an improvedyield of loaded BAs compared with the past experiments (36% yield of loaded BAs with the MicroSlider). But regardless of the improved version of the slider and its successful loading, the project was at an impasse caused by the aggregation issues. In an attempt to salvage the design, and its results so far, several strategies were followed to try and mitigate the aggregation problems. These strategies were aimed at the hypothesized causes of aggregation, hasty assembly, unwanted interactions between overhangs, and the aforementioned strain between subunits that lead to fraying.

Addressing the first hypothesis, there was an attempt at assembling the BAs at slower thermal ramps (Appendix A.1.3). Regarding the second hypothetical cause, I made several minor redesigns such as; reducing the number of DNA-PAINT docking sites to prevent transient bindings between overhangs; as a test, eliminating all the overhangs in the structure to see if a drastic change in the aggregation status was produced; and lastly adding passivating strands, poly-Ts, to sterically hinder the interaction between BAs. In

order to try and reduce the strain in the connecting regions between the strings and the bow, without changing the scaffold routing entirely, I extended the staple crossovers between the subunits by 50% and a 100% in length. All the products of these different strategies of assembly and redesign were characterised with AGE and TEM, with only one exception, all failed to make any perceivable improvement on the assemble of the 2nd iteration of the BA. This exception was the type of BA whose overhangs were entirely removed from the design, the AGE of this structure had an enriched pair of fast migrating bands and a lesser level of aggregation in the well, but, as confirmed by the TEM, it still presented a great deal of aggregation and transient dimerization.

As a last resort solution for the aggregation, gel extraction of the monomeric bands was performed, with the hopes of purifying enough material to be able to perform the loading of the MicroSlider and 2D motion unhindered. The gel extraction was done by introducing a large volume of the sample in a single, fused well, and cutting out the monomeric band.

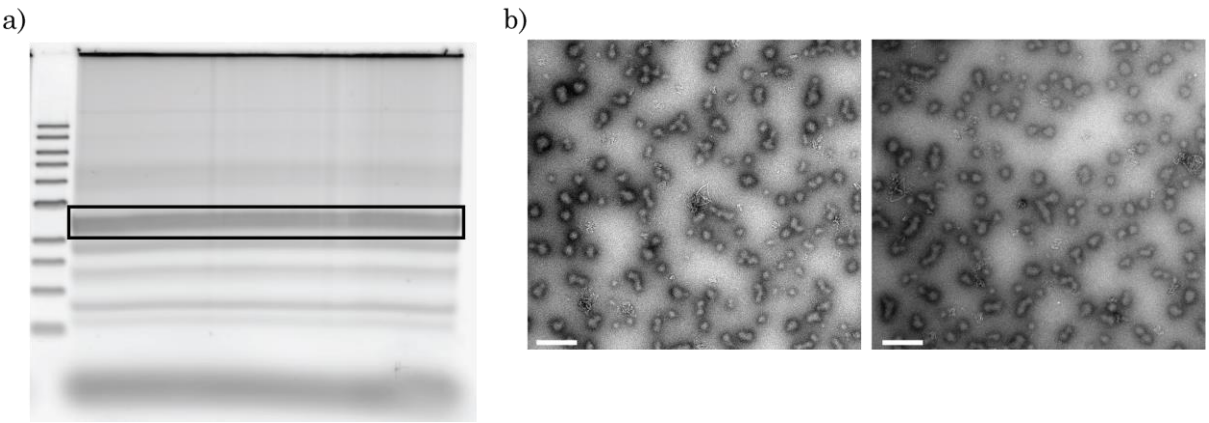

Figure 3.18. BA extraction and loading. a) AGE of 2nd Iteration BA for extraction, marked band was gel extracted. b) TEM imaging of incubation of extracted BA with the MicroSlider. All bars are 200 nm.

The AGE showed bands fast running bands beneath the monomeric band, which were indicative of the degradation of the structure. Regardless, the monomeric band had a good yield (27% of the total product) and was studied in TEM. Putting aside the poor staining of in Figure 3.18b, the yield of the extraction was extremely low (less than 10 identifiable

loaded structures) and, despite the lack of aggregation, it could not be used for the following steps of loading and 2D actuation. Given the situation I decided to redesign the BA for the third time, being very careful of including solutions for the suspected, main structural deficiencies of the heptabundles.

3.5 3rd Iteration of the 2D system

In the third and last iteration of the BA I decided to go back to using 6-helix bundles for the sub components but, unlike in the 1st BAs, the routing was made much more winding and with many crossovers between helices. The scaffold went back to the pattern of not finishing one subunit before moving to the next, requiring then two "laps" around the structure, but this time the halves of each subunit presented high levels of interaction with one another. The way these halves fit together like a puzzle could be described as a staggered seam running length-wise across the strings and perpendicularly to the bow. This allowed for plenty of interactions between the halves which, added to the heavy presence of staple crossovers, would preserve their structural integrity. The main possible issue with this routing is that, once again, the bow has to be separated into two disconnected sides; the staggered seam should prevent the many misassemblies and aggregations of the 1st BAs.

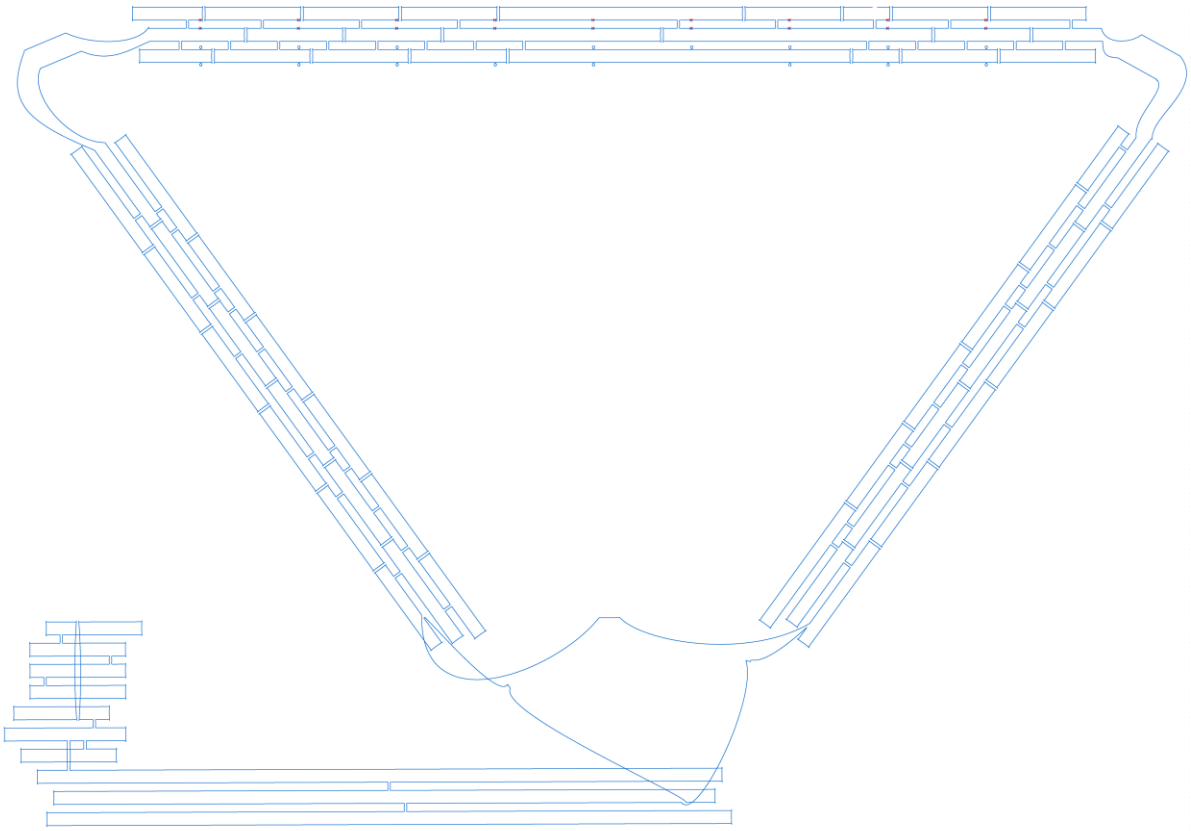

Figure 3.9. Schematic representation of the scaffold routing of the 3rd Iteration of the Bow-and-Arrow.

Another key addition was the introduction of single-stranded regions in-between the subunits. As it can be seen in Figure 3.19 in the form of straight lines connecting the bow to the strings and the strings together, sections of the scaffold were left unpaired so that they would provide a flexible joint that would reduce the overall strain of the structure once assembled. Two turns of a helix (21 nts) were left between the bows and the strings, arguably the most strained areas in the 2nd iteration, ~ one turn (10 nts) in the connection between the strings, and 4 nts between the strings and the arrow, no change was considered there given the successful attaching of the arrow in the past. The extra freedom of the subunits could be problematic but the OxDNA simulation of the structure showed promising prospects, it didn't present the fraying seen in the previous design (Figure 3.11) and maintained the expected structural cohesiveness of the BA structure (See Figure 3.20).



Figure 3.20. OxDNA simulation of the 3rd Iteration of the BA.

This simulation will be validated by the subsequent TEM imaging as monomeric structures will shape as outlines above without the issues of dimerization of the previous iteration. An aspect of the structure not present in the simulations is the flexibility of the integrant subunits, that is, the bow may appear straighter or more bent than what the design parameters will allow. Another aspect will be the possibility for the bow to be divided by the scaffold routing's seam, as it occurred in the simulation of the 1st iteration of the BA, although at a lesser rate. Regardless of these specific caveats, and as it has been argued earlier, OxDNA is a useful design tool that can help make the broader design choices before actually assembling and characterising the origami.

Following the completion of the redesign a $MgCl_2$ test and TEM imaging were done, as usual.

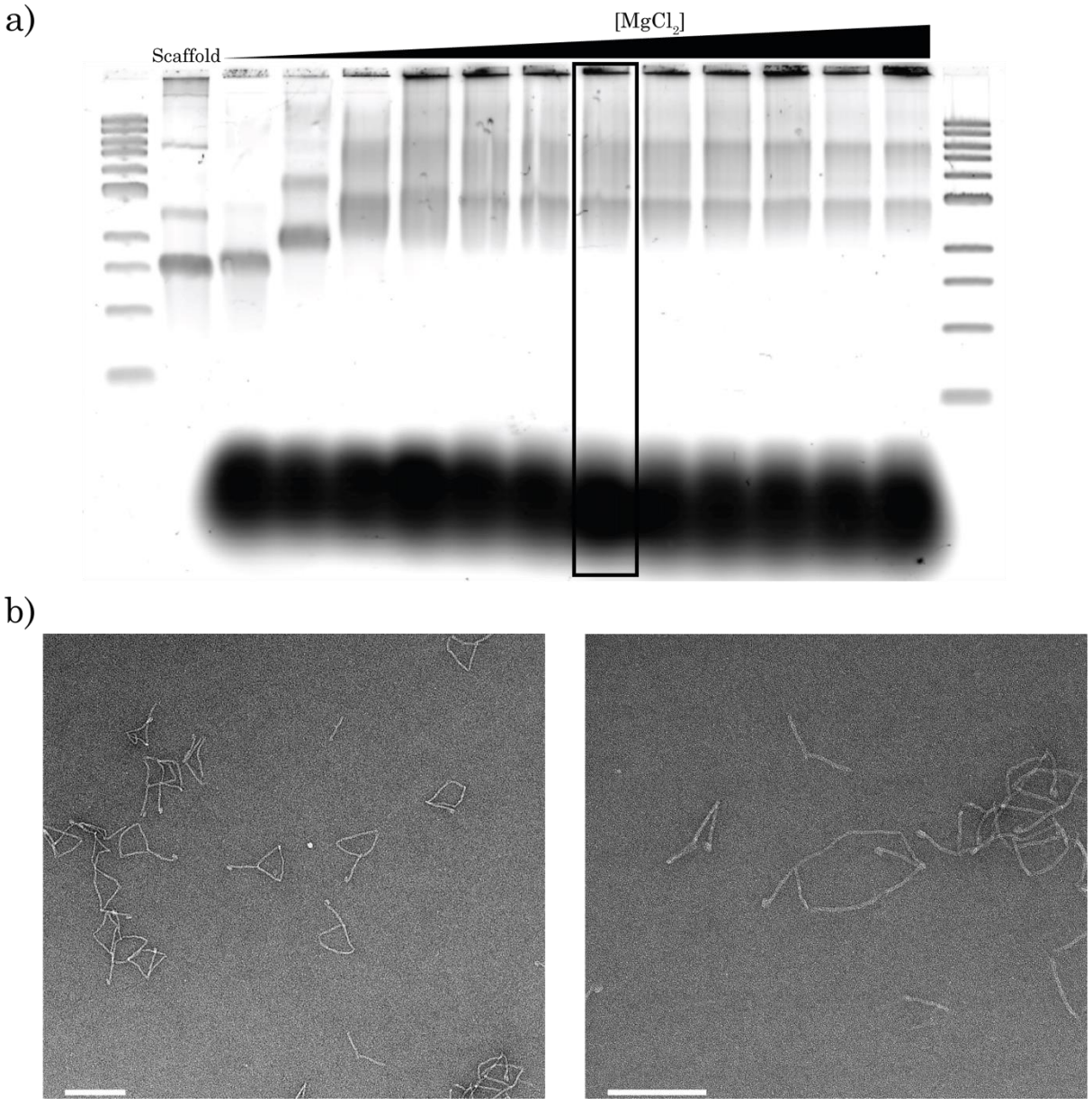

Figure 3.21. Characterisation of the 3rd Iteration BA. a) $MgCl_2$ test in AGE, the scaffold used was p8064, the gradient of concentrations go from 0 to 22 mM. In a black rectangle the chosen concentration (12 mM). b) TEM imaging of the 3rd Iteration, monomers, and misassemblies. All scale bars are 200 nm.

The concentration chosen was 12 mM $MgCl_2$ it presented a strong monomeric band (36% intensity of the total product), some aggregation in the well, although less than the previous iterations (36% of the product). A slower migrating band (27% of the product) appeared but no dimerized bands could be seen. Via TEM I could confirm that the redesign had addressed the main issues of the past versions and a good yield of monomeric structures were produced (66% of yield). No dimers were seen following the overlapping

style so predominant in the 2nd iteration, although some of the structures did aggregate; there was a partial return of the "fused" BAs, which was to be expected due to the regression to halved subunits, but their incidence was much lower (7% of the product of assembly), this I presume to be due to the aforementioned staggered seam strategies (See Appendix G.2.6. for a wide field view of the TEM image discussed above in Figure 3.21). A type of misassembly that was particular to this iteration, at least in a noticeable enough way, was what seemed to be broken BAs. Looking as if the bow had snapped, I hypothesize that these events are the prelude to the fused conformation, since the later comes to pass as the bow "breaks" from the seam and presents ends that can stick to eachother by means of the same staples. Such broken BAs remained monomeric, without joining between themselves in pairs or greater groups, and constituted 27% of the total product of assembly.

In an attempt to correct this marginal misassemblies, a slower ramp was used (Appendix A.1.3) that mimicked the ones used in the paper on bent and twisted structures (191), in lieu of the generally used 14h-long thermal ramp. Its duration was of roughly a week so I decided to compare both ramps in a gel that I would later extract bands from to compare further on TEM (See Figure 3.22).

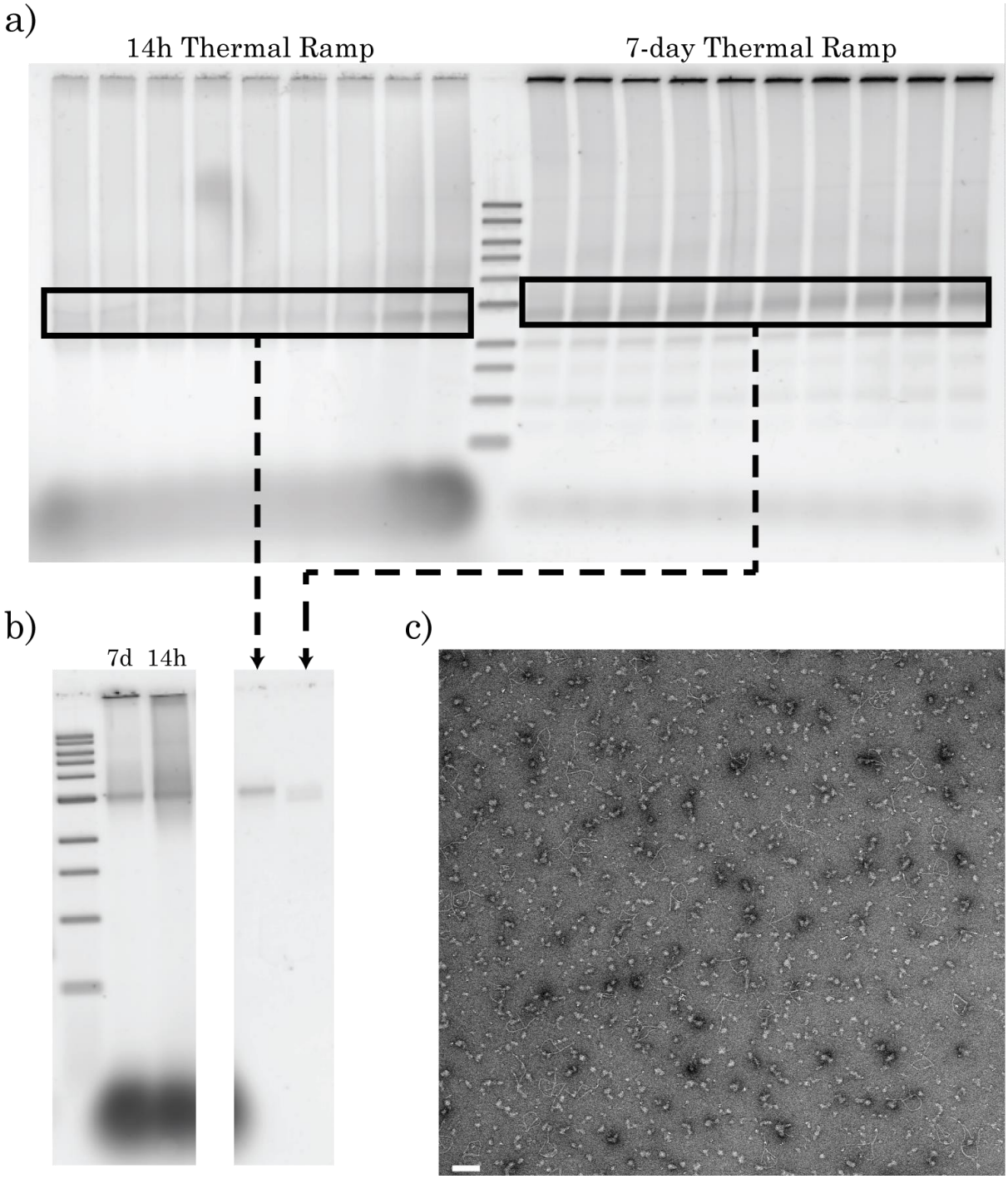

Figure 3.2. 3rd Iteration BA thermal ramps' comparisons and extraction. a) AGE of 3rd Iteration BA for extraction, marked bands were gel extracted, Lane 1 presents 3rd Iteration BA assembled in the usual 14h-long thermal ramp, unpurified; Lane 2 presents 3rd Iteration BA assembled in the week-long thermal ramp, PEG purified. b) AGE of the extracted bands and the raw samples for comparison, Lane 1 presents 3rd Iteration BA assembled in the week-long thermal ramp; Lane 2 presents 3rd Iteration BA assembled in the usual 14h-long thermal ramp; Lane 3 and 4 present the extracted bands from the gel in 3.22a, 14h- and week-long assemblies respectively. c) TEM imaging of the extracted band of 3rd Iteration BA assembled in the usual 14h-long thermal ramp. The scale bar is 200 nm.

A part from differing in the thermal ramp of assembly used, the two samples of the 3rd iteration BA differed as well in the fact that the week-long sample had been PEG-purified whereas the 14h-long sample had not. The monomeric band after the longer ramp had a good yield (41% intensity of the total product) but the purification that was not very effective, judged by the remaining staples in the run-off band. It had a very strong aggregation in the well (59% intensity), as well as many fast migrating bands that I presume come from the fragmentation of the BA over the long incubation time. In sharp contrast, the incubation that took substantially less time and was not purified showed a bettermonomeric band yield (67%), albeit a bit smeared in some of the lanes, and a comparatively low the aggregation in the well (33%). The samples were re-run alongside the extracted bands and the monomeric band from the 14h assembly was noticeably better than the week-long one (3x more intense). TEM of this band was very successful, albeit poorly stained, as it showed a great yield of exclusively monomeric structures (92%), with some minimal amounts of "broken" BAs (8%). Given these positive results, the BAs of the 3rd iteration were assembled with the 14h thermal ramp and gel extracted, not PEG purified, before doing any of the following experiments.

3.5.1 Actuation of the Arrow

Having at last obtained a good sample in which to test the loading and the 2D motion, I decided first to study the attachment/detachment of the arrow to the bow. To do so an excess of 500 nM of bridge strands to the middle position were added to the BAs, followed by an incubation at RT for 40 minutes. Since I wanted to optimize the amounts of strands added to the solution, I also attempted different concentrations, temperatures and incubation times and compared them in AGE (See Figure 3.23).

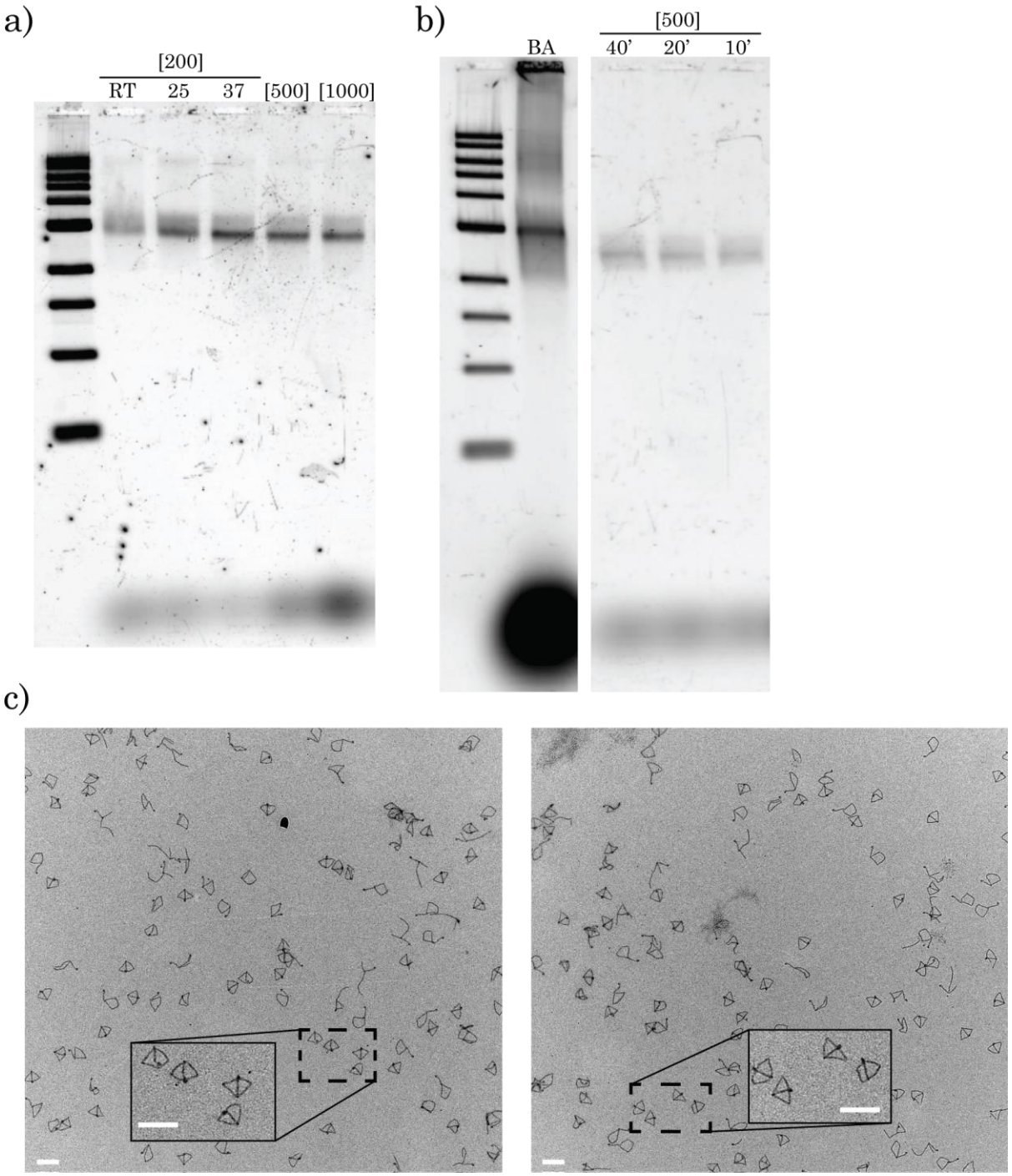

Figure 3.23. Actuation of the Arrow, attaching. a) AGE of different conditions of arrow attaching, all samples were incubated for 40 minutes, Lanes 1, 2 , and 3 present BA incubated with an excess of 200 nM of bridge strands for the middle position at RT, 25℃ (in thermal block), and 37 ℃ respectively; Lanes 4 and 5 BAs were incubated at 37 ℃ with an excess of 500 nM and 1000 nM respectively. b) AGE of different durations of incubation of arrow attaching, all samples incubated with an excess of 500 nM staples at 37 ℃, Lanes 1, 2, and 3 present incubations for 40, 20, and 10 minutes respectively. c) TEM imaging of BAs with the arrow attached in the middle after incubation with an excess of 200 nM at 37 ℃ for 40 minutes. All scale bars are 200 nm.

When attaching the arrow to the bow the structure migrates faster, consistent behaviour across all iterations, therefore it is easy to gauge the effectivity of the process in the different conditions. The process seems temperature dependent, when all other variables being the same, RT incubation provided worse results than if done at 37℃, presenting 33% less attachment of the arrow, and actual 25℃ (in thermal block) showed some smearing, although the same quantity of product as 37℃ (8% less attachment at 25℃). At 37℃ and for 40 minutes there is a smalldifference between 200, 500 or 1000 nM (13% and 19% decrease in attached arrows at 500 and 1000 nM of locking staples, respectively). As seen in Figure 3.23b, the decrease in time of incubation decreases the yield of the attachment when the concentrations of bridge strands are at an excess of 500 nM (17%, and 28% decrease of the 20, and 10 minute-long incubation products when compared to the 40 minutes-long one, respectively); the time of incubation with the bridge strands can be taken as another parameter to work with when optimizing the the arrow attachment to the bow. Due to the fact that I am working in solution and it is paramount to minimize the amount of waste strands and of strands left-over from previous steps, in order to be able to reach good demonstrations of stepping yields, the conditions chosen for the attaching of the arrow is 200 nM excess at 37℃ for 40 minutes. The successful results of this attaching were corroborated with TEM (See Figure 3.23c) with a yield of arrow attachment of 57%. The future direction of this actuation is to be on a microfluidics channel were this considerations will not be necessary, so corrections for faster conditions will be implemented; I will discuss this in more depth at the end of this chapter.

To the attachment of the arrow into place follows the reversal of this attachment with the addition of invading strands. Maintaining the temperature at 37℃, excesses of 500 and 1000 nM were tested, the presence of the previous bridge strands in excess in solution prevented me from going to the same concentration used, 200 nM. The duration of the

process was also screened for at 40, 20, and 10 minutes, the results can be seen in Figure 3.24.

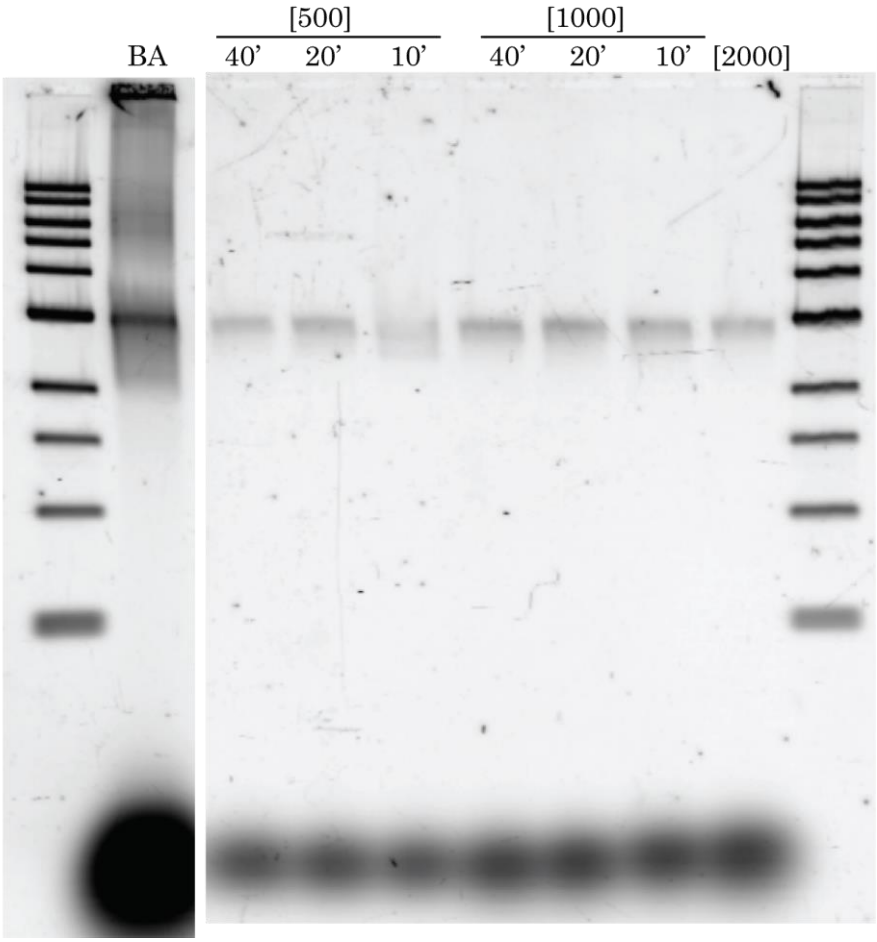

Figure 3.24. Actuation of the Arrow, detaching. AGE of different durations of incubation of arrow attaching, all samples incubated at 37 ℃, Lanes 1, 2, and 3 present BAs incubated with an excess of 500 nM of invading strands for the middle position at for 40, 20, and 10 minutes respectively; Lanes 4, 5, and 6 present BAs incubated with an excess of 1000 nM of invading strands for the middle position at for 40, 20, and 10 minutes respectively; Lane 7 presents BAs incubated with an excess of 2000 nM of invading strands for the middle position for 40 minutes.

Once the arrow is free again the band migrates slightly slower again, so from the gel the efficiency can be reliably attested. An excess of 500 nM of invading strands were capable of releasing efficiently the arrows in the 40 and 20 minute range, this efficiency dropping in the 10 minute time frame by 20%. The same occurs at 1000 mM excess of invading strands but at a lesser extent (40 and 20 minute-long incubations have the same yield, 10 minute-long incubation presented a dip in yield of successful arrow detachment

of 8%). For the same reasons as stated above, the choice in the current set-up puts the use of lower concentrations of strands before the speed of the process.

For achieving a full step cycle of the arrow, the last experiment is the reattachment of the arrow into a secondary position after being removed from the bow. As before, at a constant of 37°C, different concentrations (200, 500, and 1000 nM) and durations (10, 20, and 40 minutes) were tested for the reattachment in Figure 3.25.

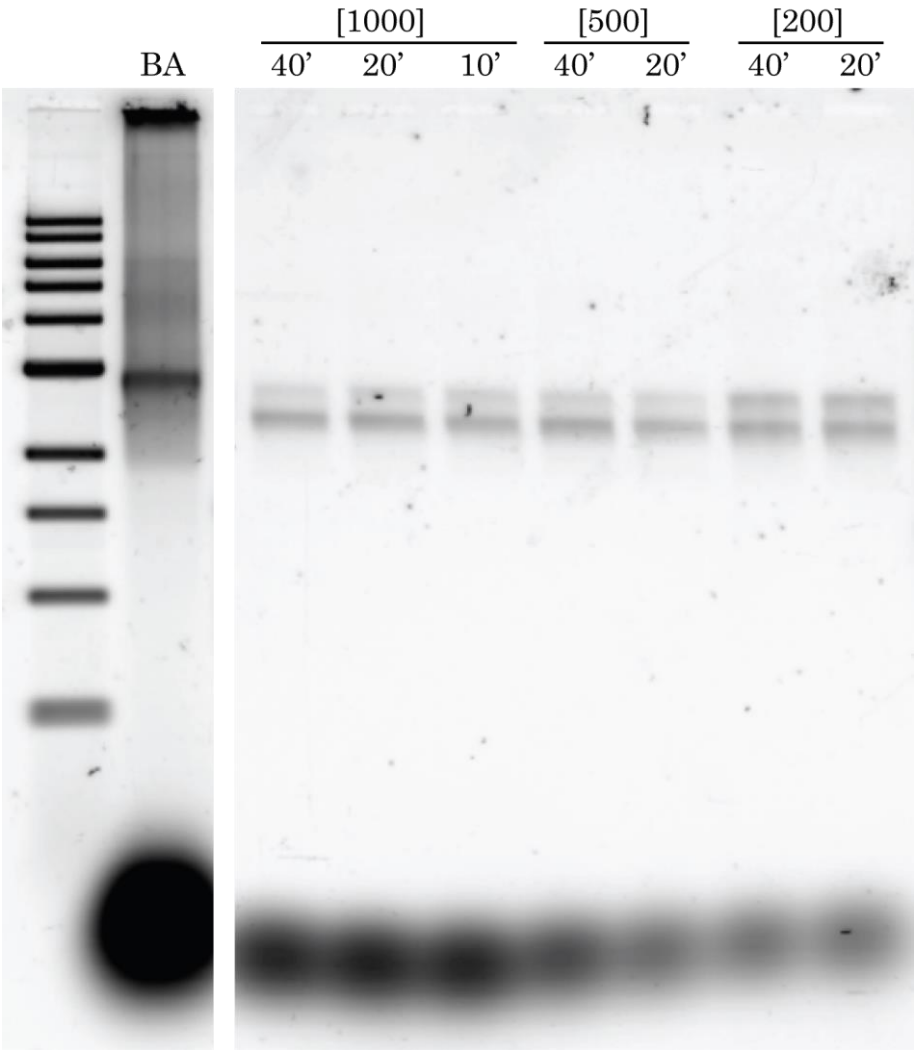

Figure 3.25. Actuation of the Arrow, re-attaching. AGE of different durations of incubation of arrow attaching, all samples incubated at 37 °C, Lanes 1, 2, and 3 present BAs incubated with an excess of 1000 nM of bridge strands for the right-most position at for 40, 20, and 10 minutes respectively; Lanes 4, and 5 present BAs incubated with an excess of 500 nM of bridge strands for the right-most position at for 40, and 20 minutes respectively; Lanes 6, and 7 present BAs incubated with an excess of 200 nM of bridge strands for the right-most position at for 40, and 20 minutes respectively.

In this case, the concentration of 200 nM was included to see the actual effect of the reduced efficiency due to the build-up of excess strands and waste complexes found in the solution at this point. Longer incubation times (40 minutes) and higher bridge strand concentrations (1000 nM) do not seem to show great improvements over shorter times (20 & 10 minutes) and lower concentrations (500 nM), or any combination thereof; the yield of the reattachment of the arrow was across all these combinations of 70%. The exception to this is the samples, where a 200 nM excess of bridge strands was used and only a partial reattachment happened, 55% of the arrows reattached. For the stepping cycle experiment the concentration of bridge strands for the secondary position was 1000 nM, incubated at 37℃ for 40 minutes; the previous steps of initial attachment and detachment were done at the preferred conditions mentioned above. Samples of the initial attachment and its secondary attachment were taken and imaged with TEM, as seen in Figure 3.26 below.

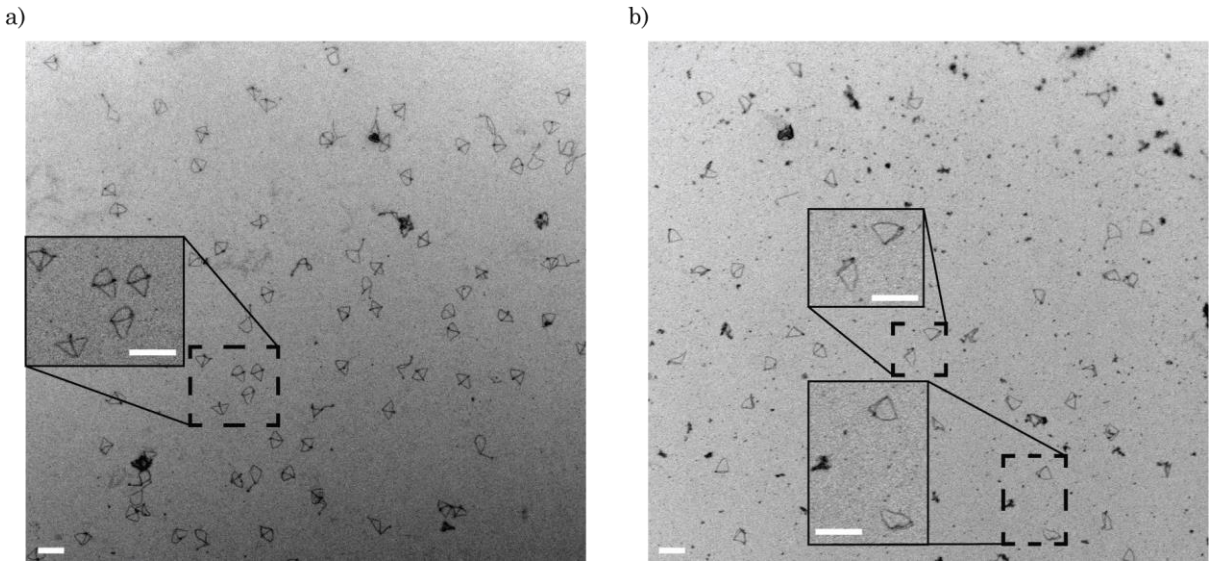

Figure 3.6. TEM characterization of a full cycle of actuation. a) BAs at the initial attaching position, middle. b) BAs at the secondary attaching position, right, after a stepping cycle. All scale bars are 200 nm.

Going from the middle position (whose initial attachment had a yield of 70% as seen in TEM) to the right extreme of the bow had good a yield,66% of successful stepping, as calculated from a collection of TEM images. Although the symmetry of the structure

causes difficulty in distinguishing one extreme of the bow from the other, the issue will be solved in the DNA-PAINT experiments at the end of the chapter.

3.5.2 Loading of the MicroSlider on the BA

Once the attaching capabilities and conditions of the BA were confirmed, the second part of the 2D motion was studied, the loading and stepping of the slider.

The initial attempts at loading the MicroSlider onto the BA, can be seen in Figure 3.27.

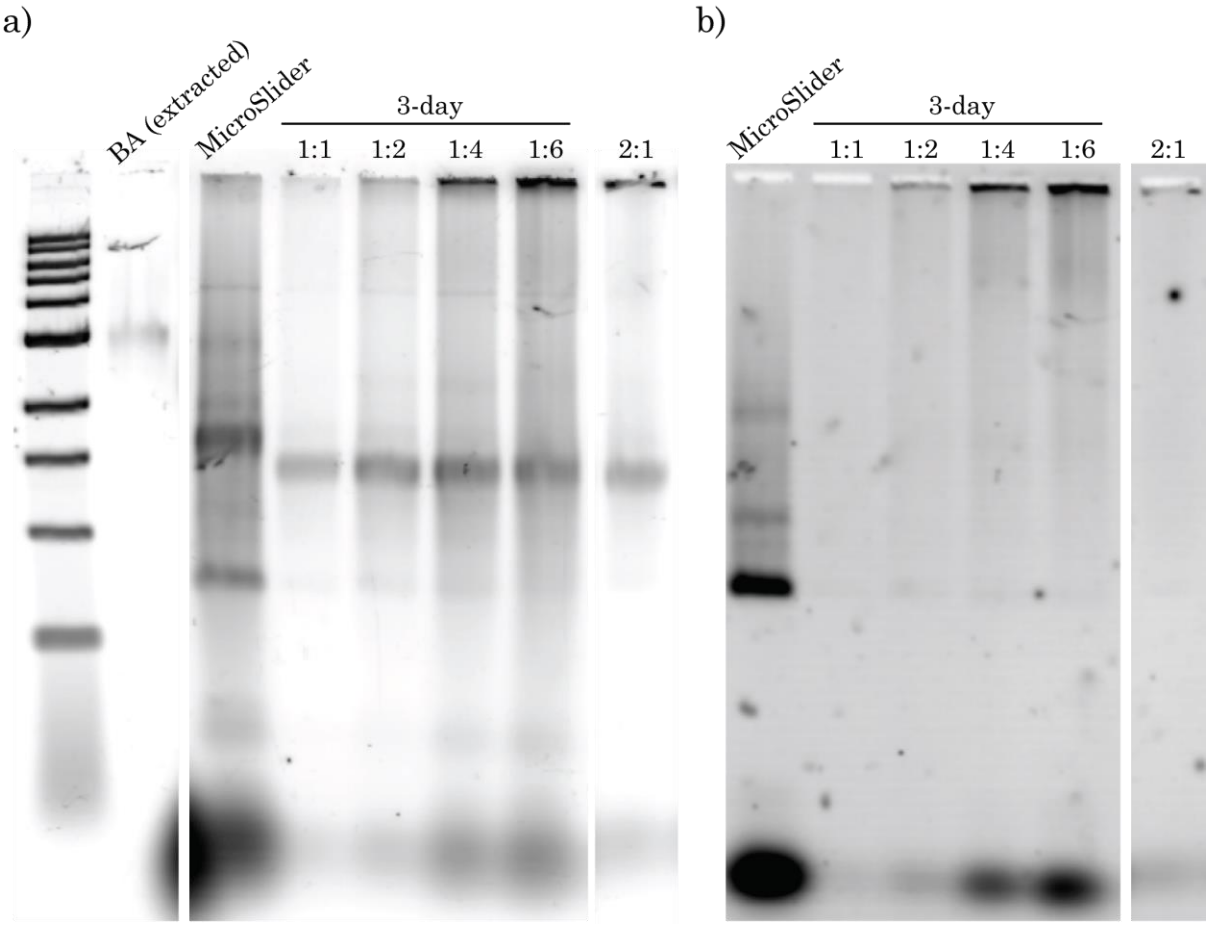

Figure 3.27. Loading of the 3rd Iteration BAs with the MicroSlider. a) AGE screening of incubation proportions and durations, Lanes 1 and 2 present the gel extracted BA and the PEG purified MicroSlider respectively; Lanes 3, 4, 5, and 6 present 3-day incubations at 37°C of the BA:Microslider in 1:1, 1:2, 1:4, and 1:6 proportions respectively; Lane 7 present a 1-day incubation at 37°C of the BA:Microslider in a 2:1 proportion. b) Same gel as in 3.26a but under FAM scan.

The proportion of MicroSlider to BA was screened to find the most appropriate; with the help of the FAM scan, the position of the sliders was easily distinguished. The first

thing to notice is that the addition of the sliders to the BA cause aggregation in the well, particularly at higher concentrations. Even when the slider concentration is low, its addition causes the migrating band of the monomeric BA to disappear completely. Given this very sudden negative result, an altered version of the original MicroSlider design was tested as well. This variation was also designed by Dr Erik Benson, its only two differences with the original version being that the new MicroSlider had two extra helices added to its circumference, making it able to wrap less tightly around the arrow shaft, and that it only had 2 FAM-labelled strands, so it was less visible in the FAM scan. The proportion of the new MicroSlider to BA was checked with AGE as well.

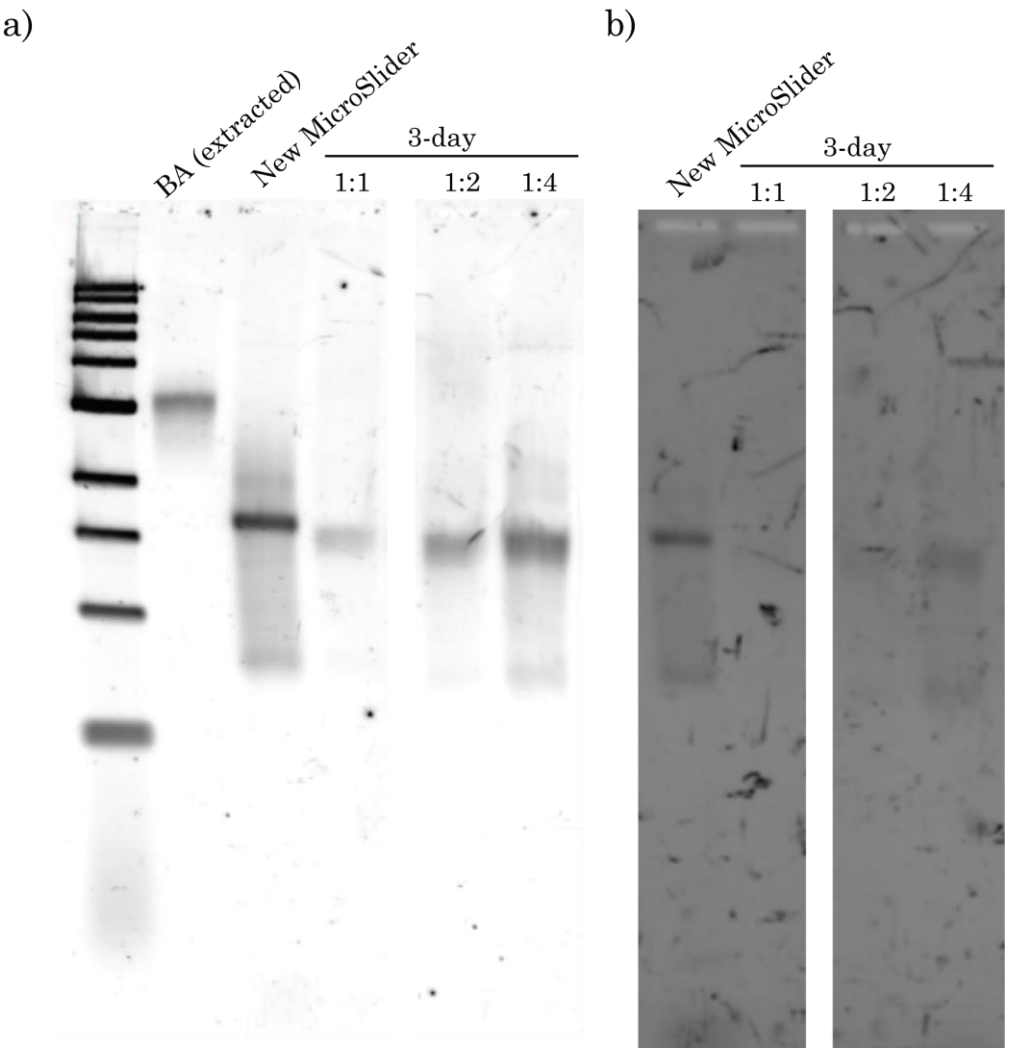

Figure 3.28. Loading of the 3rd Iteration BAs with the new MicroSlider. a) AGE screening of incubation proportions and durations, Lanes 1 and 2 present the gel extracted BA and

the Amicon purified new MicroSlider respectively; Lanes 3, 4, and 5 present 3-day incubations at 37°C of the BA:Microslider in 1:1, 1:2, and 1:4 proportions respectively. b) Same gel as in 3.28a but under FAM scan.

Despite having a less efficient yield in its assembly (15% compared to 27% of the previous MicroSlider as seen in Figure 3.17), when mixed at different concentrations with the BA extracted sample no aggregation in the well was produced. The complete disappearance of the BA monomeric band persisted but given the lack of aggregation TEM imaging and DNA-PAINT was done in order to see if the loading in a 1:1 proportion for a day at 37°C had any success (see Figure 3.29).

a)

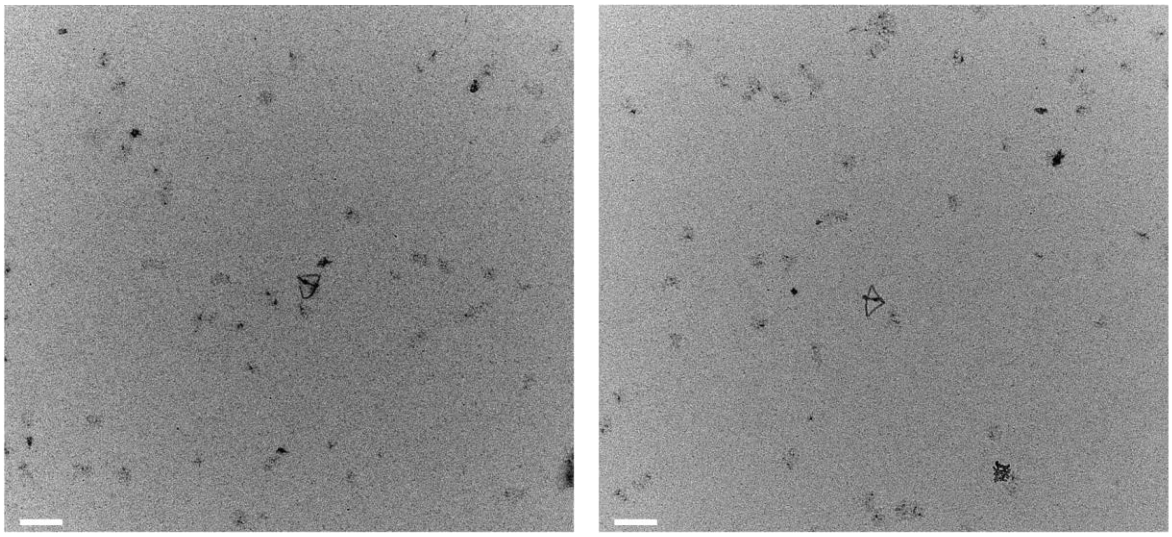

b)

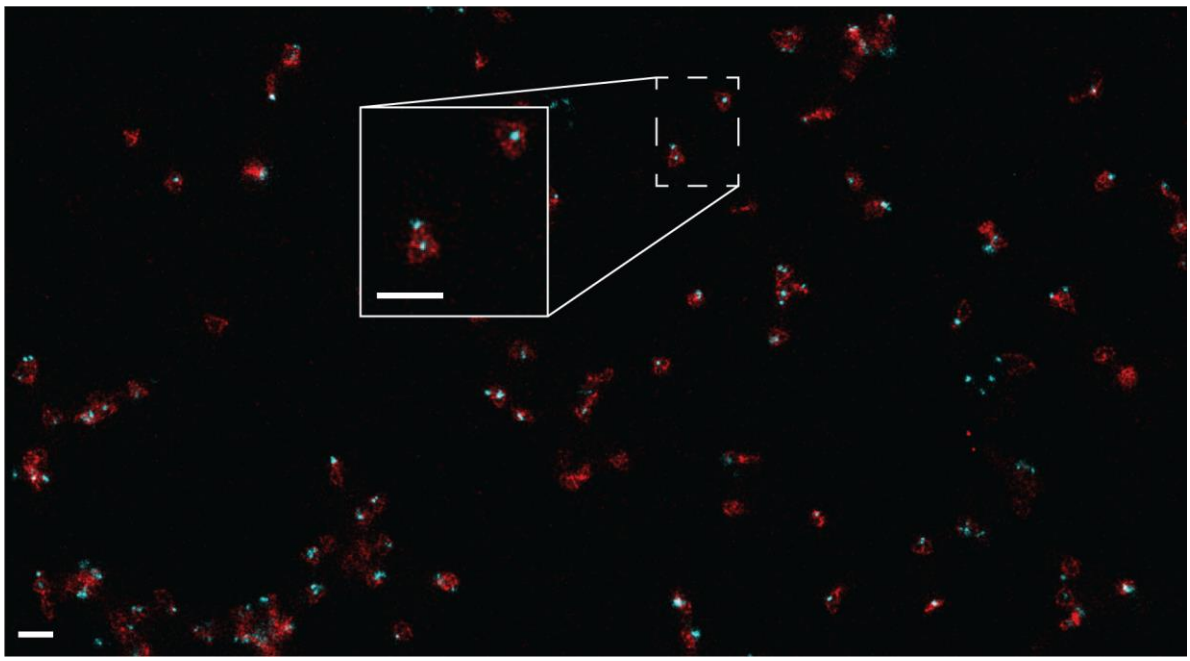

Figure 3.29. Loading of the 3rd Iteration BAs with the new MicroSlider, the BA:MicroSlider incubation was done in a 1:1 proportion at 37 ℃ for 1 day. a) TEM imaging of the loaded BAs. b) (Exchange) DNA-PAINT of the loaded BAs. All scale bars are 200 nm.

Although at a low yield (57% but from a total of 37 structures identified in the TEM grid) if only looking at the TEM images, the loading was successful; (Exchange) DNA-PAINT (190) corroborated this affirmation and showed a yield of 62% out of a total of 130 structures. Since the yield of the new MicroSlider was half the amount of the initial MicroSlider, different conditions were introduced in its assembly. The change that had

the greatest improving effect was a small modification in the PEG purification procedure; after performing the steps described in the appendix A.2.1, the samples were submerged in a water bath at 37°C for 30 minutes. This action had the effect of breaking up aggregation in the structure and greatly enriched the monomeric band, an example of this increased yield (45%) can be seen in the second lane of the gel in Figure 3.30. After this improvement in the production of the new MicroSlider, the conditions for its closing and releasing were screened for.

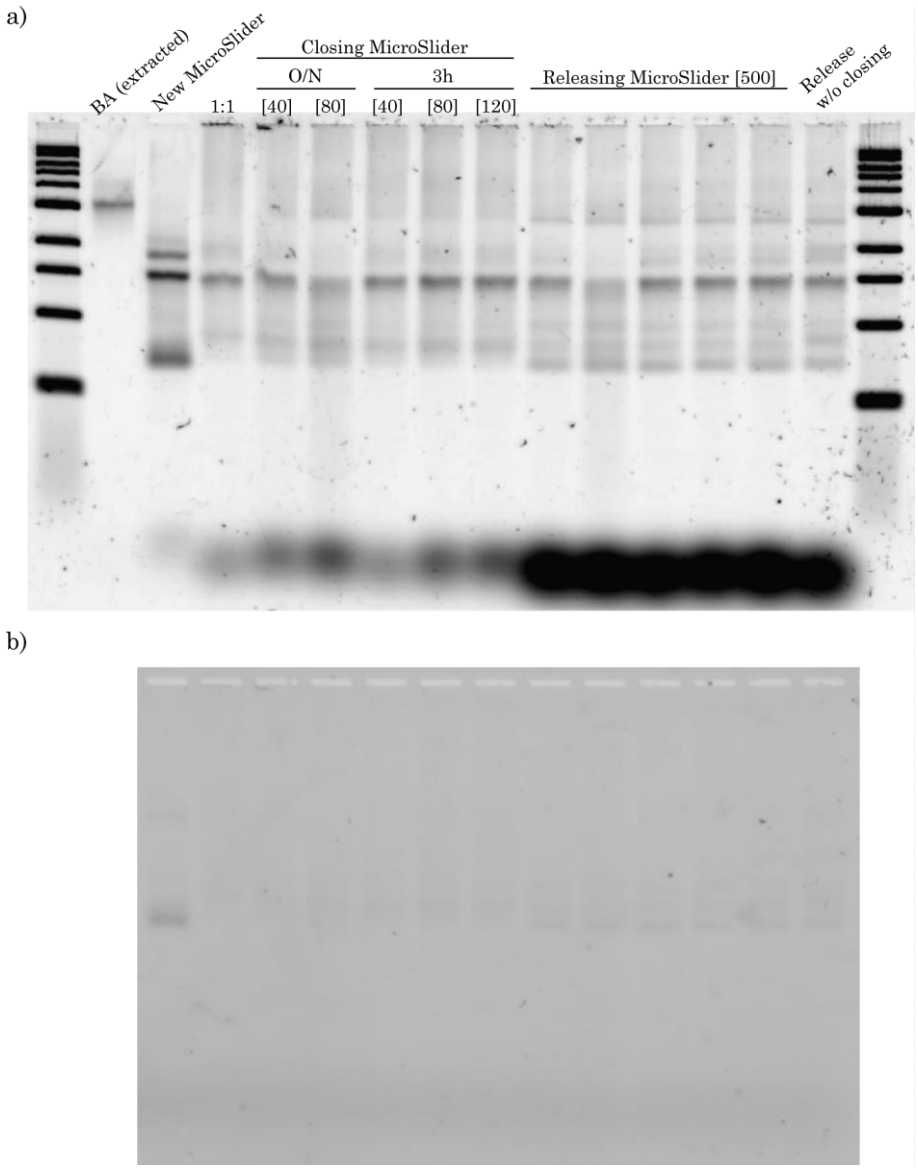

Figure 3.30. Closing and releasing of the loaded new MicroSlider on the 3rd Iteration of the BA. a) AGE screening of incubation durations and concentrations with closing and releasing strands, Lanes 1 and 2 present the gel extracted BA and the Amicon purified new

MicroSlider respectively; Lane 3 presents 1-day incubation at 37°C of the BA:Microslider in 1:1 proportion; Lanes 4 and 5 present the loaded BA incubated with closing strands at 40 and 80 nM concentrations at 37°C overnight; Lanes 6, 7, and 8 present the loaded BA incubated with closing strands at 40, 80, and 120 nM concentrations at 37°C for 3 hours; Lanes 9-13 contain the same samples each as 4-8, respectively, but they are further incubated at 37°C for 40 minutes with an excess of releasing strands of 500 nM: and Lane 14 contains the same structure of Lane 3, released as Lanes 9-13 but without prior closing. b) Same gel as in 3.30a but under FAM scan.

Aside from the persistent difficulty in distinguishing elements in the AGE lanes when looking at incubations of BAs and the sliders, there was also difficulty in discerning the effect of closing and releasing. The closing was done at 37°C for 3h or overnight, the concentration of the closing strands varying between 40, 80, and 120 nM. The releasing was done at 37°C for 40 minutes, the concentration of the releasing strands being 500 nM. When closing, 3h seemed to produce the same as overnight, and the increase in concentration did not have a visible effect. When releasing, the observation about the different conditions mirror those of the closing, but a clear development can be seen in the reappearance of the monomer slider band (with the same intensity throughout the conditions, ~20%) as well as what may be a thin band of the monomeric BA (with an intensity ~15% throughout all the conditions tested, including the one which wasn't closed before release). As in the past 1D system, this behaviour demonstrates that the closing of the slider is not a completely effective step. Since, unlike the with arrow attaching/detaching, no clear conclusions can be drawn from the gel, TEM of the two events had to be done to characterize them.

a)

b)

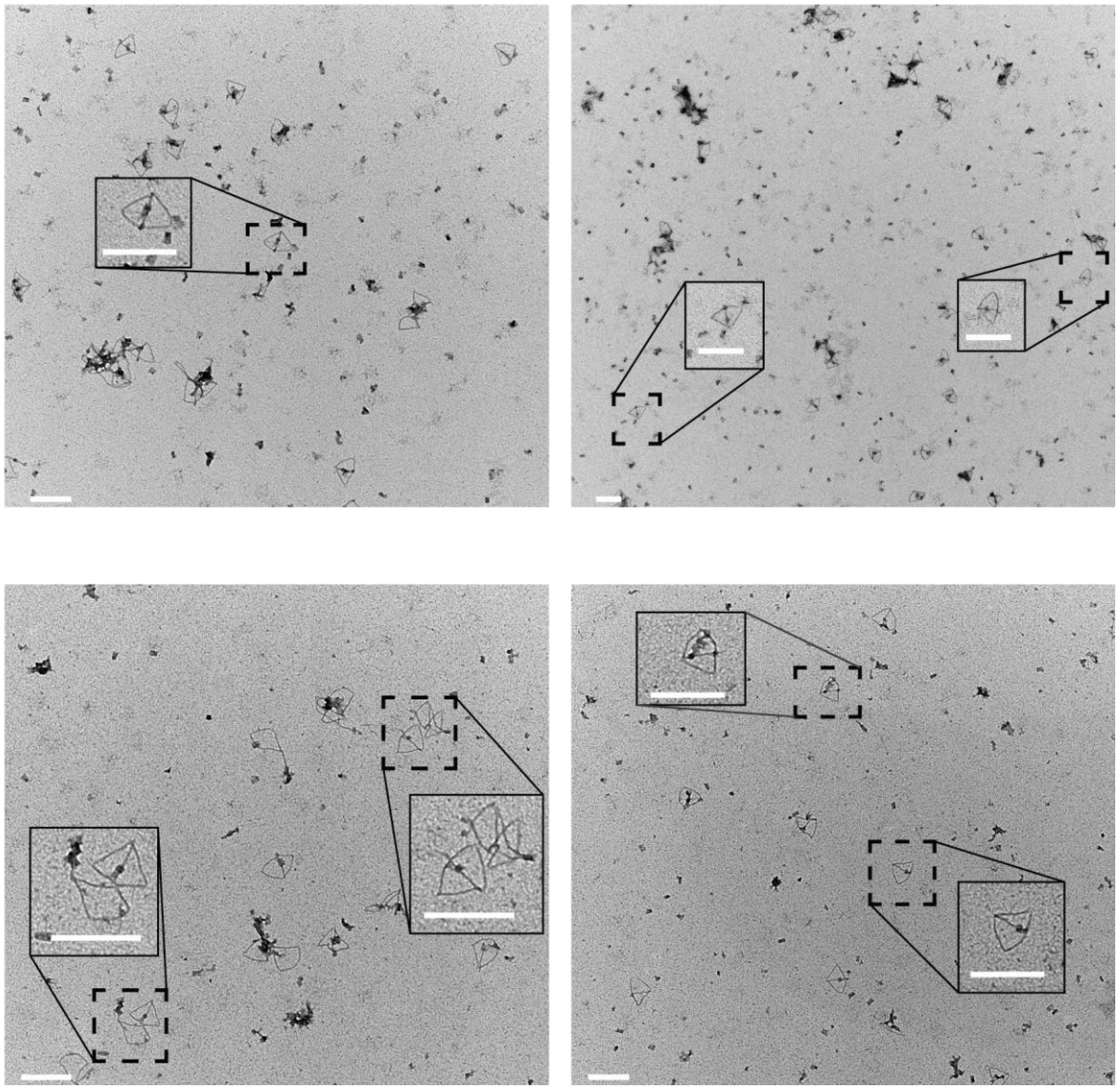

Figure 3.31. Closing and releasing of the loaded new MicroSlider on the 3rd Iteration of the BA. a) TEM imaging of the loaded BA incubated with closing strands at a 80 nM concentration at 37°C for 3 hours. b) TEM imaging of the loaded BA incubated with closing strands at a 80 nM concentration at 37°C for 3 hours, followed by an incubation at 37°C for 40 minutes with an excess of releasing strands of 500 nM. All scale bars are 200 nm.

Closing is not easily discernible with these MicroSliders, but at least a good amount of the loaded BAs can be seen (67%). When releasing the slider, if it has correctly wrapped around the arrow and closed in the previous steps, it should be possible to see the slider in different positions to that of its initial attaching site, which is found around the middle of the shaft, towards the back of the arrow. This seems to be the case as seen in the TEM imaging (56%), although the yield goes down due to the unclosed MicroSliders falling off.

As with the arrow manipulation, the last step is to attempt reattaching the slider to a secondary location in the arrow shaft. A gel was run but, following the recent trend, no clear changes could be seen when screening for concentrations of bridge strands at 37°C for 40 minutes (See Appendix G.1.3). TEM imaging was done on a sample that had its MicroSlider released and then reattached (200 nM bridge strand concentration at 37°C for 40 minutes) near the arrow tip.

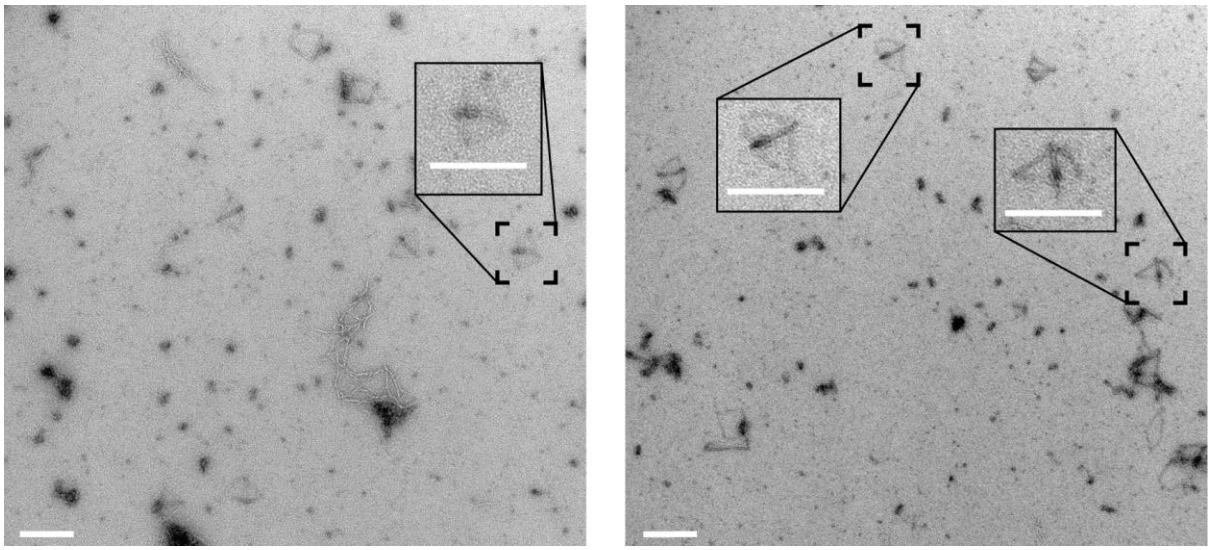

Figure 3.32. Reattaching of the loaded new MicroSlider on the 3rd Iteration of the BA. TEM imaging of the loaded BA incubated at 37°C for 40 minutes with an excess of bridge strands for the tip of the arrow position of 200 nM, this sample had previously been closed and released under the same conditions as 3.31b. All scale bars are 200 nm.

Although the quality of the image is not very high, some examples of the slider on the arrow tip could be seen (36% of all structures in the grid).

3.5.3 2D motion

Despite the room for optimization present in the MicroSlider actuation, a complete 2D motion actuation was attempted within the same sample. The procedure would consist in the incubation of the BA, arrow free, with the new Microslider (1:1 proportion at 37°C for 1 day). Following this the arrow is attached to the middle position (200 nM bridge strands, at 37°C for 40 minutes), the slider closed (40 nM closing strands, at 37°C for 3h), and released (500 nM releasing strands, at 37°C for 3h). Once this was complete the slider is

reattached by the tip of the arrow (500 nM bridge strands, at 37°C for 40 minutes), the arrow is detached from the middle (500 nM invading strands, at 37°C for 20 minutes), and reattached to the right extreme of the bow (500 nM bridge strands, at 37°C for 40 minutes. The TEM imaging of the resulting product can be seen in Figure 3.33.

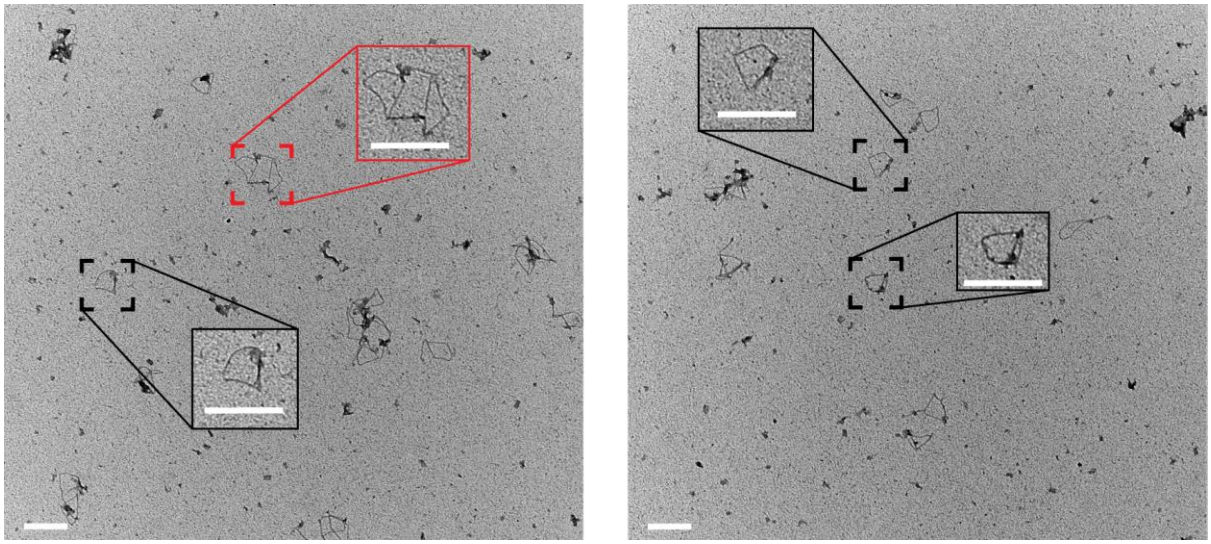

Figure 3.33. 2D motion. a) TEM imaging of the loaded BA after a sequence of stepping by both the arrow (from middle position to right-most in the bow) and the MicroSlider (from the back half of the shaft to the closest position to the tip of the arrow). In the red highlight an unsuccessful 2D step, having missed the last reattachment of the arrow to the bow. All scale bars are 200 nm.

As it can be seen as self-evident, the final accumulation of the different set of "orders" necessary to actuate the 2D motion can be very cumbersome for the efficiency of the process. Even in a suboptimal set-up such as the one I have been working in some examples of correctly positioned 2D system can be seen in the TEM (21% of the total of the structures identified). Incidentally, 25% of the structures have the slider located by the arrow tip but fall short from correct 2D actuation because the arrow did not reattach to the bow, this being the last step can be seen as the hardest one to complete successfully.

This system would be better controlled if placed in a microfluidics chamber in which the sets of strands could be added at the optimal concentrations, and therefore at a faster pace, before being flushed in prevision of the addition of the following set. This set-up would do away with the limitations of the overcrowding of the environment of the 2D

systems and could potentially allow many cycles to be run unimpeded. For the DNA-PAINT experiments this is indeed the set-up, which makes the technique the most propitious one for testing the 2D motion. Furthermore, by altering the DNA-PAINT docking sites the symmetry of the structure can be broken and a precise assessment of the success of the stepping, particularly the arrow along the bow, can be made.

For the following DNA-PAINT experiments the pattern of docking sites was modified by removing all the sites in the right string and in the arrow. When studying the structure with DNA-PAINT the only visible sections, as seen from above, will be the bow and the left string, as well as the slider. Several different positions were tested using the less optimal method of actuation (i.e. doing the steps in solution as done so far), but the imaging was done with DNA-PAINT in the Nanoimager. The samples do not come from stepping as the previous experiment but rather they come from single attaching events as I wanted to explore different positionings within the system.

a)

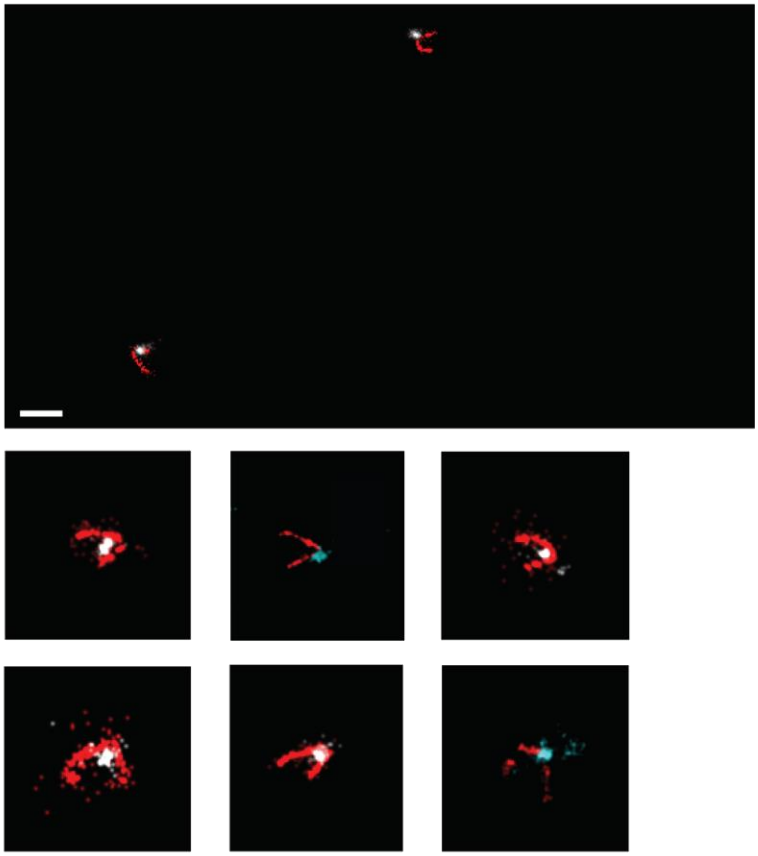

b)

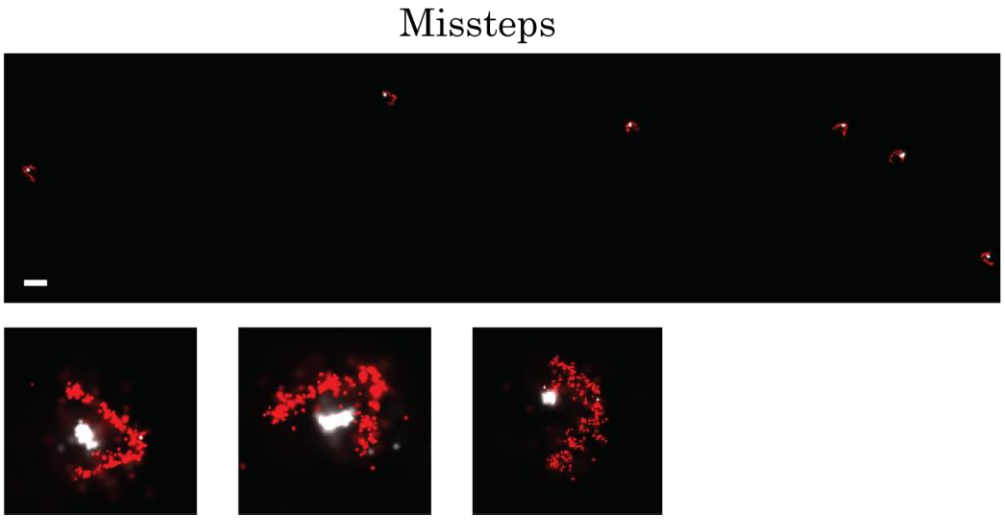

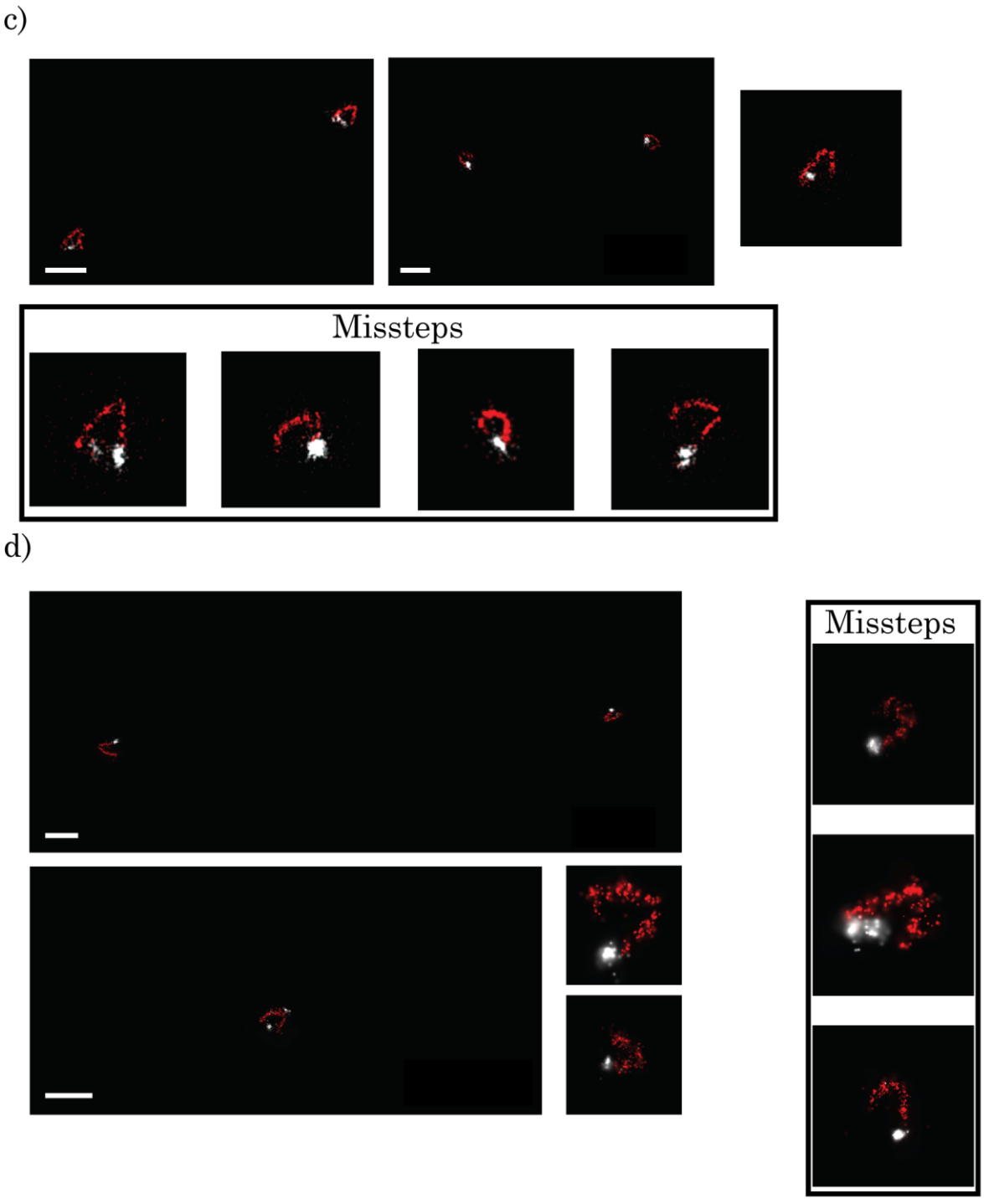

Figure 3.34. DNA-PAINT gallery of positions in the 2D system, failed positionings are labelled as missteps. a) Slider in the intersection of bow and string. b) Slider in the middle of the bow. c) Slider at the opposite end of the bow-string intersection, on the bow. d) Slider at the opposite end of the bow-string intersection, on the string. All scale bars are 200 nm.

Due to time constraints and problems with the instruments only 4 different positions could be characterized. However, the different positionings present a relative range of successful events; positioning on the middle of the bow and at the tip of the arrow (Figure

3.34b) had the lowest success with 27%; the rest of the positions, on the right of the bow and at the tip of the arrow (Figure 3.34a), on the left of the bow and at the tip of the arrow (Figure 3.34c), and on the right of the bow and at the end of the arrow (Figure 3.34d), had a successful 2D motion yield of ~45%. A common pattern in those 2D systems that failed to produce the intended positioning was that the slider had not released/reattached were it should have (42% for Figure 3.34b and ~27% for the rest of the positions. Indeed one of the limiting factors in the yield of good positionings was the relatively low levels of MicroSliders successfully loaded onto the arrows.

3.6 Summary

The developed 2D system presents a robust system for the positioning of the slider in an area of a quarter of a circle. One of the strengths of this architecture over a more straightforward square-area system, with the axes along the sides of said square, is related to the possible resolution of the slider positioning. The square area system described is a cartesian coordinates system, the resolution, if it were to have a disposition of overhangs as the one in the 2D system of this chapter, would be 21 nts, or ~7 nm. In a polar coordinates system such as the Bow-and-Arrow, the closer the slider is to the base of the arrow shaft, the smaller are the changes in position when displacing the arrow tip along the bow, and therefore, the greater the resolution is (197).

The process of producing a successful 2D system posed several design problems that had to be addressed progressively. The increased level of complexity in the design of the Bow-and-Arrow had many aspects that had to be tackled mindfully, from the right scaffold routing, the right dimensions, and the appropriate bending of the bow. With a system with so many interrelated parts reaching the necessary balance to produce a good yield of structures was not trivial and took 3 attempts. The same applied to the slider as it had to evolve and adapt to the new characteristics of the rail it had to wrap around. Ultimately

the project reached the necessary milestones but much room for optimization of the actuation remains.

The production of the 2D system had a problematic AGE profile that was not satisfactorily explained, and the incubation between both structures was not very efficient. The usage of magnetic beads was entertained to help in the purification of properly loaded BAs; MicroSliders would present overhangs that would allow it to attach to magnetic beads, any BA that had no MicroSlider attached would be washed away. The downside of this approach would be that there would be many unloaded MicroSliders in the sample but they would be washed away when the structures were introduced into the microfluidics chamber of the DNA-PAINT set-up. At that stage only the BAs, which would all be loaded, would attach to the surface and not be washed away.

In relation to that, the hypothetically optimal set-up for actuation of the system as commented above, in the microfluidics chamber, was never tested and therefore remains an untested incognita. The certainty is that the 2D actuation was achieved in a suboptimal way.

The follow-up step in the project of developing the molecular printer would be to create a printing system compatible with the 2D system, and perhaps a surface onto which the system could attach and effect the printing modifications. This surface could be a DNA canvas and the modifications introduced in it could be related to DNA oligos or chemical modifications such as the ones based on click chemistry (198).

Chapter 4

Azobenzene Actuation

In this chapter I will explore the use of photochromes as a means for the actuation of DNA structures. The molecule of choice is the azobenzene, which has been used extensively in the literature in conjunction with DNA, driving hybridisation/dehybridisation of strands by photo-induced conformation change. I will first talk about the molecule itself, how it changes conformations with determined incidental wavelengths, how it is introduced in DNA systems, and how it has been used for actuating dynamic DNA structures. Following this bibliographic review, I will describe the set of experiments I conducted in trying to achieve the preliminary evidence that these molecules could be a source of actuation for the already discussed 1D and 2D systems. I will start first with a patterned canvas (and its variations) characterised with the Nanoimager and, lastly, I will make a tweezer-like structure that was checked with fluorimetry.

4.1 Aim

Up until now in this thesis, and in many, if not most, examples of dynamic DNA origami in the literature, the means of actuation has been toehold-mediated strand displacement (TMSD). This technique, despite having the capability of being very precise and making use of the physical particularities of DNA itself, is not without drawbacks. The actuation is dependent on the kinetics of the strands, being a slow process (199), and produces waste complexes that can hinder the course of the reactions if not removed (138).

As it was mentioned in the introduction, there is a variety of ways in which a conformational change can be induced in a molecular structure. With a focus on DNA structures, electric and magnetic fields (96,98), as well as light of different wavelengths

(97,166) can be used to produce these changes, to actuate the mechanisms. Focusing on the later, many organic compounds have been studied due to their interesting optical properties, arylazopyrazoles (200), dithienylethene (201), fulgicide (202), hemithioindigo (203), and others (204–206). From the possible candidates azobenzene was chosen, given that it is one of the most widely studied and used in DNA structures on its own (207,208) and in combination with other photochromes (209). In addition to this, the azobenzene phosphoramidites necessary for incorporating these molecules in between nucleotides during the synthesis of DNA strand are readily available commercially. This simplifies and reduces the price of the synthesis of azobenzene-containing oligonucleotides of the type required for testing the viability of photoactuation of the systems developed in this thesis.

4.2 Azobenzene, a photoswitchable chemical in the DNA context

Azobenzene consists of two phenyl rings connected by a N=N bond. In its most stable conformation (trans) the azobenzene is a planar molecule, upon irradiation with a UV wavelength (300-400 nm) the molecule undergoes a photoisomerization into its cis-form. In this less stable conformation the molecule becomes non-planar. Either by thermal relaxation, in darkness, or by irradiation with visible light (>400 nm), the azobenzene returns to its trans conformation. The structures of the molecule's conformations, along with their absorption spectra can be seen in Figure 4.1.

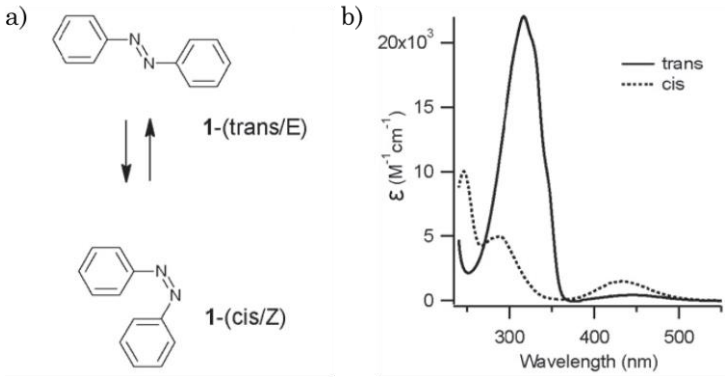

Figure 4.1. Azobenzene molecule. a) Schematic representation of both trans and cis conformations of azobenzene. b) Absorption spectra of both azo-isomers. Taken from (210).

This molecule can be incorporated into a DNA strand instead of a nucleotide during phosphoramidite synthesis; the group is connected to the phosphate backbone of the oligo. This insertion chemistry to the backbone is done with a threoninol group and it does not disrupt the single/double stranded structure of DNA when intercalated in a sequence, irrespective of its density and presence in both strands in the hybridization. Not only it does not disrupt the stability of the helix, it increases it by the reinforcement of the base pairs stacking interactions. This leads to an increase in the melting temperature of dsDNA oligos that contain azobenzenes when compared with their native-conformation versions.

In this context of intercalation in a DNA helix, among base pairs, a change of conformation due to the photoisomerization from trans to cis causes a disruption of the internal stacking; cis conformation of azobenzene is not planar and through steric hindrance it destabilizes the neighbouring base pairs. This event, given enough density of azobenzenes in a sequence and the right system temperature, leads to the dehybridisation of a DNA duplex. The process does not require addition of auxiliary oligos and does not produce waste complexes, the main caveat being that, due to the increase stability of the azo-containing duplex, the melting temperature of the duplex also increases. This translates into the need of high temperatures in order to destabilise the duplex enough to be separated by the photoisomerization of azobenzene, although

sequence modifications (e.g. introducing mismatches) is another possibility that will be explored in this thesis.

4.2.1 Modified Azobenzenes

Due to the absorption spectra being on the UV range, the change of conformation of this molecule cannot be easily applied in a biological context (e.g. biomedical applications) as the UV radiation has deleterious effects on organisms, affecting genetic material (thymine dimers) and its repair mechanisms (211). With the aim of making the molecule more suitable for such contexts and applications, along with an interest in customizing the stability of the two conformations, many modified azobenzene molecules have been produced (210,212–214). Introduction of substituents in the phenyl groups greatly affect the absorption profiles of both trans and cis conformations, causing red-shifts in the spectra of absorption or alterations in the rates of thermal relaxation, i.e. the stability of the cis conformation. Via these modifications, differently "coloured" azobenzenes could be used in parallel and actuated orthogonally.

a)

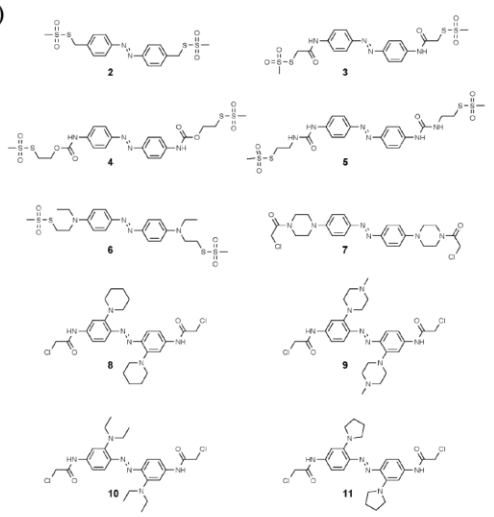

b)

compound	λ_{max} (trans)	$\tau_{1/2}$ (cis-to-trans)
2	342 nm	43 hr
3	366 nm	12 min
4	372 nm	80 sec
5	382 nm	11 sec
6	480 nm	25 ms
7	450 nm	2 sec
8	445 nm	6 sec*
9	437 nm	5 min
10	488 nm	0.8 sec*
11	530 nm	0.7 sec*

Figure 4.2. Examples of modified azobenzenes. a) Schematics of modified azobenzenes with substitutions in para and ortho. b) Table with the wavelengths of maximum absorbance for trans isomers and thermal half-lives of the cis isomers. Taken from (210).

One of the aspects of this chemical modifications that should be considered carefully is how the presence of this large structures could affect the DNA helix architecture or if it would even be possible to include them in the helix to begin with. Another interesting aspect is how these groups would affect the solubility of the DNA strands, since some of these modified azobenzenes become insoluble in water. These designs were done without their introduction into DNA sequences in mind, they were mostly developed to displace the wavelength necessary to the conformational change from the UV range into visible and near-infrared, so that they could be used in a biological setting. Due to lacking these limitations and being able to work with UV light without these concerns, simpler chemical modifications, that do not add greatly to the size of the azobenzene molecule and that do not change the physical aspects such as the solubility, have been used in parallel to drive photoactuated conformational changes in an orthogonal fashion (215).

Another variation introduced in azobenzenes is related to its phosphoramidite. The commercially available one presents insertion through threoninol to the phosphate backbone (216), the insertion of azobenzene is done via a rigid amide bond and which leads to 6 additional covalent bonds in the strand backbone. This physical constraints cause a reduced trans-to-cis photoisomerization and the great increase in the melting temperature of azo-containing duplexes (217). A solution explored in research is the change of the threoninol backbone connection for a glycerol one. The bond in the latter case is a flexible ether and forms one covalent bond less than the threoninol counterpart. This leads to a reduction of stability when compared to the “traditional” azo-containing duplexes (218). This modification solves the need of high temperatures for efficient photoactuation when working with azobenzene groups, although it is not available commercially at the time of the writing of this thesis.

4.2.2 Azobenzene in an actuation system

There are many examples in the literature of the introduction of azobenzene groups to photoactuate DNA structures. With the base of the photoactuation being the hybridisation/dehybridisation of strands upon irradiation with a specific wavelength, the change of conformation of structural elements follow. Examples of these are walkers (219,220), tweezers (207), DNAzymes (208,209), DNA capsules (221), and rotating systems (222). Some systems present interesting aspects such as the use of different photochromes (209), or modified azobenzene groups (215,220), and can use different wavelengths to actuate orthogonally different parts of the same structure.

With these examples in mind, I was interested of introducing these intercalated azobenzene groups into the overhangs of the direct attachment mechanism of the 1D system. By doing so I could control the attachment and detachment of the slider to one of the attachment points in the rail with light, using the current system.

If I were to include differently coloured azobenzenes with orthogonal isomerization wavelengths I could design a processive, photoactuated molecular motor. In this hypothetical design there would have to be at least three different types of attaching points (A, B, C) along the rail, in equidistant distribution and repeated pattern. The slider would be attached to two positions at all times, and the dehybridisation necessary to displace the slider from one of its attachment points would be driven by a specific wavelength affecting only one of the three types of azobenzenes. The azobenzenes would be present and intercalated in the overhangs coming from the slider, each of this three overhangs would only interact with a specific type of overhang in the rail (A', B', C'). When in mid-step, the slider would be attached only by one overhang but it will have the freedom of movement to diffuse to an available overhang placed forward in the rail. Once the step is completed and the slider is again bound by two overhangs, the next step will require the photoactuated dehybridisation of the strand that had remained attached in the

previous step. Continuous flashing of the wavelengths in order would be able to produce movement in either of the two possible directions on the rail.

This is a hypothetical design. The most important concern is that three azobenzenes have to be modified with very stringent characteristics; orthogonal absorption spectra for both isomers; modifications should not interfere when the azobenzenes are intercalated in duplexes; good rates of trans-to-cis isomerization; and stable cis conformations that don't immediately relax back to trans, but that are not too stable so that they are available for attachment within a complete stepping cycle (unless the cis-to-trans isomerization is also photoactuated). Additionally, the design and lengths of the overhangs have to be carefully done so that the slider is not too limited nor too free when performing the steps. If a misstep occurs there should be some sort of mechanism to correct it or the whole system would lose its precision.

Ultimately these ambitious designs cannot come into fruition or be even considered before attesting the feasibility of photoactuation in the system in mind. As I explained above, regular azobenzenes do not lack performative issues (imperfect rates of photoisomerization and the need for elevated temperatures to actuate the duplex destabilization), so they should be tested beforehand with sequences and strand lengths that mimic those of the attaching system in 1D.

4.3 Azobenzene initial actuation system

As a preliminary test for regular azobenzenes, different experimental set-ups were designed to characterize the behaviour of azobenzene-containing oligos. The one aspect that remained constant across the set-ups was the sequence of the azo-oligos.

Based on studies done on the effects of the distribution and density of azobenzene moieties in strands forming duplexes, the photochromes were introduced in one or both sequences of the duplex as seen in Figure 4.3.

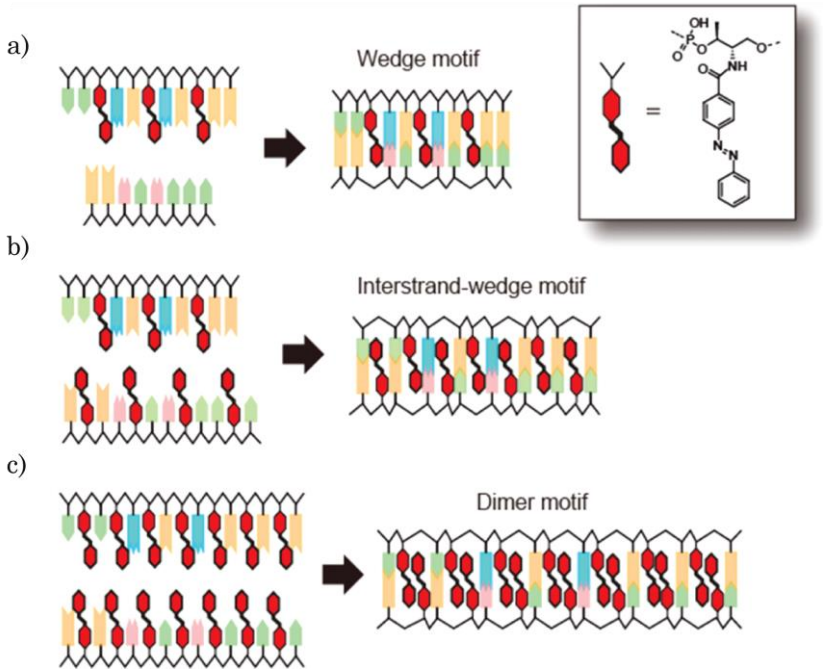

Figure 4.3. Azobenzene moieties distributions. a) Wedge motif, b) Interstrand-wedge motif, c) Dimer motif. Taken from (223).

The introduction of the azobenzene molecule to the DNA helix, even when being connected to the backbone in the same fashion, distorts the B-DNA double-stranded conformation, at least in a local fashion when only being one group is intercalated. The distortion occurs with the azobenzene group in trans conformation and from the canonical B form to the A form (224). Regardless, even in the wedge motif, the complementarity of the oligos is not affected as these azobenzene groups, due to their aromatic ring structure, intercalate between the base pairs. The deformation that will take place in the sequences that will be used is not a concern due to the prospective nature of their use; they are intended to be used as isolated strands transiently connecting separate subunits, not internal parts of wider, complex architectures that would be warped by this deformation.

The interstrand-wedge (216,225) and the dimer (226) distributions cause a great increase of the stability of the azo-oligo duplex when compared to the native band. This in turn reduces the effectivity of the dehybridisation due to a suppression of the trans-to-cis isomerization, an unwanted characteristic if I want to be able to use this system with

DNA origami structures that would be affected negatively in a > 60°C environment. Another issue with these distributions is the presence of azobenzene groups in both strands of the duplex; if I need to introduce this chemical modifications not only in key overhangs in the slider but also in every overhang in the rail, the cost of the design would increase. Because of these drawbacks in these designs, I decided to use the wedge distribution for the tests. Despite being distributed asymmetrically in the duplex, the azobenzenes do not interfere with the assembly of the strands. The melting temperature of the system still increases due to stacking of base pairs, but it is greatly reduced when the azobenzenes are photoisomerized to cis form. The more groups introduced into the sequence, the greater the efficiency of the photoactuation (223).

In anticipation of the aforementioned issue with the increased melting temperature of the azo-containing duplex, the sequence used for the azo-oligo was one designed to have a weak or transient hybridization at RT (Melting temperature of ~26°C). More specifically, the sequence used was the complementary to the P1 sequence from the probe strand used in DNA-PAINT experiments (189) (see in Appendix F, P1-Cy3 sequence). The P1-complementary sequence is 9 nts-long and contains 4 azobenzenes, each intercalated every two nucleotides. This segment of the overall azo-oligo is on the 3' end, constituting the 5' end there are 18 nts with a biotin modification capping it. The 18-nts region is the tail section used for placing the azo-oligo with the azobenzene region protruding in the different systems used.

The azo-oligo and a control oligo (same sequence minus the intercalated azobenzenes) were produced by the company ATDBio (Oxford), an industrial partner in the innovation training network (ITN) from which the funding for the project comes.

4.3.1 Azobenzene DNA origami canvas set-up

The first set-up designed for the study of the efficiency of the photoactuation of the hybridisation of the azo-oligo was based on a DNA origami canvas that had been previously designed and used in-house. The canvas was composed of a single layer of 26 helices in a square lattice distribution, ~60 nm in total width, that are ~70 nm long, it used a standard p7249 scaffold; it presented P1 docking sites for DNA-PAINT along the edges and a central overhang that was complementary to the tail section of the azo-oligo (See Figure 4.4).

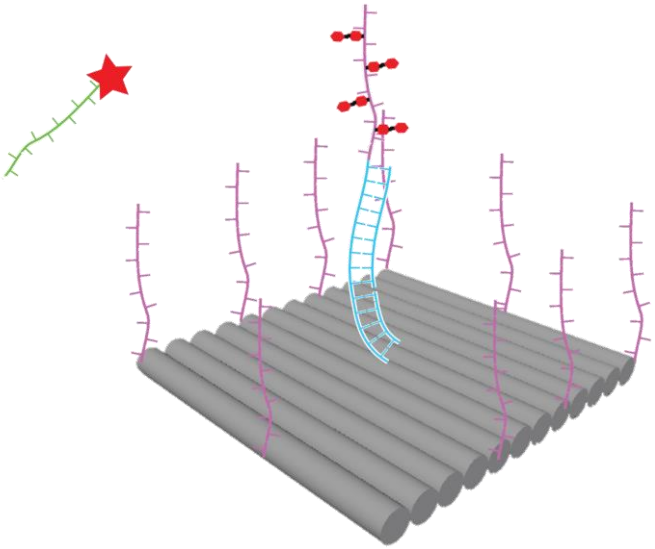

Figure 4.4. Schematic representation of the canvas. The grey cylinders represent the origami square structure, in purple the DNA-PAINT docking overhangs (the one in the middle including the azobenzene molecules intercalated), in light blue the central overhang and its complementary oligo, the tail of the azo-oligo, in light green the DNA-PAINT probe with the Cy3 fluorophore (red star).

The canvas' design was done with the intention of characterising and validating the photoactuation in the Nanoimager via DNA-PAINT. When the structure is observed in the Nanoimager a dotted rectangular shape (docking sites along the edges) should be distinguished, with a single dot in the centre coming from the azo- or the control oligo. If it is an azo-oligo, the increased stability of the hybridization (due to the azobenzenes present) will cause a more continuous localization of the fluorophore probe in this position. If compared to the control oligo, whose hybridization is more transient, the central dot

would be visible even if measured with a higher threshold for the signal representation. Regardless, the intended experiment for the validation of the photoactuation would be based on the effect of UV irradiation will have on the canvases with either the azo-oligo or the control oligo in the images registered by the Nanoimager. If the dehybridisation happens as expected, the central dot will completely disappear in the canvases with an added azo-oligo post UV irradiation.

After an iterative process to design an adequate set-up for irradiation and imaging, the first clear canvas structures were obtained (see Figure 4.5).

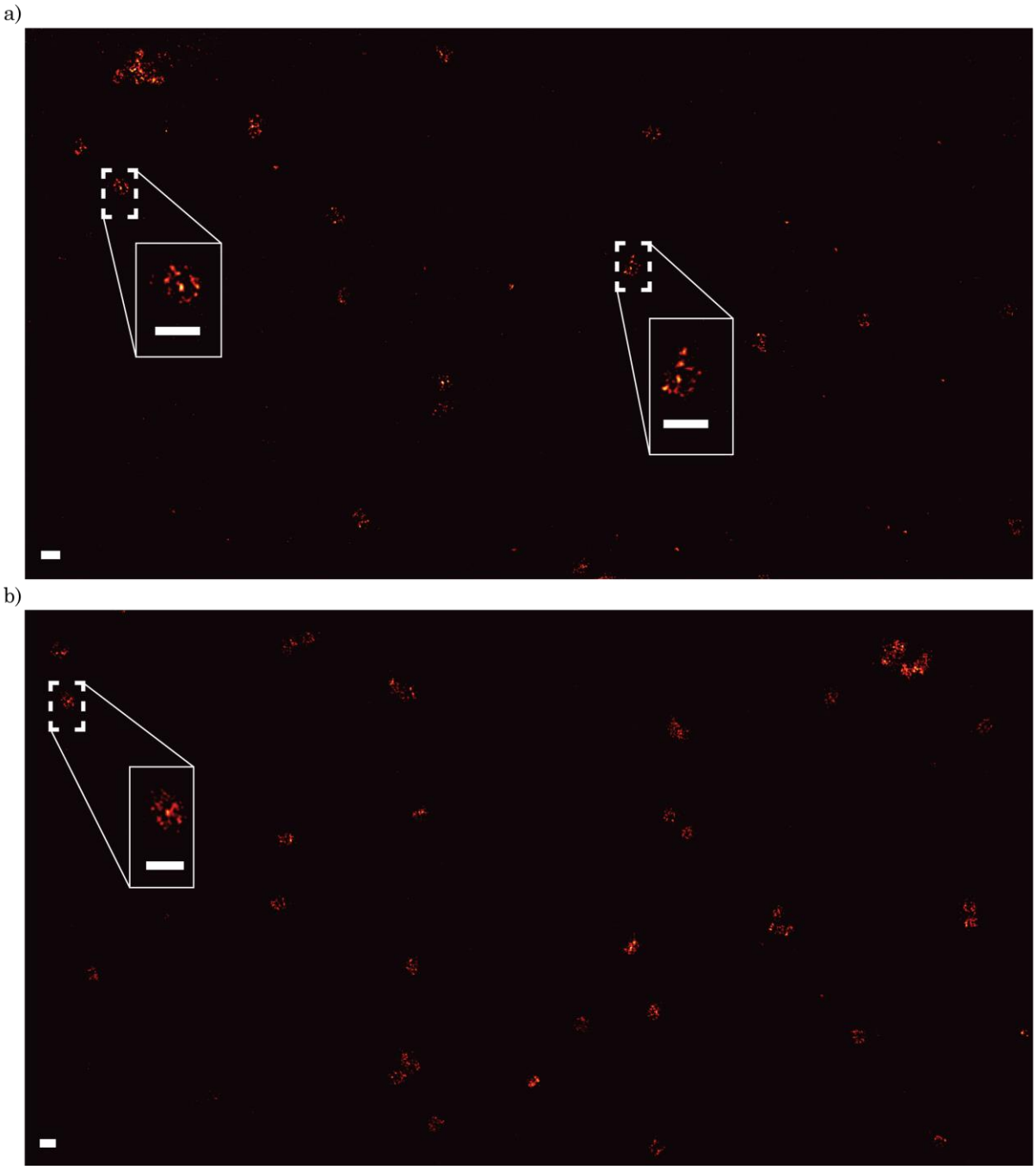

Figure 4.5. DNA-PAINT characterisation of the canvas, white circles marking the canvases with identifiable central dots. a) Canvas with the control oligo attached in the centre. b) Canvas with the azo-oligo attached in the centre. Scale bars are 100 nm.

The initial characterization of the structure was not ideal given the difficulty of distinguishing the central dot. Further optimization can be done with the experimental set-up, changing the fluorescent probe concentrations and the imaging collection parameters but, given that this experimental difficulty is not a necessary constraint, a redesign of the distribution of the overhangs in the canvas was done. In this second design

the regular DNA-PAINT docking sites were limited to two opposing sides of the square and the azobenzene oligo in the centre became a row of 5 such oligos. This was done to maximize the signal from the azobenzene-containing part of the system while minimizing the signal from the regular DNA-PAINT docking sites since it could make difficult the study of the former.

No clear results could be obtained from this new conformation either, situation which prompted me to reconsider the characterization approach with a complete redesign of the system and a change of the technique used.

4.3.2 Azobenzene DNA tweezer set-up

Due to the encountered difficulties when trying to assess the photoactuation effectivity of azobenzene with the canvas and the Nanoimager, I decided to do a more straightforward, bulk test with fluorimetry. In order to be able to use the azo-oligo, I designed a labelled tweezer structure composed of three interacting components (See Figure 4.6).

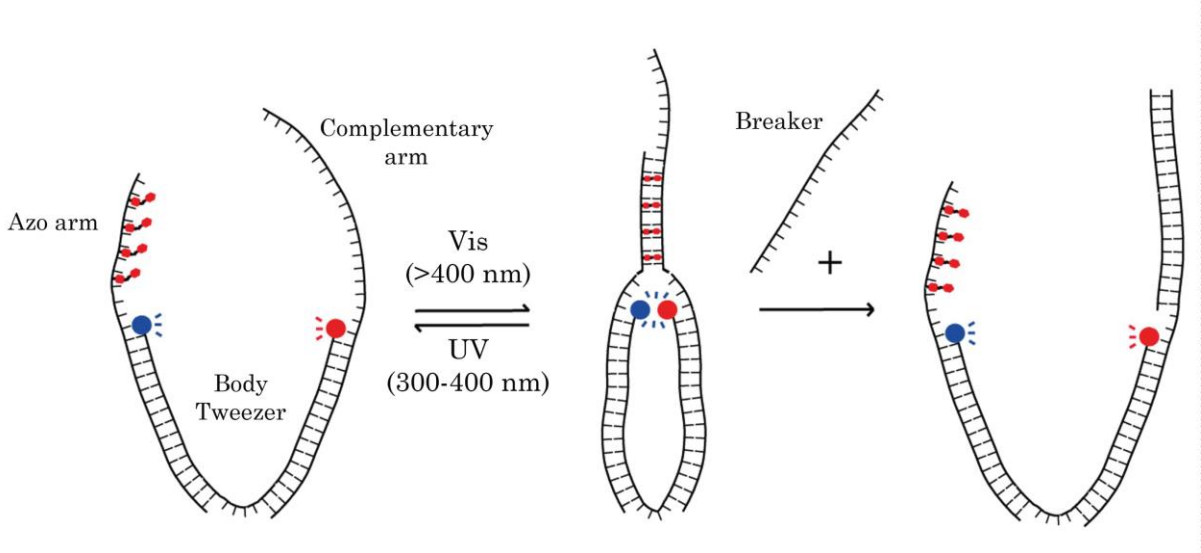

Figure 4.6. Schematic representation of the azobenzene tweezer in its possible conformations and its dynamics.

The azo-/control oligo is the so called azo-/control arm, with its 9 nts-long azobenzene containing section and a 18 nts-long tail in the 3' end that interacts with one half of the "body" of the tweezer. The complementary arm is a 35 nts-long strand constituted by 3 sections, from 5' end to 3' end these are; a 8 nts-long section that acts as a toehold that allows the tweezer to be open with a breaker strand (17 nts-long) via TMSD; a 9 nts-long section that is complementary with the azobenzene-containing section of the opposite arm; and a 18 nts-long section that is complementary to the other half of the "body" of the tweezer. The "body" of the tweezer is a 40 nts-long strand, divided in two 18 nts-long sections at each end of the strand, with a flexible, single-stranded poly-T 4 nts-long section in-between. It is doubly-labelled, Cy5 in the 5' end and Cy3 in the 3' end, so that when the tweezer is assembled there is a FRET signal. Opening the tweezer, either by using TMSD with the breaker or irradiation with UV light in the azo containing tweezer, will cause the

FRET signal to drop and the Cy3 signal to increase. These changes in the fluorescent signal would be reported by means of a fluorimeter (Appendix D).

As a first step, the components of the tweezer, and their assemblies (Appendix A.1.4), were characterised via PAGE (Appendix B.2) and can be seen in Figure 4.7.

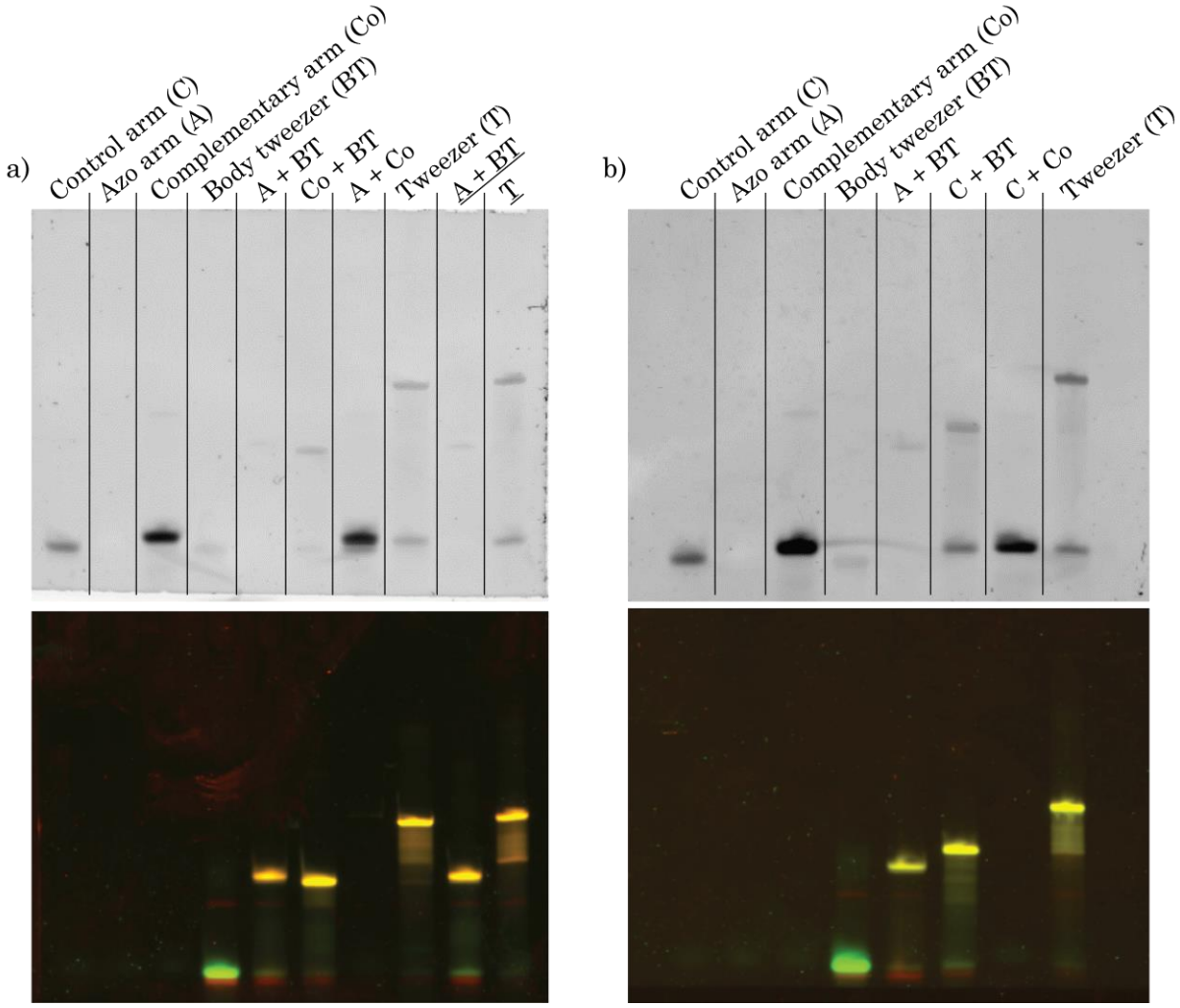

Figure 4.7. PAGE of the individual components and the assembly of the tweezer, SYBRGold scan on the top row and a superposition of Cy3 (Green) and Cy5 (red) on the bottom row. a) Azobenzene tweezer gel, the first 4 lanes are all the individual components; Lanes 5-7 present all the possible combinations of only two members of the azo-tweezer; Lane 8 presents the complete azo-tweezer; Lanes 9 & 10 present the same samples as lanes 5 & 8, respectively, the difference being that the annealing ramp used in 9 & 10 is much faster. b) Control tweezer gel, the first 4 lanes are all the individual components; Lanes 5-7 present all the possible combinations of only two members of the control tweezer; Lane 8 presents the complete control tweezer.

The individual components of the tweezer were seen correctly in the gels with two exceptions; the body of the tweezer does not stain well with SYBRGold but appears clearly

in the Cy3/Cy5 superposition scan; and the azo-arm that does not appear at all under any scan. The presence of the azobenzene groups in the arm seem to negate its staining with SYBRGold, but its presence is confirmed by the fact that the azo-arm + body tweezer lane shows a change in its migration when compared to the body tweezer alone. The product of the annealing between an arm and the body share a similar migration pattern since the weight of the incomplete tweezers is very similar. The assembly of both tweezers in a 1:1:1 proportion seems to be successful as a single, slow migrating band is generated, although some complementary arm seems to be in excess in that lane. A quick annealing of the structure is possible as the last two lanes in 4.7a demonstrate.

Once the tweezers were characterised with PAGE, I checked the stability of the different tweezers, the control and the azo-tweezer before and after UV irradiation in the RTPCR (Appendix A.1.2) as seen in Figure 4.8. As an important aside, since the UV irradiation set-up used so far is designed with the Nanoimager in mind, a change of the

irradiation source was needed for the experiments that follow. UVL-56 Handheld UV Lamp (365 nm, 6 W, UVP) was used for the irradiations.

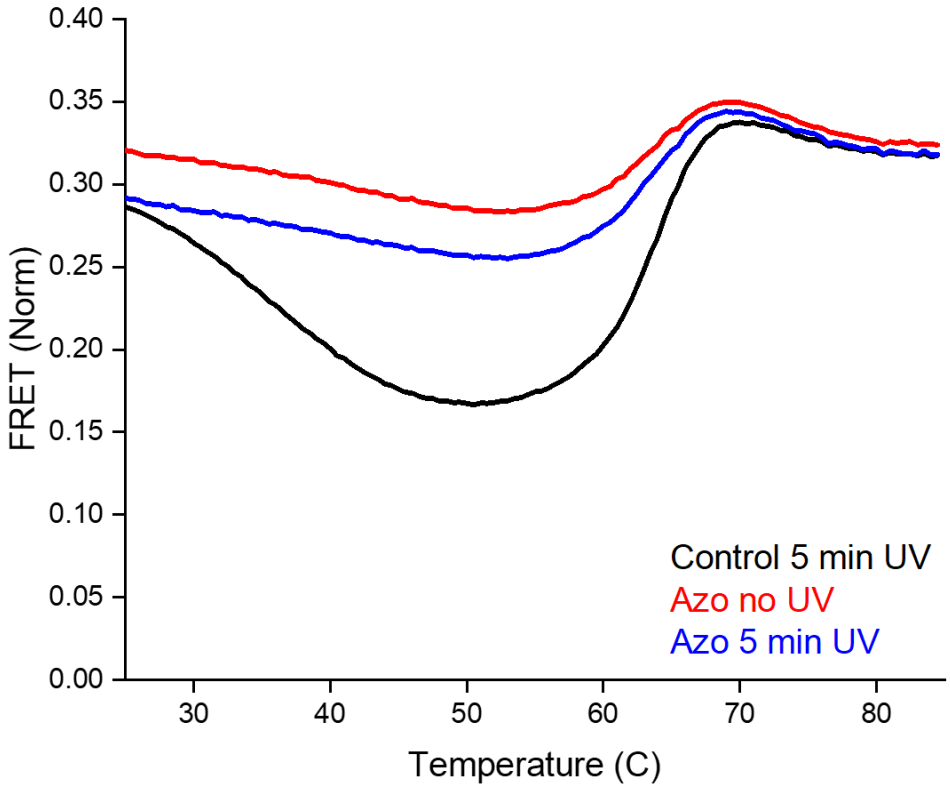

Figure 4.8. Melting curves of the tweezer in its three possible variations, control, azo-tweezer non irradiated (trans, in red), and azo-tweezer irradiated (cis, in blue).

Taking the control tweezer curve as a reference, as temperature increases to further than 30°C the tweezer starts to open and the FRET signal starts to go down. The melting temperature of the interacting region is quite low, 26°C, as noted earlier. At around the 60°C mark the FRET signal increases drastically, the assumption being that the whole system falls apart and the arms no longer add rigidity to the body of the tweezer by forming those relatively long double-stranded regions. The rigidity of the body prevented the two fluorophores from coming closer and producing FRET. The interesting aspect of this graph is that, the moment that azobenzenes are found in the tweezer, the stability of the whole system is highly increased. The FRET signal remains almost unchanged until

the whole system melts apart. The only seeming difference between pre- and post- UV irradiation tweezers is a lower initial FRET signal, the trend of the decrease in intensity being very similar. It could be that the irradiation source was not adequate for photoactuating the system or that the azobenzenes in the tweezer gave too much stability to the closed conformation. Before commenting further on this though, I will show the results of the study of the dynamics of the system in the fluorimeter.

To understand the range of variability of the FRET signal produced by the tweezer when closed and opened, the first fluorimeter experiment performed was on the control and azo tweezers and included the addition of the breaker strand. Since the breaker strand would forcibly open the tweezers I could see the expected decrease of FRET signal and compare it to the one caused by the UV irradiation. The curves can be seen in Figure 4.9.

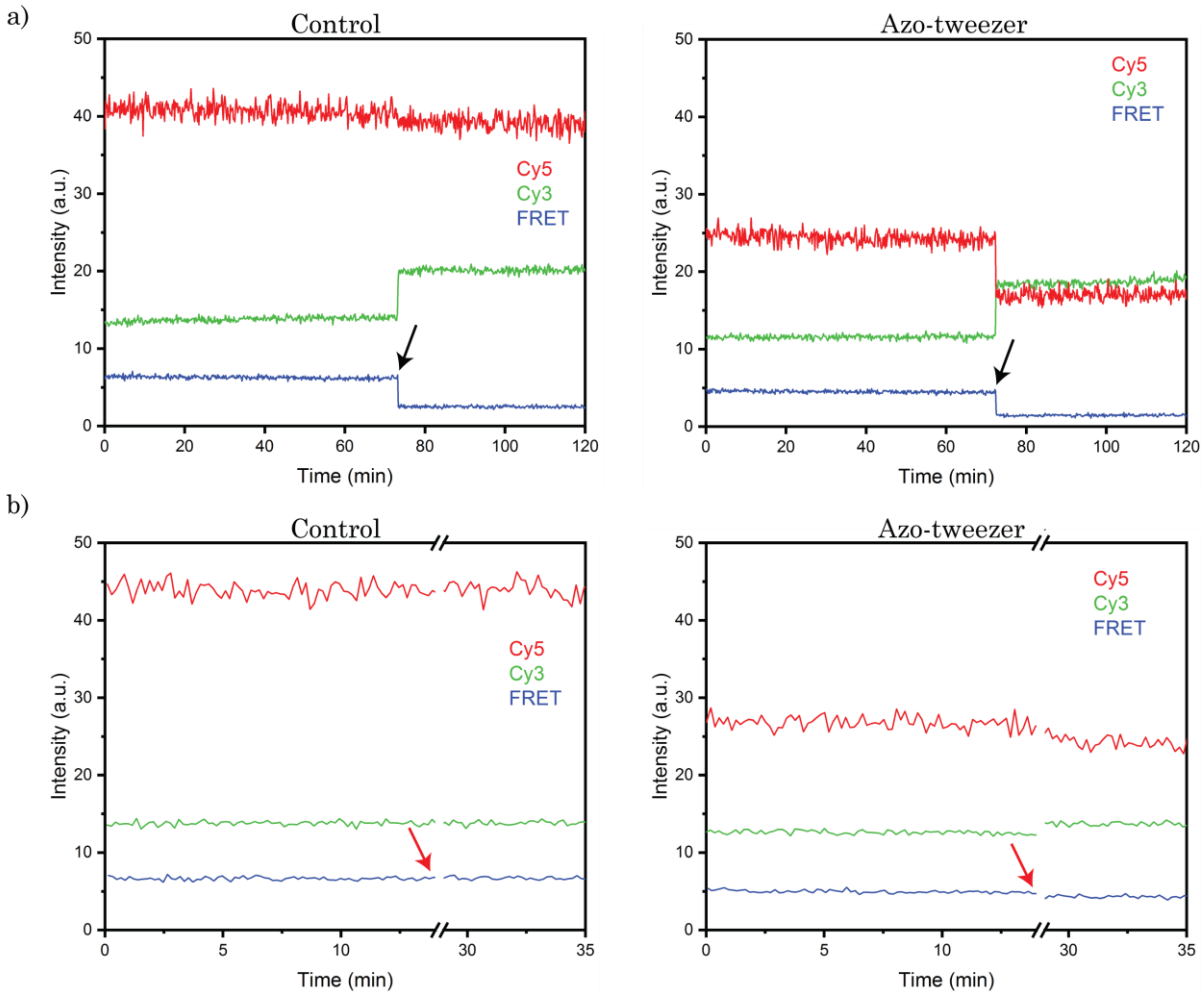

Figure 4.9. Fluorimeter measurements of the control tweezer and the azo-tweezer. a) Tweezers opening via TMSD with the breaker strand. The moment of the addition of the breaker is highlighted with a black arrow. b) Tweezers irradiated with UV light for 5 minutes at RT. The moment of the irradiation is highlighted with a red arrow.

The drop in the FRET signal (of a 68%) when the breaker strand was added to the azo-tweezers was almost instantaneous. In this case the tweezers were opened by TMSD at the point highlighted by the black arrows. The same change in the FRET signal after photoactuation was a 20% decrease in the azo-tweezers, the control tweezers were left unaffected after the irradiation. The irradiation started at the point highlighted by the red arrows and lasted for 5 minutes, which went unrecorded by the fluorimeter, hence the break in the axis. The efficiency of the photoactuation was lower than the traditional chemical actuation but it showed promise of being an alternative to TMSD. In order to

improve on the efficiency on the system, the different parameters involved in the experiment were revised.

Ultimately, the wavelength of the UV lamp (365 nm) was not adequate and that ended up being the main reason behind the initial efficiency of the photoactuation system. But before reaching to this conclusion though, the main hypothesis I was working with was based on the fact that the azo-arm increased greatly the stability of the system, as seen in the melting curves of Figure 4.8. The tweezer was tightly closed and the efficiency of the trans-to-cis isomerization was compromised, and by extension so was the photoactuation of the tweezer. Many irradiations with variations of temperature (from RT to 50°C) and duration times (from 5 to 20 minutes) were done on the fluorimeter without producing positive results.

In an attempt to compromise this highly stable duplex I approached the issue from a design perspective. I introduced self-complementarity in the complementary arm, more specifically between the region interacting with the azo region of the azo-arm and another section. This would cause the complementary arm to present a 4 nt hairpin with the key

region of interaction of the tweezer hidden in the stem. See Figure 4.10 for a schematic representation of the sequence.

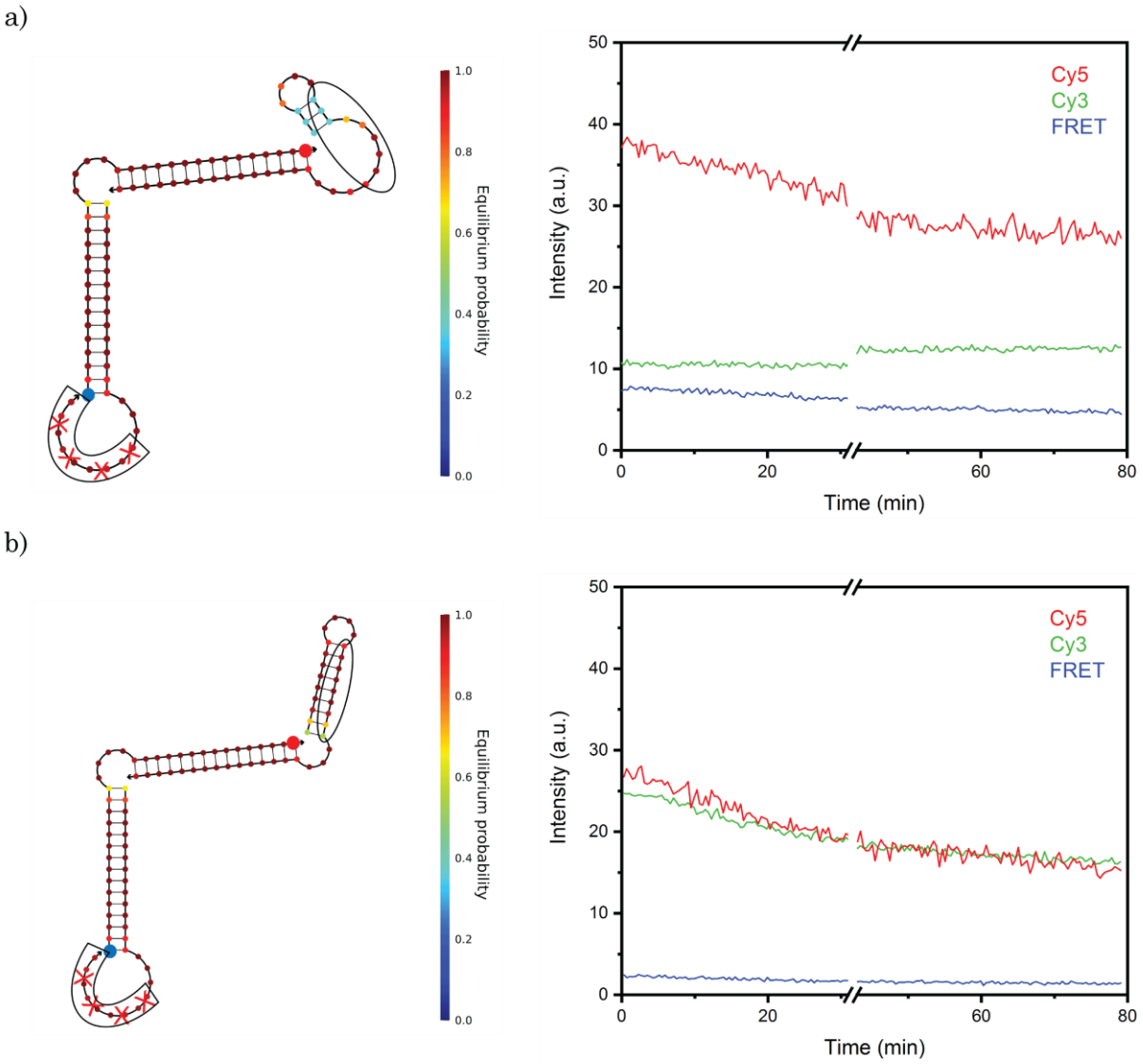

Figure 4.10. Hairpin-containing tweezers; red crosses mark the azobenzene locations, the red dot marks the Cy3 location, the blue dot marks the Cy5 location, the black outlines encompass the interacting regions of the tweezer. a) Tweezer with the weakest hairpin (3 nt-long), Nupack design and associated fluorimeter measurements. b) Tweezer with the strongest hairpin (9 nt-long), Nupack design and associated fluorimeter measurements.

The fluorimetry experiments that followed that used these hairpin-forming complementary arms did not show any substantial improvement in the photoactuation. In fact, only the weakest hairpins (3-5 nt-long stems) showed the minimal yield seen in the non-hairpin versions; the introduction of a strong hairpin completely killed the FRET slight decrease. A plausible explanation is that the hairpin strongly prevented the

interaction between the azo-arm and the complementary arm, leaving the tweezer open. Given the circumstances and the failure of the attempted changes, only one factor remained to be tested, the UV source.

As mentioned before, the wavelength of the UV lamp used thus far did not suit the photoactuation; a LED Driver for High-Power and Mounted LEDs (DC2200 LED driver, Thorlabs) with a Deep UV Mounted LED (M340L4, 340 nm, 60 mW, Thorlabs) were used in its stead from this point forward. A DYI opaque container with an appropriate holder for the fluorimeter cuvettes was produced. In this set-up the distance between the UV LED and the sample was 8 cm and the irradiance calculated to be 0.5 mW/cm^2, the same as in (207).

The fluorimeter measurements were repeated irradiating with the new UV set-up and under the conditions that had produced the best results in the first version of these tests. In these measurements the initial UV irradiation was followed up by a Vis light irradiation, completing a cycle of opening and closing the tweezer. The cycle was repeated within the same sample to study the capacity of the system to work multiple iterations (See Figure 4.11).

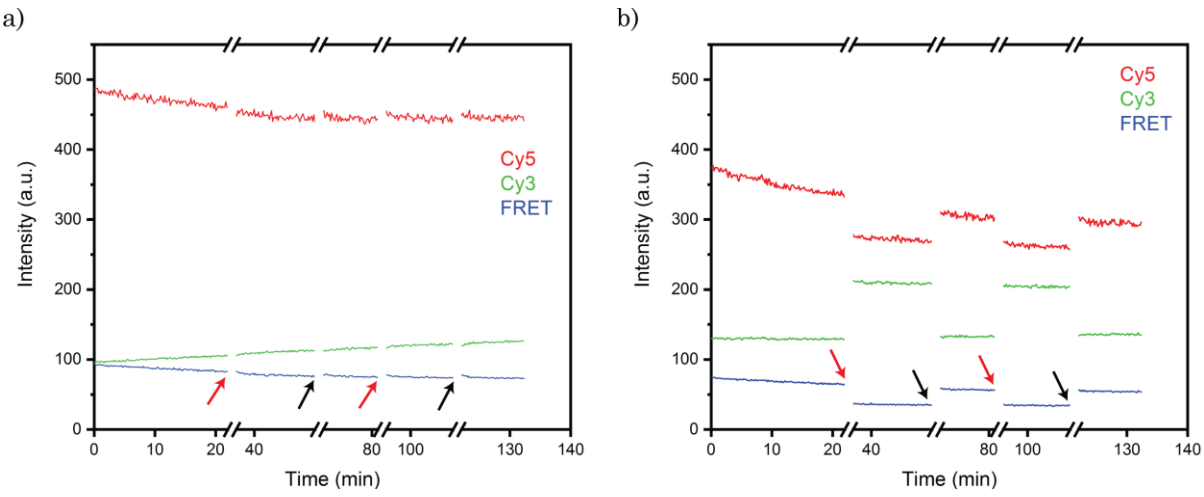

Figure 4.11. Fluorimeter measurement of tweezers (at 10x the usual concentrations) after cycled irradiations with the new UV source (red arrows) and a Vis light source (black

arrows). a) Control tweezer after 10 minute-long irradiation at RT. b) Azo-tweezer after 10 minute-long irradiation at RT

Before going over the results I would like to point out that, in this fluorimetry measurement, as well as in others in this thesis, some of the signals present a downward trends over time that seems irrespective of the point in the photoactuation or the nature of the tweezer. My hypothesis is that this decrease in signal over time must be due to a combination of photobleaching of the fluorophores and their tendency to be stuck to the walls of the cuvette as time progresses.

The control tweezer was left unaffected regardless of the type of wavelength it was irradiated with. The azo-tweezer showed a remarkable improvement in its change of conformation when irradiated with the new LED, achieving a decrease in the FRET signal of 45%. Thes system also showed the capability of switching between states with ease and maintained efficiency over time and opening cycles. This results are very encouraging as they prove that photoactuation can reach a functional level of strand displacement in the system studied, providing therefore a viable alternative to traditional TMSD for the actuation of the 1D/2D systems presented in this thesis, as well as other dynamic DNA origami structures.

Trying to improve the system, different temperatures (RT, 30°C, 40°C, 50°C), irradiation times (10, 15, 20 minutes), and combinations of the two were tested. As with the previous tests, RT was the best temperature for the system to work at; 20 minute-long irradiations with the new LED saw an improvement of 5% in the relative decrease of FRET when compared with the 10 minute-long irradiations.

Having reached the peak efficiency of the system, but having checked its viability as an actuation mechanism using strands and duplexes, like the ones in the 1D system, I decided to study another approach at further improving the photoactuated opening and closing of the tweezer. Going back with a design change, I wanted to see the effect on the

stability of the azo-containing duplex if I introduced mismatches at different positions, and in different numbers and distributions, in the interacting region of the complementary arm. For this, I made 96 different versions of the azo-arm with different mismatches, assembled them into an equal number of different azo-tweezers, and I measured their decrease of the of the FRET signal post UV irradiation in a plate, using a plate reader. From these experiments the table in Figure 4.12 was made.

a)

1 Mismatch 2 Mismatches 3 Mismatches

A		27476,67	4446,00	14113,33	3589,33	4946,00	-12055,00	-17848,00	-11398,00	-7755,33	-16090,67	-10783,33
B	9701,00	9498,67	3721,33	12024,67	12154,33	18045,67	-12719,00	-12026,00	-20737,33	-17385,33	-10848,00	-12023,00
C	10181,67	24242,00	3889,67	6431,00	4760,33	4748,33	-2972,67	-7614,33	-13916,00	-15144,00	-13473,33	-9919,33
	5491,33	4243,33	5868,00	1312,67	3950,00	1421,67	-9313,00	-14458,33	-7260,33	-12595,00	-7580,67	-8260,33
E	-2203,33	-12323,00	-4530,33	36568,33	-13643,33	-3975,00	-19441,33	-21131,33	-31301,67	-26880,33	-27734,67	-1674,67
	4644,33	-19236,00	-18884,67	-9221,67	-11277,00	-6290,67	-17180,33	-22179,67	-23325,00	-5846,67	417,33	8894,00
	-3097,33	-8191,33	-12036,00	-6606,67	-2929,33	-2831,33	-13878,67	-18260,00	-17340,33	-10081,00	-11185,67	-477,00
	-1999,33	104,67	-4158,00	-5900,33	1259,00	7138,67	3492,00	2144,33	-1276,67	-1790,00	-5563,33	-45,67

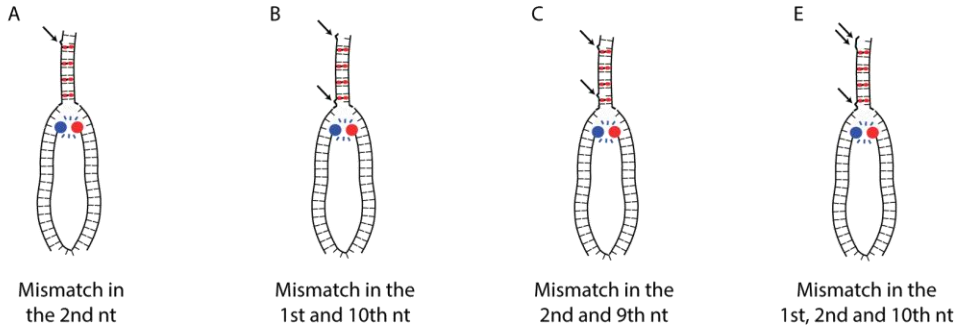

b)

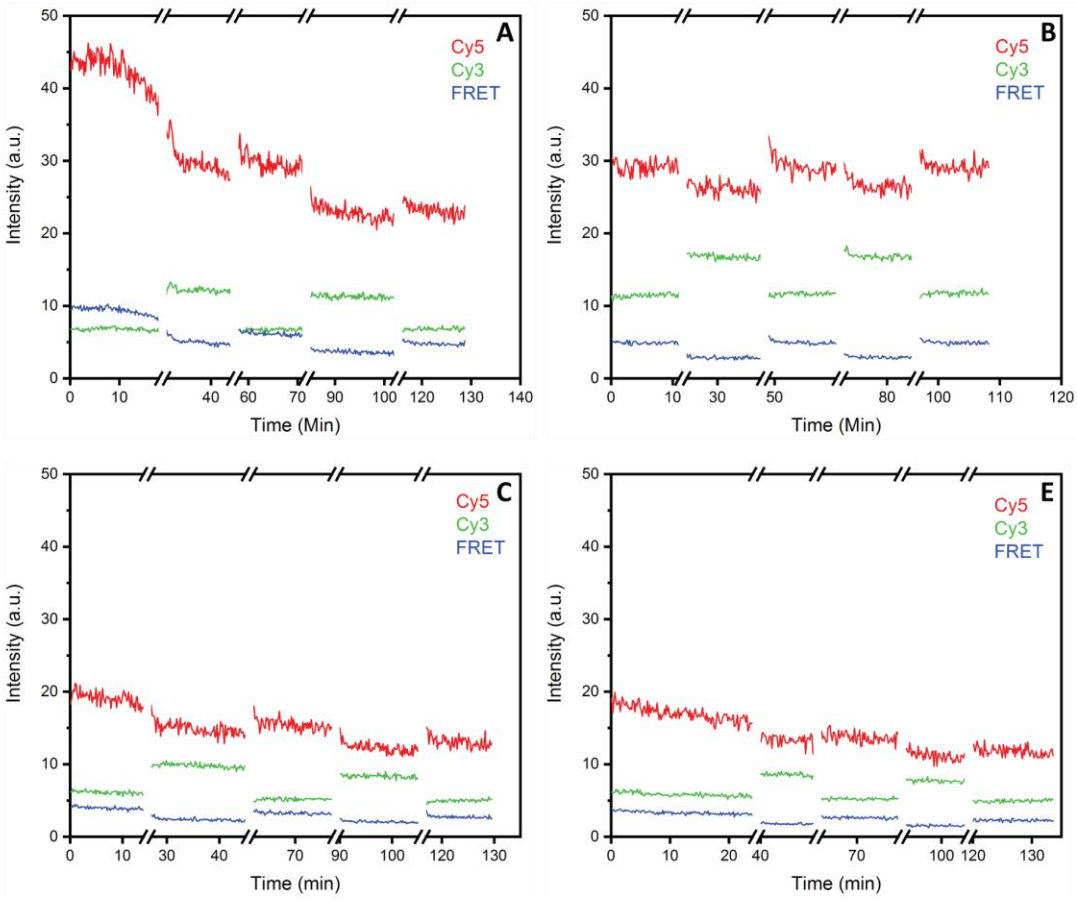

Figure 4.12. Mismatched azo-tweezers. a) Table of values of decrease of FRET signal after UV irradiation. In varying shades of green the tweezers with the mismatches that caused a decrease in FRET, in varying shades of white and red those mismatches that did not. Included below are the schematics of the shortlisted mismatched tweezers. b) Fluorimeter measurements of the shortlisted, mismatched tweezers outlined in a).

The values in the table represent the average (n=3) of the value of the decrease in FRET signal from the different mismatched azo-tweezers after UV irradiation. The higher the value, the greater efficiency at opening the tweezer. From this table the four best performing, mismatched tweezers were measured in the fluorimeter. The common pattern between these mismatched complementary arms was that they were placed at the edges of the interacting region. The graphs show that the decrease in the FRET signal is not more efficient in any of the shortlisted mismatched azo-tweezers; the best performing one, B, reached a relative decrease in the signal of 43%.

At this point I decided that, with the originally design azo-oligo, the observed FRET decrease of 50% was as the most efficient actuation that I could achieve with the azo-tweezer. Given how close it is to parity of actuation with the traditional TMSD, but lacking the drawbacks that this system presents and that have been limiting the efficiency of the structures' actuation throughout this thesis, particularly the 2D motion system, I believe that the photoactuation design hereby presented could be applied successfully in the functioning of said structures, offering an alternative and interesting venue for further development in the specifics of the actuation of these dynamic DNA origamis.

4.4 Conclusion and future perspectives for the design

Starting from an understanding on the possibilities and limitations of azobenzene as a molecule capable of driving strand displacement, and therefore actuation, in dynamic DNA structures, I developed an oligo that aimed counteract some of the drawbacks of this type of photoactuation. After some intermediate designs, the development of the azo-tweezer and its validation with fluorimetry showed the viability of using UV light and azobenzenes to drive DNA dehybridisation (50% efficiency as compared to 68% of

traditional TMSD). Following this, different design and parameter changes were introduced to try to further improve these efficiencies.

In the progression of the project I aimed at using photoactuation on the developed structures in this thesis, the following steps would consist on introducing the azobenzenes in a structure similar to the 1D rotaxane. Since the proposed system of movement described in the aim section of this chapter has a high level of complexity due to the modified azobenzenes, a simplified variation of the controlled diffusion would be necessary as a preliminary step when going using the rotaxane architecture.

In this preliminary version, instead of having a processive motor with three legs, a ratchet based on azobenzenes driving the change in potential between the stators could be designed (See Figure 4.13). The idea would be to control and drive the movement of a molecular motor by making use energy barriers and efforts "uphill", ratcheting (227).

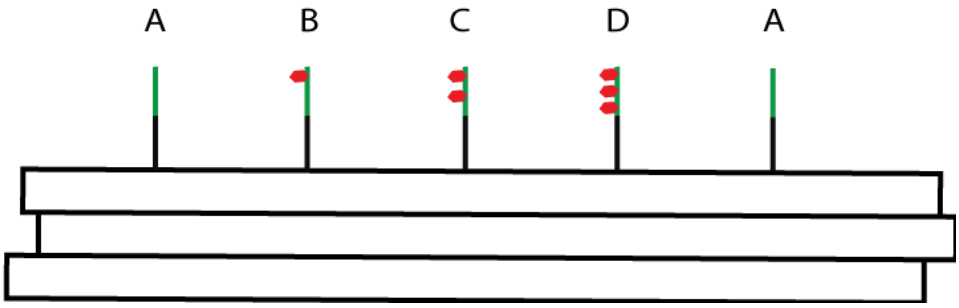

Figure 4.13. Hypothetical azo-ratchet system. In green the azo-containing sequence studied so far in the chapter; red rhombuses represent azobenzene groups.

A strand, an overhang coming from the slider in the rotaxane, could be attached anywhere and therefore be diffusing between all A-D positions. Given that there is a gradient of the presence in azobenzenes and that these provide the duplexes with greater stability, the slider could diffuse preferentially towards the stator D. If this were to be the case, after irradiating the system with UV the complementarities would be inversed, the slider preferring the stator A. In this scenario the slider could diffuse backwards or forwards but an actuated movement would be produced. Since this is pure theoretical

guesswork about the behaviour of azo-oligos, what was proposed earlier could very well not be the case. As an initial test, the different components (all 4 different stators and the slider-overhang complementary sequence) and their interactions could be studied via PAGE gels and fluorimetry (if labelled).

Other types of ratchets could be devised as well if the previous one was based on faulty logic but the rationale would be that, if these type of azo-ratchets successfully actuate the diffusion of the slider on the rail upon UV/Vis light irradiation, it would be then worthwhile to attempt producing a multicolour-azobenzene actuation system capable of inducing precise stepping in a processive molecular motor.

Chapter 5

Conclusion

The focus of this thesis was the development of the dynamic DNA origami structures necessary for the production of a controlled motion, actuated chemically or photochemically. The overarching idea was to achieve first step in the development of more complex, specialized machines that could be used in atomically precise manufacturing (APM).

The use of DNA, and DNA origami as a synthesizing method was deliberate given the flexibility, precision, and ease-of-use of the material and the design technique. However, this system has drawbacks, particularly in the precision manufacturing sense and is unsustainable for the harsher environments of industrial production. The understanding is that this constitutes a first step towards establishing the ground rules for the design, which are in turn necessary to produce better suited structures out of better suited materials. Molecular additive manufacturing works in a sense very similar to a regular/3D printer but on the nanoscale; any set-up attempting such functionalities will require movement in at least 2D, movement that has to be externally actuated and precise in its deposition of the building material.

With this in mind, I first attempted to develop a 1D molecular motor capable of placing itself in specific locations along a track, using the rotaxane architecture. When this was achieved I took the system to the next stage by adding another axis of motion, producing a 2D system with the same actuation characteristics. While developing these systems, chemically actuated (via strand displacement), I also attempted to produce an alternative actuation system based on light as a driving motor for motion.

Many efforts and different technologies have been dedicated towards achieving atomically precise manufacturing, one of these being molecular additive manufacturing. Of this technique much has been discussed regarding feasibility and possible application, the multiple hurdles that need to be cleared for its implantation in industry, and how the proposed system of this thesis could fit in the growing field. The use of DNA as a building block of choice, with its material idiosyncrasies, is prompted by the ease of design and synthesis that DNA origami provides. The nature of these DNA structures is dynamic, and exist within the realm of molecular motors. These elements are widely present in the natural world and about them much has been studied, and much more remains to be understood if we are to be able to apply them into human-designed machines/processes. Within the scope of this thesis, the ultimate goal of this motion is the design of a system capable of locating precisely subunits that have the functionality of changing a source material by addition of chemical element, acting as a molecular printer of sorts, that is in line with the MAM principles explained beforehand.

Once having set the framework and the direction that the work will take, I designed and produced the 1D system. Initially based on an example from the literature (87), the characterisation and assembly of the goal structure, the rotaxane, took me through an iterative process on the initial design. After a complete overhaul of the system, the new dedicated design suited better the desired functionalities, the controlled diffusion of the slider along the rail and its verification. Ultimately I produced a 1D motion system, based on the rotaxane architecture, with three attaching points that can be occupied after the introduction of the specific set of strands or "orders". The yield of this design was of 43% and had a highly efficient attaching mechanism with efficiencies of around 80% when performing a single attachment.

Taking the lessons learned during the design of the 1D system, and its actuation mechanism, I developed a 2D system based on a so called "Bow-and-Arrow" (BA)

architecture. In this system one axis of motion was almost exactly as the 1D one, a traditional rotaxane located in what would constitute the nocked arrow in the BA simile, but with an improved actuation. The remaining axis of motion was a radial one, going along the arc traced by the bow. Given the additional levels of difficulty related to the design, it was only after 3 iterations of different scaffold routings that a working structure could be produced with enough success to be actuated 2-dimensionally. The forces and strain imposed on the structures' scaffold routing showed necessary balance to be achieved between a robust and durable design, with multiple crossovers of staples for added stability, and a system flexible enough to be able to dissipate the strain of bent regions without breaking or fraying in sections. Overall, the yield of the final iteration of the complete 2D system reached ~65%

The actuation and the verification of the final system showed and efficiency of 66% for the attachment/detachment of the arrow, and an efficiency of 36% for the attachment/detachment of the MicroSlider. The combination of both axis of displacement showed, for a chosen position, an efficiency of 21% when doing all steps in solution and characterizing with TEM. An important aspect of this set of experiments is that 25% of all structures had failed the 2D motion in the last step, which in these conditions is the most compromised given the excess of strands and waste complexes in solution. In the favorable conditions of a flow chamber, different positions were studied, showing an average efficiency of 2D motion of 45% (with the exception of one of the positions). Although this study was not as thorough as to cover all possible positions in the 2D system, it demonstrated robust yields of actuation and set an interesting architecture to be used in the deposition or printing of molecular components on a surface with precision in the molecular scale. The following steps in this line of research would be the development of possible systems that would introduce a change on a substrate, locally, wherever the actuated section or write-head were to be positioned. These systems could be DNA-based

and dependent on further introduction of sequences that would act as an "ink" in this printing event, but they need not be limited to it. Adding in restriction enzymes, polymerases, or even click chemistries could widen and make exciting headways in the possibilities this system creates.

Lastly, I explored the parallel line of research I did while working in the 1D & 2D systems. In this line I experimented with the photochrome azobenzene as a source for inducing strand displacement (actuation in the motion systems) with the use of light. The use of a photochrome, even when as common place as azobenzene, is not exempt of technical considerations for its inclusion in dynamic DNA systems. With this in mind, I designed an azo-oligo to be used in a variety of set-ups to test its efficiency, ultimately obtaining highly encouraging results (50% efficiency) on a tweezer-like structure whose opening and closing was controlled via visible light and UV irradiations, almost reaching parity of effectiveness with the well-stablished TMSD (68% efficiency). From these results I drew future plans for how can they be included in architectures, such as mine, to be the source of motion, some of which included the use of different, chemically-modified azobenzenes with varying actuation wavelengths that could be used orthogonally to drive and closely manipulate a system's actuation.

Bibliography

1. Fang F, Zhang N, Guo D, Ehmann K, Cheung B, Liu K, et al. Towards atomic and close-to-atomic scale manufacturing. International Journal of Extreme Manufacturing. 2019;1(1):012001.

2. Chen L, Wen J, Zhang P, Yu B, Chen C, Ma T, et al. Nanomanufacturing of silicon surface with a single atomic layer precision via mechanochemical reactions. Nature Communications. 2018 Dec 1;9(1).

3. Luo Q, Hou C, Bai Y, Wang R, Liu J. Protein Assembly: Versatile Approaches to Construct Highly Ordered Nanostructures. Vol. 116, Chemical Reviews. American Chemical Society; 2016. p. 13571–632.

4. de Santis E, Ryadnov MG. Peptide self-assembly for nanomaterials: The old new kid on the block. Vol. 44, Chemical Society Reviews. Royal Society of Chemistry; 2015. p. 8288–300.

5. Habibi N, Kamaly N, Memic A, Shafiee H. Self-assembled peptide-based nanostructures: Smart nanomaterials toward targeted drug delivery. Vol. 11, Nano Today. Elsevier B.V.; 2016. p. 41–60.

6. Eskandari S, Guerin T, Toth I, Stephenson RJ. Recent advances in self-assembled peptides: Implications for targeted drug delivery and vaccine engineering. Vols. 110–111, Advanced Drug Delivery Reviews. Elsevier B.V.; 2017. p. 169–87.

7. McKee ML, Milnes PJ, Bath J, Stulz E, Turberfield AJ, O'Reilly RK. Multistep DNA-Templated Reactions for the Synthesis of Functional Sequence Controlled Oligomers. Angewandte Chemie. 2010;122(43):8120–3.

8. O'Reilly RK, Turberfield AJ, Wilks TR. The Evolution of DNA-Templated Synthesis as a Tool for Materials Discovery. Accounts of Chemical Research. 2017;50(10):2496–509.

9. Pinheiro A v., Han D, Shih WM, Yan H. Challenges and opportunities for structural DNA nanotechnology. Vol. 6, Nature Nanotechnology. Nature Publishing Group; 2011. p. 763–72.

10. Oura K, Lifshits VG, Saranin AA, Zotov A v, Katayama M. Surface science: an introduction. Springer Science & Business Media; 2013.

11. Eigler DM, Schweizer EK. Positioning single atoms with a scanning tunnelling microscope. Nature. 1990;344(April):524–6.

12. Hla SW. Atom-by-atom assembly. Vol. 77, Reports on Progress in Physics. Institute of Physics Publishing; 2014.

13. Willke P, Bae Y, Yang K, Lado JL, Ferrón A, Choi T, et al. Hyperfine interaction of individual atoms on a surface. Science (1979). 2018 Oct 19;362(6412):336–9.

14. Fuechsle M, Miwa JA, Mahapatra S, Ryu H, Lee S, Warschkow O, et al. A single-atom transistor. Nature Nanotechnology. 2012;7(4):242–6.

15. Fuechsle M, Mahapatra S, Zwanenburg FA, Friesen M, Eriksson MA, Simmons MY. Spectroscopy of few-electron single-crystal silicon quantum dots. Nature Nanotechnology. 2010;5(7):502–5.

16. Weber B, Mahapatra S, Watson TF, Simmons MY. Engineering independent electrostatic control of atomic-scale (∼4 nm) silicon double quantum dots. Nano Letters. 2012 Aug 8;12(8):4001–6.

17. Custance O, Perez R, Morita S. Atomic force microscopy as a tool for atom manipulation. Nature Nanotechnology. 2009;4(12):803–10.

18. Binnig G, Quate CF, Gerber C. Atomic Force Microscope. Physical Review Letters. 1986;56(9):930–3.

19. Giessibl FJ. Advances in atomic force microscopy. Reviews of Modern Physics. 2003;75(3):949–83.

20. Guo D, Xie G, Luo J. Mechanical properties of nanoparticles: Basics and applications. Vol. 47, Journal of Physics D: Applied Physics. 2014.

21. Sugimoto. Yoshiaki, Pou P, Custance O, Jelinek P, Abe M, Perez R, et al. Complex Patterning by Vertical Interchange Atom Manipulation Using Atomic Force Microscopy. Science (1979). 2008 Oct 17;322(October):413–7.

22. Pennycook S, Varela M, Chisholm M, Borisevich A, Lupini A, Benthem K van, et al. Scanning transmission electron microscopy of nanostructures. In: Narlikar A v., Fu YY, editors. The Oxford Handbook of Nanoscience and Nanotechnology. First. 2010. p. 205–48.

23. Susi T, Kotakoski J, Kepaptsoglou D, Mangler C, Lovejoy TC, Krivanek OL, et al. Silicon-carbon bond inversions driven by 60-kev electrons in graphene. Physical Review Letters. 2014 Sep 12;113(11).

24. Susi T, Kepaptsoglou D, Lin YC, Ramasse QM, Meyer JC, Suenaga K, et al. Towards atomically precise manipulation of 2D nanostructures in the electron microscope. Vol. 4, 2D Materials. IOP Publishing Ltd; 2017.

25. Drexler E. Productive nanosystems: the physics of molecular fabrication. Phys Educ [Internet]. 2005;40(4):339–46. Available from: www.iop.org/journals/physed

26. Drexler KE. Engines of Creation. 1986.

27. Drexler KE, Benton SA. Molecular Machinery, Manufacturing with Applications to Computation. Interdisciplinary Science. 1979;(1977).

28. Kuhlman B, Dantas G, Ireton GC, Varani G, Stoddard BL, Baker D. Design of a Novel Globular Protein Fold with Atomic-Level Accuracy. Science (1979) [Internet]. 2003;302. Available from: www.sciencemag.org

29. Huang PS, Boyken SE, Baker D. The coming of age of de novo protein design. Vol. 537, Nature. Nature Publishing Group; 2016. p. 320–7.

30. Courbet A, Hansen J, Hsia Y, Bethel N, Park YJ, Xu C, et al. Computational design of mechanically coupled axle-rotor protein assemblies. Science (1979) [Internet]. 2022;383–90. Available from: https://www.science.org

31. Boyken S, Baker D, Chen Z, Quijano Rubio A, P.King N, C.Klima J, et al. Publication Classification (54) DE NOVO DESIGN OF TUNABLE PH-DRIVEN CONFORMATIONAL SWITCHES. 2022.

32. Smalley RE. Of chemistry, love and nanobots. Sci Am. 2001;285(3):68.

33. Lee HJ, Ho W. Single-Bond Formation and Characterization with a Scanning Tunneling Microscope. Science (1979). 1999;286(November):1719–22.

34. Lyding JW, Hess K, Abeln GC, Thompson DS, Moore JS, Hersam MC, et al. Ultrahigh vacuum-scanning tunneling microscopy nanofabrication and hydrogen/deuterium desorption from silicon surfaces: Implications for complementary metal oxide semiconductor technology. Applied Surface Science. 1998;130–132:221–30.

35. Lauhon LJ, Ho W. Inducing and observing the abstraction of a single hydrogen atom in bimolecular reactions with a scanning tunneling microscope. Journal of Physical Chemistry B. 2001;105(18):3987–92.

36. Drexler KE, Forrest D, Freitas RA, Hall JS, Jacobstein, Neil McKendree T, Merkle R, et al. On Physics, Fundamentals, and Nanorobots: A Rebuttal to Smalley's Assertion that Self-Replicating Mechanical Nanorobots Are Simply Not Possible. Institute for Molecular Manufacturing; 2001.

37. Baum R. Drexler and Smalley make the case for and against "molecular assemblers." Chemical and Engineering News. 2003;37–42.

38. National Research Council. A Matter of Size: Triennial Review of the National Nanotechnology Initiative [Internet]. Washington, DC: The National Academies Press; 2006. Available from: https://www.nap.edu/catalog/11752/a-matter-of-size-triennial-review-of-the-national-nanotechnology

39. Fang F. Atomic and close-to-atomic scale manufacturing: Perspectives and measures. Vol. 2, International Journal of Extreme Manufacturing. IOP Publishing Ltd; 2020.

40. Bakke JR, Pickrahn KL, Brennan TP, Bent SF. Nanoscale Nanoengineering and interfacial engineering of photovoltaics by atomic layer. 2011;

41. Wu JY, Tzou SF, Liang CW, Chen IC. Characteristics of HfZrO x Gate Stack Engineering for Reliability Improvement on 28nm HK / MG CMOS Technology. IEEE Xplore. 2012;7–8.

42. Fang FZ, Zhang XD, Gao W, Guo YB, Byrne G, Hansen HN. Nanomanufacturing—Perspective and applications. CIRP Annals - Manufacturing Technology. 2017;66(2):683–705.

43. Battelle Memorial Institute, Foresight Nanotech Institute. Productive nanosystems: A technology roadmap. 2007.

44. Ruess FJ, Oberbeck L, Simmons MY, Goh KEJ, Hamilton AR, Hallam T, et al. Toward Atomic-Scale Device Fabrication in Silicon Using Scanning Probe Microscopy. 2004;(ii).

45. Koch K, Bhushan B, Jung YC, Barthlott W. Fabrication of artificial Lotus leaves and significance of hierarchical structure for superhydrophobicity and low adhesion. Soft Matter. 2009;5(7):1386–93.

46. Geim AK, Dubonos S v., Grigorieva I v., Novoselov KS, Zhukov AA, Shapoval SY. Microfabricated adhesive mimicking gecko foot-hair. Nature Materials. 2003;2(7):461–3.

47. Song YM, Xie Y, Malyarchuk V, Xiao J, Jung I, Choi KJ, et al. Digital cameras with designs inspired by the arthropod eye. Nature. 2013;497(7447):95–9.

48. Despont M, Brugger J, Drechsler U, Dürig U, Häberle W, Lutwyche M, et al. VLSI-NEMS chip for parallel AFM data storage. Sensors and Actuators, A: Physical. 2000;80(2):100–7.

49. Schafmeister CE, Brown ZZ, Gupta S. Shape-programmable macromolecules. Accounts of Chemical Research. 2008 Oct;41(10):1387–98.

50. Yakovchuk P, Protozanova E, Frank-Kamenetskii MD. Base-stacking and base-pairing contributions into thermal stability of the DNA double helix. Nucleic Acids Research. 2006;34(2):564–74.

51. Wilkins MHF, Stokes AR, Wilson HR. Molecular Structure of Deoxypentose Nucleic Acids. Nature. 1953;171(2):738–40.

52. Franklin RK, Gossling RG. Molecular Configuration in Sodium Thymonucleate. Nature [Internet]. 1953;171(2):740–1. Available from: https://www.nature.com/articles/171740a0.pdf

53. Crick F, Watson J. Molecular Structure of Nucleic Acids. Nature. 1953;171(2):737–8.

54. Seeman NC. Nucleic acid junctions and lattices. Journal of Theoretical Biology. 1982;99(2):237–47.

55. Hagerman PJ. Flexibility of DNA. Annu Rev Biophys Biophys Chem. 1988;17:265–86.

56. Smith SB, Cui Y, Bustamante C. Overstretching B-DNA : The Elastic Response of Individual Double-Stranded and Single- Stranded DNA Molecules Published by : American Association for the Advancement of Science Stable URL : http://www.jstor.org/stable/2889889. Science (1979). 1996;271(5250):795–9.

57. Caruthers MH, Barone AD, Beaucage SL, Dodds DR, Fisher EF, McBride LJ, et al. Chemical Synthesis of Deoxyoligonucleotides by the Phosphoramidite Method. Methods in Enzymology. 1987;154(C):287–313.

58. Carr PA, Church GM. Genome engineering. Nature Biotechnology [Internet]. 2009;27(12):1151–62. Available from: http://dx.doi.org/10.1038/nbt.1590

59. Mueller S, Coleman JR, Wimmer E. Putting Synthesis into Biology: A Viral View of Genetic Engineering through De Novo Gene and Genome Synthesis. Chemistry and Biology [Internet]. 2009;16(3):337–47. Available from: http://dx.doi.org/10.1016/j.chembiol.2009.03.002

60. Winfree E, Liu F, Wenzler LA, Seeman NC. Design and self-assembly of two-dimensional DNA crystals. Nature. 1998;394:539–44.

61. Rothemund PWK, Ekani-nkodo A, Papadakis N, Kumar A, Fygenson DK, Winfree E. Design and Characterization of Programmable DNA Nanotubes. J Am Chem Soc. 2004;(20):16344–52.

62. Yan H, Park SH, Finkelstein G, Reif JH, Labean TH. DNA-Templated Self-Assembly of Protein Arrays and Highly Conductive Nanowires. Science (1979). 2003;301(September):1882–5.

63. Chen J, Seeman NC. Synthesis from DNA of a molecule with the connectivity of a cube. Nature. 1991;350(April):3783–5.

64. Goodman RP, Berry RM, Turberfield AJ. The single-step synthesis of a DNA tetrahedron. Chemical Communications. 2004;44(February):1372–3.

65. Goodman RP, Schaap IAT, Tardin CF, Erben CM. Rapid Chiral Assembly of Rigid DNA Building Blocks for Molecular Nanofabrication. 2005;10611(December):1661–6.

66. Malo J, Mitchell JC, Vønien- C, Harris JR, Wille H, Sherratt DJ, et al. Engineering a 2D Protein–DNA Crystal. Angewandte Chemie. 2005;117:3117–21.

67. He Y, Ye T, Su M, Zhang C, Ribbe AE, Jiang W, et al. Hierarchical self-assembly of DNA into symmetric supramolecular polyhedra. 2008;452(March):198–202.

68. Rothemund PWK. Folding DNA to create nanoscale shapes and patterns. Nature. 2006;440(7082):297–302.

69. Dey S, Fan C, Gothelf K v., Li J, Lin C, Liu L, et al. DNA origami. Nature Reviews Methods Primers. 2021 Dec;1(1).

70. Han D, Pal S, Nangreave J, Deng Z, Liu Y, Yan H. DNA Origami with Complex Curvatures in Three-Dimensional Space. Science (1979). 2011;332(April):342–7.

71. Douglas SM, Dietz H, Liedl T, Högberg B, Graf F, Shih WM. Self-assembly of DNA into nanoscale three-dimensional shapes. Nature. 2009;459(May):414–8.

72. Douglas SM, Marblestone AH, Teerapittayanon S, Vazquez A, Church GM, Shih WM. Rapid prototyping of 3D DNA-origami shapes with caDNAno. Nucleic Acids Research. 2009;37(15):5001–6.

73. Ke Y, Douglas SM, Liu M, Sharma J, Cheng A, Leung A, et al. Multilayer DNA Origami Packed on a Square Lattice. 2009;(6):15903–8.

74. Castro CE, Kilchherr F, Kim D nyun, Shiao EL, Wauer T, Wortmann P, et al. A primer to scaffolded DNA origami. Nat Methods. 2011;8(3):221–9.

75. Poppleton E, Bohlin J, Sulc P, Matthies M, Sharma S, Zhang F. Design , optimization and analysis of large DNA and RNA nanostructures through interactive visualization , editing and molecular simulation. Nucleic Acids Res. 2020;48(12):1–12.

76. Snodin BEK, Randisi F, Mosayebi M, Šulc P, Schreck JS, Romano F, et al. Introducing improved structural properties and salt dependence into a coarse-grained model of DNA. Journal of Chemical Physics. 2015 Jun 21;142(23).

77. Ke Y, Sharma J, Liu M, Jahn K, Liu Y, Yan H. Scaffolded DNA Origami of a DNA Tetrahedron Molecular Container. Nano Letters. 2009;9(6):2445–7.

78. Andersen ES, Dong M, Nielsen MM, Jahn K, Subramani R, Mamdouh W, et al. Self-assembly of a nanoscale DNA box with a controllable lid. Nature. 2009;459(7243):73–6.

79. Meng W, Muscat RA, McKee ML, Milnes PJ, El-Sagheer AH, Bath J, et al. An autonomous molecular assembler for programmable chemical synthesis. Nature Chemistry. 2016;8(6):542–8.

80. Muscat RA, Bath J, Turberfield AJ. A programmable molecular robot. Nano Letters. 2011;11(3):982–7.

81. Wollman AJM, Sanchez-Cano C, Carstairs HMJ, Cross RA, Turberfield AJ. Transport and self-organization across different length scales powered by motor proteins and programmed by DNA. Nature Nanotechnology. 2014;9(1):44–7.

82. Schafmeister CE, Brown ZZ, Gupta S. Shape-Programmable Macromolecules. Accounts of Chemical Research. 2008;41(10):1387–98.

83. Seeman NC. Structural DNA Nanotechnology. In: Rosenthal SJ, Wright DW, editors. NanoBiotechnology Protocols. Totowa, NJ: Humana Press; 2005. p. 143–66.

84. Turberfield AJ, Mitchell JC, Yurke B, Mills AP, Blakey MI, Simmel FC. DNA Fuel for Free-Running Nanomachines. Physical Review Letters. 2003;90(11):4.

85. Ogura Y, Onishi A, Nishimura T, Tanida J. Optically controlled release of DNA based on nonradiative relaxation process of quenchers. Biomedical Optics Express. 2016;7(6):2142.

86. Marras AE, Zhou L, Su HJ, Castro CE. Programmable motion of DNA origami mechanisms. Proceedings of the National Academy of Sciences [Internet]. 2015;112(3):713–8. Available from: http://www.pnas.org/lookup/doi/10.1073/pnas.1408869112

87. List J, Falgenhauer E, Kopperger E, Pardatscher G, Simmel FC. Long-range movement of large mechanically interlocked DNA nanostructures. Nature Communications. 2016;7:1–7.

88. Ke Y, Ong LL, Shih WM, Yin P. Three-dimensional structures self-assembled from DNA bricks. Science (1979). 2012;338(6111):1177–83.

89. Ke Y, Ong LL, Sun W, Song J, Dong M, Shih WM, et al. DNA brick crystals with prescribed depths. Nat Chem. 2014;6(11):994–1002.

90. Andersen ES, Dong M, Nielsen MM, Jahn K, Subramani R, Mamdouh W, et al. Self-assembly of a nanoscale DNA box with a controllable lid. Nature. 2009;459(May):1–5.

91. Kuzuya A, Komiyama M. Design and construction of a box-shaped 3D-DNA origami. Chemical Communications. 2009;(28):4182–4.

92. Zadegan RM, Jepsen MDE, Thomsen KE, Okholm AH, Schaffert DH, Andersen ES, et al. Construction of a 4 Zeptoliters switchable 3D DNA box origami. ACS Nano. 2012;6(11):10050–3.

93. Douglas SM, Bachelet I, Church GM. A Logic-Gated Nanorobot for Targeted Transport of Molecular Payloads. Science (1979). 2012;335(6070):831–4.

94. Kosuri P, Altheimer BD, Dai M, Yin P, Zhuang X. Rotation tracking of genome-processing enzymes using DNA origami rotors. Nature. 2019;572(7767):136–40.

95. Tomaru T, Suzuki Y, Kawamata I, Nomura SIM, Murata S. Stepping operation of a rotary DNA origami device. Chemical Communications. 2017;53(55):7716–9.

96. Lauback S, Mattioli KR, Marras AE, Armstrong M, Rudibaugh TP, Sooryakumar R, et al. Real-time magnetic actuation of DNA nanodevices via modular integration with stiff micro-levers. Nature Communications [Internet]. 2018;9(1). Available from: http://dx.doi.org/10.1038/s41467-018-03601-5

97. Kuzyk A, Urban MJ, Idili A, Ricci F, Liu N. Selective control of reconfigurable chiral plasmonic metamolecules. Science Advances. 2017;3(4):1–7.

98. Kopperger E, List J, Madhira S, Rothfischer F, Lamb DC, Simmel FC. A self-assembled nanoscale robotic arm controlled by electric fields. Science (1979). 2018;359(January):296–301.

99. Wang F, Zhang X, Liu X, Fan C, Li Q. Programming Motions of DNA Origami Nanomachines. Small. 2019;15(26):1–10.

100. Marras AE, Zhou L, Kolliopoulos V, Su HJ, Castro CE. Directing folding pathways for multi-component DNA origami nanostructures with complex topology. New Journal of Physics. 2016;18(5).

101. Benson E, Marzo RC, Bath J, Turberfield AJ. Strategies for Constructing and Operating DNA Origami Linear Actuators. Small. 2021;17:2007704.

102. Magnasco MO. Molecular combustion motors. Physical Review Letters. 1994;72(16):2656–9.

103. Astumian RD. Thermodynamics and Kinetics of a Brownian Motor. Science (1979). 1997;276(May).

104. Schliwa M. Molecular Motors. 2003.

105. Saper G, Hess H. Synthetic Systems Powered by Biological Molecular Motors. Chemical Reviews. 2020;120(September):288–309.

106. Rayment I, Rypniewski WR, Schmidt-bdse K, Smith R, Tomchick DR, Benning MM, et al. Three-Dimensional Structure of A Molecular Motor. Science (1979). 1993;261(July):50–8.

107. Sindelar C V, Budny MJ, Rice S, Naber N, Fletterick R, Cooke R. Two conformations in the human kinesin power stroke defined by X-ray crystallography and EPR spectroscopy. Nature Structural Biology. 2002;9(11):844–8.

108. Schroer A, Disorders C, Hole W. The Role of Kinesin and Other Soluble Factors in Organelle Movement along Microtubules. The Journal of Cell Biology. 1988;107(November):1785–92.

109. Takatsuki H, Tanaka H, Rice KM. Transport of single cells using an actin bundle – myosin bionanomotor transport. Nanotechnology. 2011;22(April).

110. Groß H, Heil HS, Ehrig J, Schwarz FW, Hecht B, Diez S. Parallel mapping of optical near-field interactions by molecular motor-driven quantum dots. Nature Nanotechnology. 2018;13(August):691–6.

111. Lard M, Kumar S, Persson M, Linke H, Månsson A. Ultrafast molecular motor driven nanoseparation and biosensing. Biosensors and Bioelectronic. 2013;48:145–52.

112. Chaudhuri S, Korten T, Korten S, Milani G, Lana T, Diez S. Label-Free Detection of Microvesicles and Proteins by the Bundling of Gliding Microtubules. Nano Letters. 2018;18(December):117–23.

113. Nicolau D V, Lard M, Korten T, Delft FCMJM Van, Persson M, Bengtsson E. Parallel computation with molecular-motor-propelled agents in nanofabricated networks. Proceedings of the National Academy of Sciences. 2016;113(10):2591–6.

114. Shirai Y, Osgood AJ, Zhao Y, Kelly KF, Tour JM. Directional control in thermally driven single-molecule nanocars. Nano Letters. 2005;5(11):2330–4.

115. Simpson GJ, García-López V, Petermeier P, Grill L, Tour JM. How to build and race a fast nanocar. Nature Nanotechnology. 2017;12(7):604–6.

116. Ashton PR, Balzani V, Kocian O, Prodi L, Spencer N, Stoddart JF. A Light-Fueled " Piston Cylinder " Molecular-Level Machine. 1998;(12):11190–1.

117. Kay ER, Leigh DA, Zerbetto F. Synthetic molecular motors and mechanical machines. Vol. 46, Angewandte Chemie - International Edition. 2007. 72–191 p.

118. Stoddart JF. Mechanically Interlocked Molecules (MIMs)—Molecular Shuttles, Switches, and Machines (Nobel Lecture). Angewandte Chemie - International Edition. 2017;56(37):11094–125.

119. Bottari G, Leigh DA, Pérez EM. Chiroptical Switching in a Bistable Molecular Shuttle. J Am Chem Soc. 2003;125(44):13360–1.

120. Leigh DA, Morales MÁF, Pérez EM, Wong JKY, Saiz CG, Slawin AMZ, et al. Patterning through Controlled Submolecular Motion: Rotaxane-Based Switches and Logic Gates that Function in Solution and Polymer Films. Angewandte Chemie. 2005;117(20):3122–7.

121. Jiménez MC, Dietrich-Buchecker C, Sauvage JP. Towards synthetic molecular muscles: Contraction and stretching of a linear rotaxane dimer. Angewandte Chemie - International Edition. 2000;39(18):3284–7.

122. Pérez EM, Dryden DTF, Leigh DA, Teobaldi G, Zerbetto F. A generic basis for some simple light-operated mechanical molecular machines. J Am Chem Soc. 2004;126(39):12210–1.

123. Stoddart JF. Mechanically Interlocked Molecules (MIMs)—Molecular Shuttles, Switches, and Machines (Nobel Lecture). Angewandte Chemie - International Edition. 2017;56(37):11094–125.

124. Schill G, Luttringhaus A. The Preparation of Catena Compounds by Directed Synthesis [l]. Angew Chem, International. 1964;3(8):546–7.

125. Anelli PL, Spencer N, Stoddart JF. A molecular shuttle. J Am Chem Soc. 1991;113:5131–3.

126. Zhang L, Marcos V, Leigh DA. Molecular machines with bio-inspired mechanisms. Proc Natl Acad Sci U S A. 2018;115(38):9397–404.

127. Leigh DA, Wong JKY, Dehez F, Zerbetto F. Unidirectional rotation in a mechanically interlocked molecular rotor. Nature. 2003;424(6945):174–9.

128. Hernández J V., Kay ER, Leigh DA. A reversible synthetic rotary molecular motor. Science (1979). 2004;306(5701):1532–7.

129. Chatterjee MN, Kay ER, Leigh DA. Beyond switches: Ratcheting a particle energetically uphill with a compartmentalized molecular machine. J Am Chem Soc. 2006;128(12):4058–73.

130. Ragazzon G, Baroncini M, Silvi S, Venturi M, Credi A. Light-powered autonomous and directional molecular motion of a dissipative self-assembling system. Nature Nanotechnology. 2015;10(1):70–5.

131. Cheng C, McGonigal PR, Schneebeli ST, Li H, Vermeulen NA, Ke C, et al. An artificial molecular pump. Nature Nanotechnology. 2015;10(6):547–53.

132. Von Delius M, Geertsema EM, Leigh DA. A synthetic small molecule that can walk down a track. Nature Chemistry. 2010;2(2):96–101.

133. Barrell MJ, Campaña AG, Von Delius M, Geertsema EM, Leigh DA. Light-driven transport of a molecular walker in either direction along a molecular track. Angewandte Chemie - International Edition. 2011;50(1):285–90.

134. Simmel FC, Yurke B. Using DNA to construct and power a nanoactuator. Physical Review E - Statistical Physics, Plasmas, Fluids, and Related Interdisciplinary Topics. 2001;63(4):1–5.

135. Li JJ, Tan W. A Single DNA Molecule Nanomotor. Nano Letters. 2002;2(4):315–8.

136. Simmel FC, Yurke B. A DNA-based molecular device switchable between three distinct mechanical states. Applied Physics Letters. 2002;80(5):883–5.

137. Chen Y, Wang M, Mao C. An autonomous DNA nanomotor powered by a DNA enzyme. Angewandte Chemie - International Edition. 2004;43(27):3554–7.

138. Yurke B, Turber AJ, Jr APM, Simmel FC, Neumann JL. A DNA-fuelled molecular machine made of DNA. Nature. 2000;406(August):605–8.

139. Tian Y, Mao C. Molecular gears: A pair of DNA circles continuously rolls against each other. J Am Chem Soc. 2004;126(37):11410–1.

140. Wang C, Huang Z, Lin Y, Ren J, Qu X. Artificial DNA nano-spring powered by protons. Advanced Materials. 2010;22(25):2792–8.

141. Yurke B, Mills AP. Using DNA to Power Nanostructures. Vol. 4, Genetic Programming and Evolvable Machines. 2003.

142. Zhang DY, Winfree E. Control of DNA strand displacement kinetics using toehold exchange. J Am Chem Soc. 2009 Dec 2;131(47):17303–14.

143. Liu D, Bruckbauer A, Abell C, Balasubramanian S, Kang DJ, Klenerman D, et al. A reversible pH-driven DNA nanoswitch array. J Am Chem Soc. 2006;128(6):2067–71.

144. Mao C, Sun W, Shen Z, Seeman NC. A nanomechanical device based on the B±Z transition of DNA. Nature. 1999;397(January):144–6.

145. Tashiro R, Sugiyama H. A Nanothermometer Based on the Different π Stackings of B- and Z-DNA. Angewandte Chemie - International Edition. 2003;42(48):6018–20.

146. Sherman WB, Seeman NC. A precisely controlled DNA biped walking device. Nano Letters. 2004;4(7):1203–7.

147. Shin JS, Pierce NA. A synthetic DNA walker for molecular transport. J Am Chem Soc. 2004;126(35):10834–5.

148. Gu H, Chao J, Xiao SJ, Seeman NC. A proximity-based programmable DNA nanoscale assembly line. Nature. 2010;465(7295):202–5.

149. Wang C, Ren J, Qu X. A stimuli responsive DNA walking device. Chemical Communications. 2011;47(5):1428–30.

150. Yin P, Yan H, Daniell XG, Turberfield AJ, Reif JH. A unidirectional DNA walker that moves autonomously along a track. Angewandte Chemie - International Edition. 2004;43(37):4906–11.

151. Bath J, Green SJ, Turberfield AJ. A free-running DNA motor powered by a nicking enzyme. Angewandte Chemie - International Edition. 2005;44(28):4358–61.

152. Yin P, Choi HMT, Calvert CR, Pierce NA. Programming biomolecular self-assembly pathways. Nature. 2008;451(7176):318–22.

153. Green SJ, Bath J, Turberfield AJ. Coordinated Chemomechanical Cycles : A Mechanism for Autonomous Molecular Motion. Physical Review Letters. 2008;238101(December):20–3.

154. Omabegho T, Sha R, Seeman NC. A Bipedal DNA Brownian Motor with Coordinated Legs. Science (1979). 2009;324(April):67–71.

155. Tian Y, He Y, Chen Y, Yin P, Mao C. A DNAzyme that walks processively and autonomously along a one-dimensional track. Angewandte Chemie - International Edition. 2005;44(28):4355–8.

156. Muscat RA, Bath J, Turberfield AJ. Small molecule signals that direct the route of a molecular cargo. Small. 2012;8(23):3593–7.

157. Wickham SFJ, Bath J, Katsuda Y, Endo M, Hidaka K, Sugiyama H, et al. A DNA-based molecular motor that can navigate a network of tracks. Nature Nanotechnology. 2012;7(3):169–73.

158. Muscat RA, Bath J, Turberfield AJ. A programmable molecular robot. Nano Letters. 2011;11(3):982–7.

159. Han D, Pal S, Liu Y, Yan H. Folding and cutting DNA into reconfigurable topological nanostructures. Nature Nanotechnology. 2010;5(10):712–7.

160. Zhang F, Nangreave J, Liu Y, Yan H. Reconfigurable DNA origami to generate quasifractal patterns. Nano Letters. 2012;12(6):3290–5.

161. Wei B, Ong LL, Chen J, Jaffe AS, Yin P. Complex reconfiguration of DNA nanostructures. Angewandte Chemie - International Edition. 2014;53(29):7475–9.

162. Gerling T, Wagenbauer KF, Neuner AM, Dietz H. Dynamic DNA devices and assemblies formed by shape-complementary, non–base pairing 3D components. Science (1979). 2015;347(6229):1446–52.

163. Ketterer P, Willner EM, Dietz H. Nanoscale rotary apparatus formed from tight-fitting 3D DNA components. Science Advances. 2016;2(2):1–9.

164. Kopperger E, List J, Madhira S, Rothfischer F, Lamb DC, Simmel FC. A self-assembled nanoscale robotic arm controlled by electric fields. Science (1979). 2018;359(January):296–301.

165. Kuzyk A, Yang Y, Duan X, Stoll S, Govorov AO, Sugiyama H, et al. A light-driven three-dimensional plasmonic nanosystem that translates molecular motion into reversible chiroptical function. Nature Communications. 2016;7:1–6.

166. Yang Y, Tashiro R, Suzuki Y, Emura T, Hidaka K, Sugiyama H, et al. A Photoregulated DNA-Based Rotary System and Direct Observation of Its Rotational Movement. Chemistry - A European Journal. 2017;23(16):3979–85.

167. Anelli PL, Spencer N, Fraser Stoddart J. A Molecular Shuttle. J Am Chem Soc. 1991;113(13):5131–3.

168. Ackermann D, Schmidt TL, Hannam JS, Purohit CS, Heckel A, Famulok M. A double-stranded DNA rotaxane. Nat Nanotechnol. 2010;5:436–42.

169. Dunn KE, Dannenberg F, Ouldridge TE, Kwiatkowska M, Turberfield AJ, Bath J. Guiding the folding pathway of DNA origami. Nature. 2015;525(7567):82–6.

170. Agam G, Graiver D, Zilkha A. Studies on the Formation of Topological Isomers by Statistical Methods. J Chem Phys [Internet]. 1976;98(17):5206–14. Available from: https://pubs.acs.org/sharingguidelines

171. Wylie SR, Macartney DH. Self-Assembling Metal Rotaxane Complexes of alpha-Cyclodextrin. J Am Chem Soc. 1992;114(8):193–218.

172. Venkata T, Rao S, Lawrence DS. Self-Assembly of a Threaded Molecular Loop. J Am Chem Soc. 1990;112:3614–5.

173. Ogino H. Relatively High-Yield Syntheses of Rotaxanes. Syntheses and Properties of Compounds Consisting of Cyclodextrins Threaded by alpha, omega-Diaminoalkanes Coordinated to Cobalt(III) Complexes. J Am Chem Soc. 1981;103(5):1303–4.

174. Schill G, Zollenkopf H. Rotaxan-Verbindungen, 1'). Liebigs Ann Chem. 1969;721(1):53–74.

175. Ackermann D, Jester SS, Famulok M. Design strategy for DNA rotaxanes with a mechanically reinforced PX100 axle. Vol. 51, Angewandte Chemie - International Edition. 2012. p. 6771–5.

176. Lohmann F, Weigandt J, Valero J, Famulok M. Logic gating by macrocycle displacement using a double-stranded DNA [3]rotaxane shuttle. Angew Chem Int Ed Engl. 2014 Sep 22;53(39):10372–6.

177. Cecconello A, Lu CH, Elbaz J, Willner I. Au nanoparticle/DNA rotaxane hybrid nanostructures exhibiting switchable fluorescence properties. Nano Letters. 2013 Dec 11;13(12):6275–80.

178. Powell JT, Akhuetie-Oni BO, Zhang Z, Lin C. DNA Origami Rotaxanes: Tailored Synthesis and Controlled Structure Switching. Angewandte Chemie - International Edition. 2016 Sep 12;55(38):11412–6.

179. Li T, Lohmann F, Famulok M. Interlocked DNA nanostructures controlled by a reversible logic circuit. Nature Communications. 2014;5.

180. Lohmann F, Ackermann D, Famulok M. Reversible light switch for macrocycle mobility in a DNA rotaxane. J Am Chem Soc. 2012 Jul 25;134(29):11884–7.

181. Centola M, Valero J, Famulok M. Allosteric Control of Oxidative Catalysis by a DNA Rotaxane Nanostructure. J Am Chem Soc. 2017 Nov 15;139(45):16044–7.

182. Yu Z, Centola M, Valero J, Matthies M, Šulc P, Famulok M. A Self-Regulating DNA Rotaxane Linear Actuator Driven by Chemical Energy. J Am Chem Soc. 2021 Aug 25;143(33):13292–8.

183. Baltierra-Jasso LE, Morten MJ, Laflör L, Quinn SD, Magennis SW. Crowding-Induced Hybridization of Single DNA Hairpins. J Am Chem Soc. 2015 Dec 30;137(51):16020–3.

184. Kellis DL, Bui H, Kuang W, Graugnard E, Lee J, Hughes WL, et al. Effects of DNA Condensing Agents on DNA Nanostructures.

185. Feng B, Frykholm K, Nordén B, Westerlund F. DNA strand exchange catalyzed by molecular crowding in PEG solutions. Chemical Communications. 2010 Nov 21;46(43):8231–3.

186. Estévez-Torres A, Baigl D. DNA compaction: Fundamentals and applications. Vol. 7, Soft Matter. 2011. p. 6746–56.

187. Wagenbauer KF, Engelhardt FAS, Stahl E, Hechtl VK, Stçmmer P, Dietz H. How We Make DNA Origami. Available from: https://doi.org/10.1002/

188. Liu J, Li Q, Li M, Gao S, Liu C, Zou L, et al. Elliptical mirror-based TIRF microscopy with shadowless illumination and adjustable penetration depth. Optics Letters. 2017 Jul 1;42(13):2587.

189. Schnitzbauer J, Strauss MT, Schlichthaerle T, Schueder F, Jungmann R. Super-resolution microscopy with DNA-PAINT. Nature Protocols [Internet]. 2017;12(6):1198–228. Available from: http://dx.doi.org/10.1038/nprot.2017.024

190. Jungmann R, Avendaño MS, Woehrstein JB, Dai M, Shih WM, Yin P. Multiplexed 3D cellular super-resolution imaging with DNA-PAINT and Exchange-PAINT. Nature Methods. 2014;11(3):313–8.

191. Dietz H, Douglas SM, Shih WM. Folding DNA into twisted and curved nanoscale shapes supplementary information. Science (1979). 2009;325(5941):725–30.

192. Sengar A, Ouldridge TE, Henrich O, Rovigatti L, Šulc P. A Primer on the oxDNA Model of DNA: When to Use it, How to Simulate it and How to Interpret the Results. Vol. 8, Frontiers in Molecular Biosciences. Frontiers Media S.A.; 2021.

193. K Doye JP, Fowler H, Prešern D, Bohlin J, Rovigatti L, Romano F, et al. The oxDNA coarse-grained model as a tool to simulate DNA origami.

194. Snodin BEK, Romano F, Rovigatti L, Ouldridge TE, Louis AA, Doye JPK. Direct Simulation of the Self-Assembly of a Small DNA Origami. ACS Nano. 2016 Feb 23;10(2):1724–37.

195. Snodin BEK, Schreck JS, Romano F, Louis AA, Doye JPK. Coarse-grained modelling of the structural properties of DNA origami. Nucleic Acids Research. 2019 Feb 20;47(3):1585–97.

196. Benson E, Carrascosa Marzo R, Bath J, Turberfield AJ. Strategies for Constructing and Operating DNA Origami Linear Actuators. Small. 2021;2007704:1–8.

197. Funke JJ, Dietz H. Placing molecules with Bohr radius resolution using DNA origami. Nature Nanotechnology. 2016 Jan 1;11(1):47–52.

198. Fantoni NZ, El-Sagheer AH, Brown T. A Hitchhiker's Guide to Click-Chemistry with Nucleic Acids. Vol. 121, Chemical Reviews. American Chemical Society; 2021. p. 7122–54.

199. Omabegho T, Sha R, Seeman NC. A Bipedal DNA Brownian Motor with Coordinated Legs. Science (1979). 2009;(April):67–72.

200. Adam V, Prusty DK, Centola M, Škugor M, Hannam JS, Valero J, et al. Expanding the Toolbox of Photoswitches for DNA Nanotechnology Using Arylazopyrazoles. Chemistry - A European Journal. 2018;24(5):1062–6.

201. Roke D, Stuckhardt C, Danowski W, Wezenberg SJ, Feringa BL. Light-Gated Rotation in a Molecular Motor Functionalized with a Dithienylethene Switch. Angewandte Chemie - International Edition. 2018;57(33):10515–9.

202. Filatov M, Paolino M, Min SK, Kim KS. Fulgides as Light-Driven Molecular Rotary Motors: Computational Design of a Prototype Compound. Journal of Physical Chemistry Letters. 2018;9(17):4995–5001.

203. Wiedbrauk S, Dube H. Hemithioindigo-An emerging photoswitch. Tetrahedron Letters. 2015;56(29):4266–74.

204. Brieke C, Heckel A. Spiropyran photoswitches in the context of DNA: Synthesis and photochromic properties. Chemistry - A European Journal. 2013;19(46):15726–34.

205. Schmittel M, Pramanik S, De S. A reversible nanoswitch as an ON–OFF photocatalyst. Chemical Communications. 2012;48(96):11730–2.

206. Doi T, Kawai H, Murayama K, Kashida H, Asanuma H. Visible-Light-Triggered Cross-Linking of DNA Duplexes by Reversible [2+2] Photocycloaddition of Styrylpyrene. Chemistry - A European Journal. 2016;22(30):10533–8.

207. Liang X, Nishioka H, Takenaka N, Asanuma H. A DNA nanomachine powered by light irradiation. ChemBioChem. 2008;9(5):702–5.

208. Zhou M, Liang X, Mochizuki T, Asanuma H. A light-driven DNA nanomachine for the efficient photoswitching of RNA digestion. Angewandte Chemie - International Edition. 2010;49(12):2167–70.

209. Haydell MW, Centola M, Adam V, Valero J, Famulok M. Temporal and Reversible Control of a DNAzyme by Orthogonal Photoswitching. J Am Chem Soc. 2018;140(49):16868–72.

210. Beharry AA, Woolley GA. Azobenzene photoswitches for biomolecules. Chemical Society Reviews. 2011;40(8):4422–37.

211. Harm W. Biological effects of ultraviolet radiation. Cambridge University Press; 1980. 216 p.

212. Beharry AA, Sadovski O, Woolley GA. Azobenzene photoswitching without ultraviolet light. J Am Chem Soc. 2011;133(49):19684–7.

213. Dong M, Babalhavaeji A, Samanta S, Beharry AA, Woolley GA. Red-Shifting Azobenzene Photoswitches for in Vivo Use. Accounts of Chemical Research. 2015;48(10):2662–70.

214. Samanta S, Beharry AA, Sadovski O, McCormick TM, Babalhavaeji A, Tropepe V, et al. Photoswitching Azo compounds in vivo with red light. J Am Chem Soc. 2013;135(26):9777–84.

215. Nishioka H, Liang X, Kato T, Asanuma H. A photon-fueled DNA nanodevice that contains two different photoswitches. Angewandte Chemie - International Edition. 2012;51(5):1165–8.

216. Liang X, Mochizuki T, Asanuma H. A Supra-photoswitch Involving Sandwiched DNA Base Pairs and Azobenzenes for Light-Driven Nanostructures and Nanodevices. Small. 2009;5(15):1761–8.

217. Kou B, Guo X, Xiao S jun, Liang X. Highly Efficient Room-Temperature Photoresponsive DNA Tethering Azobenzene Through Backbone-Inserted Glycerol via Ether Bond. Small. 2013;(23):3939–43.

218. Kou B, Zhang J, Huai X, Liang X, Xiao SJ. Light-driven reversible strand displacement using glycerol azobenzene inserted DNA. RSC Advances. 2015;5(7):5055–8.

219. You M, Huang F, Chen Z, Wang RW, Tan W. Building a nanostructure with reversible motions using photonic energy. ACS Nano. 2012;6(9):7935–41.

220. Škugor M, Valero J, Murayama K, Centola M, Asanuma H, Famulok M. Orthogonally Photocontrolled Non-Autonomous DNA Walker. Angewandte Chemie - International Edition. 2019;58(21):6948–51.

221. Tanaka F, Mochizuki T, Liang X, Asanuma H, Tanaka S, Suzuki K, et al. Robust and photocontrollable DNA capsules using azobenzenes. Nano Letters. 2010;10(9):3560–5.

222. Yang Y, Tashiro R, Suzuki Y, Emura T, Hidaka K, Sugiyama H, et al. A Photoregulated DNA-Based Rotary System and Direct Observation of Its Rotational Movement. Chemistry - A European Journal. 2017 Mar 17;23(16):3979–85.

223. Kamiya Y, Asanuma H. Light-driven DNA nanomachine with a photoresponsive molecular engine. Accounts of Chemical Research. 2014;47(6):1663–72.

224. Zhang H, Fu H, Shao X, Chipot C, Monari A, Dehez F, et al. Conformational changes of DNA induced by a trans-azobenzene derivative via non-covalent interactions. Physical Chemistry Chemical Physics. 2018;20(35):22645–51.

225. Liang X, Nishioka H, Mochizuki T, Asanuma H. An interstrand-wedged duplex composed of alternating DNA base pairs and covalently attached intercalators. Journal of Materials Chemistry. 2010;20(3):575–81.

226. Asanuma H, Nishioka H, Ishikawa T, Liang X. Preparation of photoresponsive DNA tethering ortho-methylated azobenzene as a supra-photoswitch. Current Protocols in Nucleic Acid Chemistry. 2011;(SUPPL.46).

227. Ramezani H, Dietz H. Building machines with DNA molecules. Nature Reviews Genetics [Internet]. 2020;21(January). Available from: http://dx.doi.org/10.1038/s41576-019-0175-6

228. Strauss S, Jungmann R. Up to 100-fold speed-up and multiplexing in optimized DNA-PAINT. Nature Methods. 2020 Aug 1;17(8):789–91.